

Modernisations and digitalizations of fast timing  
techniques for  $\gamma - \gamma$  and  $e^- - \gamma$  timing and  
lifetime measurements in middle-heavy rare earths nuclei

**Inaugural-Dissertation**

zur  
Erlangung des Doktorgrades  
der Mathematisch-Naturwissenschaftlichen Fakultät  
der Universität zu Köln

vorgelegt von

**Nikolaus Andreas Harter**  
aus Bergisch Gladbach

Köln 2023

**Berichterstatter:**

Prof. Dr. Dr. h. c. Jan Jolie  
Prof. Dr. Peter Reiter

**Tag der letzten mündlichen Prüfung:**

25. September 2023

# Abstract

This doctoral thesis presents the modernisation and digitalization of two different experimental techniques and the results of different nuclear structure experiments in: The Orange conversion electron spectrometer setup was revised, rebuild in many hardware units and the usability has been restored by extensive software development of a control and acquisition software. Two different measurement modi are supported: a scan modes, which allows for conversion electron spectroscopy of an energy range during  $\gamma$ -source and in-beam measurements and an continuous mode, where one conversion electron energy can be selected by the strenghts of the magnetic field generated by the Orange spectrometer. Additionally, the implementation and validation of the digital fast timing technique with the recently commissioned fast-sampling digitizers Caen V1730 and additionally V1751 has been carried out. The digitizers have been installed and thoroughly been investigated and characterized in terms of time resolution and time walk and the settings of the integrated digital constant fraction discriminators have been optimized for digital fast-timing experiments. Both developments have successfully been commissioned in  $e^- - \gamma$  and  $\gamma - \gamma$  fast-timing lifetime measurements in nuclei belonging to the neutron midshell  $N = 104$ ,  $A \approx 180$  region.

The lifetime results of four tungsten and osmium isotopes are discussed within the context of the deformation and transitional phenomena in the neutron midshell  $N = 104$  region. All investigated nuclei lie at the edge of the strongly deformed region whose center is represented by the midshell-midshell nucleus  $^{170}\text{Dy}$ .

For  $^{176,178,180}\text{W}$ , fast-timing methods using the newly revised and commissioned Orange conversion electron spectrometer and the Cologne HORUS spectrometer were employed. Different fusion evaporation reactions were utilized to populate excited states in these tungsten isotopes, allowing for the measurement of lifetimes for the  $2_1^+$ ,  $4_1^+$ ,  $6_1^+$ , and  $8_1^+$  yrast states, with an additional measurement of the  $10_1^+$  state in  $^{176}\text{W}$ . The extracted quadrupole deformation parameters, reduced transition probabilities, and  $B_{4/2}$  ratios were compared with Interacting Boson Model 1 calculations, confirming the deformed prolate rotor nature of the investigated tungsten isotopes.

In the case of  $^{182}\text{Os}$  the low-lying yrast states  $2_1^+$ ,  $4_1^+$ , and  $6_1^+$  were studied using the newly implemented and commissioned digital fast-timing technique of the IKP. For the first time, lifetimes were determined for the  $4_1^+$  and  $6_1^+$  states, while the lifetime of the  $2_1^+$  state was re-evaluated to remove inconsistencies in the literature. The obtained lifetimes and extracted  $B(E2)$  values were analyzed in terms of collective signatures and transitional phenomena. The calculated  $B(E2; 4_1^+ \rightarrow 2_1^+)/B(E2; 2_1^+ \rightarrow 0_1^+)$  ratio of 1.39(7) supported the interpretation of  $^{182}\text{Os}$  as a rigid rotor, and its significance was discussed alongside neighboring isotopes and isotones within the framework of the interacting boson model 1. Furthermore, the structure of  $^{182}\text{Os}$  was investigated under consideration of the influences of competing factors such as the nearby collective deformed region,  $\gamma$ -soft rotors,  $X(5)$  symmetry, and neighboring regions of shape coexistence in low excitation states. The study of higher-lying excitation bands in osmium isotopes and the associated isotones helped explain the structural transitions occurring at  $^{182}\text{Os}$ , shedding light on the interplay of the different structural influences.





# Contents

<b>1</b>	<b>Introduction</b>	<b>3</b>
1.1	Lifetime measurements and fast-timing techniques	3
1.1.1	The fast-timing method	3
1.1.2	The analogue fast-timing setup and related analysis methods	5
1.1.3	Digital timestamp determination and digital fast-timing	6
1.1.4	Development of digital timing related software components	8
1.2	Conversion electron spectroscopy	12
1.2.1	Inner conversion	13
1.2.2	Principle of the Orange electron spectrometer	13
1.2.3	Modernisation of the Orange spectrometer setup	16
1.2.4	Exemplary Orange measurement and lifetime determination in $^{98}\text{Mo}$	19
1.3	Nuclear structure in the neutron midshell $A = 180$ mass region and nuclear models	21
1.3.1	The geometric rigid rotor model	22
1.3.2	Interacting Boson Model (IBM)	24
<b>2</b>	<b>Lifetime measurements in the tungsten isotopes <math>^{176,178,180}\text{W}</math></b>	<b>27</b>
<b>3</b>	<b>Systematic investigation of time walk and time resolution characteristics of CAEN digitizers V1730 and V1751 for application to fast-timing lifetime measurement</b>	<b>43</b>
<b>4</b>	<b>Lifetime measurements in low yrast states and spectroscopic peculiarities in <math>^{182}\text{Os}</math></b>	<b>57</b>
<b>5</b>	<b>Summary and Conclusion</b>	<b>67</b>
<b>6</b>	<b>Outlook</b>	<b>71</b>
6.1	Ongoing development and modernization at the Orange conversion spectrometer setup	71
6.1.1	Consideration about the power supply	71
6.1.2	Conversion electron calibration source	72
6.1.3	New Detector frame	73
6.2	Ongoing development in digital fast-timing methods	74
6.2.1	The new fast-timing test stand	74
6.2.2	Wave tracing and multiplicity filter for timing experiments	74
6.2.3	Machine learning and neural networks for timestamp determination	75
6.3	Future experiments using digital fast-timing and the Orange spectrometer	77
	<b>Bibliography</b>	<b>79</b>
<b>7</b>	<b>Appendix</b>	<b>83</b>
7.1	Elements of the graphical user interface of the software <code>NewOrange</code>	83
7.1.1	Main window	83
7.1.2	Orange current display	84
7.1.3	Temperature monitoring	85
7.1.4	Cup current monitoring	86

7.2	Useful tools for the Orange analysis . . . . .	87
7.2.1	Calibration of the Orange magnetic field . . . . .	87
7.2.2	Calculation of Orange current and electron residual energy . . . . .	87
7.2.3	Creation of an Orange conversion electron spectrum and heatmap . . . . .	88
7.3	Setup of the CAEN data acquisitions system to a fast-timing experiment . . . . .	91
	<b>List of Figures . . . . .</b>	<b>95</b>
	<b>List of publications . . . . .</b>	<b>97</b>
	<b>Acknowledgments . . . . .</b>	<b>99</b>
	<b>Contribution . . . . .</b>	<b>101</b>
	<b>Curriculum vitae . . . . .</b>	<b>103</b>
	<b>Erklärung zur Dissertation . . . . .</b>	<b>105</b>



# 1 | Introduction

## 1.1 Lifetime measurements and fast-timing techniques

Lifetime measurement of excited states of atomic nuclei is an important key ingredient to obtain structural information about excited nuclei and underlying electromagnetic properties [1, 2]. Knowing the lifetime of an excited state of a nucleus can help in understanding collective or single-particle structures and phase shape transitions by extracting the reduced transition probability  $B(\sigma L; J_i \rightarrow J_f)$  between two excited states [1–3]. The reduced transition probabilities, also associated with transition matrix element, can be used to classify and compare different nuclei in different theoretical frameworks and models. Throughout the evolution of nuclear physics, numerous techniques for determining lifetimes from millions of years down to femtoseconds and even lower have been developed. The lifetimes observed in this work all lie within the picosecond to nanosecond regime, hence, the fast-timing method is the selected timing method. The fast-timing method and related technical implementations are described in the following.

### 1.1.1 The fast-timing method

The fast-timing method is a reliable tool for determining lifetimes of excited nuclear states between several microseconds and a few picoseconds. Fast-timing generally works like a stop watch for a populating and depopulating transition cascade of a state of interest [4, 5]. A precise point in time, which indicates the population or the depopulation of the excited state of interest is a requirement to enable fast-timing methods. The detection of a transition depends on how the transition manifests, for example as a  $\gamma$ -ray, a conversion electron or any particle decay. In this work,  $\gamma$ -rays and conversion electrons were used as time-giving transition indicators. To determine the lifetimes of excited states,  $\gamma$ - $\gamma$ ,  $\gamma$ - $\gamma$ - $\gamma$ ,  $e^-$ - $\gamma$  and  $e^-$ - $\gamma$ - $\gamma$  correlations were used. The threefold coincidences were used to select the  $\gamma$ -ray cascade of interest to clean the coincidence and time spectra from unwanted contamination. The time stamps of incoming  $\gamma$ -rays or conversion electrons and the time-difference between two consecutive transitions is determined by different technical implementations, which are described in Sec. 1.1.2 and 1.1.3.

Due to the intrinsic time resolution of the components contained in the timing setup, the time-differences between two signals scatter statistically convoluted with the lifetime of the state of interest, leading to a delayed time-difference distribution. The delayed time-difference distribution is described by a convolution of an exponential tail and the prompt response function (PRF), which depends on the timing system [6]:

$$D(t) = n\lambda \int_{-\infty}^t PRF(t' - C^P) e^{-\lambda(t-t')} dt' + n_r, \quad \lambda = \frac{1}{\tau}, \quad (1.1)$$

where  $C^P$  is the time-difference centroid (first moment) of the PRF,  $\tau$  the lifetime of the state and  $n_r$  is the random background contribution. The PRF is the time-difference distribution obtained for two signals with a time-difference of zero in comparison to the time resolving power of the timing system. The full width at half maximum (FWHM) of the PRF, which is considered as the time resolution, and the centroid position of the PRF are dependent on detector properties, time pick-off devices and also the  $\gamma$ -ray energy. The exponential tail of the distribution becomes visible, if the lifetime between the signals is long compared to the intrinsic time resolution of the timing system. The slope method [5] can be used to directly determine lifetimes that are longer than the time resolution of the energy corresponding PRF. This method involves fitting an exponential decay to the pure exponential part (slope) of the time-difference distribution Eq. 1.1. The lifetime  $\tau$  is then obtained as the reciprocal of the decay constant.

To access lifetimes values below the time resolution of the corresponding setup, the centroid-shift method is used. In the centroid-shift method, the lifetime is derived from the time shift between the centroids of the measured delayed and the energy-corresponding prompt time-difference distributions:  $\tau = C_D - C_P$ . The centroid position of the delayed distribution  $C_D$  is defined as [6]:

$$C_D = \langle t \rangle = \frac{\int_{-\infty}^{\infty} tD(t)dt}{\int_{-\infty}^{\infty} D(t)dt}. \quad (1.2)$$

Both situations, slope method and centroid shift, are illustrated in Fig. 1. In the right part of the figure, delayed distributions of a long and a short lifetime compared to the time resolution of the PRF are shown. The exponential slope fit is indicated by the red line. The centroid shift in the case of the short lifetime is indicated by  $C_D$ . Furthermore, in Fig. 1, the presence of the energy-dependent time walk (TW) is illustrated, which is caused by technical factors within the time pick-off devices [7–9]. The amplitude of the incoming signal plays a significant role in the occurrence of time walk. Depending on the signal processing technique, such as leading-edge timing (LED) or constant fraction discrimination, the time stamp is determined differently. LED measures the time stamp when the signal surpasses a certain threshold, resulting in a relatively pronounced time walk that varies based on the signal shape and rise time (which is usually a constant of a detector system). On the other hand, constant fraction discrimination shapes the signal in a bipolar manner, and the time stamp is determined by the zero crossing, leading to smaller time walks compared to LED. In both cases, the magnitude of the time walk is influenced by the signal amplitude. Consequently, the centroid position of the PRF, denoted as  $C_P$ , shifts with the signal amplitude. If the TW is calibrated for the experimental setup, the lifetime of an intermediate state can be derived according to:

$$\tau = C^D - TW(E_{\text{feeder}}, E_{\text{decay}}). \quad (1.3)$$

In this work, LaBr<sub>3</sub>(Ce)detectors were used for all fast-timing experiments due to their exceptional balance between time and energy resolution. For an energy combination of a 779-344 keV  $\gamma$ -ray cascade emitted from <sup>152</sup>Gd, the time resolution is approximately 350 ps with a well-adjusted

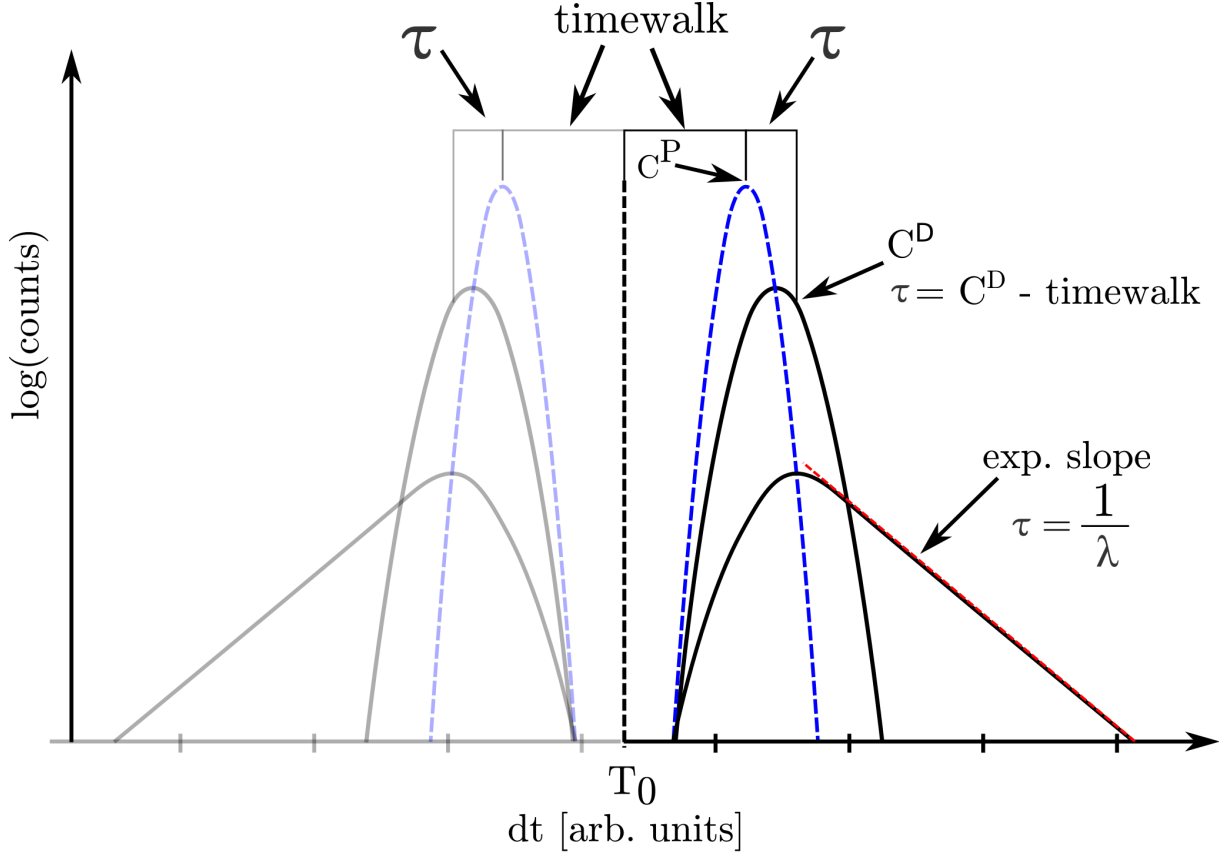


**Figure 1:** The principles of the fast-timing methods. The dashed blue distribution represents the PRF and  $C_P$  is the centroid position of the PRF. The shifted distribution is obtained when the lifetime of the state under investigation is in the range of the resolution of the PRF. The lifetime  $\tau$  is found in the delayed shift of the centroid of the time-difference distribution  $C_D$ . The exponential slope is obtained when the lifetime is greater than the resolution of the PRF. The straight line fit to the exponential part of the slope to extract the lifetime is shown in red. The right half of the figure shows the simple centroid shift approach of the fast-timing analysis. The right and pale left part together illustrate the centroid difference method. The doubled time walk is the prompt response difference, also known as PRD.

CFDs or digital CFDs [8–10]. The intermediate  $2_1^+$  state has a lifetime of 46.9(3) ps [11].

### 1.1.2 The analogue fast-timing setup and related analysis methods

The established analogue fast-timing setup is constructed by using 2 or more fast-timing detectors e.g. LaBr<sub>3</sub>(Ce). Fast-timing detectors need to provide two output signals, one for the time branch, the other for the energy branch of the fast-timing setup. In the case of the here used LaBr<sub>3</sub>(Ce) scintillators with optically coupled photomultiplier tubes (PMT), the positive dynode signals are used as energy signals and are directly digitized in the data acquisition system (DAQ). The negative anode signals are used as input signals for constant fraction discriminators (CFD). The CFD determines a precise timestamp of the signal by a constant fraction shaping procedure,

which strongly reduces the time walk [8, 9, 12].

The logical time signals coming from the CFDs are used as start and stop inputs for a time-to-amplitude converter (TAC). A TAC generates a logic signal with an amplitude proportional to the time-difference between two incoming CFD signals. The output signal of the TAC is fed into the DAQ as the corresponding time-difference associated with the two energy signals. A sketch of this setup is given in Fig. 2 taking into account all parts of the figure, also the grey shaded parts. A delay in one of the time branches enables the possibility to apply the mirror symmetric centroid difference method (MSCD) [13], where a detector combination  $D_1, D_2$  can be used in both directions as  $D_{\text{start}}$  and  $D_{\text{stop}}$  and vice versa. By interchanging start and stop, two time-difference distributions are gained, the delayed and the anti-delayed distribution with centroids  $C_D$  (delayed) and  $C_{AD}$  (anti-delayed). As described Sec. 1.1.1, the positions of the PRFs are effected by energy dependent time walk. The centroid difference of the PRFs of the time-difference distributions is called prompt response difference (PRD). The PRD has to be calibrated for every fast-timing setup using standard  $\gamma$ -ray sources, e.g.  $^{152}\text{Eu}$  and  $^{133}\text{Ba}$ . Both of these sources emit  $\gamma$ -rays with well-known energy and lifetimes of intermediate states. The lifetime  $\tau$  is than determined by [13]:

$$\tau = \frac{\Delta C - PRD(E_{\text{feeder}}, E_{\text{decay}})}{2}, \quad \text{with } \Delta C = C^D - C^{AD}. \quad (1.4)$$

The Generalized Centroid Difference (GCD) method [14] offers an easy solution for the analysis of large-scale fast-timing experiments. In the MSCD/GCD method, time-difference distributions from all detector combinations are combined, reducing the analysis effort significantly. The centroid difference method is illustrated in Fig. 1 considering left and right side of the picture, where  $PRD = 2 \cdot TW$  [15].

### 1.1.3 Digital timestamp determination and digital fast-timing

In recent years, the advent of digitally implemented CFD algorithms with picosecond precise timestamp determination has enabled digital timing techniques, that simplify both timing setups and analysis procedures. Compared to the analogue setup, no external electronic modules such as CFDs or TACs are required and the complex electrical circuits are reduced to a single cable from a detector to the DAQ. Figure 2 shows a schematic drawing of an analogue and digital setup, with parts only used in the analogue setup drawn in grey shade.

Fast sampling digitizers have sufficient sampling rates from 250 MS/s up to several GS/s to trace even short electrical detector pulses with rise times down to a few nanoseconds, e.g. pulses from a PMT in case of  $\text{LaBr}_3(\text{Ce})$ scintillation detectors. A digital wave trace is an array of numbers, where each number represents a digital representation of the amplitude  $A$  of the analogue input signal at a specific time  $t_n$ . The time-difference between two amplitude samples is called sample period and is defined by the reciprocal of the sample frequency of the digitizer. A number of different time-determining methods e.g. [16]: leading edge discrimination, peak

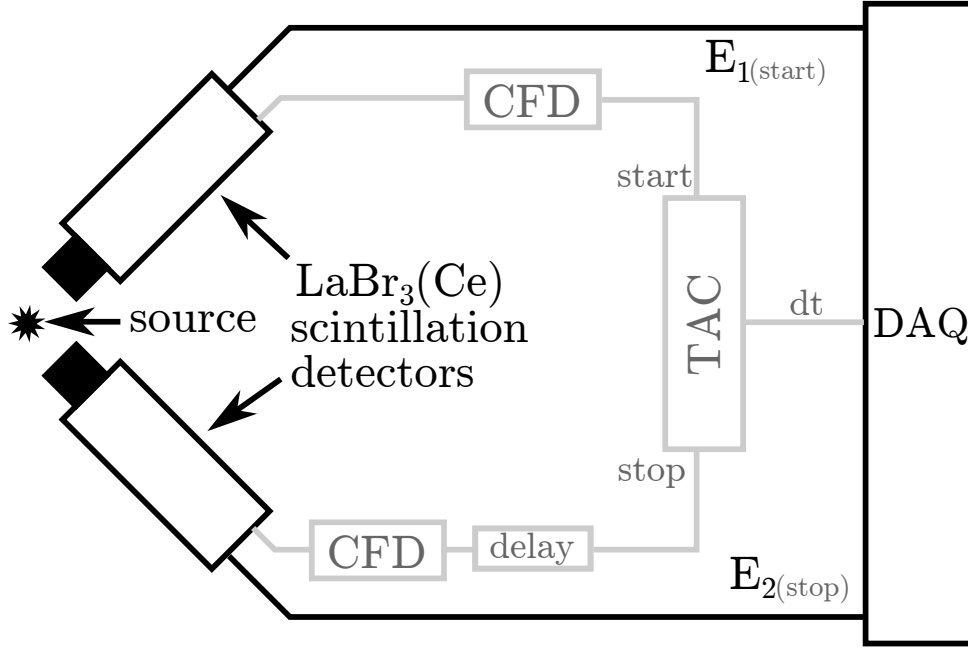


**Figure 2:** The schematic drawing depicts the differences between a digital and an analogue fast-timing setup using two LaBr<sub>3</sub>(Ce) detectors. The components that are exclusively utilized in an analogue setup are illustrated in a grey shade

discrimination, center of gravity discrimination, inflection discrimination (zero crossing of the second derivative) or constant fraction discrimination and a number of different optimizations and filters for each method can be applied to a digitized wave trace. In this work, only constant fraction discrimination was used to determine a time stamp of an incoming detector pulse.

A digitally implemented CFD algorithm basically works equal to an analogue CFD circuit: a digitized wave trace of an analogue detector pulse is duplicated, one of the duplicates is inverted and delayed by a specific delay time  $d$ , while the other one is attenuated by a defined fraction  $f$ . After applying the delay and fraction procedures, the resulting signals are added to each other to generate the typical bipolar CFD signal [12]. To achieve a timestamp precision below the sample period of a digitizer, digital CFDs utilize different interpolation procedures to determine the zero crossing between the last sample before and the first sample after the zero crossing of the constant fraction shaped digital wave. Either linear or cubic interpolation are commonly used. The timestamp of the interpolated zero crossing serves as the timestamp of the incoming signal and is up to three orders of magnitude more precise as the sample period. The digitizers of the model V1730 manufactured by CAEN S. p. A., recently established at the Institut für Kernphysik, Cologne, and used in this work, have a sample rate of 500 MS/s, 14 bit analog-digital-converters (ADC) and use linear interpolation between the last sample before the zero crossing and the first sample after the zero crossing. As presented in the second publication (see Sec. 3), these digitizers achieve time resolutions of about 350 ps for the 779-344 keV  $\gamma$ - $\gamma$  cascade with 1.5"  $\times$  1.5" LaBr<sub>3</sub>(Ce)detectors.

Digital timing is a nearly direct application of the centroid shift method [5, 6] without the



necessity of additional analogue modules to determine timestamps and time-differences. The time-differences are taken in the offline analysis by sorting algorithms consistent with the sequence of the applied energy gates. If the energy gates are applied in the sequence  $E_{\text{feeder}} - E_{\text{decay}}$ , a delayed time-difference distribution is obtained. Exchanging the energy gate sequence results in an identical but mirrored (with respect to  $T_0$  of the timing system) delayed time-difference distribution. After a time walk calibration and a calibration of the time-difference zero reference  $T_0$ , a simple centroid shift analysis can be applied to the data, where the lifetime results in

$$\tau = C^D - TW(E_1, E_2).$$

The situation in the right part of Fig. 1. The digital fast-timing system of the IKP, based on the CAEN V1730 digitizers, has been thoroughly characterized, validated, and optimized in the second publication (Sec. 3). Detailed explanations of the method, results and the commissioning of the system are provided there.

#### 1.1.4 Development of digital timing related software components

To process the raw binary data of the CAEN digitizers and address the digital timing analysis procedure, the software Fast-timing Sorting Code (FT-soco [17]), based on the former version SOCO-v2 [18], was developed as part of this work. The full code is provided in the IKP version control system gitlab under <https://gitlab.ikp.uni-koeln.de/soco/ft-soco>. FT-soco is written in parallel C++ close to the computational hardware and, hence, provides high-performance and reliability. The software is expandable and provides an easy to understand code structure. Ft-soco is able to read the binary format of the free acquisition and control software CoMPASS [19], which is used in the IKP to control the DAQ consisting of CAEN digitizers V1782 and V1730 [20] and the binary format of the NOMAD DAQ of the ILL [21], used for the data acquisition of experiments at the Lohengrin spectrometer. The binary format of one hit of the CoMPASS data format is shown in Lst. 1.1 and the implementation of the listmode readers for the CoMPASS data and the ILL data are found in the class `CaenReader` and in the namespace ILL of FT-soco, respectively.

**Listing 1.1:** Binary format of a single hit of the CoMPASS acquisition and control software in 8 bit-words (bytes).

```

1 01 02 03 04 05 06 07 08 09 10 11 12 13 14(15 16)17 18 19 20 21 22 23 24
2 BD BD CH CH TS TS TS TS TS TS TS TS AC AC(ES ES)FL FL FL FL WS WS WS WS
3
4 BD: board nr (16 bit)
5 CH: Channel nr (16 bit),
6 TS: Timestamp (64 bit),
7 AC: ADC channel (16 bit),
8 [ES: Energy Short (16 bit)] only when DPP-PSD firmware is in use by one board
9 FL: Flags (32 bit)
10 WS: Number of wave samples (32 bit)
```

Ft-soco combines all features to carry out a digital timing analysis. Core part of this analysis approach is the digital timing matrix (dt-matrix) module. A timing matrix is a matrix with one energy and one time-difference dimension

$$(E, dt)$$

and represents a projection of a timing cube. A timing cube has two energy and one time-difference dimensions

$$(E_1, E_2, dt)$$

and contains the full information of a timing experiment. The projection is done by applying an energy gate to the first energy dimension. The function `void incrementMatrix(gate_first, gate_last, hit_first, hit_last)` within this module handles three-dimensional fast-timing events that consist of at least two fast-timing detector hits and a gate sequence. It calculates the time-difference, denoted as  $dt$ , in a consistent manner using the equation:

$$dt = t_{\text{gate non-matching}} - t_{\text{gate matching}}.$$

By implementing this approach, it ensures that the time-difference is consistently measured in a specific physical direction, either feeder - decay (yielding a delayed time-difference distribution) or decay - feeder (yielding a mirrored delayed time-difference distribution), regardless of which detector detected each corresponding gamma-ray. The analogue analysis approach based on the MSCD [13] and GCD [14] produces two timing matrices, a start and a stop matrix leading to delayed and anti-delayed time-difference distributions when cuts in the matrices are applied. The approach used here generates one single matrix, which contains the information of both the former start and stop matrices. By applying a cut in this matrix, a single time-difference distribution is obtained. Hence, no centroid difference method must be used but only a simple centroid shift method can be applied like explained in Sec. 1.1.1.

The core function of the dt-matrix module of ft-soco is `void incrementMatrix(...)` and is given in Lst. 1.2. The variable `defined_zero` defines the zero point, which is half the size of the dt-matrix.

Before constructing a dt-matrix, it is necessary to correct for runtime-differences between different detector combinations, similar to TAC shifts. Each detector combination has a unique time-difference offset, which can be calibrated by creating dt-matrices for each combination for a  $\gamma$  cascade with a prompt lifetime. The time-difference distribution, obtained by a cut in these matrices have to be aligned by applying a constant offset. As exemplified in Lst. 1.3, these offsets are applied by providing a dt-shift.conf file. In Lst. 1.2, the object `dts-shifter` is an instance of the `DTsShifter` class (digital-timestamp-shifter), which provides the unique time-difference offsets of the current detector combination (as obtained from the dt-shift.conf) at line 28 in Lst. 1.2. This time offset is added to the time-difference in line 28 of Lst. 1.2.

**Listing 1.2:** Excerpt of the function `void incrementMatrix()`, which generates the time-difference between two fast-timing hits and increments the digital timing matrix.

```

1 // definition of void incrementMatrix()
2 void DTMatrix::incrementMatrix(GateConstIterator gate_first,
3                               GateConstIterator gate_last,
4                               HitConstIterator hit_first,
5                               HitConstIterator hit_last) {
6
7 // find a LaBr hit in the event which matches the given fast-timing gate
8     auto matching =
9         findMatchingLaBrHit(gate_first, gate_last, hit_first, hit_last);
10 // find a LaBr hit in the event, which not matches the given fast-timing gate
11     auto non_matching =
12         findNonMatchingLaBrHit(hit_first, hit_last, matching);
13 // set the energy value of the gate matching LaBr hit to matching_adc
14     const uint32_t matching_adc =
15         std::min(matching->adc, static_cast<uint16_t>(8191));
16 // set the energy value of the gate non-matching LaBr hit to non_matching_adc
17     const uint32_t non_matching_adc =
18         std::min(non_matching->adc, static_cast<uint16_t>(8191));
19 // get the channel id of the matching and the non-matching LaBr hits
20     const uint16_t matching_channel_id = config_[matching->id].channelID(),
21         non_matching_channel_id =
22         config_[non_matching->id].channelID();
23 // set the initial value of the time-difference to 0
24     uint64_t time_diff = 0;
25 // take the time-difference consistent to t_{non-matching}-t_{matching}
26 // and subtract it from the zero point
27     time_diff = defined_zero_ - (matching->timestamp -
28                                 non_matching->timestamp);
29 // apply the digital time stamp shift of the unique detector combination
30     time_diff = time_diff + dts_shifter_.offset(matching_channel_id,
31         non_matching_channel_id);
32 // increment the digital timing matrix at the position of the energy
33 // of the non-matching LaBr and the time-difference or the maximum of the
34 // time axis of the dt-matrix
35     sym_matrix_.increment(non_matching_adc, time_diff > MAX ? MAX :
36         time_diff);
37 }

```

**Listing 1.3:** Format of the digital timestamp shift file for four fast-timing detectors with ids 50 - 53

```
1 # channel-ID-1 channel-ID-2 shift
2 50 51 9
3 50 52 201
4 50 53 3
5
6 51 52 192
7 51 53 -6
8
9 52 53 -198
```

The module DT-Matrix of FT-soco allows some additional options for refinement of the analysis:

The use of the `-W from,to` option allows for the specification of a specific time-difference window, similar to a TAC gate in analogue fast-timing analysis. This option restricts the passage of time-differences within a defined range, starting from a specific value up to a maximum value. By employing this option, events with random coincidences, which do not contribute to the desired time-difference distribution, are eliminated. As a result, the peak-to-background ratio of the coincidence spectrum is enhanced, and the background correction procedure becomes more effective.

An experimental feature has been implemented for threefold LaBr coincidence analysis. The `-t` option enables the `dt-matrix` command to process threefold LaBr coincidences. This functionality allows for LaBr triggered fast-timing, where a specific gamma-ray cascade of interest can be selected, and the timing spectra can be cleaned from unwanted time-correlated coincidences. When the `-t` option is set, the first gate in the `gate.conf` file is assumed as the trigger gate, and the second LaBr gate defined in the `gate.conf` serves as the fast-timing gate for the desired transition.

Table 1.1 presents the available options for the `dt-matrix` command, including the `-W` option for defining the time window, the `-t` option for enabling threefold LaBr coincidence analysis, and various other optional settings for calibration, timestamp units, add-back, BGO thresholds, channel configuration, exclusion configuration, shift files, and output directory.

In addition to the capability to read the binary data obtained from the CAEN data acquisition software CoMPASS with the online determined digital CFD timestamps of the detector pulses, `ft-soco` provides a binary data reader for the waves binary format of CoMPASS, where a wave trace is recorded for every single detector signal. An offline digital CFD was implemented in `ft-soco` providing full control over the shaping parameters of the digital CFD in contrast to the limited CFD shaping parameters of the online CFD. Details about a possible usage of the offline digital CFD are given in the outlook (see Chapter. 6).

The third publication (Chap. 4) presents the results of the commissioning experiment of the newly established digital timing method using fast-sampling digitizers at the IKP in the form of lifetime measurements in  $^{182}\text{Os}$ .

Option	Description	Optional
-C calibration-config	The name of the calibration configuration file	Yes
-T timestamp-unit	sets desired timestamp unit (tick) in fractions of the DAQ timestamp accuracy	No
-W from,to	defines time window in bins (-T) relative to the gate-matching hit, in which fast-timing hits should be processed	Yes
-a	Enable add-back for segmented detector types and add-back gate support	Yes
-b bgo-thresholds	Enable Compton suppression using associated BGO channels and set BGO threshold values	Yes
-c channel-config	The name of the file containing the channel configuration	Yes
-d DT-shift-config	Set name of digital timestamp shift config file	No
-g gate-config	The name of a gate config file	Yes
-e exclude config	set name of exclusion config file	Yes
-s shift dir	set name of the shift file directory	Yes
-t	threefold LaBr coincidence is enabled. The trigger gate has to be the first gate in gate.conf	Yes
-o output-dir	The name of the output directory (created if not existent, default: "gg_matrix/")	Yes

**Table 1.1:** Excerpt from the manual (<https://gitlab.ikp.uni-koeln.de/soco/ft-soco/-/blob/master/manual/manual.pdf>): Options accepted by the ‘dt-matrix’ command. Details about the calibration configuration, the Compton suppression, the channel configuration, the gate configuration, the exclude configuration and the shift directory are given in the manual.

## 1.2 Conversion electron spectroscopy

Structural properties of nuclei such as excitation energies, transition probabilities, multipolarities and others and are preferably accessible by the detection of  $\gamma$ -rays. For transitions with high multipolarities and low  $\gamma$ -energies, the inner conversion effect increasingly replaces the  $\gamma$ -decay. Especially in heavy nuclei, inner conversion becomes more and more a competing decay mechanic, due to the  $Z^3$  dependency of the conversion effect. Additionally, E0 (electronic monopole) transitions between states of the same spin and parity, are strictly forbidden as single-photon transitions due to angular momentum selection rules [2, 22], and are only visible as conversion decays (and double-photon decay, which is much less likely than conversion [22]). Hence, conversion electron detection plays an essential role in the nuclear structure investigation of medium and heavy nuclei [23]. The accurate spectroscopy of conversion electrons requires an efficient and precise measuring device, which has been fulfilled by the Orange spectrometer, a highly effective and high resolution electron lens [24, 25]. Conversion electron spectroscopy is an established measurement method at the IKP, Cologne [26–30] and in order to ensure the ongoing capability of conversion electron spectroscopy at the IKP, the experimental setup of the Orange spectrometer

was extensively revised, modernized and optimized in the scope of this work. The modernization includes the replacement of several hardware parts, the complete redevelopment of the control and recording software as well as the realignment of the Orange spectrometer into the beamline and the commissioning of the measuring system. The modernisation are in detail addressed in Sec. 1.2.3. The modernized Orange spectrometer was commissioned in the scope of the first publication (Chap. 2) in the application for fast-timing lifetime measurements in the nuclei  $^{178,180}\text{W}$ .

### 1.2.1 Inner conversion

Inner conversion is an electromagnetic process that competes with a  $\gamma$ -decay [2]. It is possible, that the wave functions of orbital electrons  $e_i^-$  of the inner atomic shells  $i = K, L_{1,2,3}, M_{1-5}, N_{1-7}, \dots$  penetrate the nuclear volume, which is not zero as its radius is approximated by  $R = 1.2 \text{ fm} \cdot A^{\frac{1}{3}}$ . The electromagnetic multipole fields of the nucleus and the electron interact directly [2, 23]. In this case, the nucleus does not decay by a  $\gamma$ -transition but by transferring its excitation energy to the electron, which is emitted with an residual kinetic energy of

$$E_{k,i} = E_\gamma - \epsilon_i, \quad (1.5)$$

where  $\epsilon_i$  is the binding energy of the electron of a specific shell  $i$ . The probability of an inner conversion process is quantified by the conversion coefficient  $\alpha_i$ , defined as the ratio between the number of  $\gamma$ -decays  $N_\gamma$  and the number of conversion decays from the  $i$ -th atomic orbital  $N_i$  that occur within the same time [2]:

$$\alpha_i = \frac{N_i}{N_\gamma}. \quad (1.6)$$

The total conversion coefficient is the sum of all conversion coefficients of all atomic orbitals [23]:

$$\alpha_{tot} = \sum_i \alpha_i \quad , i = K, L_{1,2,3}, M_{1-5}, N_{1-7}, \dots \quad (1.7)$$

Conversion coefficients exhibit an increase proportional to  $Z^3$ , the multipolarity of the transition, and a decrease in transition energy [2]. This dependency is demonstrated in Fig. 3, which depicts the relationship between the conversion coefficient and these three variables. Very strong converted transitions are nearly invisible and E0 transitions are completely invisible in  $\gamma$ -ray spectroscopy due to selection rules of the spin quantum number. A typical conversion electron spectrum shows several electron peaks for each transition due to the different binding energies of the electrons of different atomic shells (see Fig. 5 in Sec. 1.2.2).

### 1.2.2 Principle of the Orange electron spectrometer

An Orange electron spectrometer [24] focuses electrons from a source into a detector using a magnetic field. The key components of the Orange spectrometer are specially shaped coils

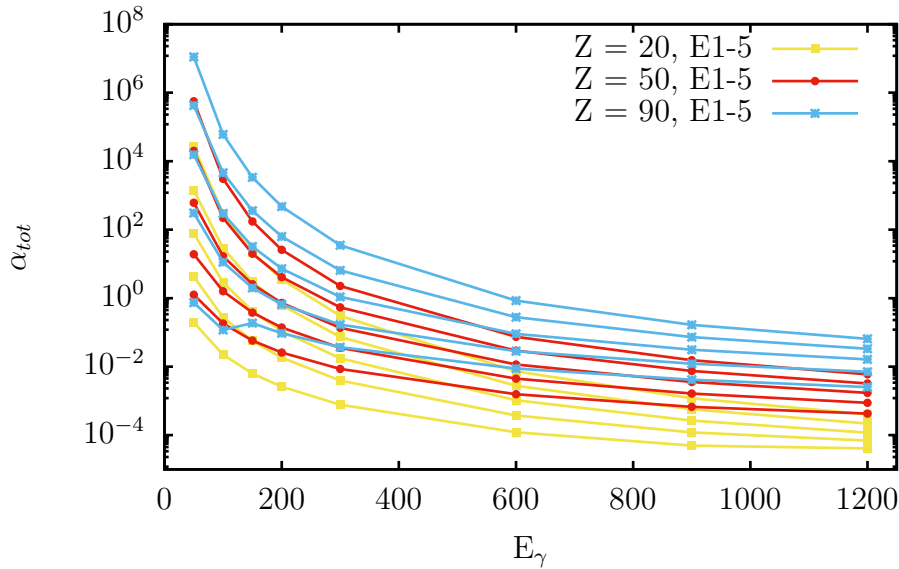


**Figure 3:** Total conversion coefficients in dependency of  $E_\gamma$ , multipolarity of transition with  $\sigma L = E1-5$  and  $Z = 20, 50, 90$ . The lowest line of each color belong to the E1 transitions and the others increase up to E5 transition. The plot looks similar for magnetic multipoles. The lines are meant to guide the eyes. Data is taken from Ref. [31].

arranged in a torus configuration with equal angles between the individual coils. By circulating current through the coils, a quasitoroidal magnetic field is induced. Electrons entering the magnetic field are deflected in such a way that the trajectories of electrons of the same kinetic energy intersect in one point. A counter is located at this point. Electrons of different kinetic energies cannot reach the counter, disregarding scattering effects and loops of the electrons (see Fig. 4) within the spectrometer in this idealized representation.

Considering a plane of a coil in cylindrical coordinates, as shown in Fig. 4, the local magnetic field  $B_\phi$  has only an azimuthal component, which is proportional to  $1/r$ , where  $r$  is the distance from the symmetry axis ( $z$ -axis) [24]:

$$B_\phi(r) = \mu_0 \frac{NI}{2\pi r} \quad (1.8)$$

where  $\mu_0$  is the magnetic permeability,  $N$  is the number of coils,  $I$  is the current through the coils.

Outside the coils, the magnetic field vanishes, allowing electrons to move undistracted. Assuming the electron source is point-like, it follows that electrons entering the magnetic field will always move in the  $(r, z)$  plane of a coil. This motion is depicted in Fig. 4 for different entrance angles.

If an electron moves with velocity  $v$  precisely within this plane, it is forced by the Lorentz force to follow a cycloid path with a radius of rotation  $\rho_B$ . For our consideration, the rotation radius

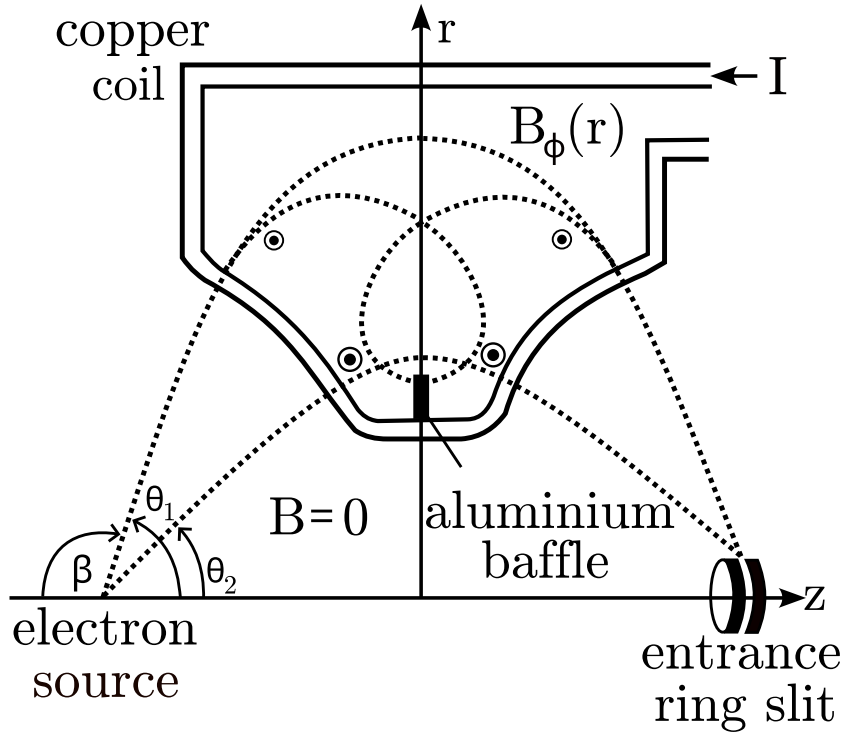


**Figure 4:** Electron trajectories with different entrance angles. Figure taken from Ref. [30].

can be approximated by the curvature radius  $\rho$  for homogeneous magnetic fields [25, 30]:

$$m \frac{v^2}{\rho} = evB_{\Phi} \quad (1.9)$$

with  $B_{\Phi}$  from Eq. 1.8 and the relativistic mass  $m = \frac{m_0}{\sqrt{1-(\frac{v}{c})^2}}$ . It follows the dependency between the electron momentum  $p$  and the current circulating in the coils  $I$  [24, 30]:

$$eB\rho = p = \frac{\rho \mu_0 N}{r 2\pi} I, \quad (1.10)$$

where  $\frac{\rho}{r}$  is a constant of the spectrometer depending on the coil's shape.

In electron spectroscopy, it is common to express the electron's momentum in terms of  $B\rho$  [25, 30], as the momentum (and not the energy) of the electron is proportional to the magnetic field or coil current. To obtain the energy- $B\rho$  relationship, Eq. 1.10 is substituted into the total relativistic energy resulting in:

$$E_{e^-} = \sqrt{(m_0c^2)^2 + e^2c^2(B\rho)^2} - m_0c^2. \quad (1.11)$$

In summary, the theory of the Orange spectrometer states that electrons with energy proportional to the coil current are selected and deflected into the counter by the magnetic field. This characteristic makes the Orange spectrometer particularly suitable for conversion electron spectroscopy [24]. The Orange spectrometer is particularly well-suited for coincidence experiments due to its



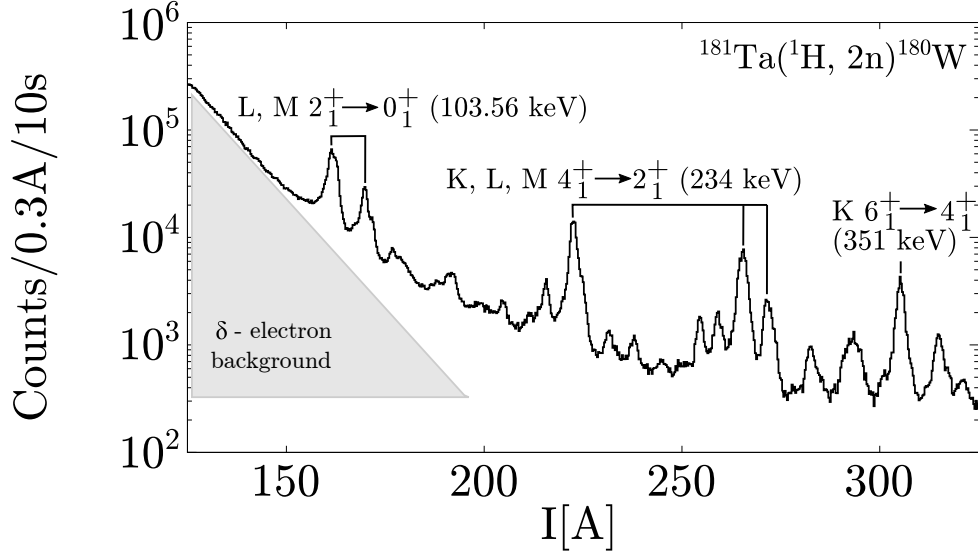


**Figure 5:** Conversion electron spectrum of  $^{180}\text{W}$  as measured with the Orange spectrometer of the IKP. Conversion electron peaks of low yrast transitions and the  $\delta$ -electron background are indicated.

high efficiency ( $>20\%$  in case of the Orange spectrometer of the IKP) and complete insensitivity to Compton events, which arise from the scattering of  $\gamma$ -rays and which typically strongly overlap with gamma spectra. Hence, no time-correlated background is detected in the electron counter. This capability enhances the reliability and accuracy of coincidence measurements performed using the Orange spectrometer, making it a valuable tool in lifetime experiments.

Figure 5 shows an exemplary conversion electron spectrum of  $^{180}\text{W}$  as measured with the Orange spectrometer of the IKP within a current range between 125 - 325 A. The current is proportional to the residual energy of the conversion electrons. The in-beam reaction and electron peaks of yrast low transitions are indicated. Electron spectra acquired from in-beam ion-scattering experiments commonly exhibit contamination from an exponentially decreasing background attributed to  $\delta$ -electrons [32]. The  $\delta$ -electrons arise from the energy transfer through inelastic Coulomb scattering, which results in the ionization of target atoms or projectile ions. Consequently, excited electrons are emitted as  $\delta$ -electrons within a cone that opens in the direction of the beam. The intensity of the  $\delta$ -electron background is influenced by factors such as target thickness, the energy and charge number of the projectile. Higher values of these parameters lead to increased  $\delta$ -electron background levels [32]. The  $\delta$ -electron background and its exponential decrease is marked in Fig. 5

### 1.2.3 Modernisation of the Orange spectrometer setup

The work on the Orange spectrometer was initiated during the state examination thesis project [33] of the author, where significant preparatory work has been conducted. However, the testing and commissioning of the Orange spectrometer setup was not possible at that time due to the

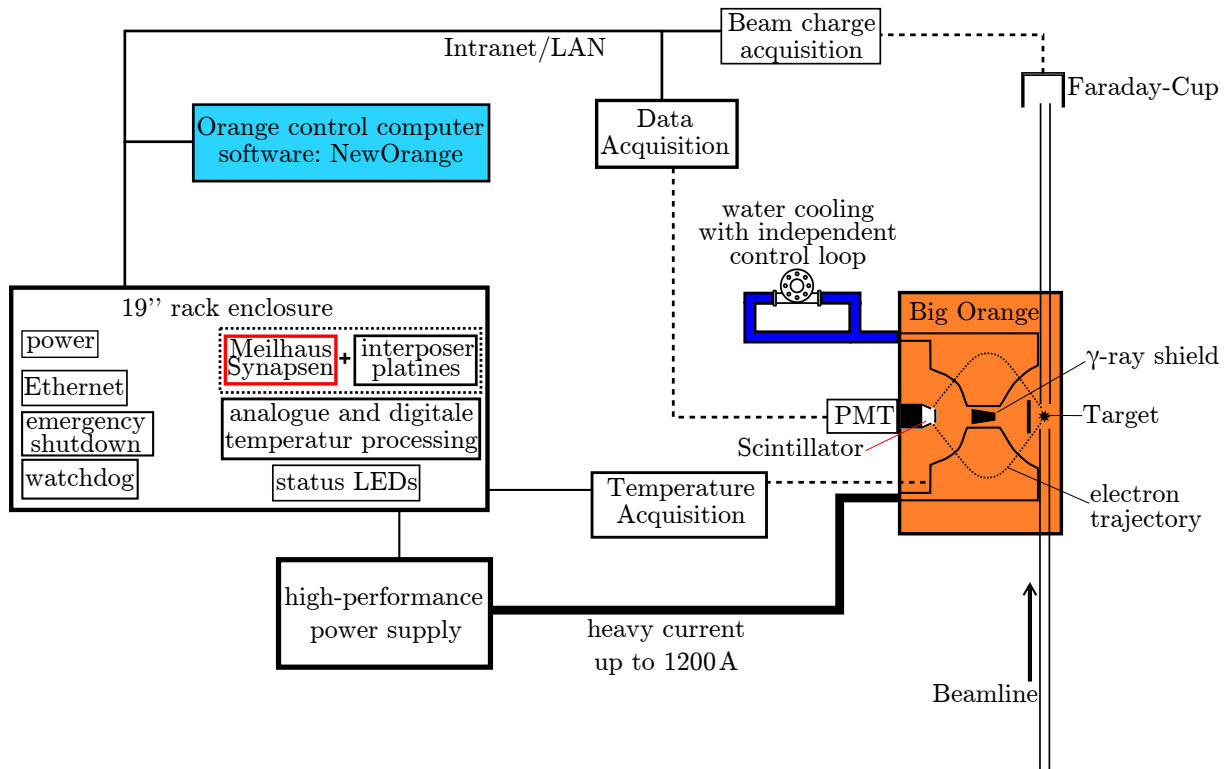
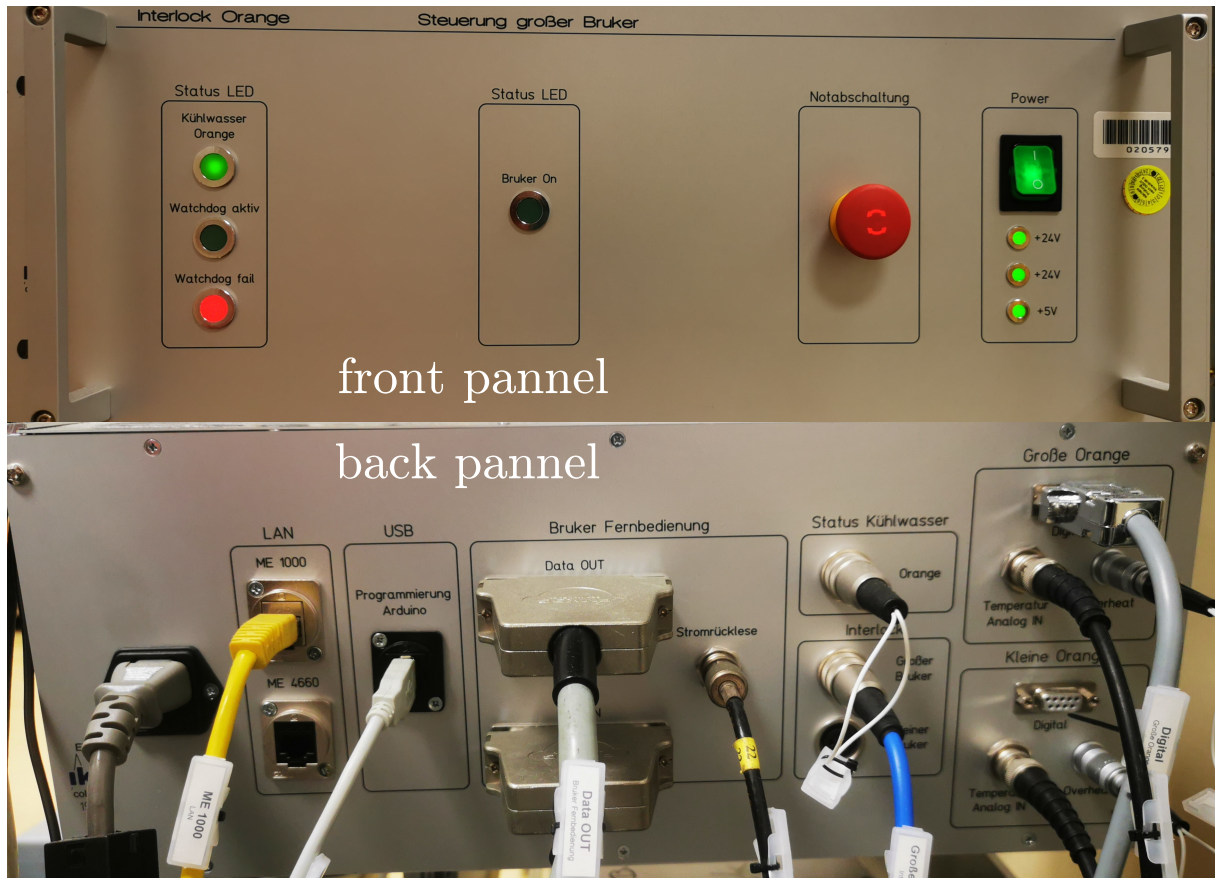


**Figure 6:** Schematic representation of the current Orange setup of the IKP. Thin solid lines represent digital input/output streams, dashed lines represent analogue data streams.

inoperability of the high-performance power supply unit of the Orange spectrometer. In the scope of this work, additional hardware components were added, and the complete software was rewritten to eliminate structural misconceptions of the first project. The complete and current experimental setup with all necessary hardware parts is illustrated in Fig. 6. In this work, nearly all hardware components, which communicate with and are controlled by the new software called **NewOrange** were installed in a newly designed 19"-rack enclosure, which is depicted in Fig. 7. This enclosure combines all controlling parts and complicated but static wiring.

The hardware parts, that were found necessary during testing and added in this work are

1. a 'watchdog', which ensures the functionality of the software **NewOrange** through an independent hardware unit in form of an Arduino Nano [34]. When the Orange spectrometer is in operation, the heavy current applied to the spectrometer can reach values of several 100 A, which heats the internal coil. The software **NewOrange** monitors the temperature of the coil, and in the event that it exceeds a specified threshold, the software initiates a shutdown of the spectrometer. To ensure proper heat control even if the software or the computer fails, the following mechanism was implemented: **NewOrange** periodically toggles a specific bit of one of the digital I/O boards. A watchdog is employed to monitor this toggle operation. If the waiting period exceeds one second, the watchdog enters an "interrupt" state and initiates the hardware-side shutdown of the high-performance power supply of the Orange spectrometer.



front pannel

back pannel

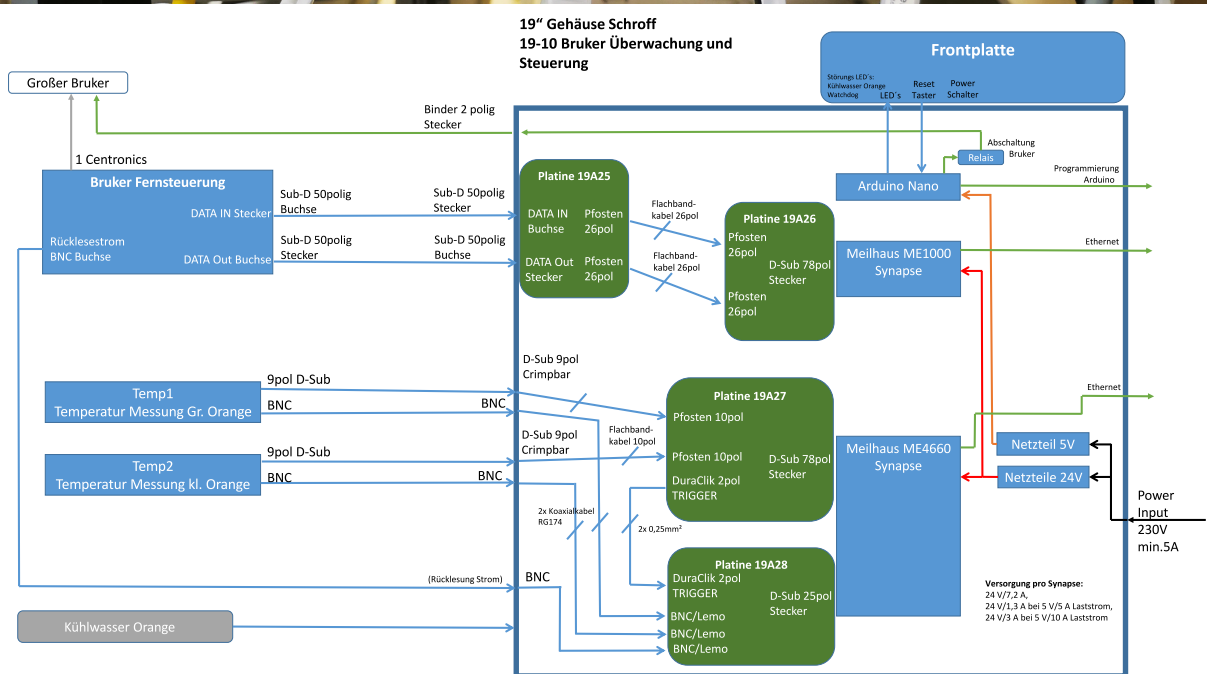


**Figure 7:** On top: Front panel of the 19" rack enclosure. Middle: Back panel of the 19" rack enclosure. Bottom: Internal structure and connections of the 19" rack enclosure.

2. a manual emergency shutdown button. This button directly initiates the hardware-side shutdown of the high-performance power supply of the Orange spectrometer.
3. water-proof temperature sensors. The previous temperature sensors of the Orange coil possess exposed electrical components that are prone to short-circuiting and malfunction caused by condensed water dripping from the coils. This occurs under conditions of excessively cold water cooling and high humidity in the surrounding air. The new sensors are cast in a block of synthetic resin and are insensitive to the influence of moisture.
4. The primary water cooling of the Orange spectrometer was extended by a control unit, which controls the water pump, that circulates the circuit in dependence of the temperature of the Orange coils. The system is functional, however, the frequency modulator of the pump controller interacts with the temperature sensing and causes malfunctions of the acquisition of the sensors. Until this interaction is resolved, the control system cannot be used and the water cooling has to be controlled manually.

The primary function of the software `NewOrange` is the precise control of the current flowing through the Orange coil and monitoring the temperature of the coil. It also performs various other tasks, such as displaying real-time measurement values online, capturing beam currents, initiating and stopping the data acquisition, and continuously reading the acquired data of the electron scintillation counter. The software operates in two main modes: the scan mode and the manual mode. The scan mode is primarily used to measure conversion electron spectra: It scans an adjustable range of currents, proportional to residual energies of electrons with a user-defined step size and a predetermined duration per step. In the manual mode, the user simply sets the current to a desired value to measure the conversion electrons of a specific transition over a long time period.

`NewOrange` is written in the object-oriented programming language C++17. The graphical user interface is set up in Qt5. The software is multi-threaded due to multiple different tasks and requirements imposed on the software. During all operations, the GUI remains responsive and fluid. The source code, documentation and user manual is stored in the gitlab of the IKP [35]. The GUI elements are presented in App. 7.1.1. Some software tool useful for an Orange analysis, as the procedure to generate an Orange conversion electron spectrum from the single scintillator spectra of each step of a scan run or the calibration of the magnetic field of the Orange coil to the residual energy of the electrons are presented in App. 7.2.

#### 1.2.4 Exemplary Orange measurement and lifetime determination in $^{98}\text{Mo}$

As an example and a demonstration of the abilities of the Orange spectrometer to detect E0-transitions with high-lying decay energies, a conversion electron spectroscopy and a lifetime measurement of the first excited  $0_2^+$  state of the nucleus  $^{98}\text{Mo}$  is presented here. A  $0.5\text{mg}/\text{cm}^2$   $^{98}\text{Mo}$  target was exposed to a proton beam at an beam energy of 6.7 MeV inside the Orange spectrometer. Excited states were populated with a  $^{98}\text{Mo}(p, p')^{98}\text{Mo}$  coulomb excitation reaction.

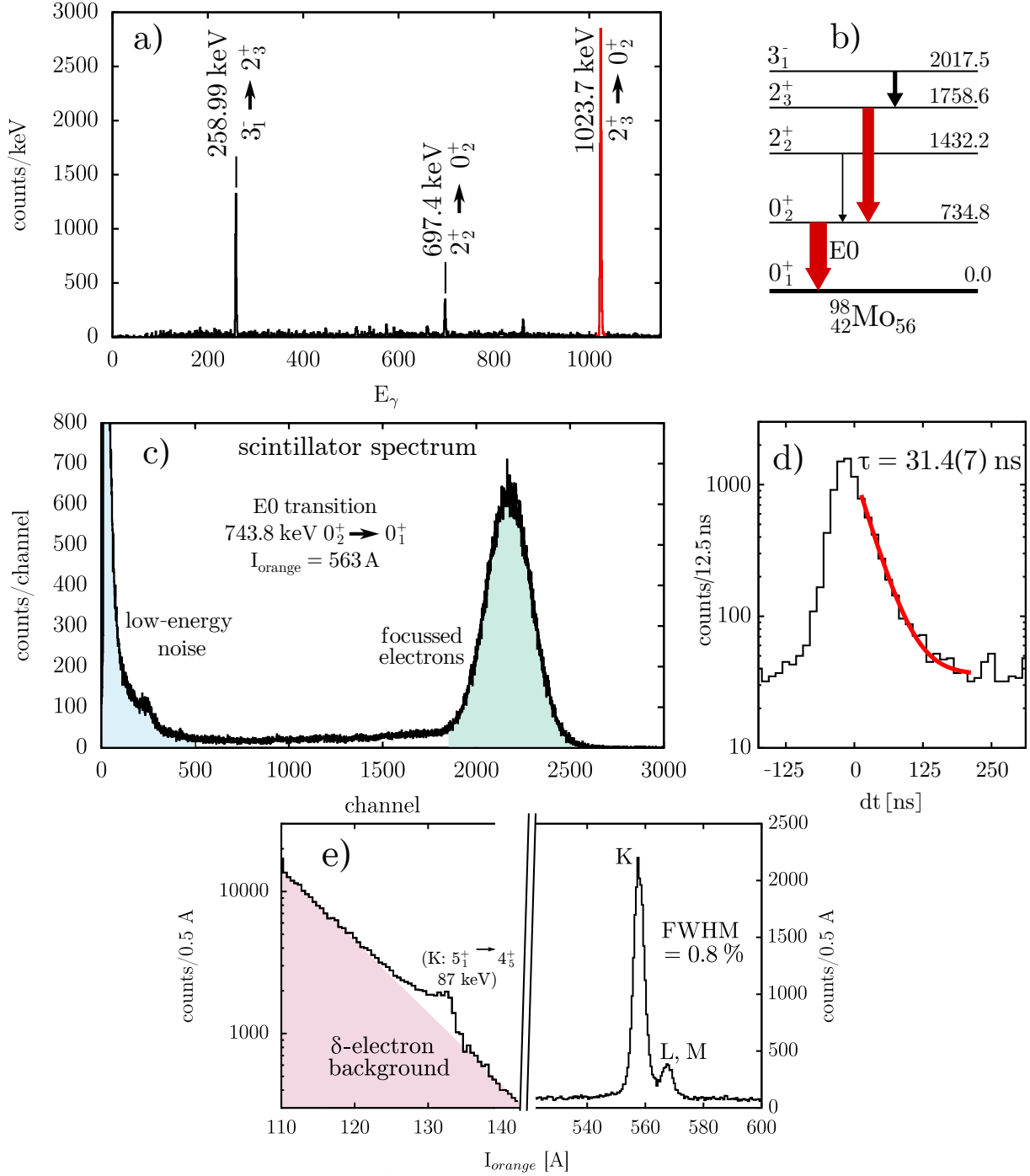


**Figure 8:** a)  $\gamma$ -ray spectrum between E0 transition  $0_2^+ \rightarrow 0_1^+$  and coincident  $\gamma$ -rays. No background subtraction was applied. The transitions in coincidence with the conversion electron decay are indicated. b) Level scheme corresponding to the coincidence spectrum. The widths of the arrows indicate the relative ratio between the transitions. c) Scintillator spectrum of the electron counter in coincidence with  $\gamma$ -ray spectrum in (a) at an Orange current of 563 A. d) Time-difference distribution between conversion electrons of the E0 transition  $0_2^+ \rightarrow 0_1^+$  with 743.8 keV. The lifetime amounts to  $\tau = 31.4(7) \text{ ns}$ . e) Conversion electron spectrum obtained from a scan of the current range 110 A to 600 A. Note the logarithmic scaling of the y-axis in the low-energy range. The  $\delta$ -electron background shows a perfect exponential decay.

The Orange spectrometer was equipped with 5 high-purity Germanium (HPGe) detectors in bismuth-germanate (BGO) active Compton suppression shields.

Figure 8 shows a spectrum of  $\gamma$ -rays detected with the HPGe detectors in coincidence with conversion electron decays of the  $0_2^+$  state to the ground state detected with the Orange spectrometer (a) and the corresponding level scheme (b). The spectrum is displayed without any background subtraction. The emphasized peak (red) was used for the lifetime analysis. Figure 8c shows the electron spectrum from the electron scintillation counter for an Orange current of 563 A. The peak corresponds to the focussed conversion electrons of the E0 transition  $0_2^+ \rightarrow 0_1^+$  with 743.8 keV, which is also depicted in the level scheme in (b). The lifetime analysis reduces to a simple slope-fit to the exponential part of the decay curve [2]:

$$A(t) = b + A_0 * e^{(-\lambda t)}$$

in the distribution of the time-differences between the conversion electrons of the  $0_2^+ \rightarrow 0_1^+$  transition measured with the Orange spectrometer and the  $\gamma$ -rays from the feeding  $2_3^+ \rightarrow 0_2^+$  transition with an energy of 1023.7 keV measured with the HPGe detectors.  $b$  represents the background level and  $\lambda$  the decay constant. The lifetime corresponds to  $\tau = 1/\lambda$ . The time-difference distribution with the slope-fit is depicted in Fig. 8d. The lifetime of the  $0_2^+$  state amounts to  $\tau = 31.4(7)$  ns and is in good agreement with the literature value of  $\tau = 31.5(13)$  ns [36]. Figure 8e shows the conversion electron spectrum of  $^{98}\text{Mo}$  in a split range between 110 A and 600 A. In the low energy range, nearly pure  $\delta$ -electron background was measured (except the weak contribution of the K-peak of the  $5_1^+ \rightarrow 4_5^+$  transition (87 keV)). In the high energy range, the K, L and M peaks of the E0  $0_2^+ \rightarrow 0_1^+$  transition are depicted. The L and M peaks are not well resolved. The energy resolution in this energy range is about 0.80 %.

The first publication included in this thesis (see Chap. 2) presents the first  $e^- - \gamma$  and  $e - \gamma - \gamma$  lifetime measurements after the modernization of the Orange spectrometer setup in the nuclei  $^{178,180}\text{W}$  for short lifetimes of  $< 100$  ps. Important insights into the structure of these nuclei were gained and the results were discussed in connection with the structural phenomena and transitions in the mass region  $A \approx 180$ .

### 1.3 Nuclear structure in the neutron midshell $A = 180$ mass region and nuclear models

All nuclei investigated with fast-timing methods in this work belong to the neutron-deficient region around  $A \approx 180$ . The nuclei of interest here,  $^{176,178,180}\text{W}$  and  $^{182}\text{Os}$ , lie close to the neutron midshell  $N = 104$  at the edge of the strongly deformed region between the neutron shell closures 82 and 126 and proton shell closures 50 and 82. The isotopic chains with  $Z = 74$  (W) and  $Z = 76$  (Os) are rich of transitional and deformation phenomena driven by a competition between the microscopic nature of single-particle structures and underlying collective shape degrees of

freedom [1, 37]. The former dominates towards the proton shell closure ( $Z = 82$ ) and the latter is particularly pronounced with increasing valence nucleons respectively holes. In all nuclei under investigation, collective deformation dominates, which is deduced from the low excitation energies of the first excited  $2_1^+$  states, the ratio of the excitation energies of the  $4_1^+$  and  $2_1^+$  states, also called  $R_{4/2}$  ratio, of around 3.3, which is called the rigid rotor limit [38], and high reduced transition probabilities of around 100 W.u. or higher. In all tungsten and osmium isotopes investigated here, these three signatures are already known yet and speak for rotor behavior. An additional and important signature is the  $B_{4/2}$ , which is defined as

$$B_{4/2} = \frac{B(E2; 4_1^+ \rightarrow 2_1^+)}{B(E2; 2_1^+ \rightarrow 0_1^+)}. \quad (1.12)$$

The main goal of the experiments conducted in this study was to determine this value for the studied nuclei via lifetime measurements of the first excited yrast states. This value holds significant importance as it provides a strong indication of the particular shape phase of a nucleus. Values of around 1.43 are a strong indication for rotational, values of around 2.0 for spherical, vibrational behavior. This will be detailed in the model descriptions in the following. The first publication (Chap. 2) presents the findings derived from lifetime measurements conducted on tungsten nuclei, while the third publication presents the results obtained from lifetime measurements on  $^{182}\text{Os}$  (Chap. 4).

As nuclei close to the neutron midshell, a considerably large number of valence nucleons/holes is found in the investigated nuclei and microscopic model approaches like the application of the nuclear shell-model becomes nearly impossible. The high dimensions of the model spaces and matrix diagonalization operations, representing the solution effort for the residual interactions between single nucleon configurations require a huge amount of computing time and memory. Therefore, the nuclear many-body system of valence nucleons is to be considered macroscopically and inner structures and transitions are considered as collective properties and motion, respectively: the rigid rotor model for deformed nuclei and the interacting boson model (IBM) are taken as frameworks to classify and understand the experimental results obtained in this work.

### 1.3.1 The geometric rigid rotor model

The geometric model developed by Bohr and Mottelson [38–40] considers a nucleus as a geometric body, which collective motion follows the intrinsic interactions among the nucleons and their arrangement in the nuclear potential resulting from the tension between electromagnetic and nuclear forces. The model provides a theoretical framework to explain the rotational motion and deformation of atomic nuclei. Shape parameters  $\beta$  (quadrupole deformation) and  $\gamma$  (axial asymmetry) are used to describe the geometry of the nucleus. The Hamiltonian of the model takes into account the potential energy based on these shape parameters and can be expanded to include various deformation shapes and phase coexistence phenomena. Different parameter

combinations lead to different shapes of nuclei [40]:

1.  $\beta = 0, \gamma = 0^\circ$  leads to spherical shapes
2.  $\beta > 0, \gamma = 0^\circ/60^\circ$  leads to prolate or oblate shapes, respectively
3.  $\beta > 0, 0^\circ < \gamma < 60^\circ$  leads to  $\gamma$ -unstable shapes, with a special case of  $\gamma = 30^\circ$  for triaxial shapes

For a specific case of a prolate nucleus with  $\beta > 0$  and  $\gamma = 0^\circ$ , the Hamiltonian simplifies to a rigid rotor:

$$\hat{H} = \frac{\hbar^2 \hat{L}^2}{2 \mathfrak{J}}, \quad (1.13)$$

where the rotational spectrum and energies of the states are described using the moment of inertia  $\mathfrak{J}$  and rotational angular momentum operator  $\hat{L}$ . The energy eigenvalues of the rotational band based on intrinsic excitations follow a pattern determined by the rotational motion, which is depicted in Fig. 9b, the middle pattern. The low-lying band head energies in deformed nuclei are typically associated with quadrupole vibrations, which are phonon excitations. The  $K = 2$  mode, known as " $\gamma$ -vibration," represents the dynamic departure from axial symmetry. The  $K = 0$  band head is often known as " $\beta$ -vibration". This mode preserves the axial symmetry, as the shape of the nucleus vibrates along the symmetry axis.

The ground state of even-even nuclei has always a nuclear spin  $J^\pi = 0^+$  and corresponds to  $K = 0$ . The rotational spectrum of the lowest-lying states, called yrast band, can be determined using the expression for rotational energy [38, 40]:

$$E_{rot}(J) = \frac{\hbar^2}{2\mathfrak{J}} J(J+1), \quad K = 0, J \text{ even.} \quad (1.14)$$

The ratio of energies between the  $4_1^+$  and  $2_1^+$  states, denoted as  $R_{4/2}$ , serves as a signature of deformation and rotational motion and the limit for rigid rotors equals  $R_{4/2} = 3.33$ .

The model also allows for the calculation of reduced E2 transition probabilities (B(E2) values), which describe the strength of an electromagnetic transition between excited states. For an intra-band transition, the reduced E2 transition probability is given as [1, 38, 39]:

$$B(E2; J_i \rightarrow J_f) = \frac{5}{16} e^2 Q_0^2 \langle J_i 0 2 0 | J_f 0 \rangle^2, \quad (1.15)$$

where  $\langle J_i 0 2 0 | J_f 0 \rangle$  is the Clebsch-Gordon coefficient [1] for an exemplary transition  $2_1^+ \rightarrow 0_1^+$ ,  $e$  is the electric charge unit and  $Q_0$  the intrinsic quadrupole moment. From Eq. 1.15 follows the second strong signature for rigid rotors next to the  $R_{4/2}$  ratio, the ratio of the B(E2) values of the  $4_1^+$  and the  $2_1^+$  states called the Alaga rule for rigid rotors [1]:

$$B_{4/2} = \frac{B(E2; 4_1^+ \rightarrow 2_1^+)}{B(E2; 2_1^+ \rightarrow 0_1^+)} = \frac{10}{7} \approx 1.43. \quad (1.16)$$

In this work, the main effort consisted of determining the  $B_{4/2}$  value for the investigated nuclei .



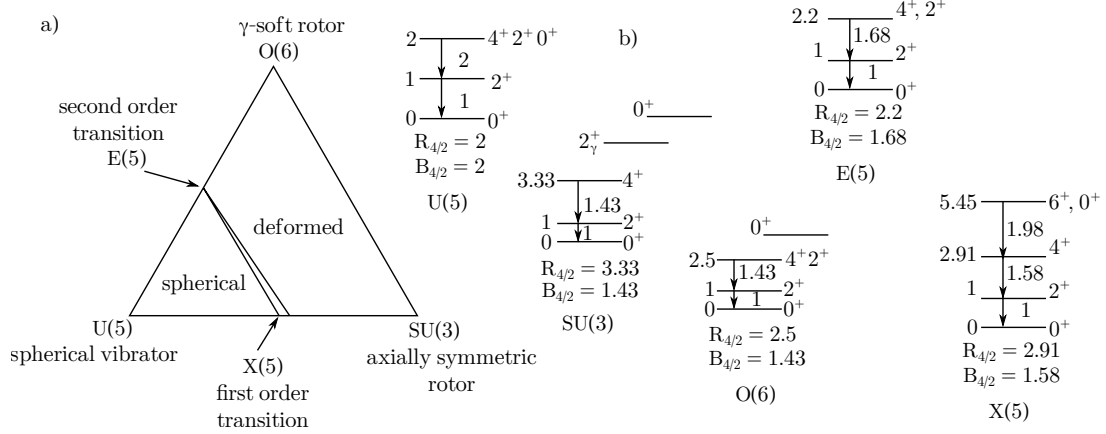


**Figure 9:** a) The Casten triangle with indicated U(5), SU(3) and O(6) symmetries and critical point symmetries X(5) and E(5) [1]. b) Level spacing,  $R_{4/2}$  and  $B_{4/2}$  signatures of each symmetry.

### 1.3.2 Interacting Boson Model (IBM)

The interacting boson model (IBM) is a group theoretical model for collective behaviour of nuclei and becomes particularly applicable far from closed shells [1, 41]. It was introduced in 1974 by F. Iachello and A. Arima as an algebraic approach to describe excitation levels and transition probabilities in even-even nuclei [1, 41, 42]. It is not in all details compatible with the geometric model of Bohr and Mottelson, but it leads to a general picture of the nucleus closely allied to the macroscopic geometric model. In the framework of the IBM, closed shells of either protons or neutrons and excitations out of them, are neglected and valence nucleons or holes, counted from the nearest closed shell, couple to bosons under specific bosonic commutation relations [1, 43]. In the sd-IBM-1, the simplest case of the model, the valence nucleons are treated in pairs as s and d bosons, with angular momenta 0 and 2. No distinction is made between proton and neutron bosons. Since an s boson has only one magnetic substate and a d boson has five, the s-d boson system can be mathematically viewed as a six dimensional space [1] with the basis states as basis. This system can be effectively described using the U(6) algebraic group structure [41]. The U(6) group has diverse subgroups and can be decomposed into different sequences of subgroups, resulting in distinct symmetries known as U(5), SU(3) and O(6) [41, 43–45]. These symmetries represent the well-defined geometric properties of spherical harmonic vibrators, axially-symmetric rigid rotors and axially-asymmetric,  $\gamma$ -soft rotors, respectively. The relationships between these symmetries are represented by the Casten triangle [1, 46], depicted in Fig. 9a. The critical point symmetries X(5) and E(5) describe the transitional points between spherical and deformed shapes via first and second order transitions, respectively [47, 48]. Not every point within the Casten triangle corresponds to a valid nuclear structure, but every distinct nuclear structure can be associated with a point within the triangle.

The IBM Hamiltonian in the form of the extended consistent Q-formalism, which is commonly

used, is given by [41]:

$$\begin{aligned}
\hat{H} &= \epsilon \hat{n}_d + a_0 \hat{P} \hat{P} + a_1 \hat{L} \hat{L} + a_2 \hat{Q}_\chi \hat{Q}_\chi + a_3 \hat{T}_3^2 + a_4 \hat{T}_4^2, \\
\text{with } \hat{n}_d &= d^\dagger \tilde{d}, \\
\hat{P} &= \frac{1}{2} (d \tilde{d}) - \frac{1}{2} (s \tilde{s}), \\
\hat{L} &= \sqrt{10} \hat{T}_1, \\
\hat{Q}_\chi &= (d^\dagger \tilde{s} + s^\dagger \tilde{d}) + \chi (d^\dagger \tilde{d})^{(2)}, \\
\hat{T}_J &= (d^\dagger \tilde{d})^{(J)} \quad \text{with } J = 0, 1, 2, 3, 4.
\end{aligned} \tag{1.17}$$

Depending on the context, this Hamiltonian reduces to different sub-combinations of the operators, e.g. the combination for the SU(3) symmetry for an ideal prolate rotor [41]:

$$\hat{H} = a_1 \hat{L} \hat{L} + a_2 \hat{Q}_\chi \hat{Q}_\chi, \text{ for } \chi = -\frac{\sqrt{7}}{2}, \tag{1.18}$$

where  $\hat{L}$  is the angular momentum operator and  $\hat{Q}$  is the quadrupole operator.

The E2 transition probability  $T(E2)$ , an important parameter for describing a nucleus, can be calculated within the IBM framework using the formula:

$$\hat{T}(E2) = e_B \hat{Q}_\chi = e_B \left[ s^\dagger \tilde{d} + d^\dagger \tilde{s} + \chi (d^\dagger \tilde{d}) \right], \tag{1.19}$$

where  $e_B$  represents the effective boson charge.



2 | Publication I:

Lifetime measurements in the tungsten  
isotopes  $^{176,178,180}\text{W}$



**Lifetime measurements in the tungsten isotopes  $^{176,178,180}\text{W}$** A. Harter,<sup>1,\*</sup> L. Knafila,<sup>1</sup> G. Frießner,<sup>1</sup> G. Häfner,<sup>1,2</sup> J. Jolie,<sup>1</sup> A. Blazhev,<sup>1</sup> A. Dewald,<sup>1</sup> F. Dunkel,<sup>1</sup> A. Esmaylzadeh,<sup>1</sup> C. Fransen,<sup>1</sup> V. Karayonchev,<sup>1</sup> K. Lawless,<sup>1</sup> M. Ley,<sup>1</sup> J.-M. Régis,<sup>1</sup> and K. O. Zell<sup>1</sup><sup>1</sup>Universität zu Köln, Mathematisch-Naturwissenschaftliche Fakultät, Institut für Kernphysik, 50937 Köln, Germany<sup>2</sup>Université Paris-Saclay, CNRS/IN2P3, IJCLab, F-91405 Orsay, France

(Received 27 October 2021; revised 7 June 2022; accepted 10 August 2022; published 24 August 2022)

Lifetimes of yrast states in the rare-earth midshell isotopes  $^{176,178,180}\text{W}$  have been measured with fast-timing methods using the Cologne iron-free Orange spectrometer and the Cologne HORUS spectrometer and with the recoil distance Doppler shift method using the Cologne coincidence plunger setup. Different fusion evaporation reactions have been used to populate excited states in the investigated nuclei. Lifetimes of the  $2_1^+$ ,  $4_1^+$ ,  $6_1^+$ , and  $8_1^+$  yrast states were measured in all three tungsten isotopes and in addition the lifetime of the  $10_1^+$  state was measured in  $^{176}\text{W}$ . Quadrupole deformation parameters, reduced transition probabilities, and  $B_{4/2}$  ratios are extracted and discussed in the context of interacting boson model 1 calculations. The results with newly determined signatures largely confirm the investigated tungsten isotopes to be deformed prolate rotors.

DOI: [10.1103/PhysRevC.106.024326](https://doi.org/10.1103/PhysRevC.106.024326)**I. INTRODUCTION**

The rare-earth midshell mass region around  $A = 178$  is characterized by a rich abundance of transitional nuclear structure phenomena [1–3]. This is caused by a competition between the microscopic nature of underlying single-particle structures and collective shape degrees of freedom [4]. The former dominates towards the proton shell closure ( $Z = 82$ ) and the latter is particularly pronounced with increasing valence nucleons or holes. The tungsten isotopes ( $Z = 74$ ) around the neutron midshell ( $N = 104$ ) lie at the edge of the strongly collective quadrupole deformed mass region around  $^{170}\text{Dy}$  [5]. Therefore, the measurement of the collective signatures of the even-even tungsten isotopes around the neutron midshell makes a decisive contribution to the delimitation of this transition region itself.

It was suggested that the investigated nuclei lie close to the X(5) critical point symmetry region [6] with a shape phase transition from spherical shapes to axially symmetric prolate shapes around  $^{178}\text{Os}$  [7–9]. This assumption could not be confirmed due to the unclear or incomplete data situation [9]. Moreover, nuclear collectivity and shape transition in rotorlike regions are usually described in terms of, e.g., the excitation energy of the first excited  $2_1^+$  state as well as its ratio to the first excited  $4_1^+$  state, called  $R_{4/2}$ , or the transition strength of the  $2_1^+ \rightarrow 0_1^+$  ground state transition and its ratio to the transition strength of the  $4_1^+ \rightarrow 2_1^+$  transition, called  $B_{4/2}$  [10]. The  $B_{4/2}$  ratio is an indication for the  $\gamma$  softness of the potential [11–13] and can also be used as a signature for shape phase transitions [6,14]. For deformed nuclei the ratio can show deviations from the Alaga rule value of 10/7. Therefore, the measurement of the tungsten isotopes  $^{176,178,180}\text{W}$ , with regard

to the transition strengths of the low-spin yrast states, forms an interesting contribution to the understanding of the nuclear structure transitions in this region.

The low excitation energies of the  $2_1^+$  states, as well as the  $R_{4/2}$  ratios, show a clear tendency towards axially symmetric rotor properties [10,15–17]. Therefore, the question arises whether this tendency is confirmed by the evolution of the  $B_{4/2}$  ratio and pronounced transition strengths of the low-spin yrast states. Consequently, the characterization of the midshell surrounding tungsten isotopes with special regard to the transition strengths of the low-spin yrast states and the  $B_{4/2}$  ratios is an interesting prospect, especially since the data are incomplete [18]. In particular, for  $^{176,180}\text{W}$  the  $B_{4/2}$  ratio is unknown. The  $B(E2; 2_1^+ \rightarrow 0_1^+)$  values are already known for all isotopes. For  $^{178}\text{W}$ , the  $B(E2; 4_1^+ \rightarrow 2_1^+)$  and an upper limit for the  $B(E2; 6_1^+ \rightarrow 4_1^+)$  were published recently [19].  $B(E2; I \rightarrow I - 2)$  values of higher-lying yrast states are completely unknown so far.

To fill these gaps, lifetime measurements of yrast states were carried out for the isotopes  $^{176,178,180}\text{W}$ . The new lifetimes allow to obtain  $B(E2)$  values for the low-spin yrast states of the given nuclei. Lifetimes of the low-spin yrast states in the investigated tungsten isotopes were measured using fast-timing methods. Additionally, lifetimes of the  $6_1^+$ ,  $8_1^+$ , and  $10_1^+$  states in  $^{176}\text{W}$  were measured with the Cologne coincidence plunger using the differential decay curve method (DDCM) [20]. The fast-timing experiments for the lifetime measurement of  $^{178,180}\text{W}$  were performed using the Cologne iron-free Orange conversion electron spectrometer. The experiment for  $^{176}\text{W}$  was performed using the Cologne HORUS cube spectrometer, equipped with  $\text{LaBr}_3(\text{Ce})$  fast-timing scintillators (LaBr) and high-resolution high-purity germanium (HPGe) detectors. Not all nuclides were measured by the plunger method because this method requires high recoil velocities of the reaction product nuclei to allow the necessary

\*Corresponding author: [aharter@ikp.uni-koeln.de](mailto:aharter@ikp.uni-koeln.de)

Doppler shifts of the  $\gamma$  lines. These were sufficiently given only in the reaction for  $^{176}\text{W}$ , and even that only at  $\gamma$  energies above 300 keV.

The excitation energies of the  $2_1^+$  states lie barely higher than 100 keV. Hence, the  $\gamma$ -ray emission is highly dominated by the internal conversion process and the emission of conversion electrons (ce) [21]. A suitable instrument to measure conversion electrons is an iron-free Orange spectrometer [22]. An Orange spectrometer consists of specially shaped copper coils to induce a magnetic field through a circulating current. Based on the applied current, electrons with a specific momentum can be selected and deflected into the narrow detector entrance window [23]. The high selectivity of the Orange spectrometer allows for a precise electron gate, specifying the cascade of interest. This allows for accurate  $e^-$ - $\gamma$  and electron tagged  $\gamma$ - $\gamma$  fast timing ( $e^-$ - $\gamma$ - $\gamma$ ) to access lifetimes in the subnanosecond regime [18,24].

The experimental details with a special emphasis on the Orange spectrometer in combination with  $\text{LaBr}_3(\text{Ce})$  fast-timing scintillators for  $e^-$ - $\gamma$ - $\gamma$  and  $e^-$ - $\gamma$  fast timing as well as the recoil distance Doppler-shift method are summarized in Sec. II. The experimental results are presented in Sec. III. The analysis of the data and the presentation of the results are followed by theoretical calculations in the framework of the interacting boson model [25] in order to be able to classify the results in a well-known context. Here, the interacting boson model 1 (IBM-1), where no distinction between protons and neutrons is made, was chosen as a successful model in collective regions [10].

## II. EXPERIMENTAL DETAILS

All experiments were conducted at the 10 MV FN Tandem accelerator of the Institut für Kernphysik (IKP) in Cologne. Excited states in  $^{176,178,180}\text{W}$  were populated via different fusion-evaporation reactions:  $^{164}\text{Dy}(^{16}\text{O}, 4n)^{176}\text{W}$  at beam energy of 80 MeV,  $^{172}\text{Yb}(^9\text{Be}, 3n)^{178}\text{W}$  at beam energy of 40 MeV, and  $^{181}\text{Ta}(^1\text{H}, 2n)^{180}\text{W}$  at beam energy of 16 MeV.

For the populating reactions the self-supporting targets  $^{164}\text{Dy}$ , 7 mg/cm<sup>2</sup> (in HORUS) and 0.9 mg/cm<sup>2</sup> (in plunger),  $^{172}\text{Yb}$ , 1 mg/cm<sup>2</sup>, and  $^{181}\text{Ta}$ , 0.5 mg/cm<sup>2</sup>, were used. The lifetimes were measured using the fast-timing technique in combination with the generalized centroid difference (GCD) method [26] as well as the recoil distance Doppler-shift (RDDS) method [27]. The reaction  $^{164}\text{Dy}(^{16}\text{O}, 4n)^{176}\text{W}$  was used both for the fast-timing experiment at the HORUS spectrometer and for the RDDS measurement at the Cologne coincidence plunger setup. The  $^{172}\text{Yb}(^9\text{Be}, 3n)^{178}\text{W}$  and  $^{181}\text{Ta}(^1\text{H}, 2n)^{180}\text{W}$  experiments were performed at the Cologne Orange spectrometer setup.

### A. Experiments with the IKP iron-free Orange spectrometer

The experiments to measure lifetimes in  $^{178,180}\text{W}$  were performed at the Orange spectrometer [22] of the IKP using  $e^-$ - $\gamma$  and  $e^-$ - $\gamma$ - $\gamma$  timing with  $\text{LaBr}_3(\text{Ce})$  scintillators. Lifetimes of the  $2_1^+$ ,  $4_1^+$ , and  $6_1^+$  states and an upper limit for the lifetime of the  $8_1^+$  state were determined for both isotopes. The conversion electron spectroscopy using the iron-free Or-

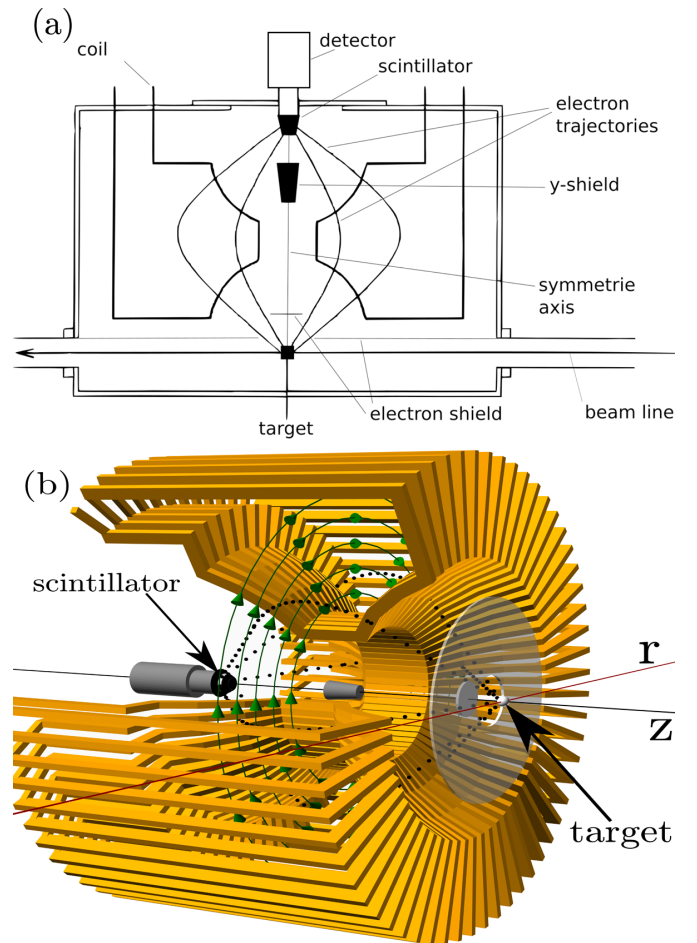


FIG. 1. (a) The elements of the Orange spectrometer, shown in a section through an  $(r, z)$  plane [30]. (b) Schematic three-dimensional model of the Orange spectrometer. The copper coils are drawn in orange. The magnetic field is indicated by the green circular arrows inside the coil volume. The circular electron shields are shown by the transparent light gray forms. The dark gray cone represents the  $\gamma$ -ray shield to shield the electron detector from unwanted  $\gamma$  rays. Possible flight trajectories of detected electrons are displayed by the black dotted curves. The symmetry axis ( $z$ ) is displayed in black and the beam axis ( $r$ ) in red.

ange spectrometer is a well-established method at the IKP [22,24,28,29]. The operating hardware as well as the controlling software was revised in 2018–2019 and, consequently, the two experiments performed in this work were also used as a commissioning of the new system.

The basic idea of an Orange spectrometer is the deflection of charged particles (i.e., conversion electrons) by a toroidal magnetic field generated by a current  $I$  circulating through specially shaped copper coils (see Fig. 1) yielding [23,31]

$$B = \mu_0 \frac{NI}{2\pi r}. \quad (1)$$

Here,  $\mu_0$  is the magnetic permeability,  $r$  the distance to the axis of symmetry, and  $N$  the number of windings. A schematic sketch of the system is presented in Fig. 1(a). The electrons are emitted from the target in a straight line towards the Orange coils and are deflected in the magnetic field towards

a plastic scintillation counter of type NE102 [22]. Based on the assumption that the electron source (target) is pointlike, it is assumed that the electrons with a selected momentum that enter the magnetic field move in the  $(r, z)$  plane of a winding, as displayed in Fig. 1(a). Electrons that do not fulfill the momentum condition do not reach the detector. An electron with velocity  $v$  is forced on a cycloid trajectory with rotation radius  $\rho_B$  which can be obtained from the radius of curvature  $\rho$  for homogeneous magnetic fields [31]:

$$m \frac{v^2}{\rho} = evB. \quad (2)$$

$B$  is calculated according to Eq. (1) and  $m = \frac{m_0}{\sqrt{1-(\frac{v}{c})^2}}$  is the relativistic mass of an electron. It follows that [23]

$$eB\rho = p = \frac{\rho}{r} \frac{\mu_0 N}{2\pi} I, \quad (3)$$

where  $\rho/r$  is a constant of the specific spectrometer depending on the shape of the coils. The electron momentum  $p$  can be expressed by the rigidity  $B\rho$  due to the proportionality of the electron momentum and the magnetic field strength or the coil current. By varying the coil current and the magnetic field, respectively, the energy of the electrons to be deflected into the plastic scintillator can be selected. By substituting Eq. (3) into the total relativistic energy

$$E_{\text{tot}} = \sqrt{(m_0c^2)^2 + p^2c^2} = E_{e^-} + m_0c^2,$$

one obtains the relationship between the electron energy and the magnetic rigidity  $B\rho$ :

$$E_{e^-} = \sqrt{(m_0c^2)^2 + e^2c^2(B\rho)^2} - m_0c^2. \quad (4)$$

The energy spectra of the scintillator counter of the Orange spectrometer are usually contaminated by an exponentially decreasing  $\delta$ -electron background, which is unavoidable in in-beam ion reaction experiments [32], as displayed in Fig. 2. The energy transfer through inelastic Coulomb scattering is sufficient to ionize the colliding target atoms and projectile ions. Thus, excited electrons are emitted as  $\delta$  electrons in a cone opening in the beam direction. The  $\delta$ -electron background increases with the target thickness and the energy and charge number of the projectile.

Electron shields consisting of aluminum are attached to the inside of the spectrometer, blocking the straight path between the target and the scintillator. The Orange spectrometer at the IKP Cologne has a spatial opening angle of  $50^\circ$  [22]. This corresponds to a solid angle coverage of approximately 15–20 % of  $4\pi$  depending on the opening width of the ring slot of the scintillator counter. In combination with the efficiency of larger than 95% of the plastic scintillator for electrons with energies more than 15 keV, this leads to an electron detection efficiency of up to 20%.

In the present experiments, electron events were used as timing signals for  $e^-$ - $\gamma$  timing and as trigger signal for  $e^-$ - $\gamma$ - $\gamma$  timing. In a first step, the Orange spectrometer is used to scan the electron spectrum and adjust the applied current according to the energy of the conversion electrons (ce). The electron counts were normalized to the beam current. Figure 2 shows scans of the electron spectra for  $^{178}\text{W}$  and  $^{180}\text{W}$

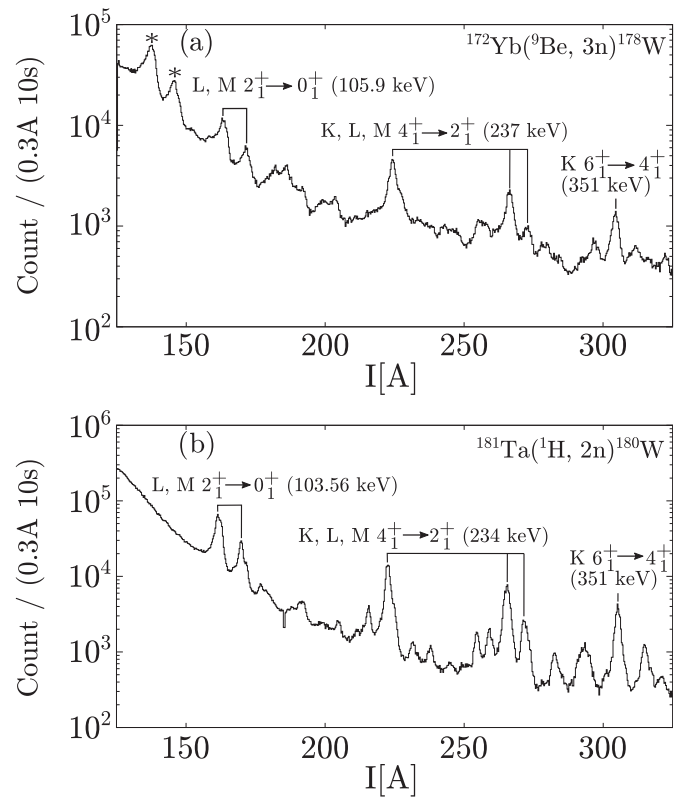


FIG. 2. Conversion electron momentum scans of  $^{178,180}\text{W}$  between 125 and 325 A corresponding to an electron residual energy range of 60 to 310 keV. The scan is performed in steps of 0.3 A with 10-s measurements and the electron counts were normalized to the beam current. The L and M peaks of the  $2^+ \rightarrow 0^+$  transition and the K, L, and M peaks of the  $4^+ \rightarrow 2^+$  of (a) the  $^{178}\text{W}$  reaction and (b) the  $^{180}\text{W}$  reaction are marked. The peaks at 137 and 144 A, marked with asterisks in (a), are the L and M peaks of the  $2^+ \rightarrow 0^+$  transition in  $^{172}\text{Yb}$  from the Coulomb excitation of the target.

between 125 and 325 A corresponding to an electron residual energy of 60 to 310 keV. The K conversion electron lines of the  $2^+ \rightarrow 0^+$  transitions with 105.9 keV for  $^{178}\text{W}$  and 103.6 keV for  $^{180}\text{W}$  are buried in the strong  $\delta$ -electron background. Therefore, the L-peaks of these transitions were used for the timing analysis. The Orange spectrometer was equipped with eight  $1.5'' \times 1.5''$  LaBr<sub>3</sub>(Ce) scintillation detectors (hereafter LaBr) and one high-purity germanium detector (hereafter HPGe) for monitoring purposes. Four of the LaBr detectors were surrounded by bismuth germanate (BGO) scintillators, which are used as an active shield to suppress background from Compton scattering. The LaBr detectors without BGO shields were excluded in the analysis due to high scattering. Effectively, this leads to a further reduction of Compton background in the shielded detectors. The dynode outputs of the LaBr detectors deliver the energy information according to the pulse height. The anode outputs of the LaBr detectors are connected to a constant fraction discriminator (CFD). The timing signals are combined into multiplexed start-stop groups according to Ref. [33] and fed into time-to-amplitude (TAC) converters. The TAC and dynode output signals are connected to a digitizer module [34]. In Figs. 3(b) and 3(c),



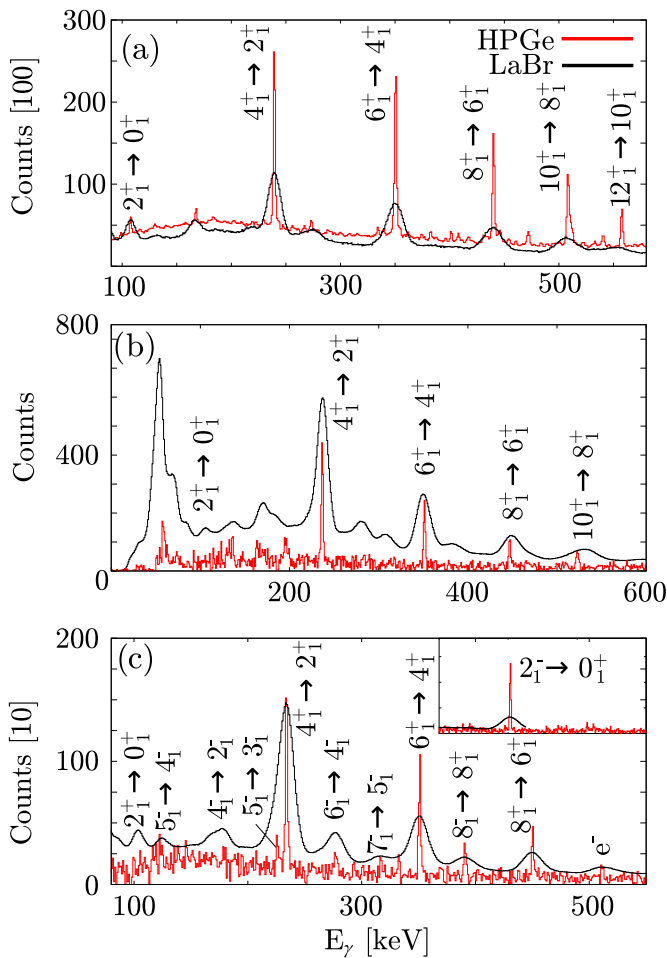


FIG. 3. LaBr spectra and HPGe spectra in coincidence with the  $2_1^+ \rightarrow 0_1^+$  transition (observed with HPGe detectors in HORUS in  $^{176}\text{W}$  and with the Orange spectrometer in  $^{178,180}\text{W}$ ) for (a)  $^{176}\text{W}$ , (b)  $^{178}\text{W}$ , and (c)  $^{180}\text{W}$  (c). In (a) and (b) the yrast cascade  $\gamma$ -ray lines are marked. In (c) the yrast  $\gamma$ -ray lines as well as some of the  $K^\pi = 2^-$  band  $\gamma$ -ray lines and the  $8_1^- \rightarrow 8_1^+$  transition from the  $K^\pi = 8^-$  band to the ground state band are marked. The small overlay box shows the 902.8 keV  $\gamma$  ray of the  $2_1^- \rightarrow 2_1^+$  transition from the  $K^\pi = 2^-$  band to the ground state band.

the measured LaBr and HPGe spectra for  $^{178,180}\text{W}$  are shown, where the current of the Orange spectrometer was set to 163.5 A (105.9 keV) and 161.5 A (103.6 keV), respectively. A partial level scheme for all three investigated tungsten isotopes in each experiment is shown in Fig. 4. In  $^{176,178}\text{W}$ , the yrast cascade up to the  $10^+$  state was detected with enough statistics for the fast-timing analysis. In  $^{180}\text{W}$ , the  $10_1^+$  state was not populated, but negative parity states from the  $K^\pi = 2^-$  octupole rotational band up to the  $7_1^-$  state band were observed [35] as well as the  $8_1^-$  state of the  $K^\pi = 8^-$  band [36].

### B. The HORUS cube spectrometer

The experiment to measure the lifetimes in  $^{176}\text{W}$  using fast timing was conducted at the HORUS cube spectrometer of the IKP Cologne [37]. The spectrometer was equipped with eight HPGe detectors and 10 LaBr fast-timing scintillators. The

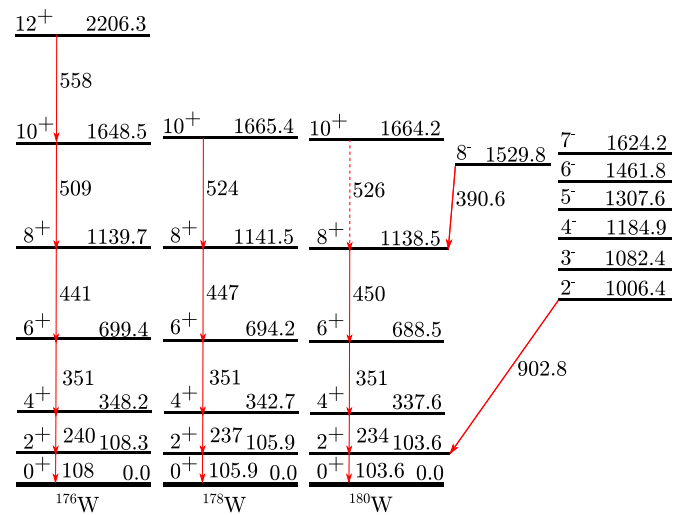


FIG. 4. Relevant level schemes of  $^{176,178,180}\text{W}$ . All transitions depicted with solid lines were used for the lifetime analysis in this work, and are labeled with their respective transition energy. The level and transition energies were adopted from the Nuclear Data Sheets [15–17].

crystals of the LaBr detectors were of two different shapes. Eight  $1.5 \times 1.5$  in.<sup>2</sup> cylindrical crystals and two smaller cone-shaped crystals were used. Six of the LaBr detectors with cylindrical crystals were surrounded by active BGO shields. A schematic drawing of the geometry of this setup is depicted in Fig. 5. This configuration has already been used for several

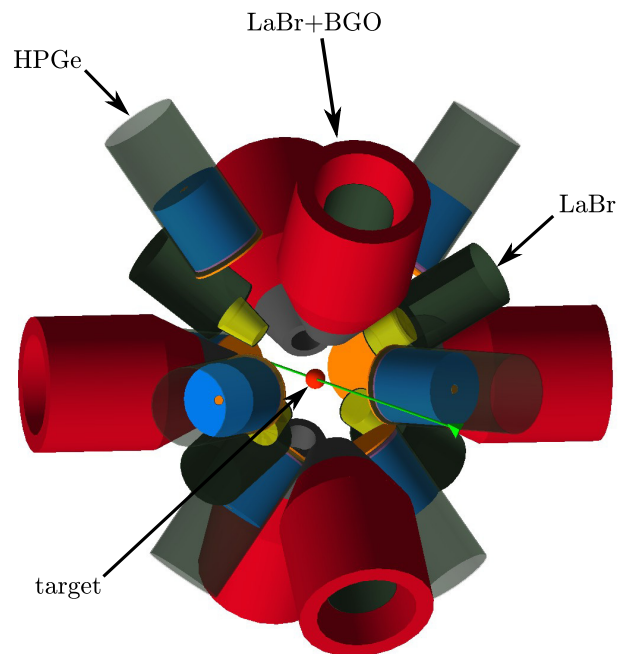


FIG. 5. Schematic drawing of the HORUS setup. The red tubes are the BGO Compton shields, the blue cylinders are the HPGe detectors. The yellow shapes are the LaBr fast-timing scintillators attached to their photo-multiplier tubes, depicted in gray. The beam direction is depicted by a green arrow.

successful fast-timing experiments and its fast-timing capabilities are well tested [38–41].

### C. The IKP plunger experiment

Lifetimes of excited states with  $J^\pi > 2^+$  in  $^{176}\text{W}$  were also measured using the IKP Cologne coincidence plunger setup [9]. The plunger setup was equipped with five HPGGe detectors with relative efficiencies between 55% and 80% under a backward angle of  $143^\circ$  relative to the beam axis and one sevenfold Euroball cluster detector [42] mounted under  $0^\circ$  resulting in a ring of six cluster segments under  $34^\circ$  plus the central segment under  $0^\circ$ . The applied target-to-stopper distances were 2, 4, 6, 9, 13, 25, 35, 50, 70, 100, 150, 190, 300, 500, 700, 1000, and  $1500 \mu\text{m}$  with respect to electrical contact of the foils. The velocity of the  $^{176}\text{W}$  recoil nuclei was determined to be  $v/c = 0.70(1)\%$  using the shifted and unshifted components of the observed yrast cascade transitions from the  $12_1^+$  down to the  $2_1^+$  state in  $^{176}\text{W}$ . The DDCM [20] was used to determine the lifetimes of the  $4^+$ ,  $6^+$ ,  $8^+$ , and  $10^+$  excited yrast states. To minimize feeding contributions from states above as well as unobserved feeders, a gate on the shifted component, that feeds the state of interest, was applied.

## III. LIFETIME ANALYSIS AND RESULTS

### A. Fast-timing analysis

The fast-timing method relies on measuring the time difference between a feeding transition and the decaying transition (either via conversion electron or  $\gamma$  rays) of the state of interest. When a start signal is given by the feeder and the stop signal by the decay, the delayed time distribution is obtained [26,43]:

$$D(t) = n\lambda \int_{-\infty}^t \text{PRF}(t' - t_i) e^{-\lambda(t-t')} dt' + n_r, \quad \lambda = \frac{1}{\tau}, \quad (5)$$

where  $n$  is the number of coincidences in the time distribution,  $n_r$  is the number of background counts, and  $\tau$  is the lifetime of the state connected by the feeder-decay cascade. The delayed time distribution  $D(t)$  is a convolution of the prompt response function (PRF) of the system and an exponential decay.

If the lifetime of a given state is long compared to the full width at half maximum (FWHM) of the PRF, the time difference spectra show an exponential decay as a slope. The slope of the spectrum can be fitted to obtain the lifetime of the exponential decay. If the lifetime of the state of interest is below the resolution of the PRF, they are accessible through the centroid difference method [26,44]. The centroid difference method is based on measuring the centroid  $C$  of delayed ( $d$ ) and antidelayed ( $ad$ ) time distribution where the latter one is obtained by inverting start and stop signals. The lifetime can then be determined according to [26]

$$\tau = \frac{1}{2}(\Delta C - \text{PRD}(E_{\text{feeder}}, E_{\text{decay}})), \quad (6)$$

where  $\Delta C = C_d - C_{ad}$  is the centroid difference and PRD is the prompt response difference that describes the  $\gamma$ - $\gamma$  zero time response of the detector system [26]. The generalization of Eq. (6) for  $N$  detectors is known as the generalized centroid difference (GCD) method [44].

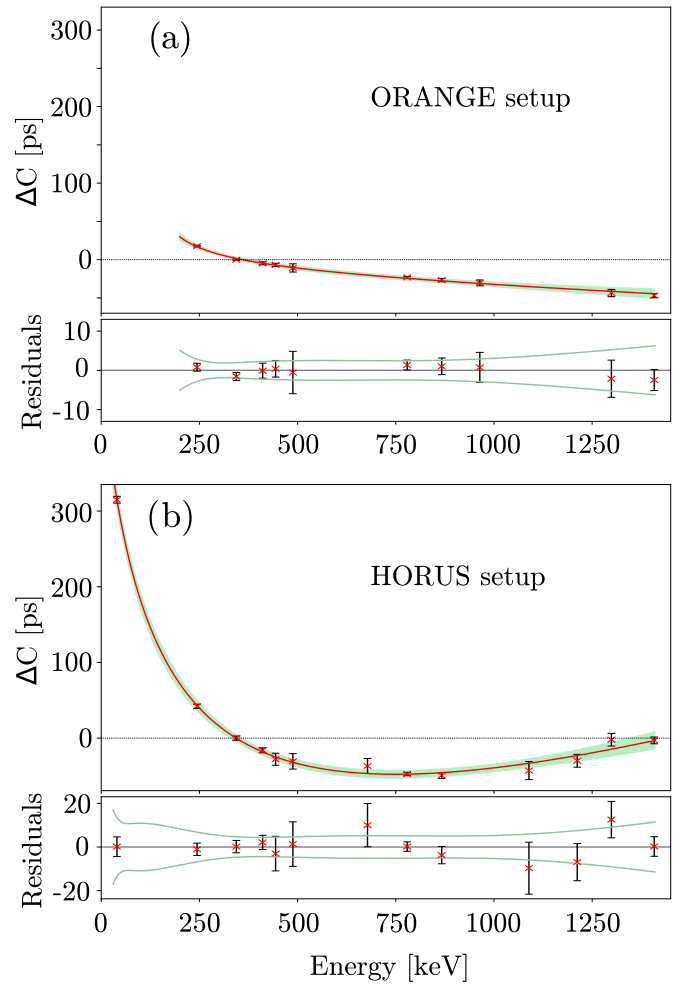


FIG. 6. The PRDs of (a) the Orange setup and (b) the HORUS setup. The upper panels in (a) and (b) show the prompt response difference curve, determined with coincident  $\gamma$  rays from a  $^{152}\text{Eu}$  source at target position. The fitted calibration functions are displayed by the red lines. The uncertainties are displayed by the green uncertainty bands. The zero reference is 344 keV in both cases. The residuals of the PRD fits with uncertainties and  $1\sigma$  interval, displayed by the green lines, are depicted in the lower panels.

The final PRD curves for both setups (HORUS and Orange) were calibrated using  $\gamma$  rays from a  $^{152}\text{Eu}$  source and are fitted using the following function [44]:

$$\text{PRD}(E_\gamma) = \frac{a}{\sqrt{(b - E_\gamma)}} + c + dE_\gamma.$$

Both curves are shown in Fig. 6. The uncertainty of the PRD is not larger than 5 ps in the energy range of interest for both setups. Note that Eq. (6) only holds under the assumption that no background is present. Time correlated background resulting from scattered coincident  $\gamma$  rays has to be corrected for. The procedure is explained in Ref. [44] and was successfully applied in Refs. [38,41,45,46]. In this analysis, the lifetimes of the  $2_1^+$  states in all three tungsten isotopes were determined using the slope method while the higher-lying excited states were measured using the GCD method.

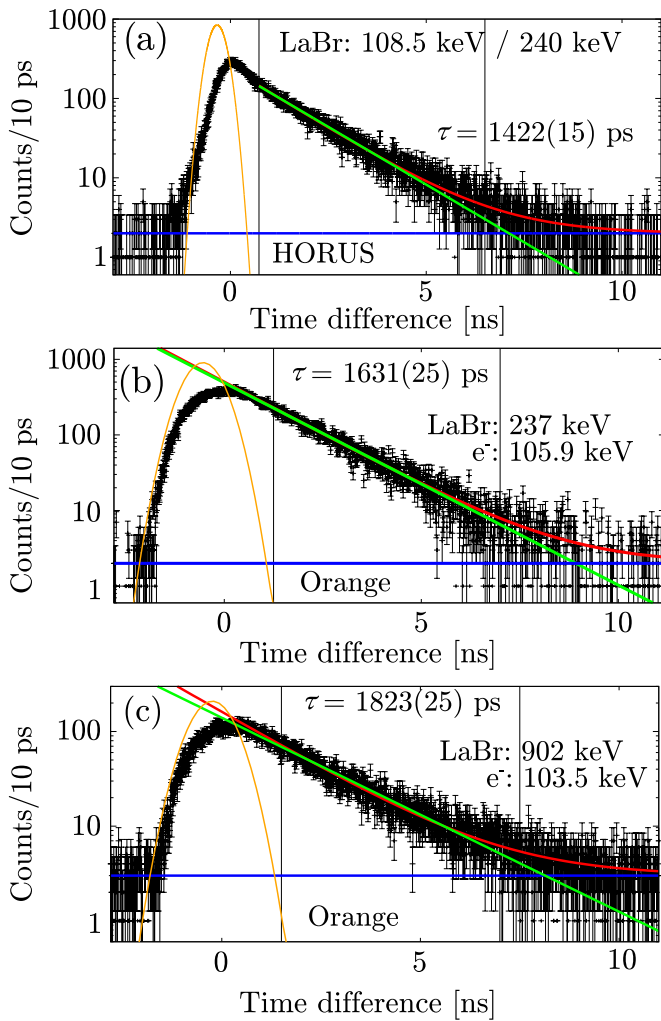


FIG. 7. Time distributions for the  $2_1^+$  states in (a)  $^{176}\text{W}$ , (b)  $^{178}\text{W}$ , and (c)  $^{180}\text{W}$ . The fits to the exponential decay are shown as green lines, the constant background contribution is indicated by blue constants, and the fit with all components by red curves. The fit ranges are indicated by vertical lines. Each panel is labeled with the respective conversion electron and LaBr gates and resulting lifetimes. The yellow centroids are the prompt response functions of the HORUS respective Orange timing systems. The time resolution of the LaBr-Orange timing system is around 1000 ps [22], indicated by the widened PRF, shown in (b) and (c), compared to the LaBr-LaBr timing system of the HORUS spectrometer with a time resolution of about 340 ps.

In Fig. 7(a) the time spectra for the lifetime measurement of the  $2_1^+$  state in  $^{176}\text{W}$  is shown. It is generated by placing a LaBr gate on the  $2_1^+ \rightarrow 0_1^+$  (108.5 keV) transition and another one on the  $4_1^+ \rightarrow 2_1^+$  (240 keV) transition.

The lifetimes of the  $2_1^+$  states in  $^{178,180}\text{W}$  were measured with the Orange spectrometer using  $e^-$ - $\gamma$  coincidences. In Fig. 7(b) the respective time spectrum for the lifetime measurements in  $^{178}\text{W}$ , with one gate on the L1 conversion electron of the  $2_1^+ \rightarrow 0_1^+$  (106 keV) transition and a narrow LaBr gate on the  $4_1^+ \rightarrow 2_1^+$  (237 keV) transition, is shown. The lifetime measurement of the  $2_1^+$  state in  $^{180}\text{W}$  is shown in Fig. 7(c). Here, the gates are placed on the  $2_1^- \rightarrow 2_1^+$  (903

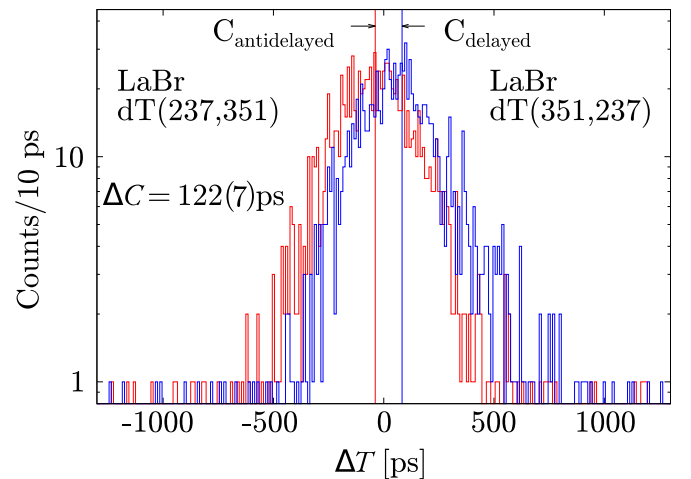


FIG. 8. Centroid difference of the  $6_1^+ \rightarrow 4_1^+ \rightarrow 2_1^+$   $\gamma$  cascade in  $^{178}\text{W}$ , generated using a conversion electron gate on the  $2_1^+ \rightarrow 0_1^+$  transition. Displayed are the time distributions for delayed (blue) and antidelayered (red) gate sequence.

keV) and  $2_1^+ \rightarrow 0_1^+$  (103.6 keV) transitions. Note that the feeding transition was the  $2_1^- \rightarrow 2_1^+$  (903 keV) and not the  $4_1^+ \rightarrow 2_1^+$  transition. The 903 keV transition has considerably less uncorrelated background compared to the 234 keV feeder, as the 234 keV peak has a contamination of the  $5_1^- \rightarrow 3_1^-$  lying in its left flank. For each time spectrum presented in Fig. 7 the corresponding exponential fit to determine the lifetimes is shown. The fit components are depicted by the colored curves: background component in blue, exponential component in green, and the combined fit in red. The final lifetimes result in  $\tau = 1422(15)$  ps for  $^{176}\text{W}$ ,  $\tau = 1631(25)$  ps for  $^{178}\text{W}$ , and  $\tau = 1823(25)$  ps for  $^{180}\text{W}$ . The uncertainties correspond to the maximum deviations of the fits from the median.

The lifetime determination using the HPGe or conversion electron triggered  $\gamma$ - $\gamma$  coincidence measurements is shown as an example for the  $4_1^+$  state in  $^{178}\text{W}$ . Figure 8 shows the delayed and antidelayered time distributions with the  $6_1^+ \rightarrow 4_1^+$  (351 keV) feeding and the  $4_1^+ \rightarrow 2_1^+$  (237 keV) decaying transition, where a trigger has been set on the conversion electron of the  $2_1^+$  decay of 105.9 keV. The centroid difference was measured to be  $\Delta C = 122(7)$  ps. This result has to be corrected for time correlated background underneath the peak of the feeding and the decaying transition. The background underneath the full-energy peak has to be interpolated from centroid difference measurements around the peak of interest according to the standard procedure discussed in Refs. [28,44]. The LaBr and HPGe reference spectra as well as the centroid differences in picoseconds, the background centroid differences, as well as the interpolated background at the respective peak positions for the  $4_1^+$  state are shown in Fig. 9. The interpolated background time response is weighted with the peak-to-background ratio and combined with the PRD value for the energies of the respective feeder-decay cascade; the lifetime of the  $4_1^+$  state, corresponding to  $\tau = 70(5)$  ps, is derived using Eq. (6). This value is consistent with the previously reported result of  $\tau = 65(6)$  ps [18].

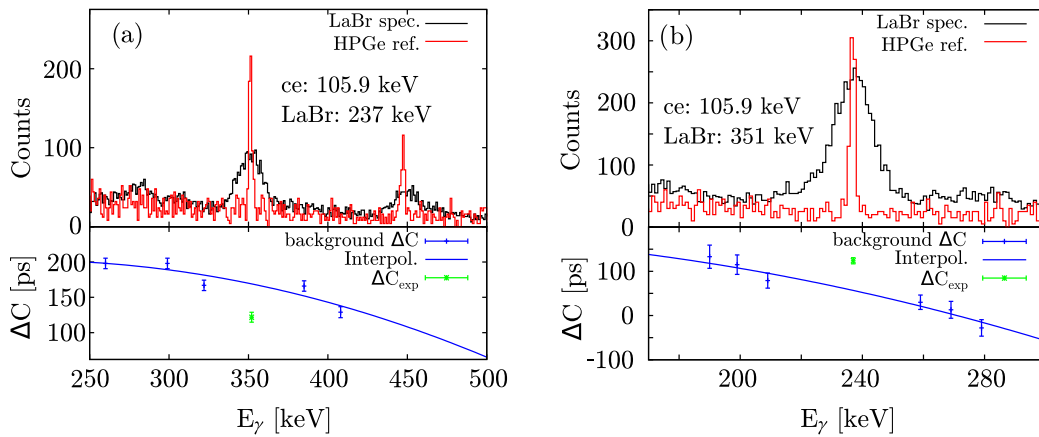


FIG. 9. Analysis of the  $4_1^+$  state of  $^{178}\text{W}$ . In red and black, double gated HPGe and LaBr energy spectra with an Orange trigger gate on the  $2_1^+ \rightarrow 0_1^+$  transition and a LaBr gate on the (a)  $4_1^+ \rightarrow 2_1^+$  (237 keV), which results in an antidelayed time spectrum, and the (b)  $6_1^+ \rightarrow 4_1^+$  (351 keV), which results in a delayed time spectrum. The peaks of interest are well separated from contaminating transitions. In the lower parts of the plots, the measured centroid difference (green) and the measured background time response and corresponding interpolations (blue) are shown.

The lifetimes of the other excited yrast states were determined in the same way with a gate from the next higher-lying yrast state each. Since the  $10_1^+$  state was not excited in  $^{180}\text{W}$ , the lifetime of the  $8_1^+$  state was determined using the  $\gamma$  cascade from the  $8_1^-$  state from the  $K^\pi = 8^-$  band. The experimental results are shown in Table I. The reduced transition probabilities were calculated using the conversion coefficients of the BrIcc database [47] and the transition energies from the evaluated Nuclear Data Sheets [15–17].

### B. RDDS and DDCM analysis

The lifetimes of the  $4_1^+$ ,  $6_1^+$ ,  $8_1^+$ , and  $10_1^+$  yrast states of  $^{176}\text{W}$  were also determined using the RDDS and DDCM. In

Fig. 10 gated spectra of the detectors under the  $143^\circ$  backward angle, with respect to the beam axis, are shown for the  $^{176}\text{W}$  experiment. The gated spectra, shown for different target-to-stopper distances between 2 and 1500  $\mu\text{m}$ , are generated by applying a gate on the  $12_1^+ \rightarrow 10_1^+$  (558 keV) transition. The  $\gamma$ -ray energies of the yrast cascade from the  $4^+$  up to the  $10^+$  state are marked with two dashed lines, where the dashed line on the left corresponds to the shifted component and the dashed line on the right to the unshifted component. For a distance of 1500  $\mu\text{m}$ , all recoiled nuclei are in flight and all  $\gamma$  rays are entirely Doppler shifted. By lowering the distance between target and stopper an increasing amount of recoiled nuclei are stopped before their  $\gamma$  decay and  $\gamma$  rays not influenced by Doppler shifts are detected. The energetically higher

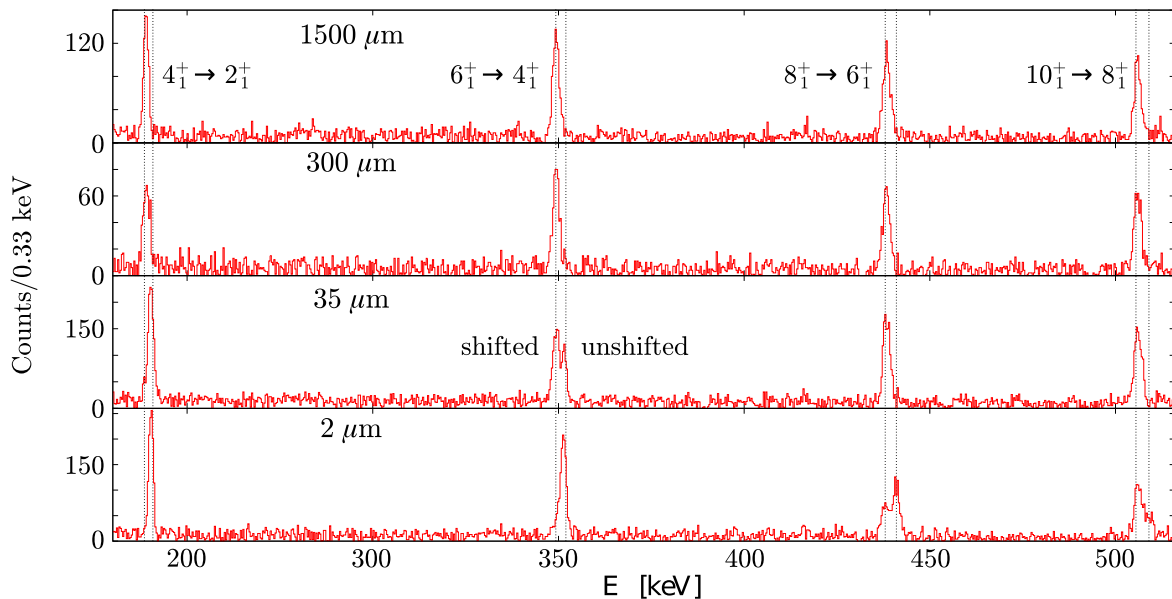


FIG. 10. Projections of the  $\gamma$ - $\gamma$  coincidences with a gate on the flight component of the  $12_1^+ \rightarrow 10_1^+$  transition in  $^{176}\text{W}$  are shown for different target-to-stopper distances under backward angle. Yrast transitions of interest are marked with dashed lines, where the left lines mark the Doppler-shifted and the right ones the unshifted components.

TABLE I. Summary of lifetimes measured in this work and derived reduced transition strengths in comparison adopted literature values and IBM-1 calculations from this work (see Sec. IV B). In the case of  $^{176}\text{W}$ , the values marked with an asterisk are resulting from the plunger experiment from Sec. III B and the unmarked values for  $^{176}\text{W}$  are derived from the HORUS fast-timing experiment. The values printed in bold are adopted for further discussion and the extraction of the  $B(E2)$  values in the case of  $^{176}\text{W}$ . For details on the selection of the adopted values see Sec. III B.

Nucleus	$I^\pi$	$\tau$ (ps)		$B(E2; I^\pi \rightarrow I^\pi - 2)$ (W.u.)		
		This work	Literature	This work	Literature	IBM-1
$^{176}\text{W}$	$2_1^+$	1422(15)	1431(9) <sup>a</sup>	170(3)	166(3) <sup>a</sup>	170
	$4_1^+$	<b>57.9(29)</b> 64.2(12)*		258(13)		244
	$6_1^+$	10.7(30)				
		<b>8.1(3)*</b>		306(11)		270
	$8_1^+$	<8				-
$^{178}\text{W}$	$10_1^+$	<b>2.1(4)*</b>		190 <sup>+44</sup> <sub>-30</sub>		283
	$2_1^+$	1631(25)	1642(21) <sup>b</sup>	154(3)	153(2) <sup>b</sup>	154
	$4_1^+$	70(4)	65(6) <sup>c</sup>	222 <sup>+13</sup> <sub>-12</sub>	238 <sup>+24</sup> <sub>-18</sub> <sup>c</sup>	224
	$6_1^+$	9.8(38)	<14.4 <sup>c</sup>	230 <sup>+134</sup> <sub>-64</sub>	>170	254
	$8_1^+$	<6		>105		>269
$^{180}\text{W}$	$2_1^+$	1823(25)	1850(70) <sup>d</sup>	141(3)	139(6)	141
	$4_1^+$	79.4(29)		204(7.7)		208
	$6_1^+$	12(3.5)		199 <sup>+82</sup> <sub>-45</sub>		234
	$8_1^+$	<8.6		>74		>247

<sup>a</sup>Reference [22].

<sup>b</sup>Reference [18].

<sup>c</sup>Reference [19].

<sup>d</sup>Reference [17].

peaks are not entirely stopped, because the time of flight of the recoiled nuclei tends to be longer than the lifetime of the respective state. But even at the lowest distance of 2  $\mu\text{m}$ ,

both components can be observed. Note that the peaks of the  $4_1^+ \rightarrow 2_1^+$  transition are not well separated. The reason is the relatively low velocity ( $\frac{v}{c} \approx 0.7\%$ ) of the recoiled reaction product of the specific fusion evaporation reaction. Due to nearly indistinguishable shifted and unshifted components of the  $4_1^+ \rightarrow 2_1^+$  transition, as visible in Fig. 10, the lifetime measurement using the RDDS method or DDCM does not generate a reasonable result. The given uncertainty does only reflect the statistical error and not the systematic error of the poorly separated shifted and unshifted components. Thus, the lifetime of the fast-timing experiment is used for further discussions about the  $4_1^+$  state. The separation of the shifted and unshifted components of the decaying transitions of the  $6^+$ ,  $8^+$ , and  $10^+$  states is sufficient and can be used to determine lifetimes. With the applicability limit of the fast-timing method being around 10 ps [26] the results of the plunger method have been used for further discussions about the yrast states with  $J^+ > 4^+$ . In Table I, the results of the plunger experiment in the case of  $^{176}\text{W}$  are indicated by asterisks. The results for  $^{176}\text{W}$  used for further discussions and the extraction of the  $B(E2)$  values are printed in bold text in Table I.

Figure 11 shows an example of the DDCM analysis for the lifetime determination of the  $6_1^+$  state, gated on the flight components of the indirect feeding  $10_1^+ \rightarrow 8_1^+$  [Fig. 11(a)] and  $12_1^+ \rightarrow 10_1^+$  in forward [Fig. 11(b)] and backward angle [Fig. 11(c)]. The lifetimes of the  $6^+$ ,  $8^+$ , and  $10^+$  states in  $^{176}\text{W}$  were determined according to the example shown in Fig. 11. A summary of the determined lifetimes including gate information and adopted values is shown in Table II.

## IV. DISCUSSION

### A. Systematic of $B(E2)$ values and quadrupole deformation

Collective signatures in atomic nuclei can be described by different parameters like the  $R_{4/2} = E_{4_1^+}/E_{2_1^+}$  ratio greater than 2 or  $B(E2; 2^+ \rightarrow 0^+)$  values larger than 10–20 W.u. [49]. Further parameters are, e.g., intrinsic electric quadrupole

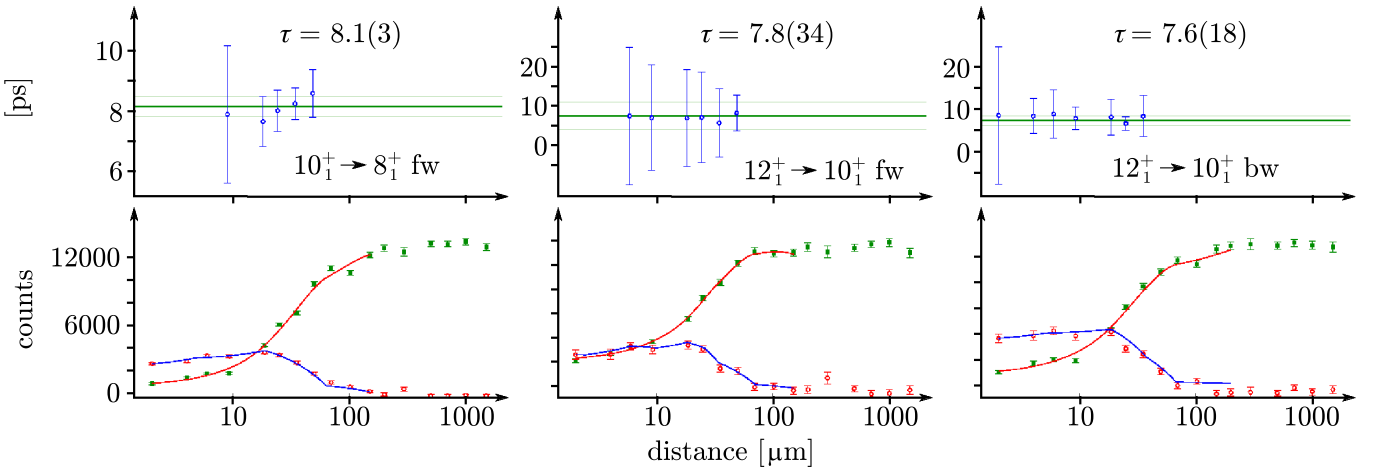


FIG. 11. Example of the DDCM analysis for the  $6_1^+$  state using the software NAPATAU [48]. The upper panels show the corresponding obtained lifetimes. The lower panels show the evolution of the shifted component intensities (green data points and red curves) and derivatives (light red data points and blue curves). The  $\tau$  plots are depicted with their corresponding gate configurations and angles, where “fw” means forward angle and “bw” means backward angle.



TABLE II. Summary of the determined lifetimes in  $^{176}\text{W}$  from the RDDS experiment with respective gates and weighted means. Forward and backward angles are marked with “fw” and “bw,” respectively. The weighted means of each lifetime are printed in bold text.

$4_1^+$		$6_1^+$	
Gate	$\tau$ (ps)	Gate	$\tau$ (ps)
$8_1^+ \rightarrow 6_1^+$ fw	64.3(14)	$12_1^+ \rightarrow 10_1^+$ fw	7.8(34)
$8_1^+ \rightarrow 6_1^+$ bw	67.7(21)	$12_1^+ \rightarrow 10_1^+$ bw	7.6(18)
$6_1^+ \rightarrow 4_1^+$ fw	62.9(12)	$10_1^+ \rightarrow 8_1^+$ fw	8.1(3)
<b>Weighted mean</b>	<b>64.2(12)</b>	<b>Weighted mean</b>	<b>8.1(3)</b>
$8_1^+$		$10_1^+$	
Gate	$\tau$ (ps)	gate	$\tau$ (ps)
$10_1^+ \rightarrow 8_1^+$ bw	3.7(7)	$12_1^+ \rightarrow 10_1^+$ bw	1.9(12)
$12_1^+ \rightarrow 10_1^+$ fw	3.9(6)	$8_1^+ \rightarrow 6_1^+$ bw	2.1(4)
<b>Weighted mean</b>	<b>3.8(5)</b>	<b>Weighted mean</b>	<b>2.1(4)</b>

moment  $Q_0$ , deformation parameter  $\beta$ , and the  $B_{4/2} = B(E2; 4_1^+ \rightarrow 2_1^+)/B(E2; 2_1^+ \rightarrow 0_1^+)$  ratio which is expected to be 1.43 for a heavy deformed nucleus [49]. The experimental data obtained in this work enable a more complete picture of the evolution of the collective signatures of the tungsten isotopes around the rare-earth neutron midshell at  $N = 104$ . As can be seen in Fig. 12(a), the tungsten isotopes around the neutron midshell show an increasing  $R_{4/2}$  ratio with a maximum at  $^{182}\text{W}_{108}$ . The ratio increases from around 2.9 at  $N = 94, 96$  to 3.29 for  $N = 108$ . For the near-midshell isotopes this suggests the interpretation of close to axially symmetric rigid rotors which have theoretical  $R_{4/2}$  ratios of 3.33 [10]. Looking at Figs. 12(a) and 13 (top), it is clear that most isotopes have exceeded the X(5) limit of  $R_{4/2} = 2.91$ , but for the lighter tungsten isotopes, this signature indicates slight hints of X(5) characteristics. The  $B(E2)$  values of the  $2_1^+ \rightarrow 0_1^+$  and  $4_1^+ \rightarrow 2_1^+$  transitions are shown in Fig. 12(b). In this mass region, the increasing  $B(E2; 2_1^+ \rightarrow 0_1^+)$  values as a function of decreasing neutron number are commonly interpreted as an increase in collectivity towards more neutron-deficient nuclei. A saturation of collectivity around  $N = 100$  to neutron midshell  $N = 104$  can be assumed, based on the current  $B(E2)$  data. The evolution of the newly acquired  $B(E2; 4_1^+ \rightarrow 2_1^+)$  values accompanies the evolution of the  $B(E2; 2_1^+ \rightarrow 0_1^+)$  values depending on the neutron number. Both evolutions follow a similar general tendency. Though the maximum of both signatures,  $B(E2; 2_1^+ \rightarrow 0_1^+)$  and  $B(E2; 4_1^+ \rightarrow 2_1^+)$ , lies near midshell, as expected in well-deformed nuclei, a satisfactory explanation for the displaced maximum of the  $B(E2)$  values towards neutron-deficient isotopes is not yet presented.

Compared to the lighter even-even hafnium, ytterbium, and erbium neighbors with  $Z = 72, 70$ , and  $68$ , a similar behavior of the  $B(E2)$  values of the low-spin yrast states is found. In these isotopes the  $B(E2; 2_1^+ \rightarrow 0_1^+)$  value peaks at  $N = 100$ ,  $N = 102$ , and  $N = 98$ , respectively, emphasizing the saturation of collectivity in this region when approaching the midshell [24,55], but with slight displacement to the neutron-deficient side. This effect of pre-midshell saturation could partly be caused by the influence of the hexadecapolar

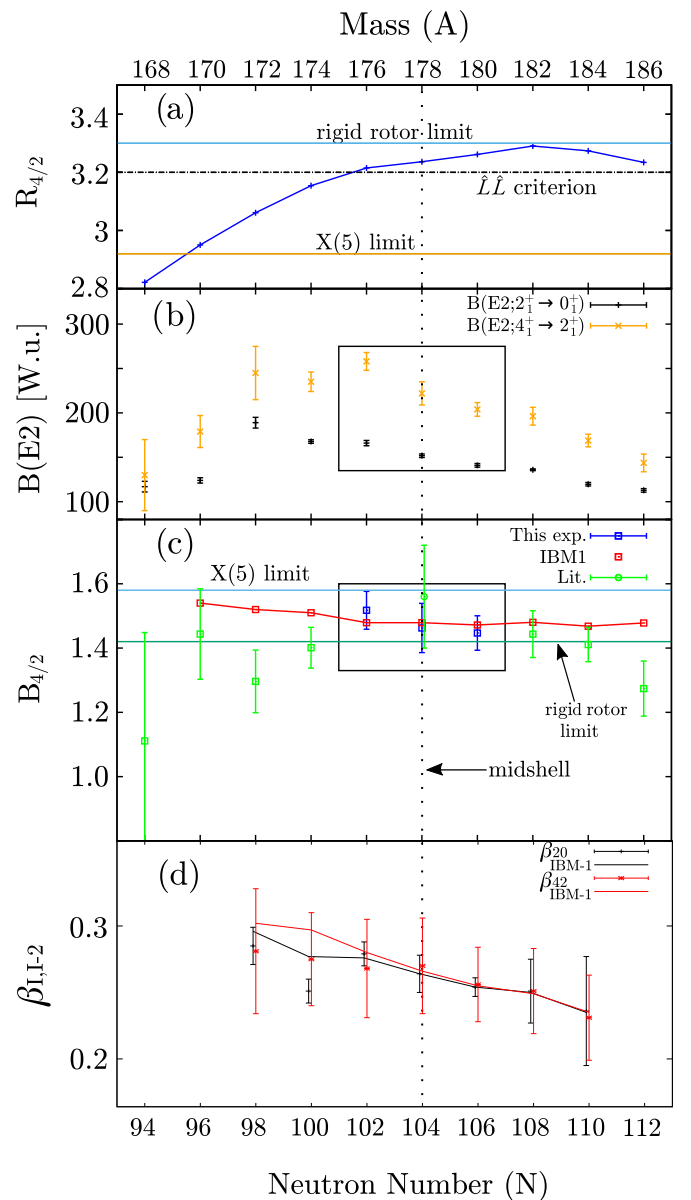


FIG. 12. The evolution of (a)  $R_{4/2}$  ratios, (b)  $B(E2)$  values, (c)  $B_{4/2}$  ratios, and (d) experimental quadrupole deformation parameters of the tungsten isotopes around  $N = 104$  compared with the IBM-1 calculations from this work. The  $\beta$  values obtained from the IBM-1 calculations are drawn with solid lines in the same color as the experimental values. Experimental values for the energies and the literature values of the  $B(E2)$  values are taken from Refs. [15–17,19,50–54]. Rigid rotor and X(5) limits are shown as horizontal lines. The  $\hat{L}\hat{L}$  criterion as mentioned in Sec. IV B is displayed as a dashed line in (a).

deformation  $\beta_4$  on the quadrupole moment  $Q_t$ , as proposed in Ref. [56], investigated and discussed for this region in Refs. [18,55]. A detailed study of the hexadecapolar deformation  $\beta_4$  for this mass region, including the tungsten isotopes, is presented in Ref. [55]. This approach, however, cannot explain the displacement entirely [55].

Figure 12(c) shows the evolution of the  $B_{4/2}$  ratio around the neutron midshell. The ratio is expected to be around

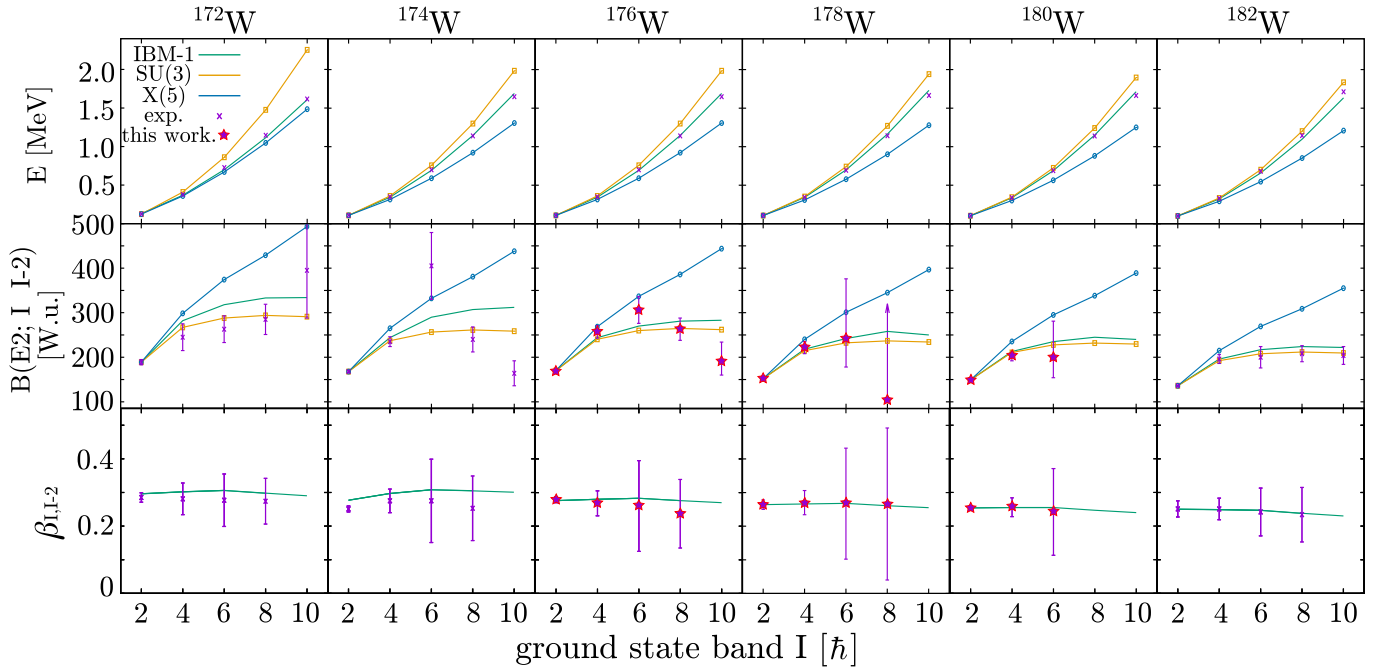


FIG. 13. Excitation energies (top), reduced transition probabilities (middle), and experimental quadrupole deformation parameters  $\beta_{1,I-2}$  (bottom) as a function of yrast spin for  $^{172-182}\text{W}$ . The upper and the middle panels compare the experimental values to the IBM-1 calculations from Sec. IV B and the SU(3) and X(5) limits. The bottom plot compares the experimental values to the IBM-1. The literature values are taken from Refs. [50,52,64,65].

1.428 for well-deformed nuclei, according to the predictions of the rigid rotor model [57] and the SU(3) limit of the interacting boson model [10,25]. In the tungsten isotopes with  $N = 94-110$ , the  $B_{4/2}$  ratio increases from 1.11(34) at  $^{168}\text{W}$  ( $N = 94$ ) towards 1.51(5) at  $^{176}\text{W}$  ( $N = 102$ ) and decreases to 1.41(5) at  $^{184}\text{W}$  ( $N = 110$ ). This increasing behavior towards midshell seems anomalous for isotopic chains in this region. In comparison, the  $B_{4/2}$  ratio decreases in the even-even hafnium and ytterbium neighbors towards midshell to about 1.43 [24,58]. In contrast, the  $B_{4/2}$  ratio of the heavier osmium and platinum isotopes also increases towards midshell starting from very small  $B_{4/2}$  ratios of approximately or smaller than 1 in the very neutron-deficient isotopes, comparable to the  $B_{4/2}$  of the tungsten isotopes [59].

All in all, the simple rotor explanation for the isotopes in this region does not seem to be fully sufficient in the tungsten isotopes. Several indications are observed that suggest a rising of previously unaccounted effects (or at least an uncommon combination of already known effects, as for example the backbending phenomenon [60–62], the hexadecapolar deformation [55], or possibly a shape coexistence phenomenon [63]) in this region: the displacement of the saturation of the  $B(E2)$  values away from midshell towards lighter isotopes [Fig. 12(b)], the displacement of the maximum of the  $R_{4/2}$  ratio away from midshell towards heavier isotopes [Fig. 12(a)], the unexpected behavior of the  $B_{4/2}$  ratios and its very small value at  $^{168}\text{W}$  of 1.11(34) [Fig. 12(c)], as well as the unexpected behavior of the tendency of the  $B(E2)$  values throughout the  $2^+-10^+$  yrast states of  $^{174,176}\text{W}$  (see Fig. 13, middle panel). Further experiments and calculations are required to explain this combination of observations.

However, most of the  $B_{4/2}$  ratios considered ( $N = 94-112$ ) agree within their uncertainties with the Alaga rule of 10/7 largely supporting the deformed character as expected from the  $R_{4/2}$  ratio near midshell.

All  $B_{4/2}$  values of the tungsten isotopes are separated from the X(5) limit of 1.58 [6]. Especially for  $^{178}\text{W}$  ( $N = 104$ ) the new results reduced the uncertainties of the  $B_{4/2}$  ratio and there is no overlap with the X(5) limit any more. As Fig. 12(c) reveals, the uncertainty of the  $B_{4/2}$  ratio for  $^{176}\text{W}$  lies very close to the X(5) limit. But the  $R_{4/2}$  ratio contradicts the assumption of a possible X(5) nucleus. Still, the  $B_{4/2}$  ratio as well as the trend of  $B(E2)$  values up to  $B(E2; 6_1^+ \rightarrow 4_1^+)$  (see Fig. 13), with respect to the new experimental data, can be interpreted as following the trend suggested by X(5). But considering all signatures,  $R_{4/2}$ ,  $B_{4/2}$ , and the evolution of the yrast  $B(E2)$  strengths,  $^{176}\text{W}$  agrees certainly more with the SU(3) limit. But the unexpected drop of the  $B(E2)$  values of the  $8_1^+ \rightarrow 6_1^+$  and  $10_1^+ \rightarrow 8_1^+$  transitions seems to be outside the scope of the models. The same effect is observed for the evolution of the  $B(E2)$  values in  $^{174}\text{W}$ . But due to the large uncertainty of the  $B(E2; 6_1^+ \rightarrow 4_1^+)$  value, the situation cannot be fully quantified.

The graphics in Figs. 12(b), 12(c) and 13 including the newly determined values add to the systematic evolution of the  $B(E2)$  values in the neutron midshell region of the tungsten isotopes around  $N = 104$ .

From the deduced  $B(E2)$  values, transitional quadrupole moments  $Q_t$  are calculated according to [49]

$$Q_t(J_i \rightarrow J_f) = \sqrt{\frac{16\pi}{5} \frac{B(E2; J_i \rightarrow J_f)}{\langle J_i K_i 2(\Delta K) | J_f K_f \rangle^2}}, \quad (7)$$

TABLE III. Experimental quadrupole moments and quadrupole deformation parameters  $\beta$  for the  $2_1^+ \rightarrow 0_1^+$ ,  $4_1^+ \rightarrow 2_1^+$ , and  $6_1^+ \rightarrow 4_1^+$  transitions for the tungsten isotopic chain. The  $Q_t$  values were calculated with Eq. (7), the  $\beta$  values with Eq. (8) using  $B(E2)$  values which were taken from this work and from the Nuclear Data Sheets [18,50–53].

Nucleus	$N$	$Q_{20}$	$\beta_{20}$	$Q_{42}$	$\beta_{42}$	$Q_{64}$	$\beta_{64}$
$^{172}\text{W}$	98	7.38(8)	0.28(3)	7.0(12)	0.28(5)	6.9(19)	0.28(8)
$^{174}\text{W}$	100	6.97(5)	0.249(8)	6.9(9)	0.27(4)	8.7(31)	0.35(12)
$^{176}\text{W}$	102	6.9(5)	0.279(2)	6.8(9)	0.27(4)	6.6(34)	0.26(13)
$^{178}\text{W}$	104	6.74(6)	0.26(3)	6.8(9)	0.27(4)	6.8(32)	0.27(16)
$^{180}\text{W}$	106	6.54(5)	0.253(5)	6.6(7)	0.26(3)	6.2(33)	0.24(12)
$^{182}\text{W}$	108	6.47(5)	0.249(2)	6.5(9)	0.25(3)	6.3(18)	0.24(7)
$^{184}\text{W}$	110	6.12(5)	0.234(2)	6.0(9)	0.23(3)	6.0(9)	0.23(4)

where  $\langle J_i K_i 2(\Delta K) | J_f K_f \rangle$  are the Clebsch-Gordan coefficients for transitions from  $J_i$  to  $J_f$  [49], where  $K$  represents the projection of the intrinsic angular momentum on the symmetry axis. The quadrupole deformation  $\beta$  is related to  $Q_t$  via

$$\beta = \frac{\sqrt{5\pi}}{3ZR^2e} Q_t, \quad (8)$$

where  $R = 1.2 \text{ fm } A^{\frac{1}{3}}$  is an approximation for the nuclear radius. The values are calculated for the tungsten isotopes between  $N = 98$  and  $N = 110$  and are given in Table III. Derived from the values in Table III, the quadrupole moments as well as the quadrupole deformation decreases from  $\beta_{20} = 0.28(3)$  in  $^{172}\text{W}$  to  $\beta = 0.234(2)$  in  $^{184}\text{W}$ . The evolution of the quadrupole deformation values  $\beta_{20}$  and  $\beta_{42}$  is depicted in Fig. 12(d) throughout the isotopic chain. Figure 13 (bottom panel) shows nearly constant quadrupole deformation for all yrast states with  $J^+ = 2^+, 4^+, 6^+$ , and  $8^+$  for the tungsten isotopes. All  $\beta$  values lie in a typical range expected for a well-deformed rotor [49]. The quadrupole deformation does not suggest a major change in structure in this isotopic chain.

The newly determined data concerning  $^{176,178,180}\text{W}$  complete the experimental database of observables relevant for the discussion of deformation phenomena. The current interpretation does not change significantly; still, the new experimental data yield an argument to support the previous assumptions for the deformation characteristics of the tungsten isotopes  $^{176,178,180}\text{W}$ . But further efforts as experiments and adjustments of the nuclear models are required to reproduce a detailed general description of the data throughout the tungsten isotopic chain.

### B. IBM-1 calculations

To describe the experimental data, theoretical calculations in the framework of the interacting boson model 1 (IBM-1), where no distinction between protons and neutrons is made [66], were performed. In the IBM-1, one assumes that low-lying collective quadrupole states can be generated as states of a system of  $N$  bosons able to occupy two levels, one with angular momentum  $J = 0$ , called s bosons, and one with angular momentum  $J = 2$ , called d bosons [67]. In the calculations, only s and d bosons are used. The ex-

TABLE IV. The fit parameters for the ECQF Hamiltonian and resulting  $e_{\text{eff}}$  values in e b.

Nucleus	$\epsilon$	$\kappa$	$\chi$	$\lambda$	$e_{\text{eff}}$ (e b)
$^{172}\text{W}^a$	0.520	-0.0154	-1.013	0.0	0.16881
$^{174}\text{W}^a$	0.553	-0.0156	-0.947	0.0	0.14950
$^{176}\text{W}^a$	0.593	-0.0158	-0.946	0.0	0.14758
$^{178}\text{W}^a$	0.615	-0.0157	-0.938	0.0006 <sup>b</sup>	0.12368
$^{180}\text{W}$	0.540	-0.0160	-0.865	0.0011	0.12812
$^{182}\text{W}$	0.500	-0.0169	-0.845	0.0016	0.13649
$^{184}\text{W}$	0.435	-0.0166	-0.800	0.0036	0.14539
$^{186}\text{W}$	0.415	-0.0170	-0.800	0.0046	0.14655

<sup>a</sup>Calculations done by Rudigier *et al.* [18].

<sup>b</sup>The  $\lambda$  value for  $^{178}\text{W}$  was added in this work.

tended consistent Q formalism (ECQF) [68] represents the IBM-1 with only few parameters which has proven to contain the essential physics ingredients to describe the low-lying states in even-even nuclei ranging from vibrational nuclei up to well-deformed rotational nuclei [69,70]. The following Hamiltonian is applied [68]:

$$\hat{H}_{\text{ECQF}} = \epsilon \hat{n}_d + \kappa \hat{Q}^x \cdot \hat{Q}^x + \lambda \hat{L} \cdot \hat{L}, \quad (9)$$

where

$$\begin{aligned} \hat{Q}^x &= (s^\dagger \tilde{d} + d^\dagger s)^{(2)} + \chi (d^\dagger \tilde{d})^{(2)}, \\ \hat{L} &= \sqrt{10} (d^\dagger \tilde{d})^{(1)}, \text{ and} \\ \hat{n}_d &= d^\dagger \cdot \tilde{d}. \end{aligned} \quad (10)$$

The quadrupole operator  $\hat{Q}^x$  is related to the  $E2$  transition probability  $T(E2)$  via the effective boson charge  $e_{\text{eff}}$  according to

$$T(E2) = e_{\text{eff}} Q. \quad (11)$$

The  $\hat{L} \cdot \hat{L}$  term corresponds to the  $\hbar^2/2I$  parameter of the collective model with  $I$  the moment of inertia and determines the  $L(L+1)$  dependence of the energies in the rotational bands.  $\hat{L}$  denotes the boson angular momentum operator [71]. The physics of the  $\hat{L} \cdot \hat{L}$  term is best seen in the pure rotational SU(3) limit of the IBM-1.

The calculations were performed using the computer code ARBMODEL [72]. The calculations were fitted to the level energies from  $2_1^+$  to  $10_1^+$  and level energies of the first three to four states of the  $\gamma$  and  $\beta$  bands, if available, and the  $B(E2; 2_1^+ \rightarrow 0_1^+)$  value. All level energies were taken from the Nuclear Data Sheets [15–17,50,52–54,64,73]. The fits yield the parameters displayed in Table IV. An IBM-1 calculation for the  $^{172,174,176,178}\text{W}$  isotopes is presented by Rudigier *et al.* in Ref. [18], where the influence of the  $\hat{L}\hat{L}$  term was not taken into account. Since the heavier tungsten isotopes  $^{182,184,186}\text{W}$  experience a strong increase of the level energies especially of the higher-lying yrast levels, the band structure could only be reproduced well by taking a small contribution of the  $\hat{L}\hat{L}$  term into account. Following Nomura *et al.* [71] this becomes evident for strongly deformed axially symmetric nuclei. Nomura *et al.* formulate  $R_{4/2} > 3.2$  as a criterion for taking the  $\hat{L}\hat{L}$  term into account. This criterion is displayed as a dashed line



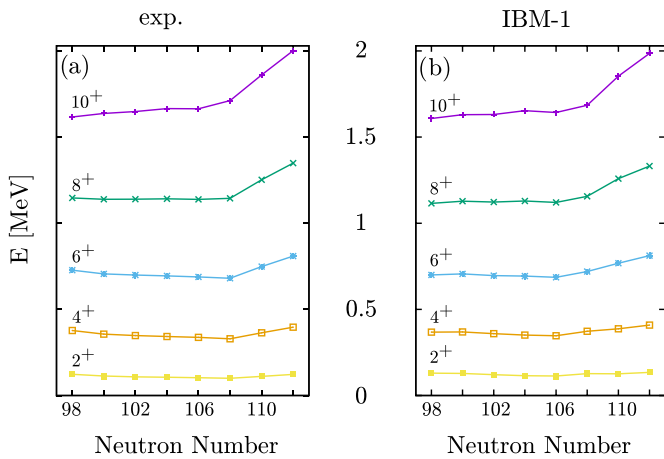


FIG. 14. (a) Experimental and (b) theoretical (IBM-1) level energies of the low-lying yrast  $2^+$ ,  $4^+$ ,  $6^+$ ,  $8^+$ , and  $10^+$  states as a function of the neutron number.

in Fig. 12(a). The parameters for  $^{178}\text{W}$ , originally calculated in Ref. [18], were supplemented by a very small  $\hat{L}\hat{L}$  contribution, indicated by footnote b in Table IV, which leads to a better reproduction of the yrast states. As can be seen in Table IV, the amounts of  $\lambda$  increase slightly with the neutron number.

The results of the calculations of the excitation energies of the yrast states are shown in Fig. 14 together with the experimental values for the tungsten isotopes. The calculated energies show an overall consistency with the measured energies. The highest deviation of the calculations from the experiments in the yrast band in all isotopes was about 20 keV. The effective boson charge was chosen to match the experimental  $B(E2; 2_1^+ \rightarrow 0_1^+)$  values and varies from  $e_{\text{eff}} = 0.12$ -0.14.

The  $B_{4/2}$  ratio of the calculated reduced transition probabilities are shown in Fig. 12(c) in comparison with the experimental values. The resulting  $B_{4/2}$  values match the experimental ones within uncertainties for  $N = 102$  ( $^{176}\text{W}$ ) to  $N = 110$  ( $^{184}\text{W}$ ) but disagree for  $N = 98, 100$ , and  $112$ . According to the model, the  $B_{4/2}$  values of all isotopes considered in the calculations lie close to the SU(3) limit of  $B_{4/2} \approx 1.43$ , similar to what is expected from the experimental values and the  $R_{4/2}$  ratios. Note the opposite movement of the experimental values of  $B_{4/2}$  compared to the model predictions and to the evolution of the  $B_{4/2}$  ratios of the neighbors with fewer protons, hafnium and ytterbium [24,58]. It should be taken into account that the adopted  $B_{4/2}$  value for  $^{172}\text{W}_{98}$  shows a large uncertainty. A reevaluation of this nucleus would be favorable to get a clearer picture of deformation and collectivity in the light tungsten isotopes.

In Fig. 13 the level energies (top) of the first yrast states and corresponding  $E2$  transition strengths (middle) are shown for the midshell tungsten isotopes. While the level energies are clearly approaching the SU(3) limit when adding neutrons, the  $B(E2)$  values do not show a totally clear structure for the midshell tungsten isotopes except for  $^{182}\text{W}$ . The  $B(E2; 6_1^+ \rightarrow 4_1^+)$  value of  $^{180}\text{W}$  and the  $B(E2; 8_1^+ \rightarrow 6_1^+)$  value of  $^{178}\text{W}$  show large uncertainties, as the lifetimes are almost at the lower boundary of the sensitivity of the fast-timing method,

and do not allow for a clear interpretation. However, within the uncertainties, they confirm the interpretation of axially symmetric prolate rotors as they are consistent with the SU(3) limit and the IBM-1 calculations. Although the excitation energies show a rotorlike structure for  $^{174,176}\text{W}$ , the  $B(E2)$  values do not allow a clear interpretation of rotational structure within the uncertainties, as described in Sec. IV A. The IBM-1 calculations place the  $B(E2)$  values of these two isotopes close to SU(3), but the experimental values for  $B(E2; 6_1^+ \rightarrow 4_1^+)$  and  $B(E2; 10_1^+ \rightarrow 8_1^+)$  show deviations from this model. The general tendency of the  $B(E2)$  values is not described by the IBM-1 for  $^{176}\text{W}$  and also  $^{174}\text{W}$ . There are significant deviations from all models for the reduced transition probabilities for these transitions (see Fig. 13, middle panel). This suggests the large deviations for the  $E2$  transitions in  $^{174}\text{W}$  and  $^{176}\text{W}$  to be a signature of a structural change within the yrast band, especially with respect to the evolution towards very unusual  $B_{4/2}$  values of the extremely neutron-deficient nuclei of, e.g.,  $B_{4/2} = 0.33(8)$  for  $^{166}\text{W}$  [74], that cannot be explained with any model so far. Using an extension of the IBM-1, allowing for multiple two particle–two hole excitation, might account for this observation [61,62]. Such a description involves many more parameters to be fitted to higher spin states. This as well as a further development of the nuclear models is considered to be outside the scope of this work.

## V. SUMMARY

Lifetimes of yrast states in the midshell tungsten isotopes with  $A = 176, 178, 180$  have been measured using fast-timing methods with  $e^- \gamma \gamma$  and  $e^- \gamma$  coincidences at the Orange spectrometer setup, HPGe triggered  $\gamma \gamma \gamma$  coincidences using the HORUS cube spectrometer, and the RDDS technique in combination with the DDCM. Lifetimes of the  $2_1^+$  states in all three isotopes as well as  $4_1^+$  and  $6_1^+$  in  $^{178}\text{W}$  have been remeasured. Lifetimes of the  $4_1^+$ ,  $6_1^+$ , and  $8_1^+$  states have been measured in all isotopes and additionally the lifetime of the  $10_1^+$  state in  $^{176}\text{W}$ . The lifetime measurements in  $^{178,180}\text{W}$  were part of the commissioning experiments of the revised Orange spectrometer and successfully demonstrate its capabilities.

From these lifetimes, the  $E2$  transition strengths, quadrupole moments  $Q_t$ , and quadrupole deformation parameters  $\beta$  have been calculated and the  $B_{4/2}$  ratios have been extracted. The newly determined  $B_{4/2}$  ratios for  $^{176}\text{W}$  and  $^{180}\text{W}$  as well as the new  $\beta$  values of the  $4^+$  and  $6^+$  states led to a more complete picture of the evolution of the quadrupole deformation for the tungsten isotopes in this region. The interpretation of the  $R_{4/2}$  values close to the SU(3) limit was confirmed by the  $B_{4/2}$  values and the evolution of the  $B(E2; I \rightarrow I - 2)$  values over the low-spin yrast states within  $^{178,180}\text{W}$ . However, a clear interpretation for  $^{176}\text{W}$  as well as the general description of the tungsten isotopic chain with special regard to the neutron-deficient side is more complicated and requires further effort. A remeasurement with modern methods of the lifetimes of  $^{172,174}\text{W}$  is recommended, due to the high uncertainties of the lifetimes of the  $2_1^+$  and  $4_1^+$  states in  $^{172}\text{W}$  and of the  $6_1^+$  state in  $^{174}\text{W}$ .

The measured values have been compared with calculations in the IBM-1 framework. The theoretical calculations in combination with the experimental  $B(E2; I \rightarrow I - 2)$  values and the theoretical and experimental quadrupole deformations of the  $2_1^+$  state support the previous interpretation of the tungsten isotopes around midshell as deformed prolate rotors.

## ACKNOWLEDGMENTS

The authors would like to thank the operator staff of the FN Tandem accelerator. This work was supported by the DFG under Grant No. JO 391 16-2. G.H. acknowledges support from the API-IDEX funding. A.E. and V.K. acknowledge the support by the BMBF under Grant No. 05P15PKFNA.

- [1] G. D. Dracoulis, P. M. Walker, and F. G. Kondev, *Rep. Prog. Phys.* **79**, 076301 (2016).
- [2] D. A. Meyer, V. Wood, R. F. Casten, C. R. Fitzpatrick, G. Graw, D. Bucurescu, J. Jolie, P. von Brentano, R. Hertzenberger, H.-F. Wirth, N. Braun, T. Faestermann, S. Heinze, J. L. Jerke, R. Krücken, M. Mahgoub, O. Möller, D. Mücher, and C. Scholl, *Phys. Rev. C* **74**, 044309 (2006).
- [3] U. Götz, H. C. Pauli, K. Alder, and K. Junker, *Nucl. Phys. A* **192**, 1 (1972).
- [4] R.F. Casten and N. Zamfir, *J. Phys. G: Nucl. Part. Phys.* **22**, 1521 (1996).
- [5] P.-A. Söderström, P. Walker, J. Wu, H. Liu, P. Regan, H. Watanabe, P. Doornenbal, Z. Korkulu, P. Lee, L. Jiajian, G. Lorusso, S. Nishimura, V. Phong, T. Sumikama, F. Xu, A. Yagi, G. Zhang, D. Ahn, T. Alharbi, and Z. Xu, *PoS INPC2016*, 072 (2017).
- [6] F. Iachello, *Phys. Rev. Lett.* **87**, 052502 (2001).
- [7] H. Xin, Z. Li-Hua, W. Xiao-Guang, H. Chuang-Ye, Z. Yun, L. Li-Hua, S. Hui-Bin, and L. Guang-Sheng, *Chin. Phys. Lett.* **28**, 020201 (2011).
- [8] O. Möller, Ph.D. thesis, Universität zu Köln (2005).
- [9] C. Fransen, A. Dewald, G. Friessner, M. Hackstein, J. Jolie, O. Möller, T. Pissulla, W. Rother, and K. O. Zell, *AIP Conf. Proc.* **1377**, 311 (2011).
- [10] P. Cejnar, J. Jolie, and R. F. Casten, *Rev. Mod. Phys.* **82**, 2155 (2010).
- [11] Krishna Kumar, *Phys. Rev. Lett.* **28**, 249 (1972).
- [12] D. Cline, *Annu. Rev. Nucl. Part. Sci.* **36**, 683 (1986).
- [13] V. Werner, P. von Brentano, and R. V. Jolos, *Phys. Lett. B* **521**, 146 (2001).
- [14] D. J. Rowe, P. S. Turner, and G. Rosensteel, *Phys. Rev. Lett.* **93**, 232502 (2004).
- [15] M.S. Basunia, *Nucl. Data Sheets* **107**, 791 (2006).
- [16] E. Achterberg, O. A. Capurro, and V. Marti, *Nucl. Data Sheets* **110**, 1473 (2009).
- [17] E. A. McCutchan, *Nucl. Data Sheets* **126**, 151 (2015).
- [18] M. Rudigier, J.-M. Régis, J. Jolie, K. O. Zell, and C. Fransen, *Nucl. Phys. A* **847**, 89 (2010).
- [19] M. Rudigier, P. M. Walker, R. L. Canavan, Zs. Podolyák, P. H. Regan, P.-A. Söderström, M. Lebois, J. N. Wilson, N. Jovancevic, A. Blazhev, J. Benito, S. Bottoni, M. Brunet, N. Cieplicka-Orynczak, S. Courtin, D. T. Doherty, L. M. Fraile, K. Hadynska-Klek, M. Heine, Å. W. Iskra *et al.*, *Phys. Lett. B* **801**, 135140 (2020).
- [20] A. Dewald, S. Harissopulos, and P. von Brentano, *Z. Phys. A: At. Nucl.* **334**, 163 (1989).
- [21] K. S. Krane, *Introductory Nuclear Physics*, Vol. 465 (Wiley, New York, 1988).
- [22] J.-M. Régis, Th. Materna, S. Christen, C. Bernards, N. Braun, G. Breuer, Ch. Fransen, S. Heinze, J. Jolie, T. Meersschat, G. Pascovici, M. Rudigier, L. Steinert, S. Thiel, N. Warr, and K. O. Zell, *Nucl. Instrum. Methods Phys. Res., Sect. A* **606**, 466 (2009).
- [23] O. Kofoed-Hansen, J. Lindhard, and O. B. Nielsen, *Mat. Fys. Medd. K. Dan. Vidensk. Selsk.* **25**, 356 (1950).
- [24] M. Rudigier, K. Nomura, M. Dannhoff, R.-B. Gerst, J. Jolie, N. Saed-Samii, S. Stegemann, J.-M. Régis, L. M. Robledo, R. Rodríguez-Guzmán, A. Blazhev, Ch. Fransen, N. Warr, and K. O. Zell, *Phys. Rev. C* **91**, 044301 (2015).
- [25] A. Arima and F. Iachello, in *Advances in Nuclear Physics* (Springer, Boston, 1984), pp. 139–200.
- [26] J.-M. Régis, H. Mach, G. S. Simpson, J. Jolie, G. Pascovici, N. Saed-Samii, N. Warr, A. Bruce, J. Degenkolb, L. M. Fraile, C. Fransen, D. G. Ghita, S. Kisyov, U. Koester, A. Korgul, S. Lalkovski, N. Marginean, P. Mutti, B. Olaizola, Z. Podolyak *et al.*, *Nucl. Instrum. Methods Phys. Res., Sect. A* **726**, 191 (2013).
- [27] A. Dewald, O. Möller, and P. Petkov, *Prog. Part. Nucl. Phys.* **67**, 786 (2012).
- [28] J.-M. Régis, Th. Materna, G. Pascovici, S. Christen, A. Dewald, C. Fransen, J. Jolie, P. Petkov, and K. O. Zell, *Rev. Sci. Instrum.* **81**, 113505 (2010).
- [29] J.-M. Régis, Diplomarbeit, Universität zu Köln (2007).
- [30] M. de Huij, Diplomarbeit, Universität Fribourg, Schweiz (1998).
- [31] E. Moll, Diplomarbeit, Technische Hochschule München (1961).
- [32] G. Soff, J. Reinhardt, B. Müller, and W. Greiner, *Phys. Rev. Lett.* **43**, 1981 (1979).
- [33] J.-M. Régis, N. Saed-Samii, M. Rudigier, S. Ansari, M. Dannhoff, A. Esmaylzadeh, C. Fransen, R.-B. Gerst, J. Jolie, V. Karayonchev, C. Müller-Gatermann, and S. Stegemann, *Nucl. Instrum. Methods Phys. Res., Sect. A* **823**, 72 (2016).
- [34] *User's Manual Digital Gamma Finder (DGF) PIXIE-16* (XIA, LLC, Newark, CA, 2009).
- [35] L. G. Mann, J. B. Carlson, R. G. Lanier, G. L. Struble, W. M. Buckley, D. W. Heikkinen, I. D. Proctor, and R. K. Sheline, *Phys. Rev. C* **19**, 1191 (1979).
- [36] J. Burde, R. M. Diamond, and F. S. Stephens, *Nucl. Phys.* **85**, 481 (1966).
- [37] A. Linnemann, Ph.D. thesis, University of Cologne (2005).
- [38] L. Knafla, G. Häfner, J. Jolie, J.-M. Régis, V. Karayonchev, A. Blazhev, A. Esmaylzadeh, C. Fransen, A. Goldkuhle, S. Herb *et al.*, *Phys. Rev. C* **102**, 044310 (2020).
- [39] L. Kaya, A. Vogt, P. Reiter, M. Siciliano, N. Shimizu, Y. Utsuno, H.-K. Wang, A. Gargano, L. Coraggio, N. Itaco, K. Arnsald, D. Bazzacco, B. Birkenbach, A. Blazhev, A. Bracco, B. Bruyneel, L. Corradi, F. C. L. Crespi, G. de Angelis, M. Droste *et al.*, *Phys. Rev. C* **100**, 024323 (2019).
- [40] V. Karayonchev, J.-M. Régis, J. Jolie, A. Blazhev, R. Altenkirch, S. Ansari, M. Dannhoff, F. Diel, A. Esmaylzadeh, C. Fransen, R.-B. Gerst, K. Moschner, C. Müller-Gatermann,

- N. Saed-Samii, S. Stegemann, N. Warr, and K. O. Zell, *Phys. Rev. C* **95**, 034316 (2017).
- [41] A. Esmaylzadeh, L. M. Gerhard, V. Karayonchev, J.-M. Régis, J. Jolie, M. Bast, A. Blazhev, T. Braunroth, M. Dannhoff, F. Dunkel, C. Fransen, G. Häfner, L. Knafla, M. Ley, C. Müller-Gatermann, K. Schomacker, N. Warr, and K.-O. Zell, *Phys. Rev. C* **98**, 014313 (2018).
- [42] M. Wilhelm, J. Eberth, G. Pascovici, E. Radermacher, H. G. Thomas, P. von Brentano, H. Prade, and R. M. Lieder, *Nucl. Instrum. Methods Phys. Res., Sect. A* **381**, 462 (1996).
- [43] Z. Bay, *Phys. Rev.* **77**, 419 (1950).
- [44] J.-M. Régis, A. Esmaylzadeh, J. Jolie, V. Karayonchev, L. Knafla, U. Köster, Y. H. Kim, and E. Strub, *Nucl. Instrum. Methods Phys. Res., Sect. A* **955**, 163258 (2020).
- [45] L. Knafla, P. Alexa, U. Köster, G. Thiamova, J.-M. Régis, J. Jolie, A. Blanc, A. M. Bruce, A. Esmaylzadeh, L. M. Fraile, G. de France, G. Häfner, S. Ilieva, M. Jentschel, V. Karayonchev, W. Korten, T. Kröll, S. Lalkovski, S. Leoni, H. Mach *et al.*, *Phys. Rev. C* **102**, 054322 (2020).
- [46] A. Esmaylzadeh, J.-M. Régis, Y. H. Kim, U. Köster, J. Jolie, V. Karayonchev, L. Knafla, K. Nomura, L. M. Robledo, and R. Rodríguez-Guzmán, *Phys. Rev. C* **100**, 064309 (2019).
- [47] T. Kibédi, Jr., T. W. Burrows, M. B. Trzhaskovskaya, P. M. Davidson, and C. W. Nestor, Jr., *Nucl. Instrum. Methods Phys. Res., Sect. A* **589**, 202 (2008).
- [48] B. Saha, Ph.D. thesis, Universität zu Köln (2004).
- [49] R. F. Casten, *Nuclear Structure from a Simple Perspective*, Vol. 23 (Oxford University Press, Oxford, 2000).
- [50] B. Singh, *Nucl. Data Sheets* **75**, 199 (1995).
- [51] M. M. Minor, *Nucl. Data Sheets* **10**, 515 (1973).
- [52] B. Singh, *Nucl. Data Sheets* **130**, 21 (2015).
- [53] C. M. Baglin, *Nucl. Data Sheets* **111**, 275 (2010).
- [54] R. B. Firestone, *Nucl. Data Sheets* **55**, 583 (1988).
- [55] J. Wiederhold, V. Werner, R. Kern, N. Pietralla, D. Bucurescu, R. Carroll, N. Cooper, T. Daniel, D. Filipescu, N. Florea, R.-B. Gerst, D. Ghita, L. Gurgi, J. Jolie, R. S. Ilieva, R. Lica, N. Marginean, R. Marginean, C. Mihai, I. O. Mitu *et al.*, *Phys. Rev. C* **99**, 024316 (2019).
- [56] N. V. Zamfir, G. Hering, R. F. Casten, and P. Paul, *Phys. Lett. B* **357**, 515 (1995).
- [57] A. Bohr and B. R. Mottelson, *Nuclear Structure: Vol. 1* (World Scientific, Singapore, 1969).
- [58] M. A. El-Khosht, *Nuovo Cimento A* **106**, 875 (1993).
- [59] B. Cederwall, M. Doncel, Ö. Aktas, A. Ertoprak, R. Liotta, C. Qi, T. Grahn, D. M. Cullen, B. S. Nara Singh, D. Hodge, M. Giles, S. Stolze, H. Badran, T. Braunroth, T. Calverley, D. M. Cox, Y. D. Fang, P. T. Greenlees, J. Hilton, E. Ideguchi *et al.*, *Phys. Rev. Lett.* **121**, 022502 (2018).
- [60] R. M. Diamond and F. S. Stephens, *Annu. Rev. Nucl. Part. Sci.* **30**, 85 (1980).
- [61] K. Heyde, P. Van Isacker, J. Jolie, J. Moreau, and M. Waroquier, *Phys. Lett. B* **132**, 15 (1983).
- [62] K. Heyde, J. Jolie, P. Van Isacker, J. Moreau, and M. Waroquier, *Phys. Rev. C* **29**, 1428 (1984).
- [63] P. E. Garrett, M. Zielińska, and E. Clément, *Prog. Part. Nucl. Phys.* **124**, 103931 (2022).
- [64] J. Gascon, P. Taras, P. Van Esbroek, H. R. Andrews, D. C. Radford, D. Ward, and A. Christy, *Nucl. Phys. A* **472**, 558 (1987).
- [65] C. Y. Wu, D. Cline, E. G. Vogt, W. J. Kernan, T. Czosnyka, K. G. Helmer, R. W. Ibbotson, A. E. Kavka, B. Kotlinski, and R. M. Diamond, *Nucl. Phys. A* **533**, 359 (1991).
- [66] A. Arima and F. Iachello, *Phys. Rev. Lett.* **35**, 1069 (1975).
- [67] A. Arima and F. Iachello, *Annu. Rev. Nucl. Part. Sci.* **31**, 75 (1981).
- [68] D. D. Warner and R. F. Casten, *Phys. Rev. Lett.* **48**, 1385 (1982).
- [69] A. Arima and F. Iachello, *Ann. Phys.* **111**, 201 (1978).
- [70] A. Arima and F. Iachello, *Ann. Phys.* **281**, 2 (2000).
- [71] K. Nomura, T. Otsuka, N. Shimizu, and L. Guo, *Phys. Rev. C* **83**, 041302(R) (2011).
- [72] S. Heinze, Ph.D. thesis, Universität zu Köln (2008).
- [73] T. Kibedi, G. D. Dracoulis, A. P. Byrne, and P. M. Davidson, *Nucl. Phys. A* **688**, 669 (2001).
- [74] B. Saygi, D. T. Joss, R. D. Page, T. Grahn, J. Simpson, D. O'Donnell, G. Alharshan, K. Auranen, T. Bäck, S. Boening, T. Braunroth, R. J. Carroll, B. Cederwall, D. M. Cullen, A. Dewald, M. Doncel, L. Donosa, M. C. Drummond, F. Ertuğral, S. Ertürk *et al.*, *Phys. Rev. C* **96**, 021301 (2017).

### 3 | Publication II:

Systematic investigation of time walk and time resolution characteristics of CAEN digitizers V1730 and V1751 for application to fast-timing lifetime measurement





## Technical notes

# Systematic investigation of time walk and time resolution characteristics of CAEN digitizers V1730 and V1751 for application to fast-timing lifetime measurement

A. Harter\*, M. Weinert, L. Knafla, J.-M. Régis, A. Esmaylzadeh, M. Ley, J. Jolie

Universität zu Köln, Institut für Kernphysik, Zùlpicher Str. 77, 50937 Köln, Germany



## ARTICLE INFO

## Keywords:

Digital CFD  
Lifetime measurement  
Fast-timing  
Centroid shift method  
Scintillation detectors

## ABSTRACT

The timing performance of the integrated digital constant fraction discriminators of the two digitizer modules V1730 and V1751 from CAEN are systematically investigated with respect to fast-timing lifetime measurements. Systematic and parameter-dependent knowledge of the time walk behavior and the time resolution of the digital constant fraction discriminators is obtained. Understanding these dependencies is crucial for properly calibrating individual fast-timing systems and a comparable investigation of these digitizers was never conducted before. Reference is made to the existing analog standard for fast-timing techniques and recent digital developments. The study shows, that the timing performance of both modules is comparable to other digital fast-timing implementations and established fast-timing setups using analog constant fraction discriminators, but with the added benefit of digital processing. The peculiarities of the modules are pointed out and described. Both digitizer modules were found to be highly effective and user-friendly instruments for modern fast-timing requirements. Best parameter sets for both digitizers as well as best energy application ranges are provided.

## 1. Introduction

The fast-timing technique is a well known and reliable tool to determine lifetimes of nuclear excited states. Knowing the lifetime of an excited state of a nucleus can help in understanding underlying structures by extracting the reduced transition probability  $B(\sigma L)$  between two excited states [1,2]. Therefore, lifetime determination is a key ingredient to obtain structural information about excited nuclei. Throughout the evolution of nuclear physics, numerous techniques for determining lifetimes from seconds down to femtoseconds have been developed [3]. For lifetimes ranging from picoseconds to several nanoseconds, the fast-timing technique is a suitable method.

The fast-timing technique essentially utilizes the time difference between the populating and depopulating  $\gamma$ -rays of an intermediate state of interest to obtain information about its lifetime. The established fast-timing setup uses a complex circuit of analog constant-fraction discriminators (CFDs) and time-to-amplitude converters (TACs) [4,5]. However, using the multiplexed start-stop technique, the complexity of the electronics of an analog fast-timing setup increases rapidly with the number of detectors [6,7].

In recent years, the emergence of digitally implemented real-time interpolating CFD algorithms integrated in fast-sampling digitizers has greatly reduced the complexity of electronic circuits, while providing

timestamps in the picosecond range usable for fast-timing analyses. For example, the  $\nu$ -Ball array and FASTER data acquisition system at the ALTO facility in Orsay was successfully equipped with 12-bit digitizers with integrated digital CFDs with a sampling rate of 500 MS/s for timing purposes for the first time in 2017/2018 for a large fast-timing and spectroscopic campaign [8–15]. Despite this recent advancements, the utilization of the new timing techniques has not been widely adopted in the fast-timing community, as the implementation of these techniques is still in its early stages of development in most institutions.

The timing performance of an individual timing system is dependent on the digitizer modules in use. The different digitizer modules available use slightly different working principles and there are no standard values for proper adjustment of detectors and digital CFD parameters for most digitizer types. As an example, the proper detector and CFD adjustment using the analog CFD model Ortec 935 in combination with LaBr3(Ce) detectors has been published in 2016 [6]. A characterization of the timing performance, especially concerning time walk and time resolution of a specific timing module, as a function of detector and CFD parameters for the dedicated application to fast-timing lifetime measurement is needed for validation of the results and proper comparison with these of other modules.

\* Corresponding author.

E-mail address: [aharter@ikp.uni-koeln.de](mailto:aharter@ikp.uni-koeln.de) (A. Harter).



This study systematically investigates the timing performance of the real-time digital CFDs of the V1730 and V1751 digitizers manufactured by CAEN S.p.A. with sampling rates of 500 MHz and 1 GHz, respectively. For the first time, a systematic investigation of the time walk behavior and the time resolution in dependence of digital CFD parameters and input amplitude has been carried out for both modules. Additionally, the timing performance of both digitizers were compared to the characteristics of their analog counterparts and the results of other digital time pick-off devices.

The primary objective of this study is to provide a validation for future fast-timing experiments employing these modules. This will be achieved by investigating the impact of various CFD tuning parameters and signal amplitudes on the time resolution and time walk characteristics. Additionally, an optimal set of parameters and best energy application ranges for the experimental conditions is suggested for both modules.

## 2. The fast-timing method

### 2.1. General information about the fast-timing principle

The fast-timing procedure is based on measuring the time difference between two  $\gamma$ -rays of a  $\gamma - \gamma$  cascade populating and depopulating an intermediate state of interest [4,5,7,16–18]. The distribution of measured time-differences is described by the delayed time-difference distribution [19]. This delayed time-difference distribution is defined by a convolution of the prompt response function (PRF), which depends on the timing system, and an exponential decay [19]:

$$D(t) = n\lambda \int_{-\infty}^t PRF(t' - C_P)e^{-\lambda(t'-C_P)} dt' + n_r, \quad \lambda = \frac{1}{\tau}, \quad (1)$$

where  $n_r$  is the random background level,  $C_P$  is the centroid (first moment) of the PRF and  $\tau$  the lifetime of the intermediate state. The PRF is the time difference distribution obtained for signals with a zero-time-difference. The centroid position and the full width at half maximum (FWHM) of the PRF, which is considered as the time resolution of a system, are dependent on detector properties, time pick-off technique (e.g. CFD, digital CFD or leading edge) and energies of detected  $\gamma$ -rays.

The centroid-shift method is used to determine lifetimes of excited states with high precision, smaller than the time resolution of the corresponding experimental setup. In centroid-shift analysis, the lifetime is determined by the time shift of the centroids of the measured delayed time-difference distributions ( $C_D$ ) relative to the centroid position of the energy-dependent PRF ( $C_P$ ) [4]:  $\tau = C_D - C_P$ . This situation is illustrated in Fig. 1, where the centroid positions considered are indicated. Further details can be found in Refs. [5,7].

The centroid position of the PRF is affected by signal-amplitude depended time walk (TW). If the TW is calibrated for the experimental setup, the lifetime of an intermediate state can be derived according to:

$$\tau = C_D - T_0 - TW(E_1, E_2). \quad (2)$$

The constant term  $T_0$  is given by  $T_0 = TW(E_1 = E_2)$ , which corresponds to the zero point of the timing system.

### 2.2. From analog to digital timing

The technical state-of-the-art for lifetime measurements using large fast-timing arrays in terms of time resolution, time walk behavior is the use of analog setups using multiplexed start and stop signals [6]. This established analog fast-timing setup is constructed using two or more fast-timing detectors, typically  $\text{LaBr}_3(\text{Ce})$  or  $\text{CeBr}_3$ . These scintillators are optically coupled to photomultiplier tubes (PMTs) [21,22] with two outputs each. The analog setup utilizes two branches, a time branch and an energy branch. The energy branch directly digitizes the energies of

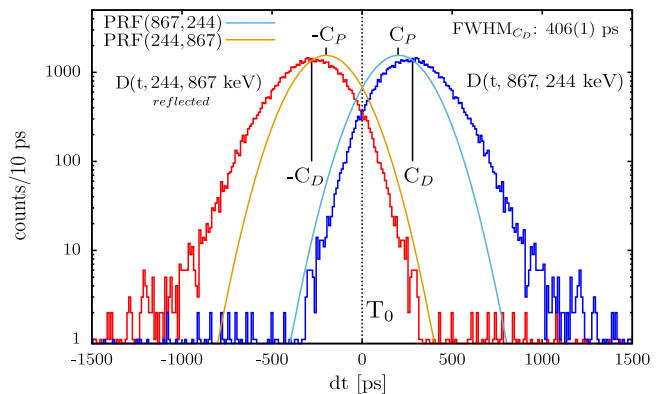


Fig. 1. The identical but mirrored time difference distributions from the 867 - 244 keV cascade in  $^{152}\text{Sm}$  with a binning of 10 ps/channel is shown.  $D(t, 867, 244 \text{ keV})$  (blue) is generated by gating in feeder-decay sequence. The reflected  $D(t, 244, 867 \text{ keV})$  (red) distribution is generated by gating in decay-feeder sequence. The intermediate state connecting both  $\gamma$ -rays has a lifetime of 80.9(11) ps [20]. The time difference distributions resulting from the centroid shift method exhibit symmetry about the time reference point  $T_0$  due to the inherent symmetry of the method.

the incoming  $\gamma$ -rays. The time branch uses a circuit of analog Fan-in-Fan-out modules, delay loops, CFDs and TACs, to determine the time difference  $dt$  between two signals [3,4]. Therefore, the information of a single fast-timing event is condensed to

$$(E_{\text{start}}, E_{\text{stop}}, dt),$$

where the energies  $E_{\text{start}}$  and  $E_{\text{stop}}$  are obtained from the energy branches and the time difference  $dt$  from the TAC in the time branch. This technique is described in detail in Refs. [4,5,7,18]. Utilizing modern TACs and CFDs this kind of analog setup is able to measure short lifetimes down to a few picoseconds.

In various measurements, tests and quantifications, the analog CFD model ORTEC 935 [23] in combination with the TAC model ORTEC 566 [24] has proven high fast-timing performance [22,25–30]. This combination of analog electronics represents the state-of-the-art of fast-timing technology and serves as the standard for comparison in this work.

In the following, the term “analog setup” refers to a configuration in which time difference information is obtained from TACs, while the term “digital setup” refers to a fully digital configuration in which analog electronic modules are not present and the direct time information of signals is measured by the digital CFDs.

Recent fast-sampling digitizers utilizing digitally implemented interpolating CFD algorithms (described in Section 3) are capable of determining sub-sample-period precision timestamps. The high precision of digital timestamp determination in the low picosecond regime and the omission of the external analog modules enables an extensive simplification of fast-timing setups. In a fully digital experimental setup, the information of a single fast-timing event is now condensed to

$$[(E_1, t_1), (E_2, t_2)], \quad (3)$$

containing the full measured information. The time difference is taken in the offline analysis in both possible directions [31]:

$$dt_{12}(E_1, E_2) = t_2 - t_1 \quad \text{and} \quad dt_{21}(E_2, E_1) = t_1 - t_2. \quad (4)$$

Conceptual, the analysis of the digital fast-timing data is identical to centroid shift analysis of  $\gamma - \gamma$  coincidence data and is discussed in detail in Refs. [4,16,31]. This symmetrization approach is appropriate when nearly equal timing conditions, e.g. similar time resolutions of detectors, mainly related to the crystal size, and time walk, mainly related to the CFD device, are given for each channel.

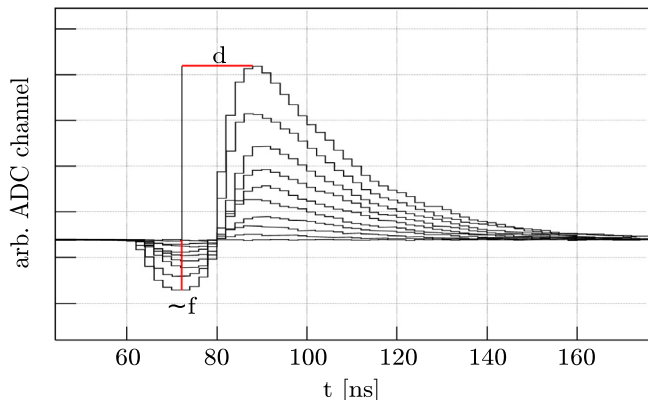


Fig. 2. Several digitally CFD shaped signals recorded by a CAEN V1730 digitizer module. The input signal was a negative anode signal originating from a LaBr detector in combination with a PMT. In this exemplary case,  $d$  marks the delay time and  $\sim f$  an approximation of the fraction value used in the shaping procedure.

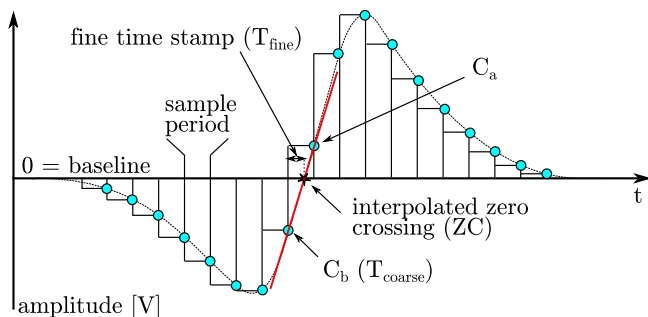


Fig. 3. A sampled CFD signal, where the interpolated polynomial of first order is indicated by a red line and the zero crossover marked by a star. The point in time of the zero crossover represents the timestamp of the original input signal with a precision smaller than the sample period.

By applying energy conditions as gates to the collection of all stored events  $[(E_1, t_1), (E_2, t_2)]$  and calculating  $dt$  according to Eq. (4), a time difference distribution is generated. In Fig. 1, two distributions are shown, both containing the full experimental data. The distributions are identical but mirrored with respect to  $T_0$ . Only the gate sequence, either  $(E_{\text{feeder}}, E_{\text{decay}})$  or  $(E_{\text{decay}}, E_{\text{feeder}})$ , determines, which distribution is generated. In Fig. 1, this process is illustrated for the 876-244 keV cascade in  $^{152}\text{Sm}$  with a lifetime of the intermediate state of 80.9(11) ps [20], populated by the electron capture decay from  $^{152}\text{Eu}$ . The symmetry of the distributions under exchange of  $E_1$  and  $E_2$  can be used for precise determination of  $T_0$  of the system. From the distributions in Fig. 1, e.g.  $D(t, E_{\text{feeder}}, E_{\text{decay}})$  the lifetime can be extracted using the centroid shift method by applying Eq. (2) with known time walk characteristics.

### 3. Digital constant fraction discrimination and timestamp interpolation

A fast-sampling analog-to-digital converter (ADC) is capable of accurately discretizing continuous input signals that have durations within the nanosecond range. This enables a digital CFD signal shaping procedure to achieve a zero crossover at the point in time the original signal reaches a constant fraction of its amplitude. The timestamp of an incoming signal is then identified as the zero crossover of a CFD shaped signal. The digital shaping procedure of the implemented CFD algorithm is analogous to the shaping procedure of an analog CFD. Specifically, the captured signal is duplicated, one of the duplicates is inverted and delayed by a specified delay time  $d$ , while the other one

is attenuated by a defined fraction  $f$  [32], see Fig. 2. The presented algorithm superimposes two processed signals to create a bipolar signal, which contains the required zero crossover to calculate a constant fraction timestamp according to [33]:

$$C_1(t) = S(t) \cdot f - S(t + d) \quad (5)$$

or

$$C_2(t) = S(t + d) - S(t) \cdot f, \quad (6)$$

where  $C_n(t)$  is the CFD sample and  $S(t)$  the original sample at time  $t$ . A sample is a measurement of the amplitude of an analog signal taken at discrete time intervals known as the sampling period. The ADC then converts each sample into a digital representation, which results in the discretization of the continuous signal pulse. The two distinct shaping sequences, as presented by Eqs. (5) and (6), represent two different implementations found in the digitizer modules investigated in this study. Fig. 2 shows a series of digitally shaped CFD signals with different amplitudes originating from the negative anode of a LaBr scintillator coupled to a PMT. These signals were recorded with a CAEN model V1730 digitizer.

The timestamp derived from the zero crossover would have a precision equal to the sample period, e.g. 2 ns for a 500 MS/s sample frequency. But to achieve timestamps with higher precision than the sample period, interpolations of low-degree polynomials between adjacent samples surrounding the zero crossover of the CFD signals are utilized. Recent developments in field-programmable gate array (FPGA) technology allow the real-time interpolation of such polynomials already on the digitizer and online sub-sample-period timestamp calculation. Recently, various interpolation algorithms including linear and cubic spline interpolations have been discussed in [34–37].

The digital CFDs of the modules under investigation in this study interpolate a first-order polynomial between the last CFD sample before the zero crossover  $C_b$  and the first CFD sample after the zero crossover  $C_a$ . As illustrated in Fig. 3, the timestamp of the interpolated zero crossover (ZC) is expressed by the sum of the timestamp of  $C_b$  ( $T_{\text{coarse}}$ , with sample period precision) and the fine timestamp  $T_{\text{fine}}$ :

$$\text{ZC} = T_{\text{coarse}} + T_{\text{fine}}.$$

$T_{\text{fine}}$  is calculated using the linear interpolation between  $C_b$  and  $C_a$  according to the linear equation:

$$T_{\text{fine}} = \frac{-C_b}{C_a - C_b} \cdot T_{\text{sample}}. \quad (7)$$

$T_{\text{sample}}$  is the sample period determined by the sample rate of the data acquisition, e.g. 2 ns for a sample rate of 500 MS/s.

In analog CFD modules, the time resolution strongly depends on the amplitude of the input signal and the amplitude resolving capability of the electronic components used in the CFD circuit [32,38]. This effect depends on the signal-to-noise ratio (SNR) [32], which is defined as the ratio of the signal amplitude to any electronic noise present in the signal. The SNR induces an additional time uncertainty which is significant at lower amplitudes since the slope at the zero crossover decreases with decreasing amplitudes. A similar effect is expected for a digitally shaped CFD signal and applied timestamp interpolation. As depicted in Fig. 4, an artificial disturbance  $p$  added to two different samples affects the interpolated timestamp depending on the amplitude. The smaller the amplitude, the larger the deviations of the timestamps  $dt$ . This causes the time resolution of digital CFDs to degrade for smaller signal amplitudes. This effect is also referred as time jitter [32].

Digital CFDs, as well as analog CFDs, are affected by an energy dependent time walk (see Section 2.1). The time walk of an analog CFD occurs due to the slope of the bipolar CFD signal at the point of zero crossover [32]. The slope at this point decreases rapidly with decreasing amplitude for amplitudes below around 400 mV [6]. Above approximately 400 mV, the slope remains nearly constant [6]. The non-linear time walk at low amplitudes is caused by the charge sensitivity



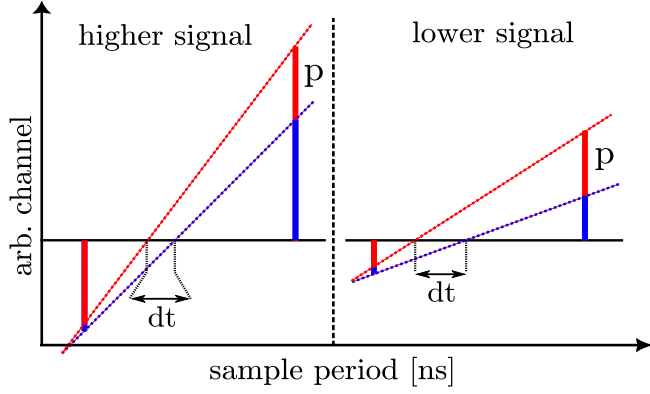


Fig. 4. Illustration of two different signal amplitudes affected by the disturbance  $p$  and effect on the timestamp interpolation. The disturbance  $p$  of the sample amplitudes, considered as noise, is the same on the larger (left) and on the lower (right) signal. The disturbance was chosen to be relatively large in order to demonstrate the effect. The interpolated timestamp of the higher signal differs in a smaller range  $dt$  than that of the smaller signal. As a result, small variations of small signals lead to larger uncertainties in the interpolation of the timestamp compared to higher signals, which is called time jitter.

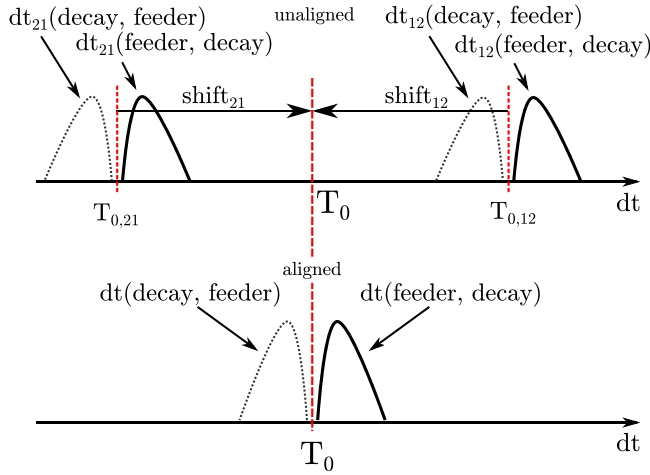


Fig. 5. Digital timestamp shift for the detector combination  $ij = 12$ . After the application of the shift constants, all time difference distributions are aligned. This is done for each detector pair  $ij$ . The dashed time difference distribution is the anti-delayed distribution, obtained by exchange of the gates. In the lower, aligned plot, both distributions are identical but mirrored with respect to  $T_0$  and each contains the full experimental statistics.

of the electronics within the CFD module, while the nearly linear time walk at higher amplitudes is related to the shaping delay time [32,38]. It is reasonable to expect similar behavior of slope-dependent time walk in digital interpolating CFDs.

#### 4. The sorting procedure of digital fast-timing data

In digital fast-timing, the time difference of two time correlated  $\gamma$ -rays is extracted from the precise timestamp information of each individual detector hit, which is done during the offline analysis. All detector hits are sorted by timestamp after the determination of potential runtime differences between individual channels outside the data acquisition system, e.g., due to different cable lengths.

For symmetric data of a digital setup, the time difference distributions for a single detector combination, calculated according to Eq. (4), have to be aligned by applying a set of  $shift_{ij}$  constants to each distribution before superposition of the data from all detector combinations. The procedure is illustrated in Fig. 5 and is representative of

the alignment of all time spectra  $dt_{ij}$ , ( $i, j \in N : i \neq j$ ) of an array with  $N$  detectors [31]. To determine the  $shift_{ij}$  constants precisely, the time difference distributions of a cascade with a short, nearly prompt lifetime, like 779-344 keV is utilized. The energy-independent shift constants are obtained by half the distance of  $dt_{12}$  and  $dt_{21}$ , where  $T_{0,ij}$  and  $T_{0,ji}$  are symmetric around  $T_0$ , according to Fig. 5:

$$shift_{ij} + dt_{ij} = shift_{ij} + t_i - t_j = dt$$

and

$$shift_{ji} + dt_{ji} = shift_{ji} + t_j - t_i = dt.$$

Once the time difference distributions have been aligned, the relationship  $dt_{ij} = dt_{ji} = dt$  is established. Fig. 5 shows that for a given detector combination  $ij$  and the following relationship holds:  $shift_{ij} = -shift_{ji}$ . Different detector combinations  $ij$  exhibit different shifts relative to the reference time  $T_0$ .

All detector hits are sorted by applying a time coincidence window and multiplicity conditions and stored as events. A minimal digital fast-timing event has multiplicity two and consists of two energy values and corresponding timestamps according to Eq. (3).

After identifying the events of interest by using the energy conditions, the desired time differences are calculated using Eq. (4). Note, for consistency we opted to always calculate the time difference between the two  $\gamma$ -ray signals of interest according to

$$dt = t_{E_{\text{second gate matching}}} - t_{E_{\text{first gate matching}}}$$

where suffix “first gate matching” corresponds to the first energy condition and “second gate matching” to the second energy condition applied to the data. This method ensures that the time difference is calculated in a consistent manner resulting in the desired distributions, as illustrated in Fig. 1.

Fig. 6 depicts the event density in an example time range of 70 ns with different zoom levels centered on one specific event of multiplicity = 2. This data was recorded during an in-beam experiment using a fast-timing array equipped with 8 LaBr scintillation detectors and detection rates of 15–20 kHz per detector. The red crosses indicate the detector hits that satisfy the conditions of a coincidence window of 10 ns and a multiplicity of exactly 2 LaBr hits. The black crosses represent all other detector hits uncorrelated in time. The figure demonstrates the accuracy of recent digital CFDs for determining timestamps. It highlights the importance of an accurate timestamp shift correction, as a coincidence window in the order of a few nanoseconds can be sufficient to measure short lifetimes in the picosecond range, as long as only LaBr hits or those of comparable fast detectors are used.

#### 5. Experimental details

This study aims to investigate the fast-timing capabilities of modern digitizers, namely CAEN modules V1730 [39] and V1751 [40], implementing digital interpolating CFD algorithms for picosecond precise timestamp determination of detector hits. The important hardware properties of these digitizers concerning digital  $\gamma - \gamma$  fast-timing are listed in Table 1. The goal of this part of the study is to optimize the time resolution of the digital CFDs in combination with the established LaBr detectors while minimizing the energy-dependent time walk in the  $\gamma$ -ray energy range of a  $^{152}\text{Eu}$  time walk calibration standard. An optimization process was conducted to identify the optimal combination of CFD algorithm parameters (see Section 5.2) providing the best balance between time resolution and minimal time walk.

##### 5.1. Digital fast-timing setup

In order to evaluate the timing performance of the implemented interpolating CFD algorithms of the V1730 and the V1751 digitizers, a fast-timing setup was constructed as shown in Fig. 7a. The setup consists of four  $1.5'' \times 1.5''$  LaBr<sub>3</sub>(Ce) scintillators optically coupled

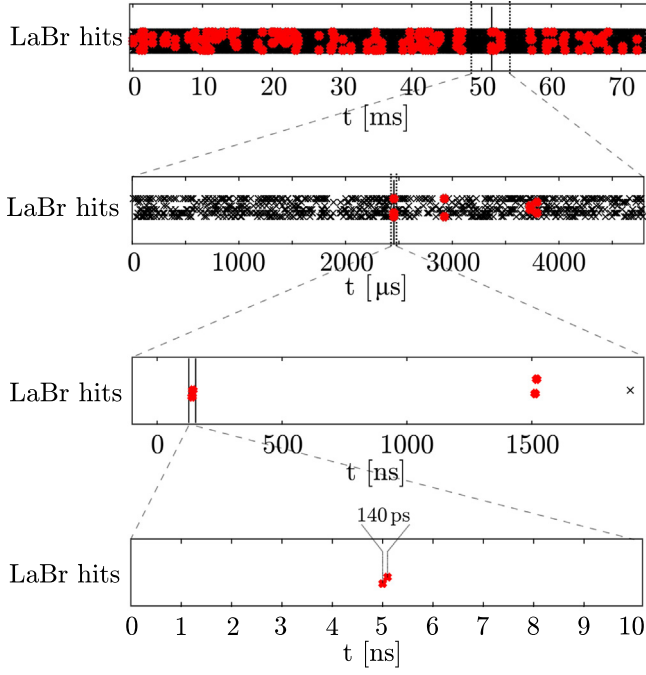


**Fig. 6.** Detector hit density for different time ranges between 70 ms to 10 ns of a fast-timing array with 8 LaBr detectors. The data was measured during an in-beam experiment with detection rates of 15–20 kHz per detector. The data is sorted with a coincidence window of 10 ns and a multiplicity of exactly two LaBr hits was required. The red crosses represent detector hits that satisfy these conditions. The two LaBr hits in the bottom plot have a time difference of only 140 ps. The figure demonstrates the accuracy of the digital timestamp determination and motivates the use of short coincidence windows of around 10 ns for digital LaBr-LaBr fast-timing. Note: the time axis were reset to zero in each plot to provide reasonable time ranges in the individual plots.

**Table 1**  
Resolution of the ADCs, internal sample rate and input dynamic range for the CAEN V1730 and V1751 digitizers.

Digitizer	ADC res.	Sample rate	Input range
V1730	14 bit	500 MS/s	0.5/2 Vpp
V1751	10 bit	1 GS/s	1 Vpp

to Hamamatsu R13435 photomultiplier tubes [41]. Each detector was connected to the digitizer with a single cable from the negative anode output of the PMT. A 90° geometry with a distance of approximately 5 cm between the detectors was applied, with only opposite detectors being used for timing coincidences. This geometry allows for a good balance between reduced inter-detector Compton scattering and sufficient statistics and efficiency [5,7]. Both digitizer modules support the same CFD shaping parameters in terms of timing capabilities: the “CFD delay”, which corresponds to the delay time  $d$ , and the “CFD fraction”, which corresponds to the constant fraction  $f$ , both described in Section 3. The CFD delay is adjustable in units of the sample period. The CFD fraction is selectable between four values (25%, 50%, 75%, and 100%) for the applied firmware of these particular modules.

An  $^{152}\text{Eu}$   $\gamma$ -ray source was used in the experiments, which offers twelve nearly Compton background-free  $\gamma$ -ray cascades with known lifetimes of intermediate states in the energy range of 200 keV to 1400 keV [20]. The time resolution observed using the strongest medium energy 779–344 keV cascade in  $^{152}\text{Gd}$  interconnecting the  $3_1^-$ ,  $2_1^+$  and  $0_1^+$  states with a short lifetime of 46.3(39) ps [20] and a nearly symmetric Gaussian time distribution is used as a benchmark during the optimization process.

In Fig. 8a, an exemplary singles  $\gamma$ -ray spectrum for the V1730 digitizer is given and Fig. 8b shows the relative energy resolution

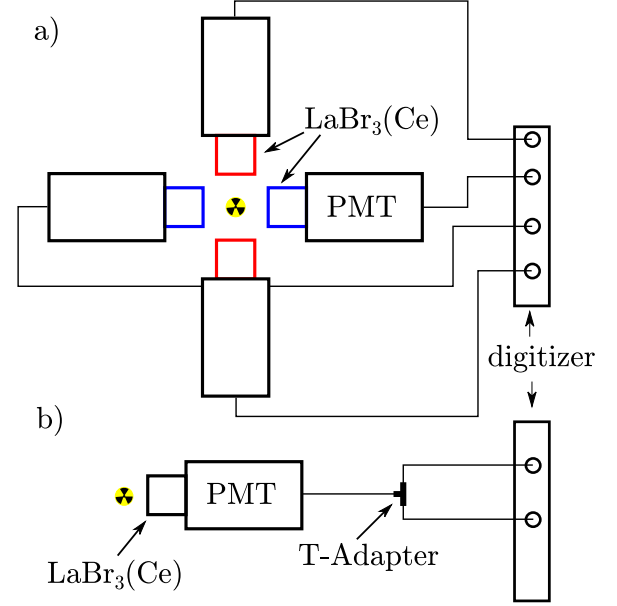


**Fig. 7.** (a) Fast-timing setup with four LaBr<sub>3</sub>(Ce) scintillators in a 90° geometry with a source-to-detector distance of 2.5 cm. Only  $\gamma$ - $\gamma$  coincidences between opposing detectors were used, which is indicated by the colors of the scintillators. This geometry grants good exposure of the scintillators and low inter-detector Compton scattering. (b) Split signal setup using one LaBr detector and a T-adapter. The two signals are fed into two different digitizer channels.

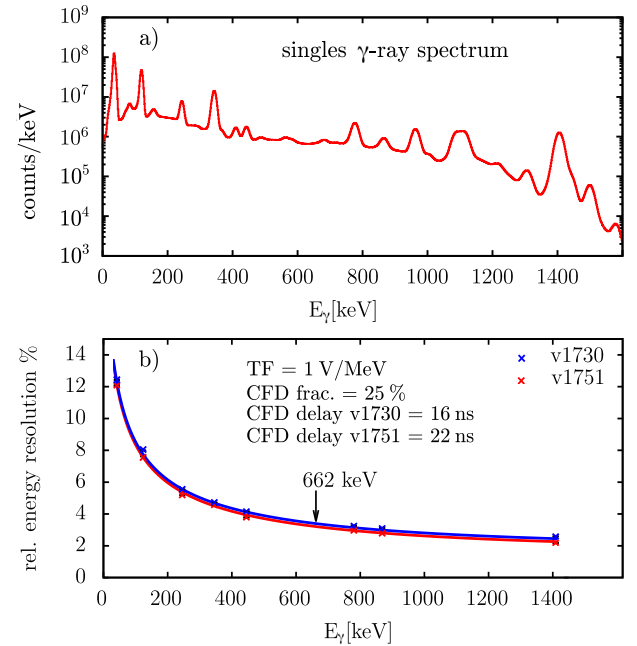


**Fig. 8.** (a) A singles  $\gamma$ -ray spectrum of the  $^{152}\text{Eu}$   $\gamma$ -ray source for the V1730 digitizer. (b) Relative energy resolutions of both digitizers shown over an energy range between approximately 100 and 1400 keV, demonstrating a decreasing behavior with respect to  $1/\sqrt{E_\gamma}$ .

$\Delta E/E$  [%] for both digitizers in an energy range between 40 and 1400 keV. The energy is obtained through charge integration inside the digitizer and the relative energy resolution is optimized through gain matching of the electron multiplication of the PMTs [42]. It amounts to 3.01(1)% and 3.18(1)% for the V1751 and the V1730 at a  $\gamma$ -ray energy of 662 keV, which is commonly used as a benchmark for energy resolution, respectively.

## 5.2. Description of dedicated measurement approaches

The crucial properties of implemented interpolating CFD algorithms in context of fast-timing techniques are the time resolution and time walk. Both properties are depending on the shaping parameters “CFD delay”, “CFD fraction” and the input signal amplitude. To classify the time resolution and time walk characteristics of the digitizers, several measurements of time periods between 10 and 24 h with different parameter settings have been conducted. Different parameter settings were used, with two of the three parameters kept fixed, while the third was varied.

The voltage applied to the PMTs was adjusted to align the input signal amplitudes of the different channels to the amplitude of the 1408 keV  $\gamma$ -ray emitted by the  $^{152}\text{Eu}$  source. The transfer function (TF) describes the relationship between the output voltage of the PMT and energy of the incident  $\gamma$ -ray. It is expressed in V/MeV and serves as a measure for the input amplitude. The TFs in the present measurements are nearly linear, as the PMTs are operated in a low to middle voltage range of 750 to 1500 V.

In order to evaluate the intrinsic time jitter of the digital CFDs, an additional measurement was conducted using a split signal configuration with a single LaBr detector, as described in previous studies [34, 37]. The anode signal from the LaBr detector was split using a T-adaptor and the two resulting signals were fed into separate signal inputs of the digitizers, as illustrated in Fig. 7b. Two digitally interpolated timestamps for the same detector pulse are acquired. Time difference distributions derived from these timestamps are free of energy-dependent time walk, lifetime effects and nearly free of other systematic effects. This approach allows for a determination of the intrinsic time jitter of the digital CFDs as a function of the input signal amplitude only effected by the SNR (see Section 3).

## 5.3. Data analysis of the measurements

The data sets obtained from the fast-timing setup with four LaBr scintillators were analyzed using the ftSOCO code [43], which was designed for the analysis of digital fast-timing data. Fast-timing events were generated requiring exactly 2 LaBr hits within a coincidence window of 20 ns, which is sufficient for the purpose of this work (see Fig. 6). If this multiplicity condition is not used in multi-detector arrays, many time-uncorrelated background events (especially inter-detector Compton scattering events) are incremented. As addressed in Section 4, small runtime differences in the arrival times of the detector signals are corrected by applying a constant timestamp offset for every detector–detector combination.

For all measurements, the centroid shift method, as described in Section 2.2, was used to determine the TW characteristic [6,31]. Each analysis for different CFD parameters or transfer functions was performed using identical energy gates on the transitions of interest to allow for comparable results.

To investigate the low energy time walk of the digitizers, a data point below 100 keV is needed. This is achieved by utilizing three-fold coincidences of the cascade 40 keV–1408 keV–122 keV (X-ray  $\rightarrow 2^- \rightarrow 2^+ \rightarrow 0^+$ ) in  $^{152}\text{Sm}$ . The 40-keV K-X-ray is emitted after the electron-capture decay of  $^{152}\text{Eu}$  to  $^{152}\text{Sm}$  within femtoseconds, which is significantly shorter than the lifetimes of the subsequent excited states in  $^{152}\text{Sm}$ . The detection of the 40-keV K-X-ray indicates the moment of population and acts as a nearly prompt feeding transition for the  $2_1^-$  state in  $^{152}\text{Sm}$  [6]. Usually, a high-resolution high-purity Germanium detector is used to apply an energy gate on the 122 keV transition. For the setup used in this work, the pairs of face-to-face detectors (same color in Fig. 7) were used for timing coincidences, while the neighboring detectors were used for the additional energy gate on the 122 keV transition. A coincidence spectrum and decay scheme for the threefold LaBr coincidences with energy gates on the 122 keV and 1408 keV  $\gamma$ -rays is shown in Fig. 9. Note, that not all measurements

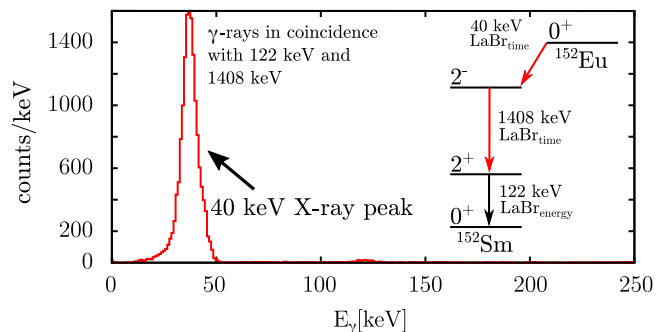


Fig. 9. Coincidence spectrum of the threefold coincidences with gates on the 122 keV and 1408 keV  $\gamma$ -rays from the  $^{152}\text{Eu}$  source. It is evident that there is relatively little background under the 40 keV X-ray peak. On the right, the decay scheme from  $^{152}\text{Eu}$  to  $^{152}\text{Sm}$ , with the transitions used for timing (40 keV and 1408 keV) marked in red, is depicted.

had sufficient statistics in the X-ray region to allow for the use of this approach.

The data obtained from the split signal setup (Fig. 7b) was analyzed using a coincidence window of 2 ns. A double gating method was employed, where the same energy gate was applied to both channels, since the same detector pulse was fed into both channels. The resulting time difference distributions provided insight into the precision of time difference determination between signals of equal energy with a consistent time difference of zero. A range of amplitude between 100 and 1000 mV was scanned using this method.

In some time difference distributions, periodic binning artifacts with low picosecond periods have been observed. These artifacts are possibly a result of the fine timestamp  $T_{\text{fine}}$  being reported as a 10-bit integer by the FPGA, resulting in a precision of  $T_{\text{sample}}/1024$ . The resulting precision of  $T_{\text{fine}}$  is  $1.953125 \approx 2$  ps in the exemplary case of the V1730 [44]. Most likely, this approximation causes an effect on the time differences, which shows up as periodic oscillations and additional beat frequencies in the time difference distributions. The binning artifacts have no influence on the centroid shift analysis but for better visual representation they were addressed by randomly blurring a calculated time difference over a two-picosecond window.

## 6. Results of the systematic investigation of timing characteristics

Modern fast-timing systems are able to achieve time resolutions between 300–400 ps for the benchmark cascade 779–344 keV [5]. For the time walk characteristic a mostly linear and flat progression is desired with variations in a range of 100 ps or less [6]. To sufficiently cover the energy range that is significant for lifetime measurements in standard nuclear structure investigations, the amplitude input range of a timing system should be maximized, but it should at least extend up to  $\gamma$ -ray energies of 1.5 MeV [5,25–30]. In the following sections, the results of our measurements obtained using different parameter combinations are presented and discussed. Specifically, the time resolution and time walk of the digital CFDs in comparison to the established analog setup concerning the above expectations are evaluated.

### 6.1. Time jitter considerations

In Fig. 10a, the progression of the time jitter as obtained from the split signal setup is illustrated. The influence of the SNR on the time jitter is observed in the low amplitude region below 400 mV where a decrease in SNR results in a corresponding increase in time jitter (see Section 3). The time jitter saturates around 25 ps and 13 ps for the selected channels of the V1730 and V1751, respectively, with a difference of 12 ps. Fig. 10b depicts time difference distributions

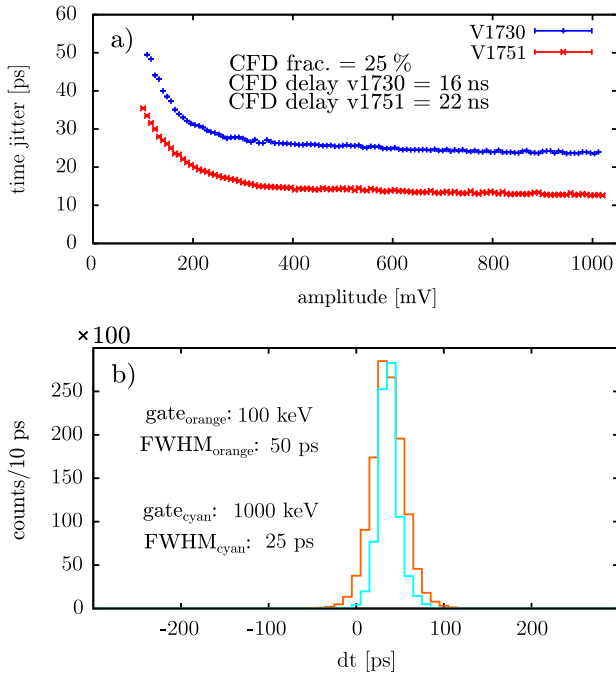


**Fig. 10.** (a) The CFD time jitter as extracted from the split signal measurement is plotted against the signal amplitude in a range from approximately 100 mV to 1000 mV. (b) Two exemplary time difference distributions of the split signal setup with a V1730 digitizer. The double gates are set on 100 keV with a FWHM of 50 ps and on 1000 keV with a FWHM of 25 ps. For details see text.

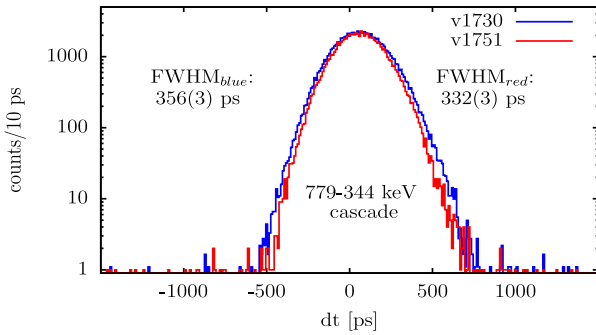


**Fig. 11.** Exemplary time difference distributions of the 779-344 keV cascade for both digitizers. The blue distribution is obtained from the V1730 and has a FWHM of 356(3) ps. The red distribution is obtained from the V1751 and has a FWHM of 332(3) ps. The parameters as displayed in Table 3 where used to generate these distributions.

for two different double-gates (described in Section 5.3) at 100 and 1000 mV for the V1730. The FWHMs obtained were 50 and 24 ps, respectively, and the uncertainties can be considered negligible.

The time difference distributions in Fig. 11, obtained from the investigated digitizers, reveal that the time resolutions between the two digitizers differ by about 25 ps for the considered channel combinations. This discrepancy in time resolution can be attributed to variations in time jitter between the digitizers. The 24 ps difference in time resolution for the investigated channel combinations of the digitizers corresponds to twice the difference in time jitter (12 ps) between the considered channel combinations of the boards. This approximation holds if all channels of one board have comparable time jitters and if the CFD contribution to the time resolution corresponds to the summed time jitters of the used channels.

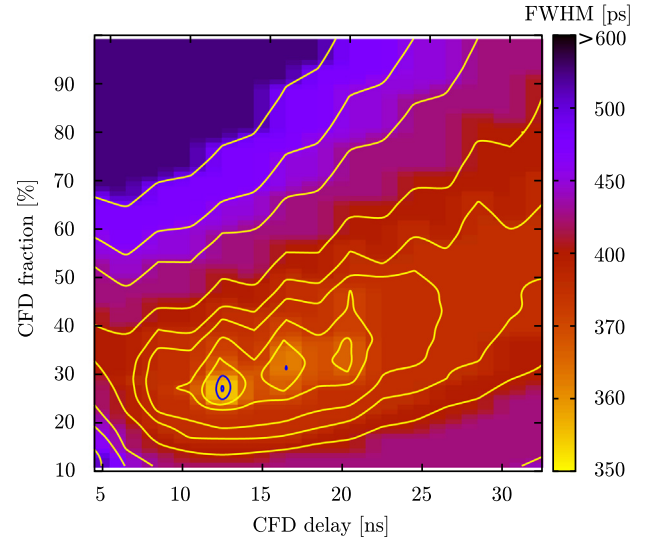


**Fig. 12.** CFD parameter scan in terms of time resolution (FWHM) of the benchmark cascade in the CFD delay - CFD fraction parameter space. Contours are given for selected heights. The best time resolutions are delivered by parameters around CFD delay = 12 ns and CFD fraction = 27%, indicated by the blue contours. The transfer function used for the measurement of this dataset was 1 V/MeV.

## 6.2. Influence of the CFD algorithm on the time resolution

During this study, the CFD algorithm from the digitizers in use was re-implemented in an offline analysis and applied to a dataset of wave traces recorded with a V1730 to get a comprehensive overview of the CFD parameter space. The offline implementation is more flexible than the online implementation since the CFD fraction is not limited to four values. A section of the CFD parameter space was scanned using the offline CFD implementation where the CFD delay was selected between 4 and 32 ns in 2 ns steps and the CFD fraction was selected between 10% and 100% in 2% steps. The heatmap shown in Fig. 12 represents the surface of the time resolution of the benchmark cascade. The yellow area around CFD delay = 14 ns and CFD fraction = 27%, marked by the blue contours, yields the best time resolution values, which is largely confirmed by the online measurements, which is discussed in the next section. With the offline parameter scan, a preliminary visualization of the parameter space was generated to reduce the amount of required experimental measurements to about 10%, and the parameters for the online measurements could be selected accordingly.

In the following, the results of the optimization process aimed at identifying the optimal combination of CFD delay, CFD fraction, and detector signal amplitude are presented and discussed in terms of their impact on the time resolution of the digital CFDs. In the plots presented in Fig. 13, the constant parameter sets utilized during the single measuring series are given. In Fig. 13a, the time resolution as a function of the CFD delay parameter is presented for both digitizers. The V1730 exhibits a minimum in time resolution at a CFD delay value of 14 ns, which fits to the prediction of the offline parameter scan, see Fig. 12. In contrast, the V1751 does not display a well-defined minimum over the range of tested CFD delay values. However, it generally exhibits a decreasing trend in time resolution when increasing the CFD delay across the majority of the tested range, remaining relatively constant above 22 ns. For comparison, in the same plot the dependence of the time resolution of the delay parameter of an analog setup using a CFD model ORTEC 935 is depicted and it moves in a comparable range [6] though the optimum parameters are not the same. The CFD delay parameters used for the further optimization process were 16 ns and 22 ns for the V1730 and the V1751, respectively.

In Fig. 13b, the time resolution as a function of the CFD fraction parameter is presented for both digitizers. The influence of the CFD



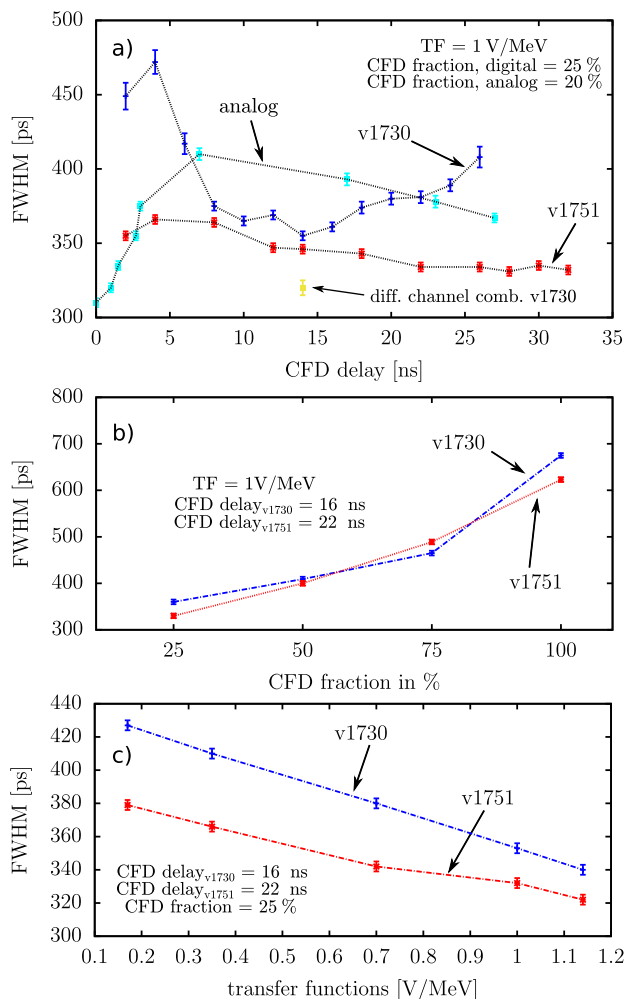


**Fig. 13.** Time resolutions (FWHM) of both digitizers versus (a) CFD delay, (b) CFD fraction and (c) transfer function in comparison with the analog measured time resolution using the CFD model ORTEC 935. For all plots, the time resolution corresponds to the FWHM of the benchmark cascade 779–344 keV obtained from a  $^{152}\text{Eu}$  source. The parameters of the CFD and the TF are given in each plot. The analog data points are taken from Ref. [6]. The dashed lines serve to guide the eye.

fraction on the time resolution is significant. As the CFD fraction increases from 25% to 100%, the time resolution degrades dramatically. For both modules the smallest available CFD fraction (25%) provided by the firmware [45] yields the best time resolution. Other studies suggest, that CFD algorithms and analog CFDs with CFD fractions around 10% provide better time resolutions than a fraction of 25% [46–48]. Based on the offline parameter scan in Fig. 12, this cannot be confirmed by this study.

In Fig. 13c, the dependency of the time resolution of the transfer function (TF) is shown. As expected from another study [49], a strong nearly linear dependence of time resolution on the TF is observed for both digitizer modules. The time resolution improves with increasing TF. The underlying reasons for this behavior are discussed in Section 3 and are mostly related to the impact of the SNR. It should be noted that the impact of the PMT voltage on the time resolution is non-negligible. Factors such as the number of photoelectrons collected [33,50] and transit time spread [51], also play a role in the improvement of the time resolution of PMT systems. These effects are mixed with that of the SNR here.

In conclusion, the optimal parameters for the CFD settings and TF with respect to the time resolution as determined in this study are provided in Table 3, along with the corresponding time resolution values for both digitizers, which are considered as the optimal

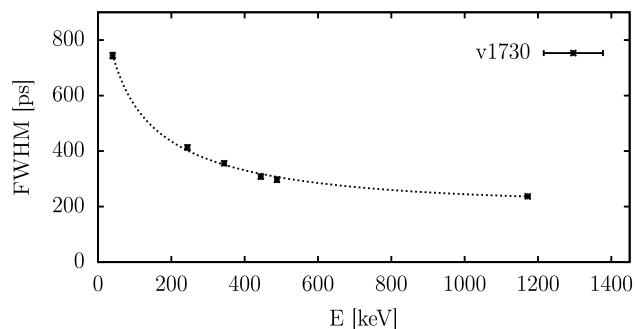


**Fig. 14.** Course of the time resolution of the V1730 digitizer over an energy range between 40 and 1173 keV measured with the best parameter sets (see Table 3). The shape of time resolution curve is related to the statistical amplitude variation of the signal and thus is proportional to  $1/\sqrt{E_\gamma}$ . The dashed line is an interpolation of the data.

**Table 2**

Time resolutions of other digitizers with comparable ADC resolution and sample rates utilizing real-time digital CFDs. The given time resolutions are all measured with the 1332.5–1173.2 keV  $\gamma$ -cascade emitted by a  $^{60}\text{Co}$  source.

ADC res.	Sample rate	Time res.	Crystal dim.	Ref.
12 bit	100 MS/s	500 ps	–	[52]
10 bit	4000 MS/s	240 ps	1.5" $\times$ 1.5"	[46]
10 bit	500 MS/s	375 ps	1.5" $\times$ 1.5"	[46]
12 bit	250 MS/s	350 ps	–	[52]
12 bit	500 MS/s	250 ps	1.5" $\times$ 1.5"	[8]
		200 ps	1" $\times$ 1"	[8]
14 bit	500 MS/s	237 ps	1.5" $\times$ 1.5"	This

Note: Not all publications provided information about the used transfer function between the PMT output and the  $\gamma$ -energy. Detector and PMT types also differ between the different publications. Accordingly, these data provide only an approximate representation of the present situation.

values obtained in this study. Fig. 14 shows the course of the time resolution versus  $\gamma$ -ray energy for the best parameter combination for the V1730 digitizer. Most publications use the prompt  $\gamma$ -cascade 1332.5 - 1173.2 keV emitted by  $^{60}\text{Co}$  source as benchmark for the time resolutions. In order to improve the clarity of the present article, it was chosen not to present all time resolution considerations again with the cobalt-cascade. Only the best parameter set of the V1730 digitizer was applied to measure the time resolution of the cobalt-cascade and was depicted in Fig. 14. Due to the limited loan period of the V1751, this measurement could only be done for the V1730 digitizer. The time resolutions for the cobalt cascade amount to 237(2) ps for the V1730. Table 2 shows the time resolutions obtained by other laboratories mostly measured using the 1332.5 - 1173.2 keV  $\gamma$ -cascade emitted by a  $^{60}\text{Co}$  source. Not all publications provided information about the used transfer functions between the PMT output and the  $\gamma$ -ray energy. Also detector and PMT types differ between the different publications, hence, these data provide only an approximate representation of the present situation.

It is noteworthy, that considerably different time resolutions were observed while using a different channel combination than the one studied in this research, which remained unchanged during the measurements. Time resolution values of about 320 ps were obtained with the same TF, detectors and CFD settings for the V1730 but utilizing a different channel combination. Apparently, the time resolution shows significant differences between the different input channels of the digitizers. In Fig. 15, a comparison of the time resolutions for a single V1730 digitizer across different channel combinations in relation to channel 0 is presented. One detector was consistently connected to channel 0, while the other one was cycled through all other channels. These differences are board and channel specific and have to be quantified separately for every board. This observation is confirmed by the time resolution values obtained in Ref. [53]. Currently, there is no

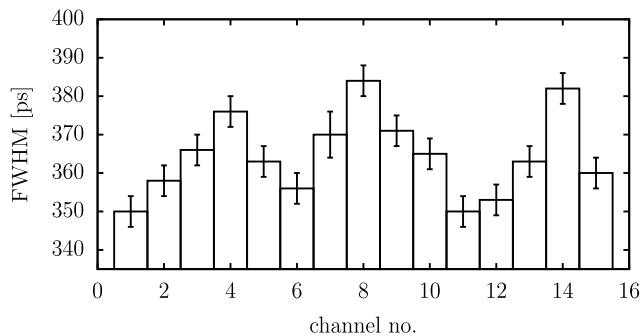


Fig. 15. Time resolutions of the different channels of a specific V1730 digitizer module in relation to channel 0. These differences are board specific and have to be quantified separately for every board. For details see text.

Table 3

The best parameter sets for the digitizer modules under investigation applicable for fast-timing in an energy range from around 100 to 1400 keV. The time resolutions of the benchmark cascade 779–344 keV are given for the PMTs and digitizer channel combinations used for the investigations and can deviate from the time resolutions of other channel combinations and PMTs. For details see text.

Parameter	V1730	V1751	
		Opt. time resol.	Opt. TW
CFD delay	14 ns	22 ns	22 ns
CFD fraction	25%	25%	25%
TF	1 V/MeV	1 V/MeV	0.7 V/MeV
Time resolution	356(3) ps	332(3) ps	342(3) ps

definitive explanation for this behavior. However, it is plausible that it is related to variations in internal reference clock runtime within the digitizer and differences in the resolution of a single sample among the different channels.

### 6.3. Results of the time walk investigations

Next, we will focus on the investigations of the time walk characteristics of the implemented interpolating CFD algorithms employed in the digitizer models under consideration. The time walk calibration is done according to Eq. (2) using:

$$TW(E_1, E_2) = C_D(E_1, E_2) - T_0 - \tau$$

The time walk can be calibrated across a 40–1408 keV  $\gamma$ -ray energy range using a  $^{152}\text{Eu}$   $\gamma$ -ray source decaying through multiple feeder–decay cascades connecting different intermediate states with well known lifetimes. The TW function is generally defined by

$$TW(E) = \frac{a}{\sqrt{E-b}} + c + dE + eE^2. \quad (8)$$

The TW calibration procedure is similar to the prompt response difference (PRD) calibration of an analog setup [6,38], which is detailed in Refs. [6,31]. TW and PRD have the same properties and are connected by [31]

$$TW(E_1, E_2) = TW(E_2) - TW(E_1) = \frac{PRD(E_1, E_2)}{2}. \quad (9)$$

For the investigation of the TW characteristics, the CFD fraction was kept constant at 25% and the TW was investigated with respect to different CFD delays and TFs. Figs. 16 and 17 show the time walk characteristics of both digitizers as a function of the  $\gamma$ -ray energy. To be able to describe the two inflection points and the strong increase of TW especially in the low-energy region in case of the V1751 with TF = 1 V/MeV (Fig. 17c), the TW function was generalized to

$$TW(E) = a(E^m - b)^{-(1/q)} + c + dE + eE^2, \\ m \in \{1, 2\}, q \in \mathbb{Q}^+.$$

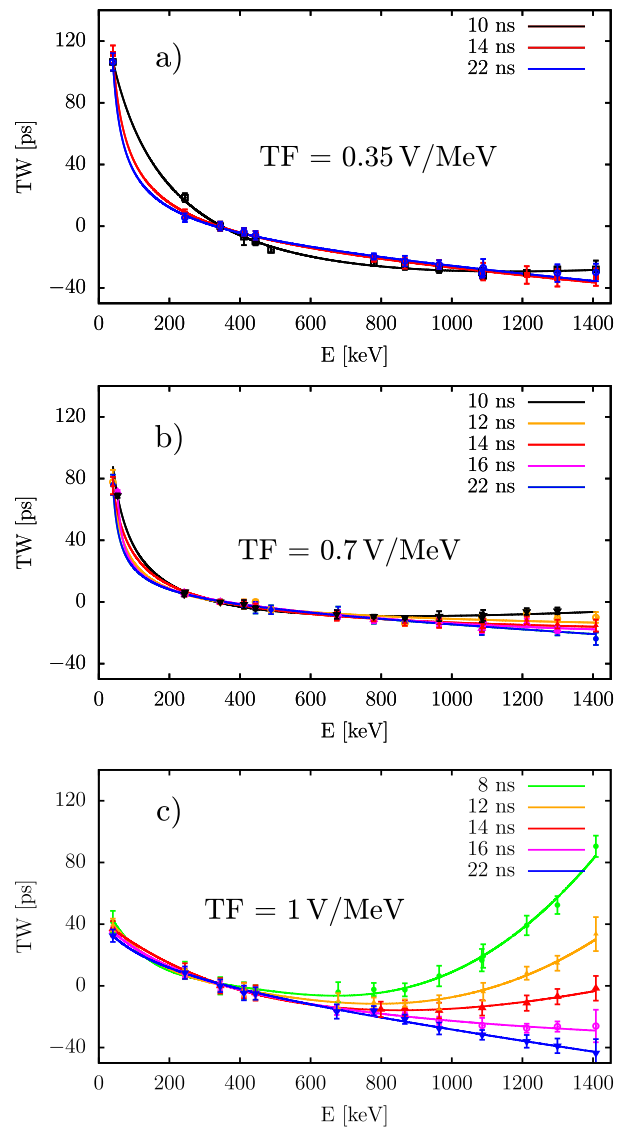


Fig. 16. Time walk characteristics of the V1730 digitizer for different TFs in dependence of the CFD delay.

Figs. 16 (a) to (c) show the evolution of the time walk characteristics of the V1730 digitizer in dependency of the CFD delay and the TF. The behavior of the TWs of the V1730 in the low amplitude range is characterized by a downward trend and in the high amplitude range, from 500 keV upward, it shows a drop, ascent, or level behavior in dependence of the CFD delay. The investigation showed, that the CFD delay has nearly negligible influence in the low-energy region. However, the progression of the high-energy time walk is dominated by the influence of the CFD delay parameter. The maximum TW difference in the energy range between 240 keV and 1300 keV lies below 100 ps for all TFs and specially below 25 ps for a TF = 0.7 V/MeV depending on the CFD delay. Moreover, Fig. 16c shows nearly the same shape and magnitude of time walk in dependence of the CFD delay time observed using ORTEC 935 with same TF = 1 V/MeV (Fig. 8 in Ref. [6]). This systematic is identical to the behavior of the analog ORTEC 935 with comparable time resolution and TW range.

Analogous, the TW behavior of the V1751 is shown in Fig. 17 (a) to (c). A mirrored behavior is observed compared to the TW characteristics of the V1730. The TW curves all show increasing behavior in the low-energy range independent from the CFD delay. The contrasting time walk behavior of the V1730 and the V1751 suggests that the CFD

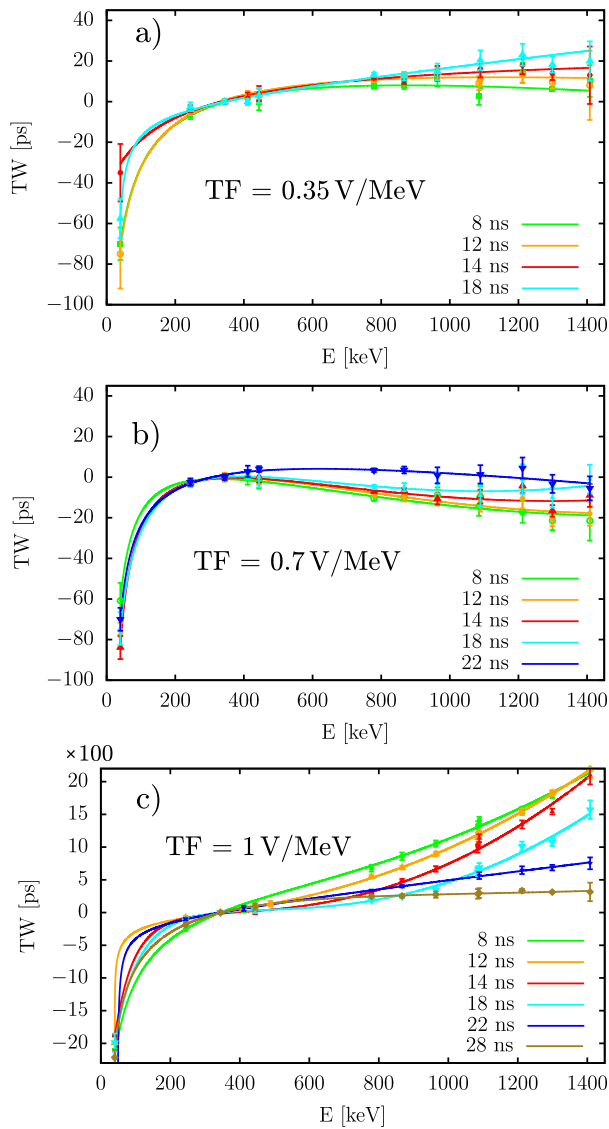


Fig. 17. Time walk characteristics of the V1751 digitizer for different TFs in dependence of the CFD delay. Note the different y-scale in c).

algorithm in the V1751 is internally inverted compared to the one in the V1730. The TW curves presented in Ref. [54], where a CFD model ORTEC 584 was used, show a similar behavior. The ORTEC 584 performs the shaping procedure in a sequence like described in Eq. (6) [55]. For a negative input signal, this leads to a negative slope at the zero crossover and thus an inverted time walk characteristic. A closer look at the manual of the firmware of the V1751 shows, that the DPP-PSD firmware of the V1751 [45] indeed uses a similar inverted CFD algorithm as the ORTEC 584.

As visible in Fig. 17a, the CFD delay shows its strongest influence in the high energy range from 500 keV upward, like in the V1730. In the low-energy range, the curves show a similar behavior nearly independent from the CFD delay. In Fig. 17b, the TW curves are plotted for delays starting from 8 ns to 22 ns with a TF of 0.7 V/MeV. The curves with CFD delays smaller than 22 ns, have two inflection points, different to all other curves presented here before. For CFD delay = 22 ns, there is a transition in the TW characteristic from a convex to a concave shape especially for energies higher than 300 keV. The progression of the TW curve reverts to the typical characteristics, showing only a single inflection point. This behavior is even more clearly observable in the progression of the TW curves for a TF =

1 V/MeV in Fig. 17c. An explanation for this transition behavior needs further investigation of the CFD algorithms and the digitizer modules and cannot be given at the state of this work.

The time walk of the CFD algorithm of the V1751 in the case of the highest TF = 1 V/MeV increases dramatically up to above 1.5 ns. The maximum time walk between 200 keV and 1300 keV in the case of TF = 0.35 V/MeV and TF = 0.7 V/MeV lies below 25 ps depending on the CFD delay. The smallest maximum range of the TW throughout the considered energy range between about 240 and 1300 keV is found for a CFD delays between 14 and 22 ns for both modules. Comprehensive studies on the time walk of other digital CFD implementations are unfortunately not available and therefore cannot be referenced. At this point, we suggest conducting such studies in the future to enable a more comprehensive comparison between different technologies.

## 7. Summary and conclusion

In this work, the digitizer modules V1730 and V1751 by CAEN S.p.A. with sample rates of 500 MS/s and 1 GS/s, respectively, were investigated with regard to the fast-timing properties of the implementations of the digital real-time interpolating CFD algorithms. Both modules provide linear interpolation algorithms to determine the timestamp of an incoming energy pulse from a LaBr<sub>3</sub>(Ce) fast-timing scintillator detector within sub-sample-period picosecond precision. To validate the usage of these digitizers and evaluate the fast-timing characteristics of the digital CFDs, a fast-timing setup, consisting of four LaBr detectors was constructed to test both digitizer modules. A standard <sup>152</sup>Eu time walk calibration source was used to systematically investigate the time resolution and time walk characteristics over a  $\gamma$ -ray energy range of 40–1408 keV in dependence of the detector settings and digital CFD parameters.

Our study showed, that the timing properties of the digital CFDs of these digitizers are comparable to the characteristics of the analog model ORTEC 935 in terms of time walk and time resolution. The time resolutions of the investigated digitizers are comparable to these of other digital CFD implementations. The determined time resolutions of about 350 ps or lower for the given 779–344 keV benchmark cascade and time walk characteristics demonstrate that both digitizers are suitable for fast-timing with modern standards.

The time walk characteristics of the V1730 has very small maximum ranges of around 25 ps in the energy range 240–1408 keV throughout all measured TFs and is comparable to the characteristics of analog modules like ORTEC 935. The low energy TW of the V1730 is in a range of 100 ps and further reduces for higher TFs. The time walk characteristics of the V1751 is comparable to the analog module ORTEC 584 for low TFs up to 0.7 V/MeV but shows limitations in usability for higher TFs. However, there are no comparable studies about the time walk characteristics of other digitizer modules and the fast-timing community is encouraged to provide additional studies about other implemented digital CFDs to .

For both the investigated digitizers, high-quality performance in fast-timing measurements providing acceptable time resolutions and very low, well characterized time walk are offered using the systematically investigated and reported optimum detector TF and CFD parameters.

Both modules have potential for further improvement, e.g. expanding the linear interpolation algorithm to a cubic one, providing more selectable CFD fraction values and expand the input dynamic range. However, other digitizers feature larger FPGAs that accommodate the proposed improvements, but further systematic studies are needed to fully explore the potential benefits especially concerning the time walk behavior.

## Declaration of competing interest

The authors declare the following financial interests/personal relationships which may be considered as potential competing interests: J.M. Régis, M. Ley reports financial support was provided by German Research Foundation. A. Esmaylzadeh reports financial support was provided by Federal Ministry of Education and Research Bonn Office.

## Data availability

Data will be made available on request.

## Acknowledgments

J.-M. R. and M. L. acknowledge the Deutsche Forschungsgemeinschaft for support under grant No. JO 391/18-1. A. E. wants to acknowledge the support of BMBF Verbundprojekt 05P2021 (ErUM-FSP T07) under grant No. 05P21PKFN1. All authors want to acknowledge and especially thank CAEN S.p.A. for the free loan of one of the V1751 digitizer modules for testing purposes.

## References

- [1] R. Casten, Nuclear Structure from a Simple Perspective, in: Oxford science publications, Oxford University Press, 2000, URL <https://books.google.de/books?id=WgkTQoX13MUC>.
- [2] K.S. Krane, Introductory Nuclear Physics, Wiley, New York, NY, 1988, URL <https://cds.cern.ch/record/359790>.
- [3] P.J. Nolan, J.F. Sharpey-Schafer, The measurement of the lifetimes of excited nuclear states, Rep. Progr. Phys. 42 (1) (1979) 1, <http://dx.doi.org/10.1088/0034-4885/42/1/001>.
- [4] H. Mach, R. Gill, M. Moszyński, A method for picosecond lifetime measurements for neutron-rich nuclei: (1) outline of the method, Nucl. Instrum. Methods Phys. Res. A 280 (1) (1989) 49–72, [http://dx.doi.org/10.1016/0168-9002\(89\)91272-2](http://dx.doi.org/10.1016/0168-9002(89)91272-2), URL <https://www.sciencedirect.com/science/article/pii/0168900289912722>.
- [5] J.-M. Régis, A. Esmaylzadeh, J. Jolie, V. Karayonchev, L. Knafla, U. Köster, Y. Kim, E. Strub, Y-y fast timing at X-ray energies and investigation on various timing deviations, Nucl. Instrum. Methods Phys. Res. A 955 (2020) 163258, <http://dx.doi.org/10.1016/j.nima.2019.163258>, URL <https://www.sciencedirect.com/science/article/pii/S016890021931527X>.
- [6] J.-M. Régis, N. Saed-Samii, M. Rudigier, S. Ansari, M. Dannhoff, A. Esmaylzadeh, C. Fransen, R.-B. Gerst, J. Jolie, V. Karayonchev, C. Müller-Gatermann, S. Stegemann, Reduced y-y time walk to below 50 ps using the multiplexed-start and multiplexed-stop fast-timing technique with labr3(ce) detectors, Nucl. Instrum. Methods Phys. Res. A 823 (2016) 72–82, <http://dx.doi.org/10.1016/j.nima.2016.04.010>, URL <https://www.sciencedirect.com/science/article/pii/S016890021630170X>.
- [7] J.-M. Régis, H. Mach, G. Simpson, J. Jolie, G. Pascovici, N. Saed-Samii, N. Warr, A. Bruce, J. Degenkolb, L. Fraile, C. Fransen, D. Ghita, S. Kisiov, U. Koester, A. Korgul, S. Lalkovski, N. Märginean, P. Mutti, B. Olaizola, Z. Podolyak, P. Regan, O. Roberts, M. Rudigier, L. Stroe, W. Urban, D. Wilmsen, The generalized centroid difference method for picosecond sensitive determination of lifetimes of nuclear excited states using large fast-timing arrays, Nucl. Instrum. Methods Phys. Res. A 726 (2013) 191–202, <http://dx.doi.org/10.1016/j.nima.2013.05.126>, URL <https://www.sciencedirect.com/science/article/pii/S0168900213007377>.
- [8] M. Lebois, N. Jovančević, D. Thisse, R. Canavan, D. Étasse, M. Rudigier, J. Wilson, The nu-ball gamma-spectrometer, Nucl. Instrum. Methods Phys. Res. A 960 (2020) 163580, <http://dx.doi.org/10.1016/j.nima.2020.163580>, URL <https://www.sciencedirect.com/science/article/pii/S0168900220301534>.
- [9] R.-B. Gerst, A. Blazhev, N. Warr, J.N. Wilson, M. Lebois, N. Jovančević, D. Thisse, R. Canavan, M. Rudigier, D. Étasse, E. Adamska, P. Adsley, A. Algora, M. Babo, K. Belvedere, J. Benito, G. Benzoni, A. Boso, S. Bottoni, M. Bunce, R. Chakma, N. Cieplicka-Oryńczak, S. Courtin, M.L. Cortés, P. Davies, C. Delafosse, M. Fallot, B. Fornal, L.M. Fraile, D. Gjestvang, A. Gottardo, V. Guadilla, G. Häfner, K. Hauschild, M. Heine, C. Henrich, I. Homm, F. Ibrahim, Ł.W. Iskra, P. Ivanov, S. Jazwari, A. Korgul, P. Koseoglou, T. Kröll, T. Kurtukian-Nieto, L. Le Meur, S. Leoni, J. Ljungvall, A. Lopez-Martens, R. Lozeva, I. Matea, K. Miernik, J. Nemer, S. Oberstedt, W. Paulsen, M. Piersa, Y. Popovitch, C. Porzio, L. Qi, D. Ralet, P.H. Regan, D. Reygadas-Tello, K. Rezykina, V. Sánchez-Tembleque, C. Schmitt, P.-A. Söderström, C. Sürder, G. Tocabens, V. Vedia, D. Verney, B. Wasilewska, J. Wiederhold, M. Yavachova, F. Zeiser, S. Ziliani, Prompt and delayed  $\gamma$  spectroscopy of neutron-rich  $^{94}\text{Kr}$  and observation of a new isomer, Phys. Rev. C 102 (2020) 064323, <http://dx.doi.org/10.1103/PhysRevC.102.064323>, URL <https://link.aps.org/doi/10.1103/PhysRevC.102.064323>.
- [10] G. Häfner, R. Lozeva, H. Naïdja, M. Lebois, N. Jovančević, D. Thisse, D. Étasse, R.L. Canavan, M. Rudigier, J.N. Wilson, E. Adamska, P. Adsley, M. Babo, K. Belvedere, J. Benito, G. Benzoni, A. Blazhev, A. Boso, S. Bottoni, M. Bunce, R. Chakma, N. Cieplicka-Oryńczak, S.M. Collins, M.L. Cortés, P.J. Davies, C. Delafosse, M. Fallot, B. Fornal, L.M. Fraile, R.-B. Gerst, D. Gjestvang, V. Guadilla, K. Hauschild, C. Henrich, I. Homm, F. Ibrahim, Ł.W. Iskra, S. Jazwari, J. Jolie, A. Korgul, P. Koseoglou, T. Kröll, T. Kurtukian-Nieto, L. Le-meur, J. Ljungvall, A. Lopez-Martens, I. Matea, L. Matthieu, K. Miernik, J. Nemer, S. Oberstedt, W. Paulsen, M. Piersa, Y. Popovitch, C. Porzio, L. Qi, D. Ralet, P.H. Regan, D. Reygadas Tello, K. Rezykina, V. Sanchez, C. Schmitt, P.-A. Söderström, C. Sürder, G. Tocabens, V. Vedia, D. Verney, N. Warr, B. Wasilewska, J. Wiederhold, M.S. Yavachova, F. Zeiser, S. Ziliani, Spectroscopy and lifetime measurements in  $^{134,136,138}\text{Te}$  isotopes and implications for the nuclear structure beyond  $N = 82$ , Phys. Rev. C 103 (2021) 034317, <http://dx.doi.org/10.1103/PhysRevC.103.034317>, URL <https://link.aps.org/doi/10.1103/PhysRevC.103.034317>.
- [11] M. Lebois, N. Jovančević, J. Wilson, D. Thisse, R. Canavan, M. Rudigier, The nu-ball campaign at ALTO, Acta Phys. Polon. B 50 (3) (2019) 425.
- [12] G. Häfner, R. Lozeva, A. Blazhev, R.L. Canavan, D. Étasse, J. Jolie, N. Jovančević, R.B. Gerst, T. Kröll, M. Lebois, P.H. Regan, M. Rudigier, D. Thisse, N. Warr, J.N. Wilson, the N-SI-109 collaboration, Lifetime measurement around  $^{132}\text{Sn}$  with the nu-ball array, J. Phys. Conf. Ser. 1643 (1) (2020) 012135, <http://dx.doi.org/10.1088/1742-6596/1643/1/012135>.
- [13] G. Häfner, R. Lozeva, H. Naïdja, M. Lebois, N. Jovančević, D. Thisse, D. Étasse, R.L. Canavan, M. Rudigier, J.N. Wilson, E. Adamska, P. Adsley, M. Babo, K. Belvedere, J. Benito, G. Benzoni, A. Blazhev, A. Boso, S. Bottoni, M. Bunce, R. Chakma, N. Cieplicka-Oryńczak, S.M. Collins, M.L. Cortés, P.J. Davies, C. Delafosse, M. Fallot, B. Fornal, L.M. Fraile, R.-B. Gerst, D. Gjestvang, V. Guadilla, K. Hauschild, C. Henrich, I. Homm, F. Ibrahim, Ł.W. Iskra, S. Jazwari, J. Jolie, A. Korgul, P. Koseoglou, T. Kröll, T. Kurtukian-Nieto, L. Le-meur, J. Ljungvall, A. Lopez-Martens, I. Matea, L. Matthieu, K. Miernik, J. Nemer, S. Oberstedt, W. Paulsen, M. Piersa, Y. Popovitch, C. Porzio, L. Qi, D. Ralet, P.H. Regan, D. Reygadas Tello, K. Rezykina, V. Sanchez, C. Schmitt, P.-A. Söderström, C. Sürder, G. Tocabens, V. Vedia, D. Verney, N. Warr, B. Wasilewska, J. Wiederhold, M.S. Yavachova, F. Zeiser, S. Ziliani, Spectroscopy and lifetime measurements in  $^{134,136,138}\text{Te}$  isotopes and implications for the nuclear structure beyond  $N = 82$ , Phys. Rev. C 103 (2021) 034317, <http://dx.doi.org/10.1103/PhysRevC.103.034317>, URL <https://link.aps.org/doi/10.1103/PhysRevC.103.034317>.
- [14] M. Rudigier, R. Canavan, P. Regan, P. Soderstrom, M. Lebois, J. Wilson, N. Jovančević, S. Bottoni, M. Brunet, N. Cieplicka-Oryńczak, et al., Isomer spectroscopy and sub-nanosecond half-life determination in  $^{178}\text{W}$  using the NuBall array, Acta Phys. Polon. B 50 (3) (2019) 661–667.
- [15] M. Rudigier, P. Walker, R. Canavan, Z. Podolyák, P. Regan, P.-A. Söderström, M. Lebois, J. Wilson, N. Jovančević, A. Blazhev, J. Benito, S. Bottoni, M. Brunet, N. Cieplicka-Oryńczak, S. Courtin, D. Doherty, L. Fraile, K. Hadynska-Klek, M. Heine, L. Iskra, J. Jolie, V. Karayonchev, A. Kennington, P. Koseoglou, G. Lotay, G. Lorusso, M. Nakhostin, C. Nita, S. Oberstedt, L. Qi, J.-M. Régis, V. Sánchez-Tembleque, R. Shearman, W. Witt, V. Vedia, K. Zell, Multi-quasiparticle sub-nanosecond isomers in  $^{178}\text{W}$ , Phys. Lett. B 801 (2020) 135140, <http://dx.doi.org/10.1016/j.physletb.2019.135140>, URL <https://www.sciencedirect.com/science/article/pii/S0370269319308627>.
- [16] H. Mach, F. Wahn, G. Molnár, K. Sistemich, J.C. Hill, M. Moszyński, R. Gill, W. Krips, D. Brenner, Retardation of  $B(E2; 01+ \rightarrow 21+)$  rates in  $90\text{-}96\text{Sr}$  and strong subshell closure, Nuclear Phys. A 523 (2) (1991) 197–227, [http://dx.doi.org/10.1016/0375-9474\(91\)90001-M](http://dx.doi.org/10.1016/0375-9474(91)90001-M), URL <https://www.sciencedirect.com/science/article/pii/037594749190001M>.
- [17] M. Moszyński, H. Mach, A method for picosecond lifetime measurements for neutron-rich nuclei: (2) timing study with scintillation counters, Nucl. Instrum. Methods Phys. Res. A 277 (2) (1989) 407–417, [http://dx.doi.org/10.1016/0168-9002\(89\)90770-5](http://dx.doi.org/10.1016/0168-9002(89)90770-5), URL <https://www.sciencedirect.com/science/article/pii/0168900289907705>.
- [18] J.-M. Régis, G. Pascovici, J. Jolie, M. Rudigier, The mirror symmetric centroid difference method for picosecond lifetime measurements via y-y coincidences using very fast LaBr $_3$ (Ce) scintillator detectors, Nucl. Instrum. Methods Phys. Res. A 622 (1) (2010) 83–92, <http://dx.doi.org/10.1016/j.nima.2010.07.047>, URL <https://www.sciencedirect.com/science/article/pii/S0168900210016578>.
- [19] Z. Bay, Calculation of decay times from coincidence experiments, Phys. Rev. 77 (1950) 419, <http://dx.doi.org/10.1103/PhysRev.77.419>, URL <https://link.aps.org/doi/10.1103/PhysRev.77.419>.
- [20] M. Martín, Nuclear data sheets for  $A=152$ , Nucl. Data Sheets 114 (11) (2013) 1497–1847, <http://dx.doi.org/10.1016/j.nds.2013.11.001>, URL <https://www.sciencedirect.com/science/article/pii/S0090375213000744>.
- [21] S.V. Polyakov, Chapter 3 - photomultiplier tubes, in: A. Migdall, S.V. Polyakov, J. Fan, J.C. Bienfang (Eds.), Single-Photon Generation and Detection, in: Experimental Methods in the Physical Sciences, vol. 45, Academic Press, 2013, pp. 69–82, <http://dx.doi.org/10.1016/B978-0-12-387695-9.00003-2>, URL <https://www.sciencedirect.com/science/article/pii/B9780123876959000032>.
- [22] J.-M. Régis, Fast Timing with LaBr $_3$ (Ce) Scintillators and the Mirror Symmetric Centroid Difference Method (Ph.D. thesis), Verlag Dr. Hut, Universität zu Köln, 2011.



- [23] ORTEC, Model 935 quad constant-fraction 200-MHz discriminator operating and service, 2003, URL <http://www.ortec-online.com/download/935-MNL.pdf>, Printed in USA, Advanced Measurement Technology, Inc., 2003 [Online].
- [24] ORTEC, Model 566 time-to-amplitude converter (TAC) operating and service manual, 2011, URL <https://www.ortec-online.com/-/media/ametekortec/manuals/5/566-mnl.pdf?la=en&revision=9b548347-6150-4d97-af90-dbe8b40c1930>, Printed in USA, Advanced Measurement Technology, Inc., 2011 [Online].
- [25] A. Esmaylzadeh, J.-M. Régis, Y.H. Kim, U. Köster, J. Jolie, V. Karayonchev, L. Knafla, K. Nomura, L.M. Robledo, R. Rodríguez-Guzmán, Lifetime measurements and shape coexistence in  $^{97}\text{Sr}$ , Phys. Rev. C 100 (2019) 064309, <http://dx.doi.org/10.1103/PhysRevC.100.064309>, URL <https://link.aps.org/doi/10.1103/PhysRevC.100.064309>.
- [26] A. Harter, L. Knafla, G. Frießner, G. Häfner, J. Jolie, A. Blazhev, A. Dewald, F. Dunkel, A. Esmaylzadeh, C. Fransen, V. Karayonchev, K. Lawless, M. Ley, J.-M. Régis, K.O. Zell, Lifetime measurements in the tungsten isotopes  $^{176,178,180}\text{W}$ , Phys. Rev. C 106 (2022) 024326, <http://dx.doi.org/10.1103/PhysRevC.106.024326>, URL <https://link.aps.org/doi/10.1103/PhysRevC.106.024326>.
- [27] V. Karayonchev, A. Blazhev, A. Esmaylzadeh, J. Jolie, M. Dannhoff, F. Diel, F. Dunkel, C. Fransen, L.M. Gerhard, R.-B. Gerst, L. Knafla, L. Kornweibel, C. Müller-Gatermann, J.-M. Régis, N. Warr, K.O. Zell, M. Stoyanova, P. Van Isacker, Lifetimes in  $^{211}\text{At}$  and their implications for the nuclear structure above  $^{208}\text{Pb}$ , Phys. Rev. C 99 (2019) 024326, <http://dx.doi.org/10.1103/PhysRevC.99.024326>, URL <https://link.aps.org/doi/10.1103/PhysRevC.99.024326>.
- [28] L. Knafla, P. Alexa, U. Köster, G. Thiamova, J.-M. Régis, J. Jolie, A. Blanc, A.M. Bruce, A. Esmaylzadeh, L.M. Fraile, G. de France, G. Häfner, S. Ilieva, M. Jentschel, V. Karayonchev, W. Korten, T. Kröll, S. Lalkovski, S. Leoni, H. Mach, N. Märginean, P. Mutti, G. Pascovici, V. Pazių, Z. Podolyák, P.H. Regan, O.J. Roberts, N. Saed-Samii, G.S. Simpson, J.F. Smith, T. Soldner, C. Townsley, C.A. Ur, W. Urban, A. Vancraeynest, N. Warr, Lifetime measurements in the odd- $A$  nucleus  $^{177}\text{Hf}$ , Phys. Rev. C 102 (2020) 054322, <http://dx.doi.org/10.1103/PhysRevC.102.054322>, URL <https://link.aps.org/doi/10.1103/PhysRevC.102.054322>.
- [29] A. Esmaylzadeh, L.M. Gerhard, V. Karayonchev, J.-M. Régis, J. Jolie, M. Bast, A. Blazhev, T. Braunroth, M. Dannhoff, F. Dunkel, C. Fransen, G. Häfner, L. Knafla, M. Ley, C. Müller-Gatermann, K. Schomacker, N. Warr, K.-O. Zell, Lifetime determination in  $^{190,192,194,196}\text{Hg}$  via  $\gamma-\gamma$  fast-timing spectroscopy, Phys. Rev. C 98 (2018) 014313, <http://dx.doi.org/10.1103/PhysRevC.98.014313>, URL <https://link.aps.org/doi/10.1103/PhysRevC.98.014313>.
- [30] V. Karayonchev, J.-M. Régis, J. Jolie, A. Blazhev, R. Altenkirch, S. Ansari, M. Dannhoff, F. Diel, A. Esmaylzadeh, C. Fransen, R.-B. Gerst, K. Moschner, C. Müller-Gatermann, N. Saed-Samii, S. Stegemann, N. Warr, K.O. Zell, Evolution of collectivity in the  $N = 100$  isotones near  $^{170}\text{Yb}$ , Phys. Rev. C 95 (2017) 034316, <http://dx.doi.org/10.1103/PhysRevC.95.034316>, URL <https://link.aps.org/doi/10.1103/PhysRevC.95.034316>.
- [31] J.-M. Régis, M. Dannhoff, J. Jolie, A simple procedure for  $\gamma-\gamma$  lifetime measurements using multi-element fast-timing arrays, Nucl. Instrum. Methods Phys. Res. A 897 (2018) 38–46, <http://dx.doi.org/10.1016/j.nima.2018.04.047>, URL <https://www.sciencedirect.com/science/article/pii/S0168900218305552>.
- [32] T.J. Paulus, Timing electronics and fast timing methods with scintillation detectors, IEEE Trans. Nucl. Sci. 32 (3) (1985) 1242–1249, <http://dx.doi.org/10.1109/TNS.1985.4337024>.
- [33] A. Fallu-Labruyere, H. Tan, W. Hennig, W. Warburton, Time resolution studies using digital constant fraction discrimination, Nucl. Instrum. Methods Phys. Res. A 579 (1) (2007) 247–251, <http://dx.doi.org/10.1016/j.nima.2007.04.048>, URL <https://www.sciencedirect.com/science/article/pii/S0168900207006213>, Proceedings of the 11th Symposium on Radiation Measurements and Applications.
- [34] S. Lipschutz, R. Zegers, J. Hill, S. Liddick, S. Noji, C. Prokop, M. Scott, M. Solt, C. Sullivan, J. Tompkins, Digital data acquisition for the low energy neutron detector array (LENDa), Nucl. Instrum. Methods Phys. Res. A 815 (2016) 1–6, <http://dx.doi.org/10.1016/j.nima.2016.01.050>, URL <https://www.sciencedirect.com/science/article/pii/S0168900216000668>.
- [35] V. Modamio, J. Valiente-Dobón, G. Jaworski, T. Hüyük, A. Triossi, J. Egea, A. Di Nitto, P.-A. Söderström, J. Agramunt Ros, G. de Angelis, G. de France, M. Erduran, S. Ertürk, A. Gadea, V. González, J. Kownacki, M. Moszynski, J. Nyberg, M. Palacz, E. Sanchis, R. Wadsworth, Digital pulse-timing technique for the neutron detector array NEDA, Nucl. Instrum. Methods Phys. Res. A 775 (2015) 71–76, <http://dx.doi.org/10.1016/j.nima.2014.12.002>, URL <https://www.sciencedirect.com/science/article/pii/S0168900214014430>.
- [36] V. Sanchez-Tembleque, V. Vedia, L. Fraile, S. Ritt, J. Udias, Optimizing time-pickup algorithms in radiation detectors with a genetic algorithm, Nucl. Instrum. Methods Phys. Res. A 927 (2019) 54–62, <http://dx.doi.org/10.1016/j.nima.2019.02.017>, URL <https://www.sciencedirect.com/science/article/pii/S0168900219301925>.
- [37] W.K. Warburton, W. Hennig, New algorithms for improved digital pulse arrival timing with sub-GSPs ADCs, IEEE Trans. Nucl. Sci. 64 (12) (2017) 2938–2950, <http://dx.doi.org/10.1109/TNS.2017.2766074>.
- [38] J.-M. Régis, M. Rudigier, J. Jolie, A. Blazhev, C. Fransen, G. Pascovici, N. Warr, The time-walk of analog constant fraction discriminators using very fast scintillator detectors with linear and non-linear energy response, Nucl. Instrum. Methods Phys. Res. A 684 (2012) 36–45, <http://dx.doi.org/10.1016/j.nima.2012.04.088>, URL <https://www.sciencedirect.com/science/article/pii/S0168900212004937>.
- [39] S.p.A. CAEN, User manual UM2792 V1730/VX1730 and V1725/VX1725, 2021, URL <https://www.caen.it/v1730>, 2021 [Online].
- [40] S.p.A. CAEN, User manual UM3350 V1751/VX1751 4/8 channels 10bit 2/1 GS/s digitizer, 2017, URL <https://www.caen.it/products/v1751/>, 2017 [Online].
- [41] H.P. K.K., Photomultiplier tubes and assemblies, 2017, URL [https://www.hamamatsu.com/content/dam/hamamatsu-photonics/sites/documents/99\\_SALES\\_LIBRARY/etd/High\\_energy\\_PMT\\_TPMZ0003E.pdf](https://www.hamamatsu.com/content/dam/hamamatsu-photonics/sites/documents/99_SALES_LIBRARY/etd/High_energy_PMT_TPMZ0003E.pdf), REVISED APR. 2017 [Online].
- [42] B. Leskovar, C. Lo, Single photoelectron time spread measurement of fast photomultipliers, Nucl. Instrum. Methods 123 (1) (1975) 145–160, [http://dx.doi.org/10.1016/0029-554X\(75\)90090-7](http://dx.doi.org/10.1016/0029-554X(75)90090-7), URL <https://www.sciencedirect.com/science/article/pii/0029554X75900907>.
- [43] A. Harter, N. Saed-Samii, fSOCO - fast timing sorting code, 2023, URL <https://gitlab.ikp.uni-koeln.de/soco/ft-soco>.
- [44] S.p.A. CAEN, User manual UM5960 compass, 2022, URL <https://www.caen.it/products/compass/>, 2022 [Online].
- [45] S.p.A. CAEN, UM8762 FELib PSD parameters user manual, 2022, URL <https://www.caen.it/products/dpp-psd/>, 2022 [Online].
- [46] M. Nakhostin, Z. Podolyak, P.H. Regan, Digital processing of signals from LaBr $_3$ :Ce scintillation detectors, J. Instrum. 9 (12) (2014) C12049, <http://dx.doi.org/10.1088/1748-0221/9/12/C12049>.
- [47] W. McDonald, D. Gedcke, Time resolution studies on large photomultipliers, Nucl. Instrum. Methods 55 (1967) 1–14, [http://dx.doi.org/10.1016/0029-554X\(67\)90103-6](http://dx.doi.org/10.1016/0029-554X(67)90103-6), URL <https://www.sciencedirect.com/science/article/pii/0029554X67901036>.
- [48] L.G. Hyman, Time resolution of photomultiplier systems, Rev. Sci. Instrum. 36 (2) (1965) 193–196, <http://dx.doi.org/10.1063/1.1719516>.
- [49] S. Bhattacharya, S. Das, S. Bhattacharyya, R. Banik, S. Dar, D. Pandit, A. Choudhury, K. Banerjee, D. Mondal, S. Mukhopadhyay, Energy response and fast timing characteristics of  $1.5'' \times 1.5''$  CeBr $_3$  scintillator, Nucl. Instrum. Methods Phys. Res. A 1014 (2021) 165737, <http://dx.doi.org/10.1016/j.nima.2021.165737>, URL <https://www.sciencedirect.com/science/article/pii/S0168900221007221>.
- [50] M. Aykac, F. Bauer, C. Williams, M. Loope, M. Schmand, Timing performance of hi-rez detector for time-of-flight (TOF) PET, in: IEEE Nuclear Science Symposium Conference Record, 2005, Vol. 4, 2005, pp. 2035–2040, <http://dx.doi.org/10.1109/NSSMIC.2005.1596733>.
- [51] F. de la Barre, Influence of transit time differences on photomultiplier time resolution, Nucl. Instrum. Methods 102 (1) (1972) 77–86, [http://dx.doi.org/10.1016/0029-554X\(72\)90523-X](http://dx.doi.org/10.1016/0029-554X(72)90523-X), URL <https://www.sciencedirect.com/science/article/pii/0029554X7290523X>.
- [52] C. Prokop, S. Liddick, B. Abromeit, A. Chemey, N. Larson, S. Suchyta, J. Tompkins, Digital data acquisition system implementation at the national superconducting cyclotron laboratory, Nucl. Instrum. Methods Phys. Res. A 741 (2014) 163–168, <http://dx.doi.org/10.1016/j.nima.2013.12.044>, URL <https://www.sciencedirect.com/science/article/pii/S0168900213017488>.
- [53] P.-A. Söderström, E.A. ksöz, D. Balabanski, F. Camera, L. Capponi, G. Ciocan, M. Cuciuc, D. Filipescu, I. Gheorghe, T. Glodariu, J. Kaur, M. Krzysiek, C. Matei, T. Roman, A. Rotaru, A. Șerban, A. State, H. Utsunomiya, V. Vasilca, ELIGANT-GN — ELI Gamma above neutron threshold: The Gamma-neutron setup, Nucl. Instrum. Methods Phys. Res. A 1027 (2022) 166171, <http://dx.doi.org/10.1016/j.nima.2021.166171>, URL <https://www.sciencedirect.com/science/article/pii/S0168900221010494>.
- [54] S. Das, S. Bhattacharyya, S. Bhattacharya, R. Banik, S. Chakraborty, S. Dar, Timing characteristics of the R13089-100 photomultiplier tube coupled with  $1.5'' \times 1.5''$  CeBr $_3$  scintillators and its application in lifetime measurements, J. Instrum. 17 (09) (2022) P09012, <http://dx.doi.org/10.1088/1748-0221/17/09/P09012>.
- [55] ORTEC, Model 584 constant-fraction discriminator operating and service manual, 2002, URL <https://www.ortec-online.com/-/media/ametekortec/manuals/5/584-mnl.pdf?la=en&revision=2fd8025-2b93-47c1-b766-17ad4c659f74>, Printed in USA, Advanced Measurement Technology, Inc., 2002 [Online].

## 4 | Publication III:

Lifetime measurements in low yrast states  
and spectroscopic peculiarities in  $^{182}\text{Os}$



**Lifetime measurements in low yrast states and spectroscopic peculiarities in  $^{182}\text{Os}$** A. Harter <sup>\*</sup>, A. Esmaylzadeh , L. Knafla , C. Fransen , F. v. Spee , J. Jolie , M. Ley ,  
V. Karayonchev ,<sup>†</sup> J. Fischer , and A. Pfeil *Universität zu Köln, Mathematisch-Naturwissenschaftliche Fakultät, Institut für Kernphysik, 50937 Cologne, Germany*

(Received 2 June 2023; accepted 21 July 2023; published 9 August 2023)

Lifetimes of the low-lying yrast states  $2^+$ ,  $4^+$ , and  $6^+$  of the unstable nucleus  $^{182}\text{Os}$  were measured using digital fast-timing techniques. The lifetimes of the  $4^+$  and  $6^+$  states were determined for the first time. The remeasured value for the lifetime of the  $2_1^+$  state was taken into account to evaluate the discrepancy between two inconsistent literature values. The lifetimes and extracted  $B(E2)$  values are presented and discussed in terms of collective signatures and transitional phenomena. The  $B(E2; 4_1^+ \rightarrow 2_1^+)/B(E2; 2_1^+ \rightarrow 0_1^+)$  ratio of 1.39(7) supports the interpretation of  $^{182}\text{Os}$  as a rigid rotor. This value is discussed in the context of these of the neighboring isotopes and isotones and calculations in the framework of the interacting boson model 1. Additionally, competing influences from the near lying collective deformed region,  $\gamma$ -soft rotors, X(5) symmetry, and neighboring regions of shape coexistence in low excitation states are assumed to influence the structure of the nucleus of interest: The trend of the excitation energies of the  $\gamma$ - and  $K^\pi = 0$ -bands in the osmium isotopic chain change remarkably at  $^{182}\text{Os}$ . This consideration helps to us delimit and understand the structural transitions in the isotopic and isotonic chains that intersect at  $^{182}\text{Os}$ .

DOI: [10.1103/PhysRevC.108.024305](https://doi.org/10.1103/PhysRevC.108.024305)**I. INTRODUCTION**

Nuclei with masses  $A \approx 180$  in the region around the neutron midshell at  $N = 104$  lie at the edge of the strongly deformed region between the neutron shell closures 82 and 126 and proton shell closures 50 and 82. Especially, the isotopes with proton numbers 74 (W), 76 (Os), 78 (Pt), and 80 (Hg) offer a variety of deformation and transition phenomena, e.g., well deformed prolate rotor behavior, X(5) critical point symmetry,  $\gamma$  softness and triaxial phenomena, and shape coexistence near the shell closure  $Z = 82$  [1–6]. Figure 1 depicts the nucleus under investigation in this study,  $^{182}\text{Os}$  (highlighted by a red circle), positioned precisely at the center of the regions primarily influenced by prolate deformation in the tungsten and hafnium isotopes [7–11], shape coexistence in the mercury and lead isotopes [4],  $\gamma$  softness and triaxiality in the neutron rich osmium and platinum isotopes [12–16], and X(5) critical point symmetry in the lighter osmium isotopes  $^{176,178}\text{Os}$  [6,17] and  $^{182}\text{Pt}$  [5].

Signatures for collectivity and quadrupole deformation are low excitation energies of the  $2_1^+$  states, large  $B(E2; 2_1^+ \rightarrow 0_1^+)$  values [18], which are connected to the deformation parameter  $\beta_2$ , and  $E_{4_1^+}/E_{2_1^+}$  ratios (hereafter  $R_{4/2}$ ) of about 3.3 [18–21]. As Fig. 2 shows, the  $R_{4/2}$  ratios of the midshell osmium isotopes lie between the prolate deformed tungsten isotopes with values around the rotational limit of 3.3 and the platinum isotopes, which exhibit  $\gamma$ -soft, triaxial and already spherical signs with  $R_{4/2}$  ratios between 2.6 and 2.1. Addition-

ally, the  $\beta_2$  values of the osmium isotopes with  $N = 100$ –112 ( $\beta_2 \approx 0.25$ –0.18 [11]) also lie in the descending flank of the  $\beta_2$  values of the strongly deformed region with masses of  $A = 150$ –180 ( $\beta_2 < 0.3$  [18]). The dominating phenomena in  $^{182}\text{Os}$  are suggested to be collective rotation and moderate quadrupole deformation, especially in comparison with the neighboring isotopes  $^{180,184}\text{Os}$  [23–25] and tungsten isotopes  $^{178,180,182}\text{W}$ , which are suggested to be prolate rotors as well [7]. An excitation energy of the  $2_1^+$  state of 126.9 keV, an  $R_{4/2} = 3.15$ , a reduced transition probability of  $B(E2; 2_1^+ \rightarrow 0_1^+) = 122(11)$  W.u., and a  $\beta_2 = 0.23(1)$  ([26], evaluated values of different works) support this assumption. In the platinum isotopes clear signs of rotor behavior are missing, on the other hand. An ideal rotor shows a  $B(E2; 4_1^+ \rightarrow 2_1^+)/B(E2; 2_1^+ \rightarrow 0_1^+)$  (hereafter  $B_{4/2}$ ) of about  $10/7 \approx 1.43$ , known as the Alaga rule of the geometric model [19,20]. The osmium isotopic chain is known for notable deviations from the established theoretical limits of 1.43 (rotor) and 2 (vibrator). Especially in the neutron-deficient isotopes very small values of around and smaller than 1 were repeatedly the subject of studies but could not be doubtlessly explained so far [27–29]. As a meeting point of the main influences [strong collectivity, shape coexistence,  $\gamma$  softness, and X(5) critical point symmetry; see Fig. 1], interesting behavior of the level energies in the osmium isotopes around the neutron midshell is observed. Specifically, the investigation of the impact of shape coexistence phenomena, as shown by the occurrence of rotational intruder bands in mercury isotopes [4], and particularly in  $^{186}\text{Hg}$ , which is separated from  $^{182}\text{Os}$  by only four protons, is an interesting approach.

Only the  $B_{4/2}$  ratios of the osmium isotopes 176, 182Os are unknown, hence, the investigation of the transition

<sup>\*</sup>Corresponding author: [aharter@ikp.uni-koeln.de](mailto:aharter@ikp.uni-koeln.de)<sup>†</sup>Present address: Argonne National Laboratory, 9700 South Cass Ave., Argonne, IL 60439, USA.

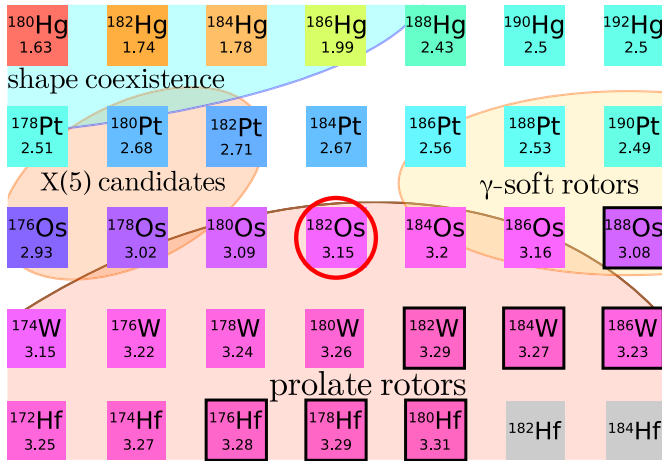


FIG. 1. Even-even isotopes around  $A = 180$ . The regions of shape coexistence,  $\gamma$  softness, X(5) critical point symmetry, and rotational prolate deformation are roughly identified by elliptic shapes. The nucleus of interest  $^{182}\text{Os}$  is indicated by a red circle. The chart is extracted from The colourful nuclide chart by Simpson [22]. The color code of the individual nuclei illustrate the  $R_{4/2}$  ratios, which are taken from Ref. [11].

probabilities of the three lowest rotational states in  $^{182}\text{Os}$  appears to be a conclusive contribution to delimit the quadrupole deformed region of the rare earths and to understand the transition phenomena in the  $A = 180$  region. The lifetimes of these states were expected to be in a fast-timing suitable range and were measured with the recently commissioned digital fast-timing technique [30] using the well established HORUS fast-timing setup [7,31–33].

## II. EXPERIMENTAL DETAILS

Excited states in  $^{182}\text{Os}$  were populated with the fusion evaporation reaction  $^{174}\text{Yb}(^{12}\text{C}, 4n)^{182}\text{Os}$ . A  $^{174}\text{Yb}$  target of about  $4\text{ mg/cm}^2$  was exposed to an average beam current of  $1\text{ p nA}$  with an energy of  $66\text{ MeV}$ , which was provided

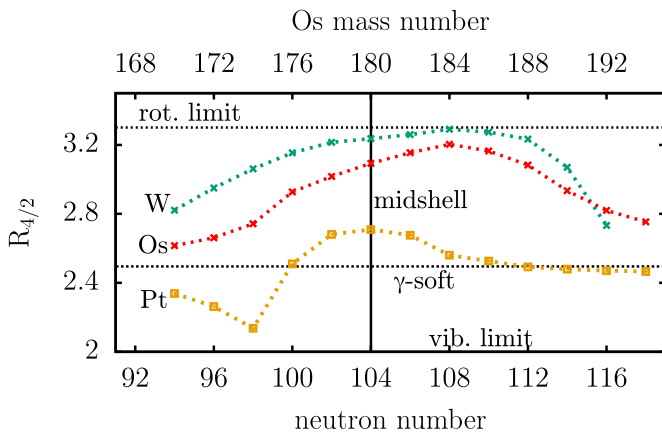


FIG. 2.  $R_{4/2}$  ratios of platinum, osmium, and tungsten isotopes. The neutron midshell and the expectation values for rotational and  $\gamma$ -soft limits are indicated in the plot. The lines connecting the data points are meant to guide the eyes. All values are taken from [11].

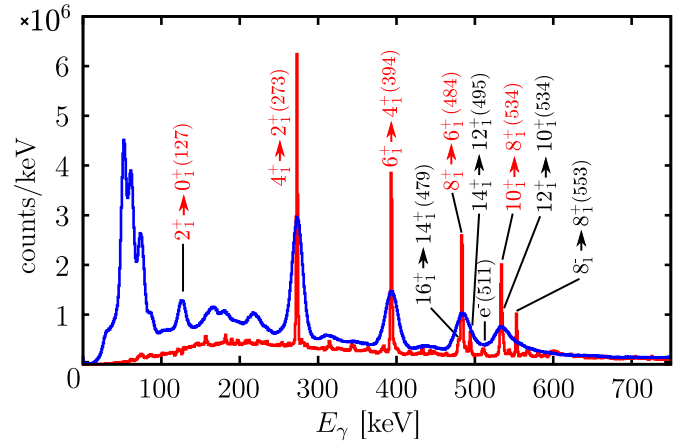


FIG. 3. Spectrum of strongest observed  $\gamma$  rays in coincidence with the  $2_1^+ \rightarrow 0_1^+$  ground state transition observed with HPGe detectors for both detector groups: LaBr in blue and HPGe in red. The transitions used for the lifetime analysis are labeled in red. The energy labels are rounded to full keV. The remaining coincidence contribution in the  $127\text{ keV } 2_1^+ \rightarrow 0_1^+$  transition is due to random coincidence. The HPGe detectors were shielded by 2 mm copper and lead plates to prevent high count rates due to intensive x rays in the sub-100 keV region.

by the Cologne 10 MV FN-Tandem accelerator for about 120 hours. A combined stopper of  $196\text{ mg/cm}^2$  bismuth and  $180\text{ mg/cm}^2$  copper was attached to the target to stop the reaction fragment and the beam to prevent further reactions with the beamline and to enhance the heat dissipation. The yrast band was populated by the fusion evaporation up to the  $16^+$  state. A negligible population of higher yrast states and states in other excitation bands was detected (see Fig. 3).

The HORUS spectrometer was equipped with ten  $\text{LaBr}_3(\text{Ce})$  fast-timing scintillators (LaBr) and eight high-purity germanium detectors (HPGe). The HPGe detectors were shielded against x rays with 2 mm copper and lead plates. Six of the LaBr detectors were surrounded with bismuth germanate (BGO) active Compton suppression shields. The LaBr detector signals were recorded with a fast sampling digitizer of type V1730, manufactured by CAEN S.p.A., with a sampling rate of  $500\text{ MS/s}$  and an analog-to-digital converter (ADC) resolution of 14 bits. The module is equipped with an on-board real-time digital interpolating constant fraction discriminator that provides picosecond-level accuracy in time stamps for the fast LaBr detector pulses. The highly accurate time stamps enable the digital fast-timing method [30].

## III. DATA ANALYSIS

The expected lifetimes of the  $2_1^+$ ,  $4_1^+$ , and  $6_1^+$  states in  $^{182}\text{Os}$  were in the time range between 5 ps and some nanoseconds, to be analyzed with fast-timing methods. The fast-timing method relies on measuring the time difference between a feeding and a depopulating transition of the state of interest. When one signal is given by the feeder of an intermediate state and the other one by the depopulating  $\gamma$  ray,

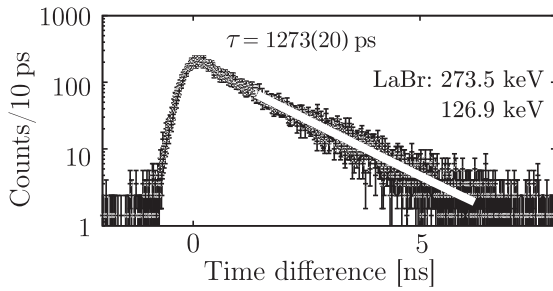


FIG. 4. Time-difference distribution obtained by a direct HPGe energy gate on the  $6_1^+ \rightarrow 4_1^+$  transition, feeding the  $4_1^+$  state to clean the cascade of interest. The LaBr gates were applied to the  $4_1^+ \rightarrow 2_1^+$  (273.5 keV) and the  $2_1^+ \rightarrow 0_1^+$  (126.9 keV) transitions. The straight line represents the slope fit to the exponential part of the distribution.

the delayed time distribution is obtained [34]:

$$D(t) = n\lambda \int_{-\infty}^t \text{PRF}(t' - C_P) e^{-\lambda(t-t')} dt' + n_r, \quad \lambda = \frac{1}{\tau}, \quad (1)$$

where  $C_P$  corresponds to the centroid position of the prompt response function (PRF) of the timing system,  $n$  is the number of coincidences in the time distribution,  $n_r$  is the number of background counts, and  $\tau$  is the lifetime of the state connected by the feeder-decay cascade. The delayed time distribution  $D(t)$  is a convolution of the PRF of the system and an exponential decay.

The lifetime of the  $2_1^+$  state was analyzed using the well established slope method [35]. The lifetimes of the  $4^+$  and the  $6^+$  state both lie in the picosecond regime and were analyzed using the digital centroid shift method as described in Ref. [30].

A spectrum of the observed  $\gamma$  rays in coincidence with the  $2_1^+ \rightarrow 0_1^+$  ground state transition for both detector groups (LaBr and HPGe) is depicted in Fig. 3. The transitions used for the lifetime analysis are indicated in red. The  $\gamma$ -ray spectrum shows the typical back-bending behavior of the  $\gamma$  rays between the states with  $I = 10$ –16 [36]. This phenomenon is assumed to have an influence on the lifetime determination of the  $6_1^+$  state, because the feeding transition  $8_1^+ \rightarrow 6_1^+$  is contaminated by the decays of the  $16_1^+$  and the  $14_1^+$  states. This will be addressed in Sec. III.

#### A. Lifetime of the first $2^+$ state

The lifetime of the  $2_1^+$  state was analyzed using the slope method, and a plot of the time-difference distribution with the fitted exponential decay is presented in Fig. 4. The time-difference distribution was generated with a direct HPGe gate using the  $6_1^+ \rightarrow 4_1^+$  (393.8 keV) transition, feeding the  $4_1^+$  state to select the cascade of interest. The LaBr gates were applied to the  $4_1^+ \rightarrow 2_1^+$  (273.5 keV) and the  $2_1^+ \rightarrow 0_1^+$  (126.9 keV) transitions. The total counts in the time-difference distribution amount to approximately  $n = 25\,000$ . The background level is approximately  $n_r = 0.2/10$  ps. The lifetime amounts to  $\tau = 1273(20)$  ps. The lifetime of the  $2_1^+$  state was previously reported with two disagreeing results of 1173(14) and 1370(144) ps [37,38]. The remeasured value here supports the

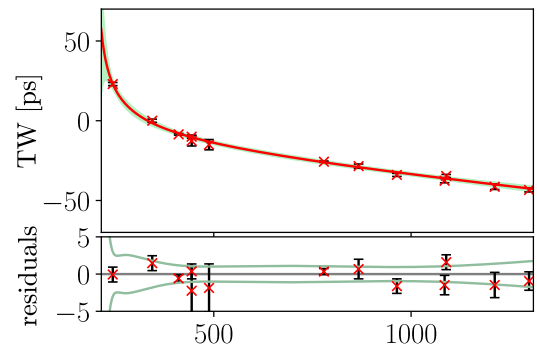


FIG. 5. Time walk calibration for the energy range between 240 and 1300 keV. The maximum time walk range is below 50 ps in the energy range under consideration. The uncertainty band in the lower plot represents the  $1\sigma$  interval and is considered as the TW uncertainty throughout this work.

second one and an evaluation of all three values amounts in an adopted lifetime of  $\tau = 1272(49)$  ps, which will be used for further discussion.

#### B. The centroid shift analyses

The lifetimes of the  $4_1^+$  and  $6_1^+$  states were analyzed using the centroid shift method [35] with the digital approach described in detailed in Ref. [30]. The lifetime is extracted from the centroid shift of the delayed time-difference distribution from the zero reference time  $T_0$  of the timing system, and is given by

$$\tau = C_D - T_0 - \text{TW}(E_1, E_2), \quad (2)$$

where  $C_D$  corresponds to the centroid position of the delayed time-difference distribution,  $T_0 = 0$  here and  $\text{TW}(E_1, E_2)$  represents the energy-dependent time walk between the energies of the two involved transitions, which has to be calibrated for every timing system. The TW was calibrated using a standard  $^{152}\text{Eu}$  calibration source, providing several  $\gamma$ -ray cascades connecting excited states with well known lifetimes [39] and the recently significantly improved lifetime for the  $2_1^+$  state of  $^{152}\text{Gd}$  [40] of  $\tau(2_1^+, ^{152}\text{Gd}) = 46.9(3)$  ps using the procedure detailed in Ref. [41]. The time walk curve in use is defined by

$$\text{TW}(E) = \frac{a}{\sqrt{E-b}} + c + dE, \quad (3)$$

where  $a$ ,  $b$ ,  $c$ , and  $d$  are the free fit parameters of the time walk function, which depend on the properties of the constant fraction discriminator, that is used as a time pick-off device. The time walk characteristic for the digital timing setup is illustrated in Fig. 5 and has a maximum TW range of around 50 ps in the energy range between 200 and 1300 keV. The time-correlated Compton background under the peak of interest was corrected according the considerations in Ref. [42], Sec. 3.3. The corrected centroid of the time-difference distribution of the full-energy peak (FEP) of interest is defined as [42]

$$C_{\text{FEP}} = C_{\text{exp.}} + \frac{t_{\text{cor.}}(E_1) + t_{\text{cor.}}(E_2)}{2}, \quad (4)$$



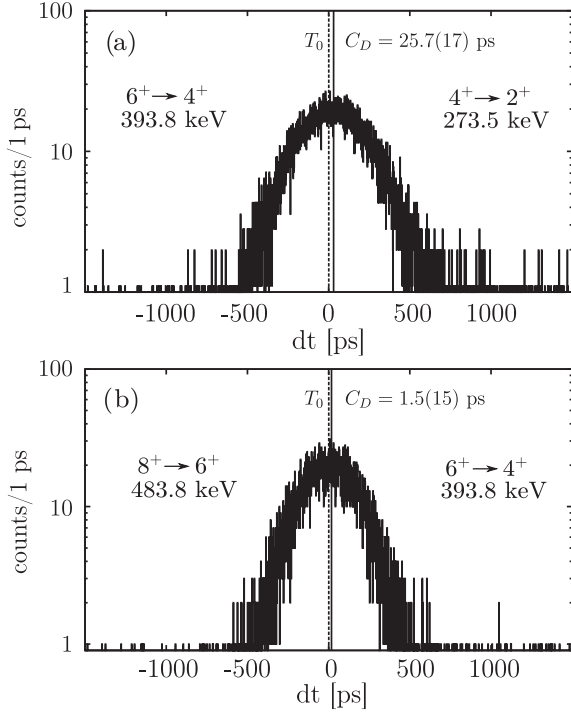


FIG. 6. (a) Time-difference distribution obtained with energy gates applied to the  $2_1^+$  state (127 keV) in HPGe detectors and to the  $6_1^+$  state (393.8 keV) and  $4_1^+$  state (273.5 keV) in LaBr detectors. (b) Time-difference distribution obtained with energy gates applied to the  $2_1^+$  state (126.9 keV) in HPGe detectors and to the  $8_1^+$  state (483.8 keV) and  $6_1^+$  state (393.8 keV) in LaBr detectors. In both plots, the centroid position  $C_D$  and the time reference of the system  $T_0$  are indicated and the energy gates applied to the LaBr detectors are provided.

where the background time correction term is given as [42]

$$t_{\text{cor.}} = \frac{C_{\text{exp.}} - C_{\text{BG}}}{p/b}. \quad (5)$$

The quantity  $p/b$  corresponds to the ratio of the counts in the FEP to the counts in the background of the energy gate that is used to generate the experimental time-difference distribution.

### 1. Lifetime of the first $4_1^+$ state

An exemplary time-difference distribution for the determination of the lifetime of the  $4_1^+$  state containing the full experimental statistics after a HPGe gate on the  $2_1^+ \rightarrow 0_1^+$  (126.9 keV) transition and two LaBr gates on the  $6_1^+ \rightarrow 4_1^+$  (393.8 keV) and  $4_1^+ \rightarrow 2_1^+$  (273.5 keV) transitions is depicted in Fig. 6(a). The system zero time reference  $T_0 = 0$  and the centroid position  $C_D$  are indicated in the plot. The lifetime was determined using two different HPGe gates to select the  $\gamma$  cascade of interest: one on the  $2_1^+ \rightarrow 0_1^+$  (126.9 keV) transition, the other on the  $8_1^+ \rightarrow 6_1^+$  (483.8 keV) transition. In Fig. 7, a gated energy spectrum of the region around the  $4_1^+ \rightarrow 2_1^+$  transition (a) and the time-correlated background correction procedure (b) are exemplarily illustrated for a HPGe gate on the  $2_1^+ \rightarrow 0_1^+$  transition. The centroid position  $C_D$  obtained lies at  $C_D = 25.7(17)$  ps (depending on the

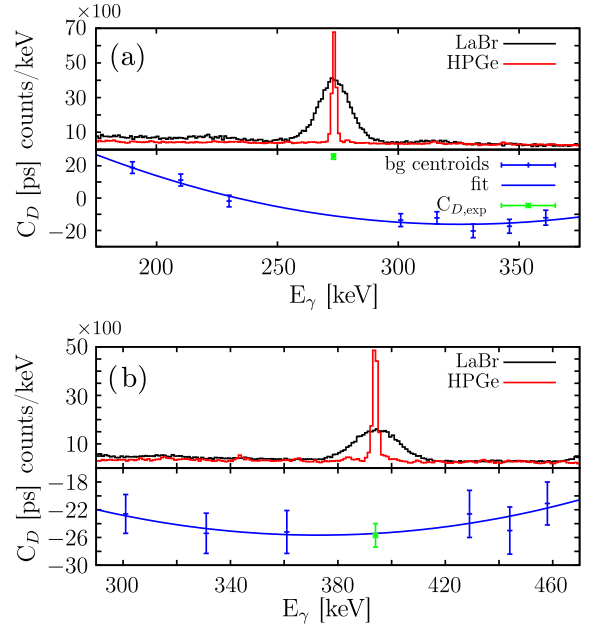


FIG. 7. Exemplary lifetime analysis and background correction for the  $4_1^+$  state. (a) LaBr spectrum and HPGe reference spectrum with energy gates applied to the  $2_1^+ \rightarrow 0_1^+$  (127 keV) transition in HPGe detectors and to the  $6_1^+ \rightarrow 4_1^+$  (393.8 keV) transition in LaBr detectors. The lower part of the figure shows the background correction procedure for the  $4_1^+ \rightarrow 2_1^+$  transition. The centroid positions taken in the background around the peak of interest and the fit are depicted in blue. The experimental centroid position  $C_{D,\text{exp}}$  is indicated in green. (b) LaBr spectrum and HPGe reference spectrum with energy gates applied to the  $2_1^+$  state (127 keV) in HPGe detectors and to the  $4_1^+ \rightarrow 2_1^+$  (273.5 keV) transition in LaBr detectors. The lower part of the figure shows the background correction procedure for the  $6_1^+ \rightarrow 4_1^+$  transition. The centroid positions taken in the background around the peak of interest and the fit are depicted in blue.

triggering HPGe gate). The time walk between the involved  $\gamma$  energies amounts to  $\text{TW}(393.8 \text{ keV}, 273.5 \text{ keV}) = -18.3(8)$  ps. The peak-to-background ratios amount to  $p/b_{273.5 \text{ keV}} = 4.3(1)$  and  $p/b_{393.8 \text{ keV}} = 3.3(1)$ . The individual lifetime values obtained from the different HPGe gates agree within the uncertainties and an adopted lifetime of  $\tau = 48.1(14)$  ps is obtained using a Monte Carlo uncertainty propagation. The results are summarized in Table I.

### 2. Lifetime of the first $6_1^+$ state

The lifetime of the  $6_1^+$  state was determined using the timing cascade  $8_1^+ \rightarrow 6_1^+ \rightarrow 4_1^+$  (483.8–393.8 keV) and two different HPGe gates to select the  $\gamma$ -cascade of interest on  $2_1^+ \rightarrow 0_1^+$  (127 keV) and  $4_1^+ \rightarrow 2_1^+$  (273 keV). All analyses were carried out according to that of the lifetime of the  $4_1^+$  state. Figure 6(b) shows an exemplary time-difference distribution of the energy gate sequence  $8_1^+ \rightarrow 6_1^+ \rightarrow 4_1^+ \rightarrow 2_1^+$  with energy gates on LaBr-LaBr-HPGe, respectively.  $T_0 = 0$  and the centroid position  $C_D$  are indicated in the plot. The time-correlated background correction was applied similarly to the background correction of the lifetime of the  $4_1^+$  state. The time walk between the involved transition energies

TABLE I. Summary of lifetimes measured in this work and derived reduced transition strengths in comparison to literature values and IBM-1 calculations from this work; see Sec. IV. The lifetime values printed in bold are obtained from a Monte Carlo uncertainty propagation and adopted for further discussion and the extraction of the  $B(E2)$  values. The lifetime value for the  $2_1^+$  state is obtained from a Monte Carlo uncertainty propagation of the newly determined value and the two literature values.

$I^\pi$	HPGe gate	$\tau$ (ps)		$B(E2)$ ( $10^{-2} e^2 b^2$ )		
		This work	Lit.	This work	Lit.	IBM-1
$2_1^+$	$6_1^+ \rightarrow 4_1^+$	1273(20)	1173(16) <sup>a</sup> 1370(144) <sup>b</sup>		76.8(13) 66(8)	
		<b>1272(49)</b>		71(3)		71
$4_1^+$	$2_1^+ \rightarrow 0_1^+$	48.7(21)				
	$8_1^+ \rightarrow 6_1^+$	47.5(17)				
		<b>48.1(14)</b>		99(3)		101
$6_1^+$	$2_1^+ \rightarrow 0_1^+$	8.4(18)				
	$4_1^+ \rightarrow 2_1^+$	7.9(18)				
		<b>8.1(12)</b>		$102^{+33}_{-13}$		110

<sup>a</sup>Reference [37].

<sup>b</sup>Reference [38].

amounts to  $TW(483.8 \text{ keV}, 393.8 \text{ keV}) = -6.3(5)$  ps. The centroid position is about  $C_D = 1.5(15)$  ps (depending on the HPGe gate) and the peak-to-background ratios amount to  $p/b_{393.8 \text{ keV}} = 4.0(2)$  and  $p/b_{483.8 \text{ keV}} = 4.0(1)$ . The individual lifetime values depending on the HPGe gates agree within the uncertainties. The lifetime of  $\tau = 8.1(12)$  ps is obtained for the  $6_1^+$  state using a Monte Carlo uncertainty propagation. The previously mentioned  $14_1^+$  and  $16_1^+$  decays due to the back-bending phenomenon contaminate the lifetime analysis of the  $6_1^+$  state. The contaminating peaks at 495 keV ( $14_1^+ \rightarrow 12_1^+$ ) and 479 keV ( $16_1^+ \rightarrow 14_1^+$ ) have an intensity of around 10% of the  $8_1^+ \rightarrow 6_1^+$  transition for both contaminating transitions. Efforts were made to minimize the impact of potential contamination through the use of narrow gates on the 483.8 keV transition and the background correction, although it is possible that the lifetime is still a bit overestimated. Hence, the negative uncertainty is extended about 0.8 ps, which corresponds to another 10%. Hence, the adopted lifetime amounts to  $\tau = 8.1_{-2}^{+1.2}$  ps.

All individual and adopted lifetimes are summarized in Table I alongside with deduced  $B(E2)$  values (see Sec. IV) and  $B(E2)$  values from IBM-1 calculations (see Sec. IV).

#### IV. DISCUSSION

The neutron-midshell region of interest (see Fig. 1) is well characterized in most of the signatures important for quadrupole deformation of nuclei. Especially, the osmium isotopic chain provides one of the longest chains with consecutively known spectroscopic data for even-even isotopes on the entire chart of nuclei [11]. All  $R_{4/2}$  ratios as well as all  $B(E2; 2^+ \rightarrow 0^+)$  values and most of the  $B_{4/2}$  values with the notable exception of  $^{176,182}\text{Os}$  are known for the even-even isotopes of the W, Os, Pt, and Hg isotopic chains around neutron midshell,  $N = 104$  [11]; see Fig. 2. The previously

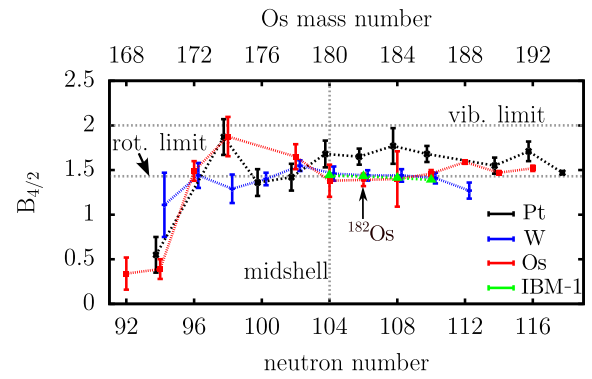


FIG. 8.  $B_{4/2}$  ratios for the osmium, platinum, and tungsten isotopic chains. The newly determined value of  $^{182}\text{Os}_{106}$  is indicated by a dashed box. The orange triangles represent the results of the IBM-1 calculations; see Sec. IV. The dashed lines connecting the data points are meant to guide the eyes. The theoretical limits of ideal rotors and vibrators as well as the neutron midshell are shown with grey dashed lines. The values for  $^{172,176,180}\text{Pt}$ ,  $^{176,178,180}\text{W}$ , and  $^{168,172,174,178}\text{Os}$  are taken from Refs. [7,17,27–29]. All other values taken from nuclear data sheets [11].

unknown  $B_{4/2}$  ratio of  $^{182}\text{Os}$  was determined in this work and amounts to 1.39(7). Within the uncertainties, this value agrees with the rotational limit of 1.43 (see Fig. 8). As Fig. 8 shows, the  $B_{4/2}$  ratios of the neighboring osmium and tungsten isotopes also stick close to the rotor limit. The  $B_{4/2}$  ratios of neighboring platinum exhibit a slight increase towards the vibrational limit. As suggested by the  $R_{4/2}$  ratio of  $^{182}\text{Os}$  of 3.15, the  $B_{4/2}$  ratio of 1.39(7) allows for an interpretation as a rigid, quadrupole deformed rotor [19,20]. The absolute value for the quadrupole deformation  $\beta_2$  was recalculated using the rotational model based on the adopted value of the lifetime of the  $2_1^+$  state and amounts to 0.22(4). The quadrupole deformation of the  $4_1^+$  state also amounts to 0.22(2) and the one of the  $6_1^+$  state amounts to 0.21(8). This corresponds to a moderate quadrupole deformation throughout all measured states of  $^{182}\text{Os}$  [18].

Still, some peculiarities are observed in  $^{182}\text{Os}$ : A possible change in structure of higher excitation bands is taking place at the neutron number  $N = 106$  or the neighboring  $N = 107$  isotope. The excitation energies of the lowest yrast states exhibit an expected trend, as demonstrated by Fig. 9(a), with a minimum value observed close to the neutron midshell at  $N = 104$ . However, the excitation energies of the  $2_2^+$  and  $0_2^+$  states indicate a departure from the previously observed trends in the isotopic chain close to or at  $^{182}\text{Os}_{106}$ , respectively.

The energies of the  $2_2^+$  state, which serves as the bandhead of the  $\gamma$ -rotational band in most osmium isotopes, are around 900 keV for the lighter osmium isotopes ( $96 < N < 108$ ) with a maximum at  $^{184}\text{Os}_{108}$ . As more neutrons are added, the  $\gamma$ -band energies exhibit a sharp break and a beginning even-odd staggering behavior, indicating the emergence of  $\gamma$  softness around  $^{184-192}\text{Os}$  [12–15,43]. At  $N = 114$ ,  $E_{4_1^+}$  and  $E_{2_2^+}$  intersect and are almost equal, which is an indication of  $\gamma$ -soft nuclei [44] (and also vibrational structures, which is, however, not expected in this context at all). The excitation energies of the  $0_2^+$  state perform an opposite movement: the



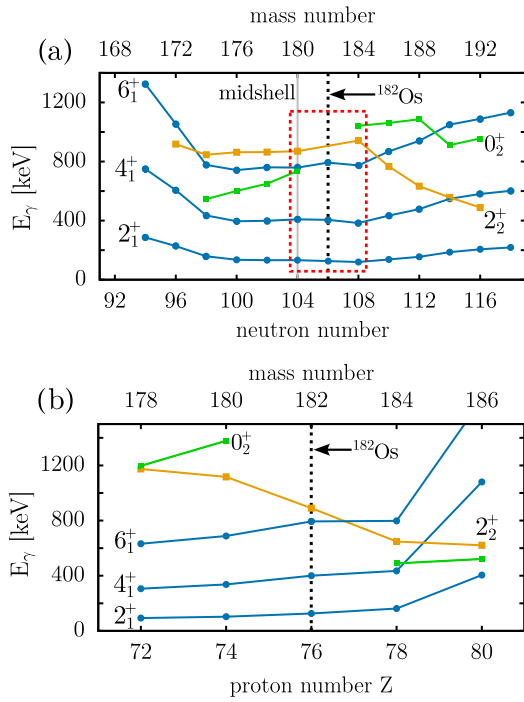


FIG. 9. (a) Evolution of level energies of the osmium isotopes around neutron midshell,  $N = 104$ . The red dashed box marks the area of interest. The blue dots represent the level energies of the  $2_1^+$ ,  $4_1^+$ ,  $6_1^+$  states of the ground state band. The orange squares are the energies of the  $2_2^+$  states and the green squares are the energies of the  $0_2^+$  state. (b) Energies of the first three yrast states and  $2_2^+$  and  $0_2^+$  states versus proton number  $Z$  of the isotones with  $N = 106$ . The lines connecting the data points are meant to guide the eyes. All values are taken from [11].

$E_{0_2^+}$  for the osmium isotopes with  $N = 108, 110, 112$  are observed to be around 1000 keV, but decrease to below 800 keV for  $^{180}\text{Os}$  and lower as neutrons are removed. In particular, no  $0_2^+$  state has been previously reported for  $^{182}\text{Os}$  at all. The drop in  $E_{0_2^+}$  is an indication of the emergence of the X(5) critical point symmetry in the lighter osmium isotopes  $^{176,178}\text{Os}$ , where  $E_{6_1^+}$  and  $E_{0_2^+}$  are expected to be degenerate [45]. From this point of view,  $^{182}\text{Os}$  is suggested as a transition point between the fading influence of the  $\gamma$  softness, where  $E_{0_2^+}$  lies above  $E_{2_2^+}$  [44], in the heavier isotopes and the X(5) symmetry in the lighter isotopes. Figure 9(b) shows the evolution of the same states as in Fig. 9(a) but along the isotonic chain with  $N = 106$ , at the end of which is  $^{186}\text{Hg}$ , where a weakly oblate-deformed ground state band coexists with a prolate intruder band in low-spin states [4,46]. The yrast band structure rises as expected, when approaching a closed shell. But as evidenced by the dropping excitation energies of the  $0_2^+$  and  $2_2^+$  states, also from the isotonic perspective  $^{182}\text{Os}$  might represent a transition point between the prevailing prolate deformation from proton-deficient isobars and the dominating shape coexistence characteristic when adding protons.

These depicted discontinuities, however, do not influence the lower excited yrast states of  $^{182}\text{Os}$ , and this nucleus can be considered the first in the  $N = 106$  isotonic chain to show distinct rotor signs. The strongly deformed rare-earth region

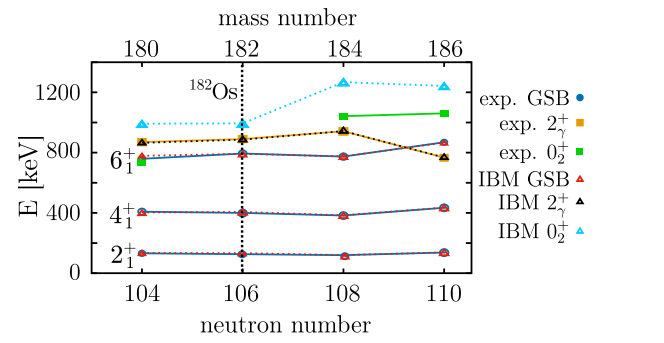


FIG. 10. Experimental and theoretical level energies of first three ground state band states and  $2_2^+$  and  $0_2^+$  states of  $^{180-186}\text{Os}$ . IBM values are illustrated with triangles of different colors. The theoretical values for the ground state bands and the  $2_2^+$  states are taken from Ref. [12]. The theoretical values for the  $0_2^+$  states were calculated in the scope of this paper. The lines are meant to guide the eyes.

far from the closed shells finds an edge here, as the  $^{184}\text{Pt}$  yet deviates from the rotor limits in  $R_{4/2}$  and  $B_{4/2}$  signatures and  $E_{2_2^+}$  and  $E_{0_2^+}$ .

Interacting boson model 1 (IBM-1) [21] calculations were made based on calculations of Sorgunlu and van Isacker [12] for the isotopes  $^{180-186}\text{Os}$ , where the calculations including a Hamiltonian and fit parameters are detailed. In Ref. [12], the ground state band energies up to  $I = 10$  and  $\gamma$ -band energies up to the least known  $I = 6-10$  were fitted. The energies of the  $0_2^+$  state were additionally calculated here. The level energies of the yrast band and the  $\gamma$  band are reproduced with root mean square deviations of  $\sigma = 5-19$  keV for all calculated levels, as Fig. 10 illustrates. The results of the calculations reproduce the discontinuities regarding the level energies of  $2_2^+$  and  $0_2^+$ . The level energies of the  $0_2^+$  state are overestimated by the model. However, the jump of the theoretical values of  $E_{0_2^+}$  between  $^{182}\text{Os}$  and  $^{184}\text{Os}$  are reproduced, as depicted in Fig. 10. Figure 8 shows that the calculated  $B_{4/2}$  values are well reproduced for the isotopes  $^{180-186}\text{Os}$ , including the newly determined  $B_{4/2}$  of  $^{182}\text{Os}$ . It places the  $B_{4/2}$  value close to the rotational limit of  $\approx 1.43$  and agrees with the experimental value within its uncertainties. This calculation shows that the IBM-1 in a simple form, as used here, is excellently able to describe the rotors with boson numbers from 11 to 14 at the edge of the collective region with  $A \approx 180$ .

## V. CONCLUSION

Lifetimes of the first excited  $4^+$  and  $6^+$  states in  $^{182}\text{Os}$  have been measured for the first time and amount to  $\tau_{4_1^+} = 48.1(14)$  ps and  $\tau_{6_1^+} = 8.1(12)$  ps. The lifetime of the first excited  $2^+$  state has been remeasured with high precision and supports one of the previously measured literature values. The evaluated lifetime between all three values obtained by Monte Carlo uncertainty propagation amounts to  $\tau_{2_1^+} = 1272(49)$  ps and was adopted for further discussions. With the newly determined and evaluated lifetimes, the  $B(E2)$  values between the  $6_1^+$ ,  $4_1^+$ , and  $2_1^+$  states and corresponding deformation parameters  $\beta_2$  were extracted. A  $B_{4/2}$  value of 1.39(7) of  $^{182}\text{Os}$  was determined and classified in the context

of the neighboring isotopes. In accordance with IBM-1 calculations the collective and rotorlike structure is suggested by the  $B_{4/2}$  value, as expected from the already known collective signatures.  $^{182}\text{Os}$  marks the edge of the strongly deformed rare-earth region in the  $N = 106$  isotonic chain as  $^{184}\text{Pt}$  cannot serve with clear collective signs. Still,  $^{182}\text{Os}$  shows transitional behavior in higher lying excitation bands between the heavier  $\gamma$ -soft and the lighter  $X(5)$  candidates in the osmium isotopes and the strongly deformed rotors in the lighter isotones, e.g., tungsten and hafnium, and the onset of coexisting shapes in low excitation levels of the heavier isotones platinum and mercury. Further lifetime measurements of the higher yrast states and the  $2_2^+$  state potentially with the recoil-distance Doppler shift method and the subsequent  $B(E2)$  values as

well as spectroscopic measurements to potentially discover a  $K^\pi = 0^+$  band can provide more clarity about the onset of the shape coexistence phenomena and slight  $\gamma$  softness in  $^{182}\text{Os}$ .

#### ACKNOWLEDGMENTS

The authors would like to thank the operator staff of the FN Tandem accelerator at the Institut für Kernphysik, Cologne. M.L. acknowledges the Deutsche Forschungsgemeinschaft (DFG) for support under Grant No. JO 391/18-1. A.E. wants to acknowledge the support of BMBF Verbundprojekt 05P2021 (ErUM-FSP T07) under Grant No. 05P21PKFN1. We acknowledge the DFG for the upgrade of the used German detectors under grant INST 216/988-1 FUGG.

- 
- [1] D. T. Joss, S. L. King, R. D. Page, J. Simpson, A. Keenan, N. Amzal, T. Bäck, M. A. Bentley, B. Cederwall, J. F. C. Cocks, D. M. Cullen, P. T. Greenlees, K. Helariutta, P. M. Jones, R. Julin, S. Juutinen, H. Kankaanpää, H. Kettunen, P. Kuusiniemi, M. Leino *et al.*, *Nucl. Phys. A* **689**, 631 (2001).
- [2] M. C. Drummond, D. T. Joss, R. D. Page, J. Simpson, D. O'Donnell, K. Andgren, L. Bianco, B. Cederwall, I. G. Darby, S. Eeckhauht, M. B. Gomez-Hornillos, T. Grahn, P. T. Greenlees, B. Hadinia, P. M. Jones, R. Julin, S. Juutinen, S. Ketelhut, A.-P. Leppänen, M. Leino *et al.*, *Phys. Rev. C* **87**, 054309 (2013).
- [3] D. T. Joss, K. Lagergren, D. E. Appelbe, C. J. Barton, J. Simpson, B. Cederwall, B. Hadinia, R. Wyss, S. Eeckhauht, T. Grahn, P. T. Greenlees, P. M. Jones, R. Julin, S. Juutinen, H. Kettunen, M. Leino, A.-P. Leppänen, P. Nieminen, J. Pakarinen, P. Rakkila *et al.*, *Phys. Rev. C* **70**, 017302 (2004).
- [4] K. Heyde and J. L. Wood, *Rev. Mod. Phys.* **83**, 1467 (2011).
- [5] G. Häfner, A. Esmaylzadeh, J. Jolie, J.-M. Régis, C. Müller-Gatermann, A. Blazhev, C. Fransen, R.-B. Gerst, V. Karayonchev, L. Knafla, N. Saed-Samii, and K.-O. Zell, *Eur. Phys. J. A* **57**, 5 (2021).
- [6] A. Dewald, O. Möller, B. Melon, T. Pissulla, B. Saha, S. Heinze, J. Jolie, K. O. Zell, P. Petkov, D. Bazzacco, S. Lunardi, C. A. Ur, E. Farnea, R. Menegazzo, G. De Angelis, D. Tonev, D. R. Napoli, N. Marginean, T. Martinez, M. Axiotis *et al.*, in *Frontiers in Nuclear Structure, Astrophysics, and Reactions - FINUSTAR*, 12–17 September 2005, Isle of Kos, Greece, edited by S. V. Harissopoulos, P. Demetriou, and R. Julin, AIP Conf. Proc. No. 831 (AIP, New York, 2006), p. 195.
- [7] A. Harter, L. Knafla, G. Frießner, G. Häfner, J. Jolie, A. Blazhev, A. Dewald, F. Dunkel, A. Esmaylzadeh, C. Fransen, V. Karayonchev, K. Lawless, M. Ley, J.-M. Régis, and K. O. Zell, *Phys. Rev. C* **106**, 024326 (2022).
- [8] J. Wiederhold, V. Werner, R. Kern, N. Pietralla, D. Bucurescu, R. Carroll, N. Cooper, T. Daniel, D. Filipescu, N. Florea, R.-B. Gerst, D. Ghita, L. Gurgi, J. Jolie, R. S. Ilieva, R. Lica, N. Marginean, R. Marginean, C. Mihai, I. O. Mitu *et al.*, *Phys. Rev. C* **99**, 024316 (2019).
- [9] M. Rudigier, K. Nomura, M. Dannhoff, R.-B. Gerst, J. Jolie, N. Saed-Samii, S. Stegemann, J.-M. Régis, L. M. Robledo, R. Rodríguez-Guzmán, A. Blazhev, C. Fransen, N. Warr, and K. O. Zell, *Phys. Rev. C* **91**, 044301 (2015).
- [10] P. J. R. Mason, Z. Podolyák, N. Mărginean, P. H. Regan, P. D. Stevenson, V. Werner, T. Alexander, A. Algora, T. Alharbi, M. Bowry, R. Britton, A. M. Bruce, D. Bucurescu, M. Bunce, G. Căta-Danil, I. Căta-Danil, N. Cooper, D. Deleanu, D. Delion, D. Filipescu *et al.*, *Phys. Rev. C* **88**, 044301 (2013).
- [11] Evaluated nuclear structure data file (ensdf), online database, accessed on 2023-03-31.
- [12] B. Sorgunlu and P. Van Isacker, *Nucl. Phys. A* **808**, 27 (2008).
- [13] C. Wheldon, G. Dracoulis, R. Newman, P. Walker, C. Pearson, A. Byrne, A. Baxter, S. Bayer, T. Kibédi, T. McGoram, S. Mullins, and F. Xu, *Nucl. Phys. A* **699**, 415 (2002).
- [14] P. Bond, R. Casten, D. Warner, and D. Horn, *Phys. Lett. B* **130**, 167 (1983).
- [15] P. R. John, V. Modamio, J. J. Valiente-Dobón, D. Mengoni, S. Lunardi, T. R. Rodríguez, D. Bazzacco, A. Gadea, C. Wheldon, T. Alexander, G. de Angelis, N. Ashwood, M. Barr, G. Benzoni, B. Birkenbach, P. G. Bizzeti, A. M. Bizzeti-Sona, S. Bottoni, M. Bowry, A. Bracco *et al.*, *Phys. Rev. C* **90**, 021301 (2014).
- [16] Z. Podolyák, S. J. Steer, S. Pietri, F. R. Xu, H. L. Liu, P. H. Regan, D. Rudolph, A. B. Garnsworthy, R. Hoischen, M. Górska, J. Gerl, H. J. Wollersheim, T. Kurtukian-Nieto, G. Benzoni, T. Shizuma, F. Becker, P. Bednarczyk, L. Caceres, P. Doornenbal, H. Geissel *et al.*, *Phys. Rev. C* **79**, 031305 (2009).
- [17] O. Möller, Ph.D. thesis, Universität zu Köln, 2005.
- [18] R. F. Casten, *Nuclear Structure from a Simple Perspective*, Oxford Studies in Nuclear Physics Vol. 23 (Oxford University Press, Oxford, 2000).
- [19] A. Bohr and B. R. Mottelson, *Nuclear Structure: Vol. 1* (World Scientific, Singapore, 1969).
- [20] A. Bohr and B. R. Mottelson, *Nuclear Structure: Vol. 2* (World Scientific, Singapore, 1975).
- [21] A. Arima and F. Iachello, in *Advances in Nuclear Physics, Vol. 13*, edited by J. W. Negele and E. Vogt (Springer, New York, 2012), p. 139.
- [22] E. C. Simpson, *J. Phys.: Conf. Ser.* **1643**, 012168 (2020).
- [23] C. M. Baglin, *Nucl. Data Sheets* **111**, 275 (2010).
- [24] E. McCutchan, *Nucl. Data Sheets* **126**, 151 (2015).
- [25] R. Kaczarowski, U. Garg, A. Chaudhury, E. G. Funk, J. W. Mihelich, D. Frekers, R. V. F. Janssens, and T. L. Khoo, *Phys. Rev. C* **41**, 2069 (1990).

- [26] S. Raman, C. W. Nestor, and P. Tikkanen, *At. Data Nucl. Data Tables* **78**, 1 (2001).
- [27] B. Cederwall, M. Doncel, O. Aktas, A. Ertoprak, R. Liotta, C. Qi, T. Grahn, D. M. Cullen, B. S. Nara Singh, D. Hodge, M. Giles, S. Stolze, H. Badran, T. Braunroth, T. Calverley, D. M. Cox, Y. D. Fang, P. T. Greenlees, J. Hilton, E. Ideguchi *et al.*, *Phys. Rev. Lett.* **121**, 022502 (2018).
- [28] T. Grahn, S. Stolze, D. T. Joss, R. D. Page, B. Saygi, D. O'Donnell, M. Akmal, K. Andgren, L. Bianco, D. M. Cullen, A. Dewald, P. T. Greenlees, K. Heyde, H. Iwasaki, U. Jakobsson, P. Jones, D. S. Judson, R. Julin, S. Juutinen, S. Ketelhut *et al.*, *Phys. Rev. C* **94**, 044327 (2016).
- [29] A. Goasduff, J. Ljungvall, T. R. Rodríguez, F. L. Bello Garrote, A. Etile, G. Georgiev, F. Giacoppo, L. Grente, M. Klintefjord, A. Kuşoğlu, I. Matea, S. Rocchia, M.-D. Salsac, and C. Sotty, *Phys. Rev. C* **100**, 034302 (2019).
- [30] A. Harter, M. Weinert, L. Knafla, J.-M. Régis, A. Esmaylzadeh, M. Ley, and J. Jolie, *Nucl. Instrum. Methods Phys. Res., Sect. A* **1053**, 168356 (2023).
- [31] L. Knafla, G. Häfner, J. Jolie, J.-M. Régis, V. Karayonchev, A. Blazhev, A. Esmaylzadeh, C. Fransen, A. Goldkuhle, S. Herb, C. Müller-Gatermann, N. Warr, and K. O. Zell, *Phys. Rev. C* **102**, 044310 (2020).
- [32] A. Esmaylzadeh, L. M. Gerhard, V. Karayonchev, J.-M. Régis, J. Jolie, M. Bast, A. Blazhev, T. Braunroth, M. Dannhoff, F. Dunkel, C. Fransen, G. Häfner, L. Knafla, M. Ley, C. Müller-Gatermann, K. Schomacker, N. Warr, and K.-O. Zell, *Phys. Rev. C* **98**, 014313 (2018).
- [33] V. Karayonchev, A. Blazhev, A. Esmaylzadeh, J. Jolie, M. Dannhoff, F. Diel, F. Dunkel, C. Fransen, L. M. Gerhard, R.-B. Gerst, L. Knafla, L. Kornwebel, C. Müller-Gatermann, J.-M. Régis, N. Warr, K. O. Zell, M. Stoyanova, and P. Van Isacker, *Phys. Rev. C* **99**, 024326 (2019).
- [34] Z. Bay, *Phys. Rev.* **77**, 419 (1950).
- [35] H. Mach, R. Gill, and M. Moszyński, *Nucl. Instrum. Methods Phys. Res., Sect. A* **280**, 49 (1989).
- [36] K. S. Krane, D. Halliday *et al.*, *Introductory Nuclear Physics*, (John Wiley & Sons, New York, 1988).
- [37] R. Broda, J. Golczewski, A. Z. Hryniewicz, R. Kulesa, and W. Walus JINR Technical Report No. JINR-E6-5070, 1970 (unpublished).
- [38] B. R. Erdal, M. Finger, R. Foucher, J. P. Husson, J. Jastrzebski, A. Johnson, N. Perrin, R. Henck, R. Regal, P. Siffert, G. Astner, A. Kjelberg, P. Patzelt, A. Hoglund, and S. Malmkog, in Proceedings of International Conference on Properties of Nuclei far from the Region of Beta-Stability, 1970 (unpublished).
- [39] M. Martin, *Nucl. Data Sheets* **114**, 1497 (2013).
- [40] L. Knafla, A. Harter, M. Ley, A. Esmaylzadeh, J.-M. Régis, D. Bittner, A. Blazhev, F. von Spee, and J. Jolie, *Nucl. Instrum. Methods Phys. Res., Sect. A* **1052**, 168279 (2023).
- [41] J.-M. Régis, N. Saed-Samii, M. Rudigier, S. Ansari, M. Dannhoff, A. Esmaylzadeh, C. Fransen, R.-B. Gerst, J. Jolie, V. Karayonchev, C. Müller-Gatermann, and S. Stegemann, *Nucl. Instrum. Methods Phys. Res., Sect. A* **823**, 72 (2016).
- [42] J.-M. Régis, M. Dannhoff, and J. Jolie, *Nucl. Instrum. Methods Phys. Res., Sect. A* **897**, 38 (2018).
- [43] X. Q. Yang, L. J. Wang, J. Xiang, X. Y. Wu, and Z. P. Li, *Phys. Rev. C* **103**, 054321 (2021).
- [44] R. Casten, P. Von Brentano, K. Heyde, P. Van Isacker, and J. Jolie, *Nucl. Phys. A* **439**, 289 (1985).
- [45] F. Iachello, *Phys. Rev. Lett.* **87**, 052502 (2001).
- [46] L. P. Gaffney, M. Hackstein, R. D. Page, T. Grahn, M. Scheck, P. A. Butler, P. F. Bertone, N. Bree, R. J. Carroll, M. P. Carpenter, C. J. Chiara, A. Dewald, F. Filmer, C. Fransen, M. Huysse, R. V. F. Janssens, D. T. Joss, R. Julin, F. G. Kondev, P. Nieminen *et al.*, *Phys. Rev. C* **89**, 024307 (2014).

## 5 | Summary and Conclusion

Modernisations and digitalizations of fast-timing methods for  $e^--\gamma$  and  $\gamma-\gamma$  timing was carried out in the scope of this work. The measuring capability of the iron-free Orange spectrometer in Cologne was restored through extensive hardware innovation and software development and commissioned in fast-timing experiments. The digital fast timing technique was implemented with fast-sampling digitizers using LaBr<sub>3</sub>(Ce)detectors by setting up the required hardware and developing software required for the timing analysis. The new technique was extensively tested, optimized and established. With the help of the new developments, nuclear structure experiments have been successfully conducted:

Lifetimes of excited states in different tungsten and osmium nuclei in the  $A \approx 180$  region around the neutron midshell  $N=104$  were measured to investigate the underlying collective structure of these nuclei. The lifetimes ranging from a few picoseconds up to two nanoseconds were measured using analogue and digital fast-timing techniques with un-triggered and  $\gamma$  or  $e^-$  triggered  $\gamma-\gamma$  – and  $e^--\gamma$  timing. A summary of the developments, experiments and results is given in the following sections.

### **Modernization and restored usability of the Orange conversion electron spectrometer and 'Lifetime measurements in the tungsten isotopes <sup>176,178,180</sup>W'**

Lifetimes of yrast states in the midshell tungsten isotopes <sup>176,178,180</sup>W have been studied using different timing techniques. The main focus lies particularly on the modernized and restored usability of the Orange conversion electron spectrometer. The Orange spectrometer has been renewed in many hardware components, most of which have been combined in a 19" rack enclosure for easy usability. The new multi-threaded control and acquisition software **NewOrange** was written, which communicates primarily via the LAN/Ethernet protocol with the different hardware units and is therefore independent of specially created communication channels. Different test and commissioning runs were conducted. In the first publication, lifetime measurements were performed with fast-timing methods using the Cologne iron-free Orange spectrometer and the Cologne HORUS spectrometer. Additionally, results from a recoil distance Doppler shift experiment using the Cologne coincidence Plunger setup were presented. Excited states in the investigated nuclei were populated through different fusion evaporation reactions. Lifetimes of several yrast states, including  $2_1^+$ ,  $4_1^+$ ,  $6_1^+$ , and  $8_1^+$ , were measured in all three tungsten isotopes, with an additional measurement of the  $10_1^+$  state in <sup>176</sup>W.

The obtained lifetimes were used to extract E2 transition strengths, quadrupole moments  $Q_t$ , quadrupole deformation parameters  $\beta$ , and  $B_{4/2}$  ratios. The newly determined  $B_{4/2}$  ratios for

$^{176}\text{W}$  and  $^{180}\text{W}$ , along with the  $\beta$  values of the  $4^+$  and  $6^+$  states, provide a more comprehensive understanding of the quadrupole deformation evolution in the tungsten isotopes at the edge of the strongly deformed rare-earths region. The interpretations of  $R_{4/2}$  values near the SU(3) limit were confirmed by the  $B_{4/2}$  values and the evolution of  $B(E2; I \rightarrow I - 2)$  values over the low-spin yrast states within  $^{178,180}\text{W}$ . However, a clear interpretation of the results for  $^{176}\text{W}$  and the description of the tungsten isotopic chain, particularly the neutron-deficient side, further investigation are required.

The experimental measurements were compared with calculations within the IBM-1 framework. The theoretical calculations, combined with experimental  $B(E2; I \rightarrow I - 2)$  values and theoretical and experimental quadrupole deformations of the low yrast states, support the previous interpretation of the tungsten isotopes around the neutron midshell  $N = 104$  as deformed prolate rotors.

## **'Systematic investigation of time walk and time resolution characteristics of CAEN digitizers V1730 and V1751 for application to fast-timing lifetime measurement'**

In the scope of this work, the digital fast-timing technique using fast-sampling digitizers of the type V1730 from CAEN S. p. A. was implemented, thoroughly tested and optimized and established in several experiments at the FN tandem accelerator facility at the IKP, Cologne. The newly developed fast-timing sorting code `ft-soco` combines all software components necessary for a digital fast timing analysis. The software is written close to the computational hardware in parallel C++ and provides high-performance and reliability next to an easy to understand and expandable code-level structure.

The emergence of digitally implemented real-time interpolating CFD algorithms in fast-sampling digitizers has simplified the electronics of fast-timing setups. The study presented in the second publication investigates the timing performance of the V1730 and V1751 digitizers manufactured by CAEN S. p. A. in terms of time walk behavior and time resolution, based on digital CFD shaping parameters and input amplitude of the signals. The timing properties of the digital CFDs are comparable to analogue models, such as ORTEC 935. The time resolutions with values around 350 ps or lower are suitable for fast-timing experiments. The time walk characteristics are well characterized, and both digitizers demonstrate good performance within specific energy ranges. Optimal parameters and energy application ranges for the experimental conditions using these digitizers are obtained. The optimal shaping parameters for the V1730 digitizer are a CFD delay of 14 ns and a CFD fraction of 25 %. There is still potential for further improvements, such as expanding the interpolation algorithm to a cubic one and expanding the input dynamic range. Overall, this study provides validation of this technique for future fast-timing experiments using the V1730 and V1751 digitizers, showcasing their suitability and performance in fast-timing

measurements in nuclear physics.

## Lifetime measurements in low yrast states and spectroscopic peculiarities in $^{182}\text{Os}$

Lifetime measurements of the low-lying yrast states  $2_1^+$ ,  $4_1^+$  and  $6_1^+$  in the unstable nucleus  $^{182}\text{Os}$  were performed using the newly commissioned digital fast timing technique using CAEN V1730 digitizers at the FN tandem accelerator facility of the IKP.  $B(E2)$  values for the transitions  $4_1^+ \rightarrow 2_1^+$  and  $6_1^+ \rightarrow 4_1^+$  are extracted for the first time. A mismatch of two different literature values was clarified. The obtained results shed light on the collective signatures and quadrupole deformation in this nucleus as the  $B_{4/2}$  of  $^{182}\text{Os}$  was determined the first time.

The rotational structure of  $^{182}\text{Os}$  suggested by the low lying  $2_1^+$  state and an  $R_{4/2}$  ratio of 3.2 and the rotor behavior of the neighboring osmium and tungsten isotopes was confirmed by the  $B_{4/2}$  value of 1.39(7), which agrees with the alaga rule for rigid rotors of 1.43. Higher lying excitation bands were investigated and considered in terms of the influences by various factors including nearby  $\gamma$ -soft rotors in the heavier osmium isotopes, X(5) critical point symmetry in the lighter osmium isotopes and neighboring region with shape coexistence at low excitation states in the mercury isotopes. Transitional behavior is observed in the  $\gamma$ -band head  $2_2^+$  and the  $0_2^+$  states of the neighboring nuclei, indicating the interplay between neighboring heavier  $\gamma$ -soft and lighter X(5) candidates in osmium isotopes, as well as strongly deformed rotors in lighter isotones, and the onset of coexisting shapes in low excitation levels of heavier isotones like platinum and mercury. The results concerning  $^{182}\text{Os}$  align with predictions from the interacting boson model 1, suggesting a collective and rotor-like structure as expected from already known collective signatures.

It was concluded that  $^{182}\text{Os}$  marks the edge of the strongly deformed rare-earth region in the  $N = 106$  isotonic chain, as  $^{184}\text{Pt}$  lacks clear collective signs. Future investigations involving lifetime measurements of higher yrast states and the  $2_2^+$  state using techniques such as recoil distance doppler shift method, and subsequent  $B(E2)$  values, as well as spectroscopic measurements to potentially identify a  $K^\pi = 0^+$  band, hold promise for gaining further clarity on the structural transitions in  $^{182}\text{Os}$

Finally, it can be stated that the developments and modernizations around the Orange conversion electron spectrometer and the digital fast timing technique have been successfully established. Nuclear structure experiments as lifetime measurements using fast-timing techniques have been carried out based on the new developments. The understanding of nuclear structure in the  $A=180$  neutron midshell region has been further enhanced and the strongly deformed rare-earth region has been better delimited through these experimental results. The IBM in form of the sd-IBM-1 has proven to be effective in reproducing the experimental results in this region.



## 6 | Outlook

### 6.1 Ongoing development and modernization at the Orange conversion spectrometer setup

#### 6.1.1 Consideration about the power supply

The Orange conversion spectrometer needs electric currents of up to 1200 A or even more, depending on the kinetic energy on the conversion electrons to detect. Power supplies, which are able to provide currents in this range need sufficient cooling. The power supply currently in use, the model 100/1200 from the manufacturer Bruker, is susceptible to condensation water and water short circuits when the water cooling system operates at low temperatures ( $< \approx 13^\circ\text{C}$ ). To mitigate this, the warm water cooling circuit of the cooling system of the IKP is connected to the power supply. However, it has been observed that this cooling circuit is not always capable of maintaining a consistent 3-bar pressure difference between the input and output because of many consumers. This occasionally results in a limited output current or even a complete operational interruption of the power supply.

To overcome this problem, potential solutions are proposed:

- The construction of a dedicated secondary cooling circuit is being considered. This circuit would incorporate its own water pump and a heat exchanger to the cold water cooling of the cooling system of the IKP, ensuring independent and reliable cooling for the power supply. To avoid too low temperatures and condensed water within the power supply, a control loop is proposed, that keeps the temperature of the power supply above about  $20^\circ\text{C}$ .
- The secondary water cooling system of the unused small Orange spectrometer could be reconfigured to support the power supply. This approach would leverage existing infrastructure and provide a stable cooling solution.
- Another viable option is to replace the current water-cooled power supply with an array of air-cooled and newer power supplies, for example the Delta Electronica SM6000 Series, which is already utilized in other systems at the IKP. One of the SM6000 has a maximum power of 6 kW and it is possible to connect multiple of this modules in parallel to achieve the required current. This transition would not only eliminate the maintenance challenges associated with the aging power supply from Bruker but also offer improved reliability and efficiency.

The choice among these possibilities will depend on factors such as feasibility, cost-effectiveness. In my opinion, the most practical, simplest and most cost-effective solution is the first suggestion: the installation of a dedicated secondary circuit as depicted in Fig. 10. Through careful evaluation



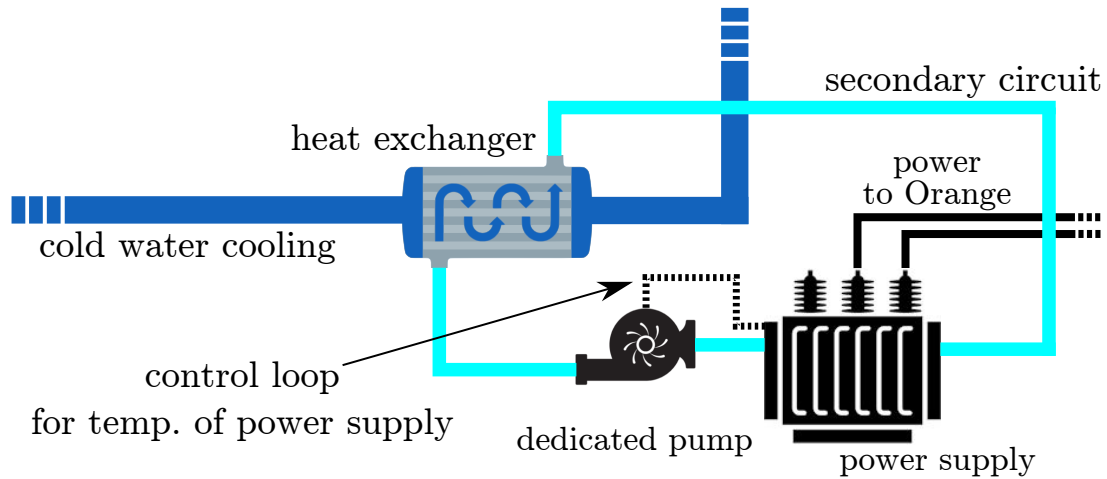


**Figure 10:** Proposed water cooling system for the Bruker power supply.

and collaboration with the operators staff in the IKP, the aim is to implement a solution that ensures stable and efficient power supply operation while minimizing maintenance efforts and potential risks of damage of the power supply. By addressing this important aspect, the Orange spectrometer will be prepared for enhanced performance and durability.

### 6.1.2 Conversion electron calibration source

The Orange spectrometer requires a calibration source to accurately calibrate the spectrometer with known conversion electron energies for time walk and energy. The calibration source has to be as point-like as possible to ensure optimal focus relative to the spectrometer and to minimize energy straggling of the emitted conversion electrons providing optimal conditions for calibration. Due to legal requirements, the calibration source needs to be sealed and at the same time capable of withstanding vacuum conditions. This is achieved using a thin, few micrometers thick coverage foil ( $\approx 5 \mu\text{m}$ ), which the electrons can pass without too high loss of kinetic energy. The preferred source material for the calibration source is  $^{133}\text{Ba}$  due to the well-known conversion electron spectrum and lifetimes of intermediate states of  $^{133}\text{Cs}$ .  $^{133}\text{Cs}$  is the daughter isotope of  $^{133}\text{Ba}$  and is formed through electron capture decay [49].

Currently, the available calibration source is constructed as an aluminum plate with dimensions similar to an Orange target frame (the design is stored by the engineering workshop of the IKP). It features a small 1 mm x 1 mm hole at the target position, where a solution of  $^{133}\text{Ba}$  is deposited, dried, and covered with the thin foil. However, the positioning of the source spot in the current source frame is unfavorable, resulting in a spread of approximately 5 mm radius instead of the desired point-like shape. Consequently, this source is ill-suited for achieving optimal calibration of the spectrometer.

To address these issues, a new source frame design is proposed. This design involves incorporating a conical drilling from the rear side of the aluminum plate, with a 1 mm x 1 mm hole at the end

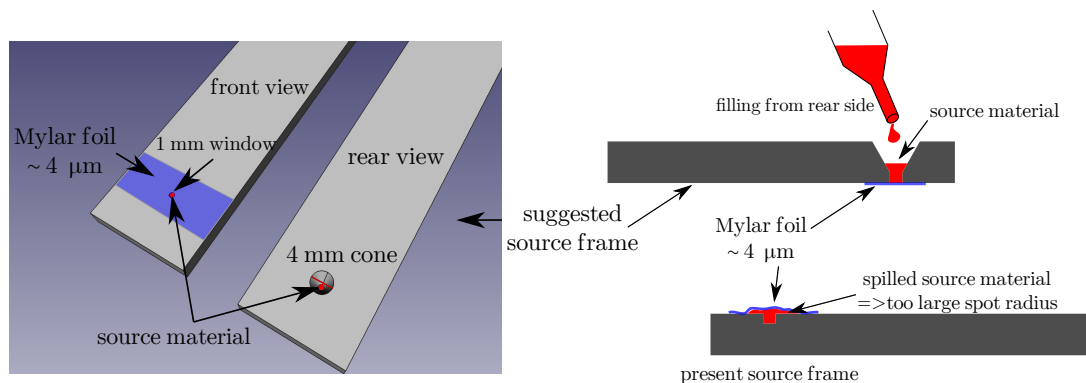


**Figure 11:** Left: CAD drawing of the proposed source frame for the calibration source of the Orange spectrometer. Right: Schematic drawing of the new, proposed (top) and the old, ill-suited (bottom) source frame.

of the cone that connects to the front side of the frame, like a window. With this configuration, the coverage foil can be attached from the front side first, and the source liquid can be filled from the rear side, allowing it to dry and be covered from the same side. This design ensures a point-like source shape from the front side, thereby enabling precise focusing of the source. For visual reference, both the old source frame and the suggested new design are depicted in Figure 11.

### 6.1.3 New Detector frame

An important aspect of the planned developments and modernizations at the Orange spectrometer involves addressing the challenges associated with the detector mount system. Currently, the spectrometer is predominantly used in a fast-imaging setups with 6 to 8 LaBr detectors and at least one HPGe detector. However, the existing detector mount frame (see Ref. [29]) does not support the widely adopted triangle plug-in system that has been established some years ago at the IKP. Additionally, the old frame only provides space for up to 4 BGO-capsuled LaBr detectors.

This limitation presents multiple issues. First, it complicates the installation of BGO shields and germanium detectors and poses the risk of physical damage to the detectors. Additionally, the structural deficiencies of the frame pose a safety risk to the personnel involved in the installation process, increasing the potential for physical injuries.

To overcome these challenges, a solution is proposed to replace the old and unsupported plug-in system with the new one already in use at the IKP. The plan involves installing the existing and discarded detector frame of the Plunger setup, which is no longer needed for its original purpose, because the new detector frame for the Plunger setup was recently installed. This recycled detector frame will feature the new plug-in system, enabling easy and secure installation of the detectors. In this configuration, the frame will accommodate seven BGO-capsuled detectors arranged in a hexagonal pattern, as depicted in Fig. 12. This arrangement ensures efficient detector performance and straightforward installation procedures. By implementing this solution,

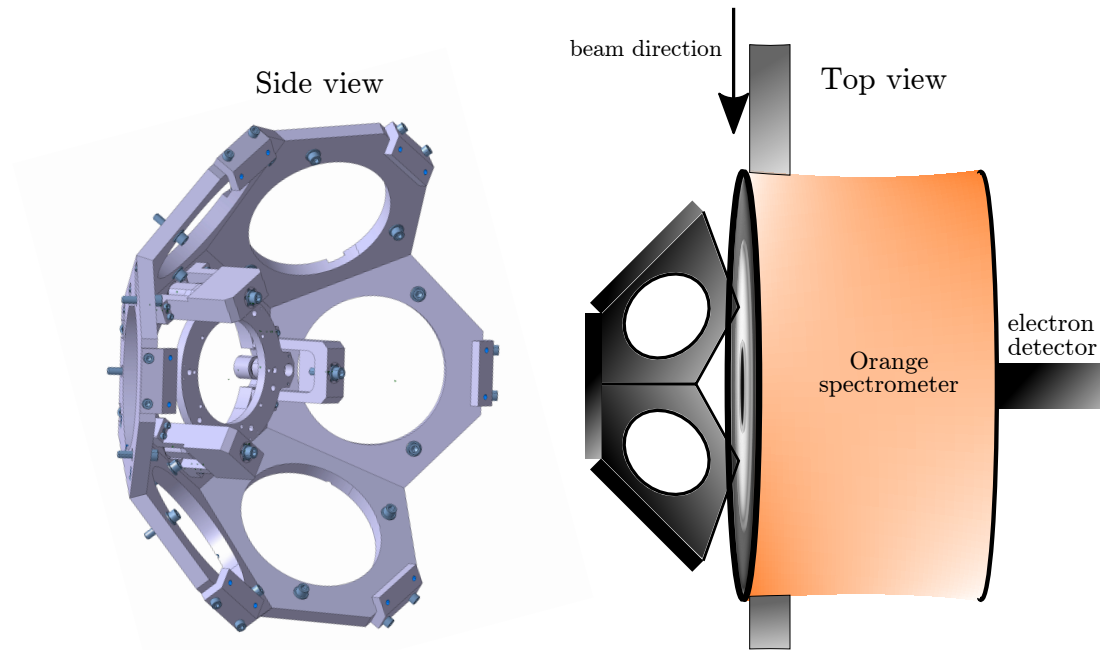


**Figure 12:** Left: Side view of the new honeycomb shaped detector mount frame, taken over by the Cologne Plunger setup. Right: Schematic top view of the Orange spectrometer in combination with the new detector mount frame.

the Orange spectrometer will benefit from improved detector compatibility, enhanced safety during installation, and optimized experimental conditions (better Compton suppression due to 6 BGO shields for LaBr detectors and one for a HPGe detector.)

## 6.2 Ongoing development in digital fast-timing methods

### 6.2.1 The new fast-timing test stand

Ongoing developments in fast-timing techniques, particularly the digital fast timing method, are a focal point of future research at the fast-timing group of the IKP. To facilitate this, a specialized fast timing source test stand has been constructed in collaboration with the IKP's mechanical workshop. The test stand accommodates four LaBr detectors, allowing for flexible and precise angle between the detectors and distance to the source. The detectors are arranged radial around the source socket, which is in the focal point of all detectors. The source socket is interchangeable to accommodate different source geometries. The test stand ensures reproducibility and consistent results across different experiments. A CAD drawing of the test stand is given in Fig. 13.

### 6.2.2 Wave tracing and multiplicity filter for timing experiments

In recent developments, the main focus was on the implementation of life digital constant fraction discrimination (dCFD) within fast-sampling digitizers, although online implementations of life

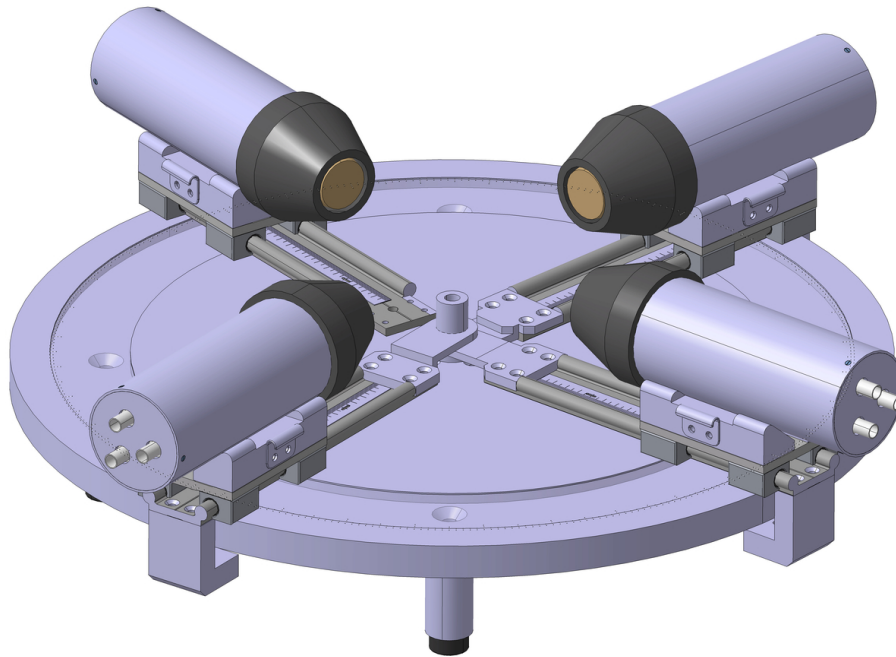


**Figure 13:** Fast-timing test stand for four LaBr detectors and a source socket.

dCFDs are typically less flexible and precise. We have achieved better performance by optimized and more complicated offline dCFDs applied to wave traced LaBr signals. However, tracing signals poses a challenge due to the significant increase in data required for the experiment. To address this issue, we plan to integrate a multiplicity filter into the setup, which is available in the new DAQ system of the IKP. This filter will selectively retain events based on a predefined multiplicity criterion, such as a minimum of 2 detectors firing in a defined time window. By implementing this filter, we can reduce the data size by approximately 90%, compensating for the increased amount of occupied data due to the storage of the wave traces. The benefits of this approach include enhanced control over the time stamp determination of LaBr detectors and the flexibility to adapt the dCFD or any other timestamp determination procedure as needed.

### 6.2.3 Machine learning and neural networks for timestamp determination

In the field of timestamp determination procedures, various methods have been developed and tested, including interpolated timing (like dCFD or interpolation of the whole signal with e.g. sinc algorithm [50]), ratio timing, centroid timing [50], and even machine learning filters using genetic algorithms [51] to enhance the timing information of a signal. While conventional CFD algorithms, such as dCFDs, have proven to be effective and reliable, there is room for exploring alternative approaches to enhance timing properties.

In recent years, there has been a significant increase in the application of artificial, digital neural

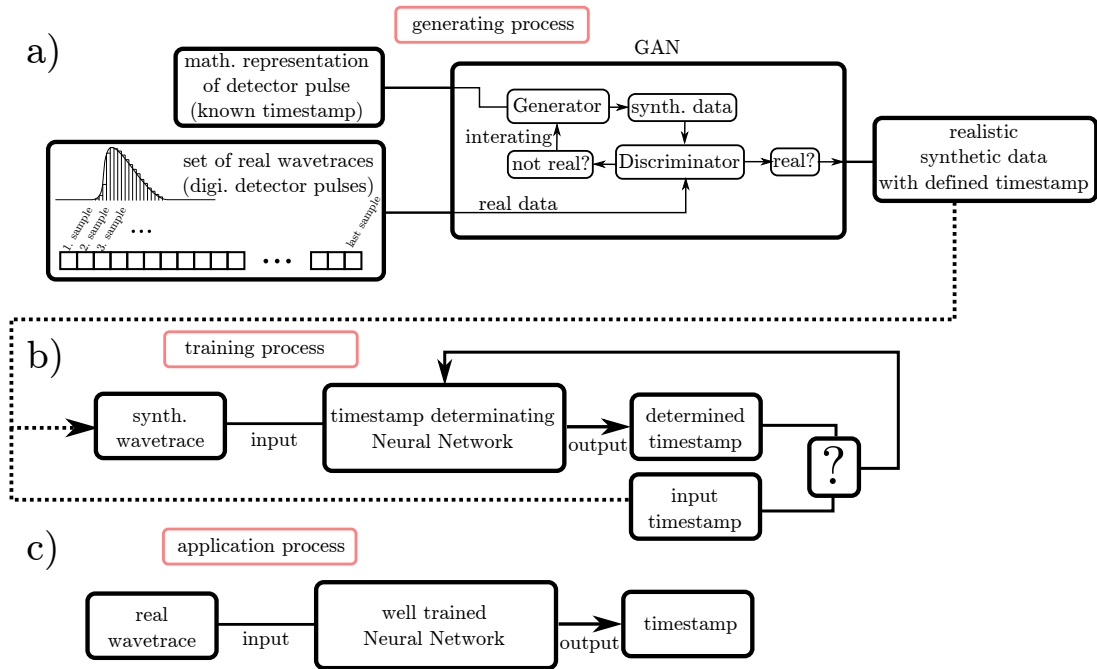


**Figure 14:** Schematic drawing of the generation of synthetic data (a), the training process of the timestamp determining neural network with synthetic data with well-defined timestamp (b) and the application of the well-trained neural network to real data (c).

networks [52] across various fields. Also in different disciplines of physics, deep learning and neural networks have gained significant importance. Our proposed idea involves utilizing neural networks and deep learning algorithms as described for example in Ref. [52], to analyze the overall signal shape and accurately determine the timestamp by the sample period and evaluation of the phase shift between the signal and the digitizer’s sampling period. This approach promises to determine the absolute timestamp of incoming signals with high precision.

To implement this idea, the first step is to establish a realistic mathematical description of the LaBr + PMT signal, commonly used in fast-timing experiments. This description can be obtained by adopting the methodology described for example in Ref. [50]. Once a mathematically represented signal and a training dataset of real data are available, the second step involves generating synthetic signals with precisely known properties (especially precisely known timestamp) to train the neural network, which has to determine the timestamp of the signal. This can be achieved using techniques outlined in Ref. [53], which employ e.g. Generative Adversarial Networks (GANs) to create synthetic data samples and rates their authenticity. By considering the rating of a discriminator, the synthetic waveform generator of the GAN can iteratively refine the generated data until it achieves a satisfactory level of authenticity.

With realistic synthetic data that possesses precisely known properties (including the timestamp) a neural network can be trained to recognize the timestamp of a signal based on its wavetrace. This approach holds promise for advancing the field of timestamp determination and improving

the overall performance of fast-timing experiments. A schematic drawing of the data generation and training process is illustrated in Fig. 14.

### 6.3 Future experiments using digital fast-timing and the Orange spectrometer

The recent developments and investigations in digital fast timing have proven to be highly rewarding. These advancements have led to significant time savings and reduced mistakes within the timing setups during experiment preparation. Several experiments utilizing the digital fast timing technique implemented in the scope of this work, have been successfully conducted, such as lifetime measurements in  $^{201,203}\text{Bi}$  [54] and  $^{207,210,213,214}\text{Rn}$ ,  $^{214}\text{Po}$ ,  $^{188,190}\text{Pt}$ ,  $^{92}\text{Mo}$ ,  $^{94}\text{Ru}$  and  $^{93}\text{Tc}$ , where most of the data are currently undergoing analysis or in a publication process. The forthcoming results are eagerly awaited. Additionally, there are plans to employ digital fast timing in future experiments. Especially, future studies should consider re-measuring the lifetimes of the low yrast states in  $^{172,174}\text{W}$  using modern methods to address the uncertainties associated with the  $2_1^+$  and  $4_1^+$  states in  $^{172}\text{W}$  and the  $6_1^+$  state in  $^{174}\text{W}$  to contribute to the improvement of the structural knowledge of the  $A = 180$  region [55–57].

As a testament to its effectiveness, the IKP fast-timing group has fully transitioned to utilizing digital fast timing techniques across its fast-timing endeavors. Even our partner research institutions as the ILL in Grenoble, recently applied the digitalization of the fast-timing technique at the Lohengrin [58] setup using CAEN V1730 digitizers and ft-soco, as developed in this work.

The Orange spectrometer, with its exceptional ability to detect high-energy conversion electrons with high resolution and efficiency, opens up possibilities for various experimental approaches. These include determining conversion coefficients, assigning multipolarities of transitions, confirming E0 transitions and  $\rho(\text{E0})$  determination, and conducting lifetime measurements for electron-gamma timing for strongly converted transitions or electron-triggered gamma-gamma timing. The most promising approaches are the investigations of shape coexistence in the neutron midshell surrounding tellurium ( $Z = 52$ ) isotopes: In the neutron mid-shell cadmium ( $Z = 48$ ) isotopes, strong experimental evidence supports the existence of shape coexistence in low lying excitation. Various observables, including level energy systematic, absolute transition strengths, and population in transfer reactions, provide support for this concept [59, 60]. Absolute E0 transitions play a significant role in studying shape coexistence, as the  $\rho^2(\text{E0})$  values [22] of transitions between spin-0 states are sensitive to changes in nuclear radius. Nuclei exhibiting shape coexistence often exhibit relatively large  $\rho^2(\text{E0})$  values. For instance, in  $^{112}\text{Cd}$ , a measurement yielded a relatively large value of  $34(9) \times 10^3 \rho^2(\text{E0})$  [22].

The mid-shell tellurium isotopes exhibit similarities to the mid-shell cadmium isotopes in various aspects. The low-lying level structures are remarkably similar, and the  $\text{B}(\text{E}2; 2_1^+ \rightarrow 0_1^+)$  systematic also show a strong resemblance. However, the study of tellurium isotopes is not as extensive

as that of cadmium isotopes, and the role of shape coexistence in tellurium isotopes remains unclear. One crucial missing piece of information is the  $\rho^2(\text{E}0)$  values between the  $0_2^+$  state and the ground state. Determining this value requires two experimental components: the lifetime of the  $0_2^+$  state and the  $X(\text{E}2/\text{E}0)$  ratio [22]. Tab. 6.1 shows the state-of-the-art of the already known and unknown E0 properties in the isotopes  $^{114,116,118,120,122}\text{Te}$ . It is known that the  $0_2^+$  states in

**Table 6.1:** State of the art which experimental observables to determine  $\rho^2(\text{E}0)$  values in mid-shell Te isotopes. The only known  $\rho^2(\text{E}0)$  value has an error of 90%. Data taken from Ref. [22, 61] and nuclear data sheets.

	$^{114}\text{Te}$	$^{116}\text{Te}$	$^{118}\text{Te}$	$^{120}\text{Te}$	$^{122}\text{Te}$
$E(0_2^+ \rightarrow 0_1^+)$ [keV]	1348	1059	957	1103	1357
$X(\text{E}2/\text{E}0)$	no	no	0.0070(6)	no	0.0123(12)
$\tau$ [ps]	no	<80(preliminary)	50(20)	no	up. limit
$10^3 \rho^2(\text{E}0)$	no	no	3.7(6)	no	up. limit

mid-shell Te isotopes are populated by  $\beta$ -decays from the iodine ( $Z = 53$ ) isobars. The energies of the E0 transitions all lie in an appropriate range to measure with the Orange spectrometer: the applied current lies in a range between 650 - 890 A. To explore these states, we therefore propose conducting pulsed beam experiments using the following reactions [62]:

- $^{106}\text{Cd}(^{10}\text{B},^2\text{n})^{114}\text{I}$ , alternative:  $^{106}\text{Cd}(^{11}\text{B},^3\text{n})^{114}\text{I}$
- $^{107}\text{Ag}(^{13}\text{C},^3\text{n})^{116}\text{I}$
- $^{108}\text{Cd}(^{13}\text{C},^3\text{n})^{118}\text{Xe}$
- $^{110}\text{Cd}(^{13}\text{C},^3\text{n})^{120}\text{Xe}$
- $^{112}\text{Cd}(^{13}\text{C},^3\text{n})^{122}\text{Xe}$

To ensure accurate data acquisition, the beam pulse lengths will be adjusted to match the half-life of the respective decays: the data will only be recorded in the off-beam periods. The experimental setup will involve coupling the Orange spectrometer with HPGe detectors to extract the  $X(\text{E}2/\text{E}0)$  ratio, and LaBr detectors will be used to measure the lifetimes of the  $0_2^+$  states. By implementing these approaches, we aim to obtain valuable insights into the characteristics of the  $0_2^+$  states in mid-shell Te isotopes, contributing to the current understanding of the shape coexistence phenomena in the neutron midshell tellurium isotopes.

# Bibliography

- [1] R. Casten. Nuclear Structure from a Simple Perspective. Oxford Science Publications. Oxford University Press, 2000.
- [2] K. S. Krane, D. Halliday, et al. Introductory nuclear physics. Vol. 465. Wiley New York, 1988.
- [3] P. Cejnar, J. Jolie and R. F. Casten. “Quantum phase transitions in the shapes of atomic nuclei.” *Rev. Mod. Phys.* 82 (2010), 2155–2212.
- [4] A. Schwarzschild. “A survey of the latest developments in delayed coincidence measurements.” *Nuclear Instruments and Methods* 21 (1963), 1–16.
- [5] H. Mach, R. Gill and M. Moszyński. “A method for picosecond lifetime measurements for neutron-rich nuclei: (1) Outline of the method.” *Nuclear Instruments and Methods in Physics Research Section A: Accelerators, Spectrometers, Detectors and Associated Equipment* 280.1 (1989), 49–72.
- [6] Z. Bay. “Calculation of Decay Times from Coincidence Experiments.” *Phys. Rev.* 77 (1950), 419–419.
- [7] T. J. Paulus. “Timing Electronics and Fast Timing Methods with Scintillation Detectors.” *IEEE Transactions on Nuclear Science* 32.3 (1985), 1242–1249.
- [8] J.-M. Régis, N. Saed-Samii, M. Rudigier, S. Ansari, M. Dannhoff, A. Esmaylzadeh, C. Fransen, R.-B. Gerst, J. Jolie, V. Karayonchev, C. Müller-Gatermann and S. Stegemann. “Reduced  $\gamma$ - $\gamma$  time walk to below 50 ps using the multiplexed-start and multiplexed-stop fast-timing technique with LaBr<sub>3</sub>(Ce) detectors.” *Nuclear Instruments and Methods in Physics Research Section A: Accelerators, Spectrometers, Detectors and Associated Equipment* 823 (2016), 72–82.
- [9] J.-M. Régis, M. Rudigier, J. Jolie, A. Blazhev, C. Fransen, G. Pascovici and N. Warr. “The time-walk of analog constant fraction discriminators using very fast scintillator detectors with linear and non-linear energy response.” *Nuclear Instruments and Methods in Physics Research Section A: Accelerators, Spectrometers, Detectors and Associated Equipment* 684 (2012), 36–45.
- [10] A. Harter, M. Weinert, L. Knafla, J.-M. Régis, A. Esmaylzadeh, M. Ley and J. Jolie. “Systematic investigation of time walk and time resolution characteristics of CAEN digitizers V1730 and V1751 for application to fast-timing lifetime measurement.” *Nuclear Instruments and Methods in Physics Research Section A: Accelerators, Spectrometers, Detectors and Associated Equipment* 1053 (2023), 168356.
- [11] L. Knafla, A. Harter, M. Ley, A. Esmaylzadeh, J.-M. Régis, D. Bittner, A. Blazhev, F. von Spee and J. Jolie. “Improving fast-timing time-walk calibration standards: Lifetime measurement of the 21+ state in 152Gd.” *Nuclear Instruments and Methods in Physics Research Section A: Accelerators, Spectrometers, Detectors and Associated Equipment* 1052 (2023), 168279.
- [12] D. Gedcke and W. McDonald. “Design of the constant fraction of pulse height trigger for optimum time resolution.” *Nuclear Instruments and Methods* 58.2 (1968), 253–260.



- [13] J.-M. Régis, G. Pascovici, J. Jolie and M. Rudigier. “The mirror symmetric centroid difference method for picosecond lifetime measurements via  $\gamma$ - $\gamma$  coincidences using very fast LaBr<sub>3</sub>(Ce) scintillator detectors.” *Nuclear Instruments and Methods in Physics Research Section A: Accelerators, Spectrometers, Detectors and Associated Equipment* 622.1 (2010), 83–92.
- [14] J.-M. Régis, H. Mach, G. Simpson, J. Jolie, G. Pascovici, N. Saed-Samii, N. Warr, A. Bruce, J. Degenkolb, L. Fraile, C. Fransen, D. Ghita, S. Kisyov, U. Koester, A. Korgul, S. Lalkovski, N. Mărginean, P. Mutti, B. Olaizola, Z. Podolyak, P. Regan, O. Roberts, M. Rudigier, L. Stroe, W. Urban and D. Wilmsen. “The generalized centroid difference method for picosecond sensitive determination of lifetimes of nuclear excited states using large fast-timing arrays.” *Nuclear Instruments and Methods in Physics Research Section A: Accelerators, Spectrometers, Detectors and Associated Equipment* 726 (2013), 191–202.
- [15] J.-M. Régis, M. Dannhoff and J. Jolie. “A simple procedure for  $\gamma$ - $\gamma$  lifetime measurements using multi-element fast-timing arrays.” *Nuclear Instruments and Methods in Physics Research Section A: Accelerators, Spectrometers, Detectors and Associated Equipment* 897 (2018), 38–46.
- [16] X. Li, B. Yang, X. Xie, D. Li and L. Xu. “Influence of Waveform Characteristics on LiDAR Ranging Accuracy and Precision.” *Sensors* 18.4 (2018).
- [17] A. Harter and N. Saed-Samii. ftSOCO - Fast timing Sorting Code. Version 1.0. 29, 2022.
- [18] N. Saed-Samii and A. Harter. SOCO-v2 - Sorting Code Cologe. Version 1.0. 29, 2019.
- [19] S. p. A. CAEN. User Manual UM5960 CoMPASS. 2022 [Online]. 2022.
- [20] S. p. A. CAEN. User Manual UM2792 V1730/VX1730 and V1725/VX1725. 2021 [Online]. 2021.
- [21] P. Mutti, F. Cecillon, A. Elaazzouzi, Y. Le Goc, J. Locatelli, H. Ortiz and J. Ratel. “Nomad more than a simple sequencer.” *Proc. ICALEPCS*. 2011.
- [22] T. Kibédi and R. Spear. “Electric monopole transitions between  $0^+$  states for nuclei throughout the periodic table.” *At. Data. Nucl. Data Tables* 89.1 (2005), 77–100.
- [23] E. Church and J. Weneser. “Nuclear structure effects in internal conversion.” *Annual review of nuclear science* 10.1 (1960), 193–234.
- [24] O. Kofoed-Hansen, J. Lindhard and O. B. Nielsen. *Mat. Fys. Medd. Dan. Vid. Selsk.* 25.16 (1950).
- [25] E. Moll. Diplomarbeit. Technische Hochschule München, 1961.
- [26] W. Neumann, L. Cleemann, J. Eberth, N. Wiehl and V. Zobel. *Nuclear Instruments and Methods* 164.3 (1979), 539–545.
- [27] G. L. Bianco, P. Paruzzi, K. Schmittgen, R. Reinhardt, A. Gelberg, K. Zell and P. V. Brentano. *Nuclear Physics A* 470.2 (1987), 266–284.
- [28] M. Rudigier, K. Nomura, M. Dannhoff, R.-B. Gerst, J. Jolie, N. Saed-Samii, S. Stegemann, J.-M. Régis, L. M. Robledo, R. Rodríguez-Guzmán, A. Blazhev, C. Fransen, N. Warr and K. O. Zell. *Phys. Rev. C* 91 (2015), 044301.
- [29] J.-M. Régis, T. Materna, S. Christen, C. Bernards, N. Braun, G. Breuer, C. Fransen, S. Heinze, J. Jolie, T. Meersschaut, G. Pascovici, M. Rudigier, L. Steinert, S. Thiel, N. Warr and K. Zell. *Nucl. Instrum. Meth. Phys. Res. A* 606 (2009), 466.

- [30] J.-M. Régis. Diplomarbeit. Universität zu Köln, 2007.
- [31] T. Kibédi, T. Burrows, M. B. Trzhaskovskaya, P. M. Davidson and C. W. Nestor Jr. *Nucl. Instr. Meth. Phys. Res. A* 589.2 (2008), 202–229.
- [32] G. Soff, J. Reinhardt, B. Müller and W. Greiner. *Phys. Rev. Lett.* 43.17 (1979), 1981–1984.
- [33] A. Harter. “Entwicklung der Steuerungssoftware des Orange-Konversionselektronenspektrometers.” MA thesis. 2018.
- [34] Arduino. <https://www.arduino.cc/>. Accessed: May 23, 2023.
- [35] A. Harter. NewOrange. Version 1.2. 23, 2023.
- [36] D. Burch, P. Russo, H. Swanson and E. Adelberger. “Lifetime of the first excited state in  $^{96}\text{Zr}$ .” *Physics Letters B* 40.3 (1972), 357–359.
- [37] R. Casten and N. Zamfir. *J. Phys. G* 22 (1999), 1521.
- [38] A. Bohr and B. Mottelson. “Report of the International Physics Conference, Copenhagen, June, 1952; Kgl.” *Danske Vid. Selsk. Mat. Fys. Medd* 27 (1953), 16.
- [39] A. N. Bohr and B. R. Mottelson. Collective nuclear motion and the unified model. Tech. rep. 1955.
- [40] G. Gneuss and W. Greiner. “Collective potential energy surfaces and nuclear structure.” *Nuclear Physics A* 171.3 (1971), 449–479.
- [41] A. Arima and F. Iachello. “The interacting boson model.” *Annual Review of Nuclear and Particle Science* 31.1 (1981), 75–105.
- [42] A. Arima and F. Iachello. “Collective Nuclear States as Representations of a  $\text{SU}(6)$  Group.” *Phys. Rev. Lett.* 35 (1975), 1069–1072.
- [43] F. Iachello. “Electron scattering in the interacting boson model.” *Nucl. Phys. A* 358 (1981), 89–112.
- [44] F. Iachello and A. Arima. The Interacting Boson Model. Cambridge Monographs on Mathematical Physics. Cambridge University Press, 1987.
- [45] F. Iachello and A. Arima. “Boson symmetries in vibrational nuclei.” *Phys. Lett. B* 53.4 (1974), 309–312.
- [46] R. Casten and E. McCutchan. “Quantum phase transitions and structural evolution in nuclei.” *Journal of Physics G: Nuclear and Particle Physics* 34.7 (2007), R285.
- [47] F. Iachello. “Dynamic Symmetries at the Critical Point.” *Phys. Rev. Lett.* 85 (2000), 3580–3583.
- [48] F. Iachello. “Analytic Description of Critical Point Nuclei in a Spherical-Axially Deformed Shape Phase Transition.” *Phys. Rev. Lett.* 87 (2001), 052502.
- [49] G. P. S. Sahota, H. Singh, H. S. Binarh, B. S. Pallah and H. S. Sahota. “Sum Peak Comparison Measurement of K-Capture Probabilities to the Levels of  $^{133}\text{Cs}$ .” *J. Phys. Soc. Jpn.* 61 (1992), 3518.
- [50] W. K. Warburton and W. Hennig. “New Algorithms for Improved Digital Pulse Arrival Timing With Sub-GSps ADCs.” *IEEE Transactions on Nuclear Science* 64.12 (2017), 2938–2950.

- [51] V. Sanchez-Tembleque, V. Vedia, L. Fraile, S. Ritt and J. Udias. “Optimizing time-pickup algorithms in radiation detectors with a genetic algorithm.” *Nuclear Instruments and Methods in Physics Research Section A: Accelerators, Spectrometers, Detectors and Associated Equipment* 927 (2019), 54–62.
- [52] C. M. Bishop. *Neural Networks and their Applications*. Prentice Hall, 1995.
- [53] S. I. Nikolenko. “Synthetic Data for Deep Learning.” *CoRR* abs/1909.11512 (2019).
- [54] D. Bittner. Masterarbeit. University of Cologne, Institut für Kernphysik, 2023.
- [55] A. Harter, L. Knafla, G. Frießner, G. Häfner, J. Jolie, A. Blazhev, A. Dewald, F. Dunkel, A. Esmaylzadeh, C. Fransen, V. Karayonchev, K. Lawless, M. Ley, J.-M. Régis and K. O. Zell. “Lifetime measurements in the tungsten isotopes  $^{176,178,180}\text{W}$ .” *Phys. Rev. C* 106 (2022), 024326.
- [56] B. Singh. *Nuclear Data Sheets* 75.2 (1995), 199–376.
- [57] M. Minor. *Nuclear Data Sheets* 10 (1973), 515–552.
- [58] P. Armbruster, M. Asghar, J. Bocquet, R. Decker, H. Ewald, J. Greif, E. Moll, B. Pfeiffer, H. Schrader, F. Schussler, G. Siegert and H. Wollnik. “The recoil separator Lohengrin: Performance and special features for experiments.” *Nuclear Instruments and Methods* 139 (1976), 213–222.
- [59] P. E. Garrett, T. R. Rodríguez, A. Diaz Varela, K. L. Green, J. Bangay, A. Finlay, R. A. E. Austin, G. C. Ball, D. S. Bandyopadhyay, V. Bildstein, S. Colosimo, D. S. Cross, G. A. Demand, P. Finlay, A. B. Garnsworthy, G. F. Grinyer, G. Hackman, B. Jigmeddorj, J. Jolie, W. D. Kulp, K. G. Leach, A. C. Morton, J. N. Orce, C. J. Pearson, A. A. Phillips, A. J. Radich, E. T. Rand, M. A. Schumaker, C. E. Svensson, C. Sumithrarachchi, S. Triambak, N. Warr, J. Wong, J. L. Wood and S. W. Yates. “Shape coexistence and multiparticle-multihole structures in  $^{110,112}\text{Cd}$ .” *Phys. Rev. C* 101 (2020), 044302.
- [60] P. E. Garrett, T. R. Rodríguez, A. D. Varela, K. L. Green, J. Bangay, A. Finlay, R. A. E. Austin, G. C. Ball, D. S. Bandyopadhyay, V. Bildstein, S. Colosimo, D. S. Cross, G. A. Demand, P. Finlay, A. B. Garnsworthy, G. F. Grinyer, G. Hackman, B. Jigmeddorj, J. Jolie, W. D. Kulp, K. G. Leach, A. C. Morton, J. N. Orce, C. J. Pearson, A. A. Phillips, A. J. Radich, E. T. Rand, M. A. Schumaker, C. E. Svensson, C. Sumithrarachchi, S. Triambak, N. Warr, J. Wong, J. L. Wood and S. W. Yates. “Multiple Shape Coexistence in  $^{110,112}\text{Cd}$ .” *Phys. Rev. Lett.* 123 (2019), 142502.
- [61] A. Giannatiempo, A. Nannini, A. Perego and P. Sona. “Electric monopole transitions in  $^{122}\text{Te}$ .” *Phys. Rev. C* 36 (1987), 2528–2532.
- [62] F. v. Spee. Private communication. 2023.
- [63] A. Harter. OrangeAnalyse. Version 1.0. 6, 2023.

# 7 | Appendix

## 7.1 Elements of the graphical user interface of the software NewOrange

### 7.1.1 Main window

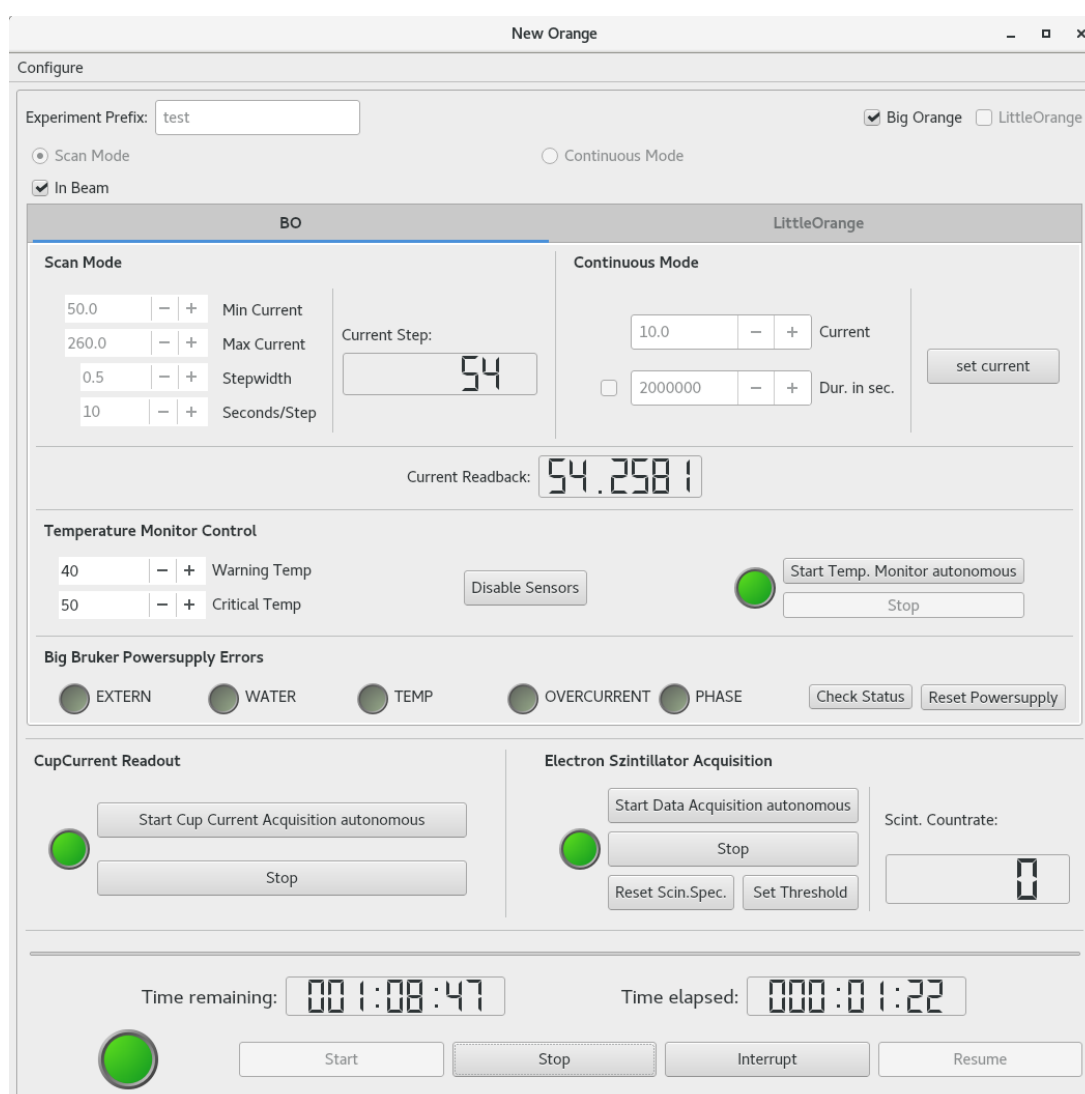


**Figure 15:** The main window of the software NewOrange during the operation of a conversion electron scan. The single control elements are labeled. The status LEDs indicate the states of the different sub-processes like temperature monitoring, cup current monitoring or scintillator count rate.

### 7.1.2 Orange current display

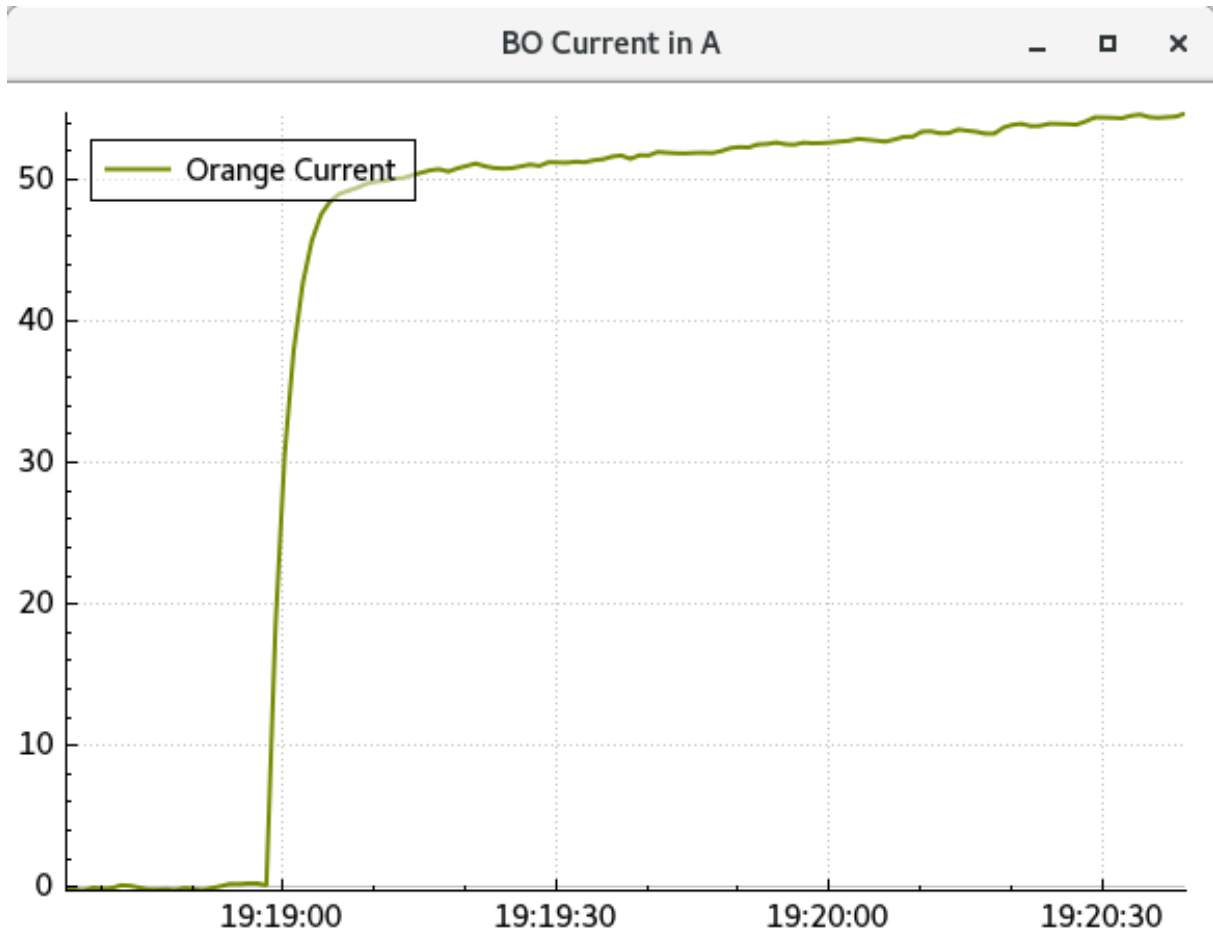


**Figure 16:** The monitoring window for the current applied to the Orange spectrometer. Here, the Orange spectrometer is running in a scan mode: the current successively rises.

### 7.1.3 Temperature monitoring

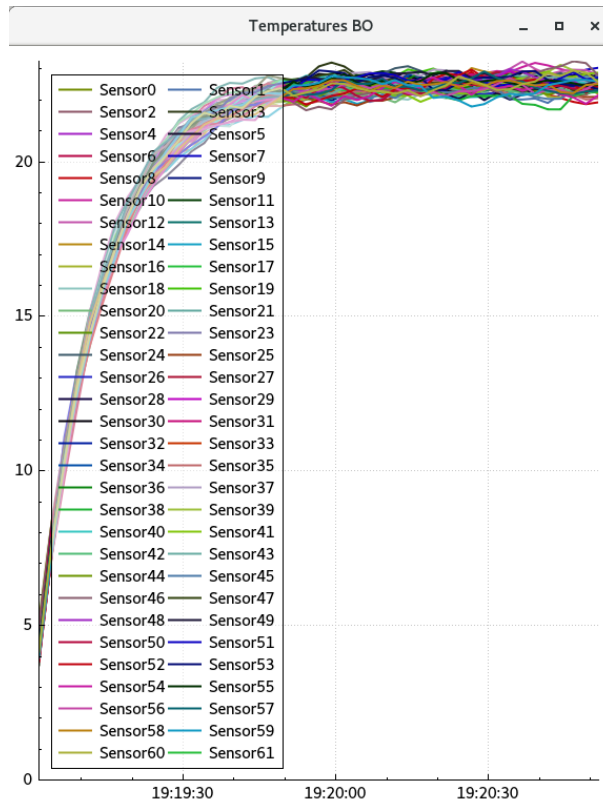


**Figure 17:** The monitoring window for the temperatures of the coils in overview mode.

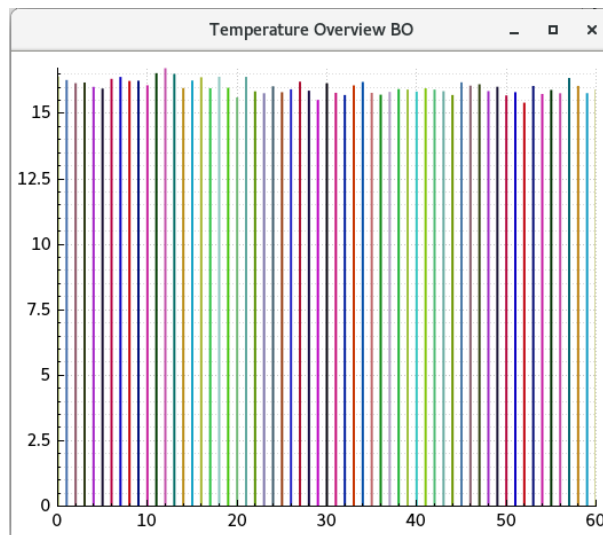


**Figure 18:** The monitoring window for the temperatures of the single coils in detailed mode. The x-axis represents the sensor number.

### 7.1.4 Cup current monitoring

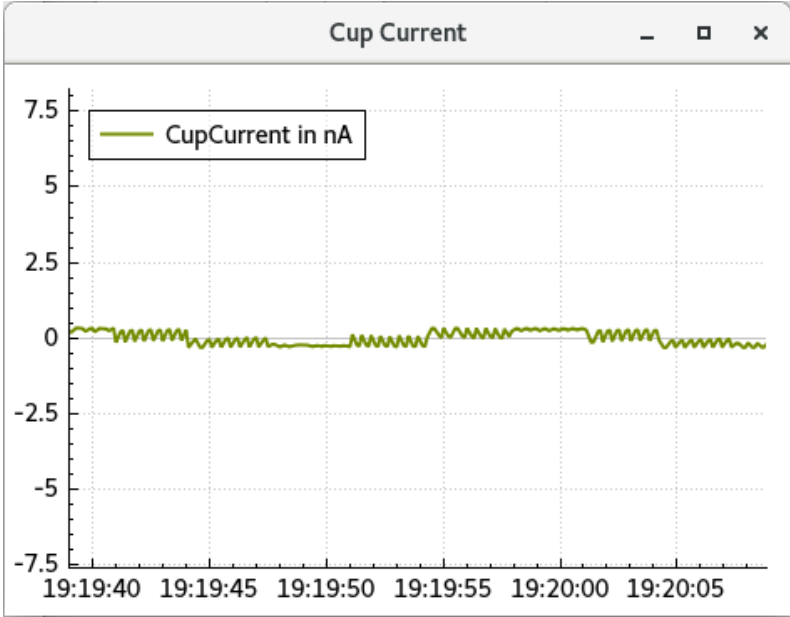


Figure 19: The monitoring window for the cup current.



## 7.2 Useful tools for the Orange analysis

To simplify the preparation of Orange experiments and the analysis of Orange conversion electron scan data, some useful software tools have been placed in the OrangeAnalyse repository in the version control system gitlab of the IKP [63].

### 7.2.1 Calibration of the Orange magnetic field

The magnetic field of the Orange spectrometer, which corresponds to the applied current, has to be calibrated to the residual energy the electrons. The script `calB_rho.py` calculates a linear calibration according to Eq. 1.8 and 1.10 based on two peak positions in a conversion electron spectrum (like Fig. 5) and corresponding residual energies of electrons. A well known electron spectrum is required. Figure 20 shows the usage and output of the `calB_rho.py` script. The output of the script are the parameters  $a$  and  $b$  of the linear calibration.

```
[aharter@analyse orangeanalyse]$ cat peak.lst
161.5 92.59
557.5 714.8
[aharter@analyse orangeanalyse]$ ./calB_rho.py
Stroeme:
161.5
557.5

Restenergien(Elektron):
92.59
714.8

B_rho:
1070.8225508507146
3714.027136027452
a_poly = 0.14981814204651192 , b_poly = 1.0713549700394114
a = 0.14981814204651192 , b = 1.0713549700394083
[aharter@analyse orangeanalyse]$
```

Figure 20: Input file `peak.lst` and output of the `calB_rho.py` script.

### 7.2.2 Calculation of Orange current and electron residual energy

After the calibration of the Orange magnetic field, Orange currents and electron residual energies can be converted into each other. To do so, two little scripts are placed in the OrangeAnalyse repository: `I_element.pl` converts a given Orange current into the corresponding residual energy and makes suggestions of possible transitions based on the element, which is given as input by the user. `E_element.pl` does the same thing but in reverse. The calibration parameters extracted from `calB_rho.py` have to be placed in the file as the variables  $a$  and  $b$ . Figure 21 shows the usage and output of both scripts.

```

[aharter@analyse orangeanalyse]$ vim E_element.pl
[aharter@analyse orangeanalyse]$ ./I_element.pl
This scripts prints the orange current depending on the paramenters a and b from script calB_rho.py.

Which element (symbol e.g. W for tungsten)?
Te

Which transition energy [keV] in Te?
957
B_rho_K = 4474.00165857785 [Gcm], Ekin= 925.186 [keV], I=671.357970971186 [A]
B_rho_L1 = 4569.73027875525 [Gcm], Ekin= 952.061 [keV], I=685.699854986839 [A]
B_rho_L2 = 4570.89351698954 [Gcm], Ekin= 952.388 [keV], I=685.874129177859 [A]
B_rho_L3 = 4571.8575188763 [Gcm], Ekin= 952.659 [keV], I=686.018554149462 [A]
B_rho_M1 = 4583.71876568847 [Gcm], Ekin= 955.994 [keV], I=687.795584109217 [A]
B_rho_M2 = 4584.19953871416 [Gcm], Ekin= 956.1292 [keV], I=687.867612630672 [A]
for transition energy = 957 keV in Te.
[aharter@analyse orangeanalyse]$ ./E_element.pl
This scripts prints the residual energy depending on the paramenters a and b from script calB_rho.py.

Welches Element(Symbol)?
Te

Welche Stromstaerke ([A]) bei Te?
671
Konversions-Restenergie = 924.515851137666 keV,
mögliche. Übergangsenergien ([keV]) im Te sind:
956.329851137666 (K),
929.454851137666 (L1),
929.127851137666 (L2),
928.856851137666 (L3),
925.521851137666 (M1),
925.386651137666 (M2),
925.335851137666 (M3), u.s.w.

```

Figure 21: Usage and output of I\_element.pl and E\_element.pl.

### 7.2.3 Creation of an Orange conversion electron spectrum and heatmap

When the software `NewOrange` runs in scan mode, an scintillator spectrum is written to the hard drive for every  $N$  current steps of the scan range. In case of an in-beam experiment, a file containing  $N$  charge values is written to the hard drive based on the number of current steps and the accumulated beam charge measured by the Faraday cup at the end of the beamline during each step of the scan. These values are needed for the normalization of the number of the counted electrons per each scan step to the fluctuating beam intensity during this step. Of course this is only needed under in-beam conditions and not for a source measurement.

The algorithm, that generates the conversion electron spectrum, implemented in the script `create_ospec.py`, performs integration over the channel range corresponding to the presence of conversion electrons in each scintillator spectrum. However, the channel range differs between the single scintillator spectra because of the different energies of the electrons counted in the scintillator. The script provides the options of a constant window, a linear sliding window and a quadratic sliding window to address the step-wise shift of the electron peaks throughout the single scintillator spectra. The options of the script `create_ospec.py` are displayed in Lst. 7.1. In the constant window option (-c), only a left and a right integration limit are requested. In the linear sliding window option (-l), a first and a second current step and corresponding left and right integration limits are requested by the script, to calculate the linear sliding integration limits for each scintillator spectrum. In the quadratic sliding window option (-q), additional third

**Listing 7.1:** Usage and help message of the script `create4_ospec.py`.

```
1 [aharter@analyse ScintSpecs]$ create\_ospec.py -h
2 usage: create_ospec.py [-h] [-c LEFT RIGHT]
3                       [-l FIRST SECOND LEFT1 RIGHT1 LEFT2 RIGHT2]
4                       [-n FIRST SECOND LEFT1 RIGHT1 LEFT2 RIGHT2]
5                       [-q QUADRATIC QUADRATIC QUADRATIC QUADRATIC QUADRATIC
6                       QUADRATIC QUADRATIC QUADRATIC QUADRATIC]
6 optional arguments:
7   -h, --help            show this help message and exit
8   -c LEFT RIGHT, --constant LEFT RIGHT
9                       set a constant integration window: [first] [last]
10  -l FIRST SECOND LEFT1 RIGHT1 LEFT2 RIGHT2, --linear FIRST SECOND LEFT1 RIGHT1
11  LEFT2 RIGHT2
12                       set a linear sliding window [first current] [second
13  current] [left1] [right1] [left2] [right2]
14  -n FIRST SECOND LEFT1 RIGHT1 LEFT2 RIGHT2, --linear-normalized FIRST SECOND
15  LEFT1 RIGHT1 LEFT2 RIGHT2
16                       set a linear sliding window [first current] [second
17  current] [left1] [right1] [left2] [right2],
18  normalizing the spectrum to the charges given in
19  cup_charges.dat
20  -q FIRST SECOND THIRD LEFT1 RIGHT1 LEFT2 RIGHT2 LEFT3 RIGHT3, --quadratic
21  FIRST SECOND THIRD LEFT1 RIGHT1 LEFT2 RIGHT2 LEFT3 RIGHT3
22                       set a quadratic sliding window [first current] [second
23  current] [third current]
24  [left1] [right1] [left2] [right2] [left3] [right3]
```

current step and integration limits are requested to calculate the quadratic sliding integration limits for each scintillator spectrum.

Additionally to the `create_ospec.py` script, a script `heatmap.py` was written, which produces a heatmap of the plane 'channel of the scintillator spectrum  $\times$  Orange current [A]'. Figure 22 shows the connection between the individual scintillator spectra emerging from each current step during the Orange scan, the conversion electron spectrum and the heatmap. In the heatmap, three different integration window methods are illustrated: the dashed light-blue limits indicate the integration of the scintillator spectra as a whole including the low amplitude noise, the dashed green limits indicate the same but without the low amplitude noise, and the purple limits indicate the linear sliding window with an increasing integration interval. On the right, the corresponding conversion electron spectra as generated from the individual scintillator spectra using the `create_ospec.py` script are depicted.

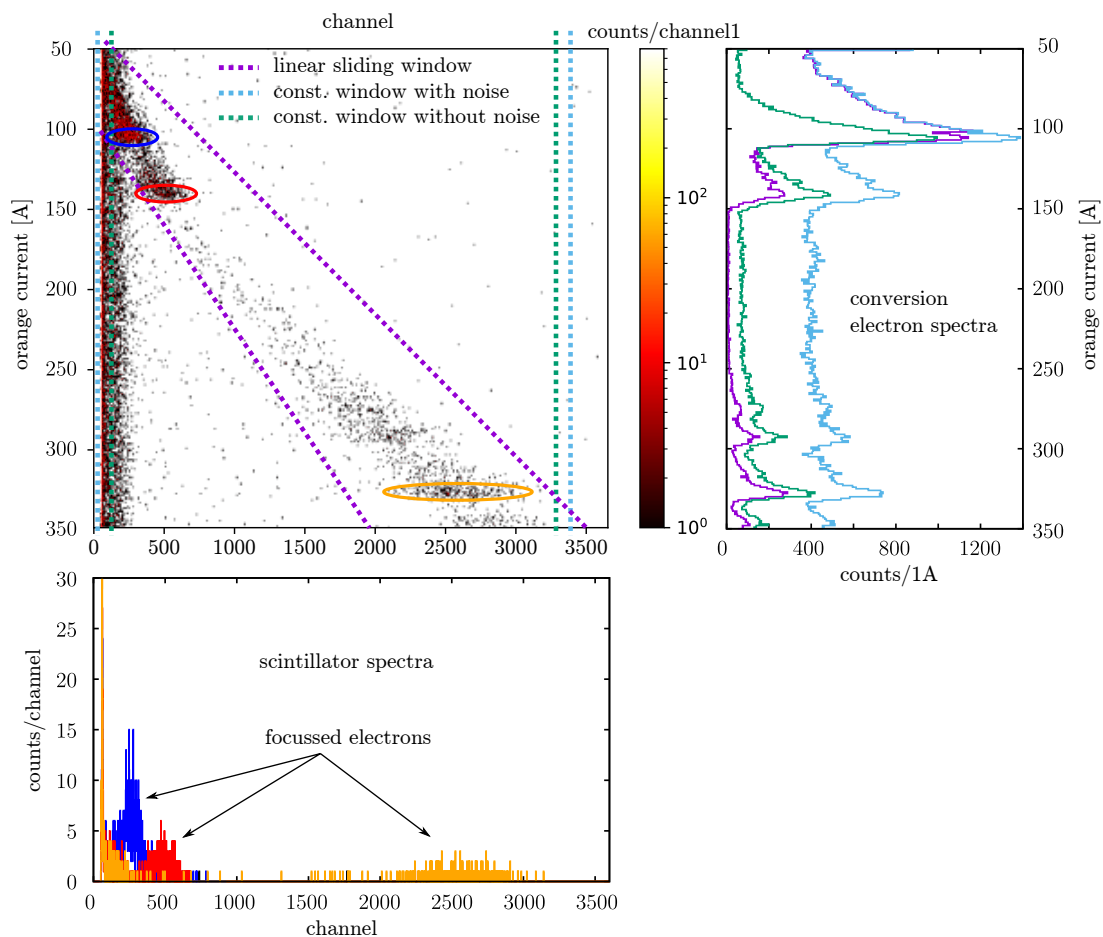


**Figure 22:** The connection between the individual scintillator spectra of each current step from the scan, the conversion electron spectra generated by `create_ospec.py` and the heatmap generated by `heatmap.py`. In the heatmap, the colored integration limits correspond to the conversion electron spectra on the right. The colors of the scintillator spectra (bottom) correspond to the marked areas in the heatmap.

## 7.3 Setup of the CAEN data acquisitions system to a fast-timing experiment

This manual provides instructions for setting up the data acquisition system for a fast timing setup. For a general setup of the CAEN DAQ system of the IKP, please refer the dedicated Manual for the new DAQ system of the IKP.

This short manual addresses the following questions:

- Is the cabling done correctly?
- Is the firmware set up correctly?
- Is the PLL lock checked?
- How to setup the BGOs?

### Cable Setup

Ensure proper cable connections:

- Optical daisy chain: Connect the optical cable coming from the server to the lower port of the leftmost board. Continue daisy chaining to the next board, always connecting from the upper to the lower optical port.
- Clock cable: Connect the clock cable from left (clock-out) to right (clock-in).
- Trigger cable: Connect the trigger cable from left (trig-out) to right (trig-in).

### Firmware Check

- Verify the firmware version.
- Check the settings for PSD/PHA (Pulse Shape Discrimination/Pulse Height Analysis).
- Ensure that the PUC (Product Upgrade Code) license is installed. Note that PHA does not require PUC, while PSD does.
- Use the CAENUpgraderGUI for firmware installation:
  - Select "Install Firmware" -> Choose the board -> Optical Link -> Select the desired optical link (0,X) -> Install.

### PUC Installation

- Use the CAENUpgraderGUI to install the PUC:
  - Select "Store PUC on board" -> Find the appropriate PUC in the PUCs file -> Optical Link -> Select the desired optical link.

## PLL File Installation

- Use the CAENUpgraderGUI to store the PLL file on the board:
  - Select "Store PLL file on board" -> Find the correct PLL file -> Optical Link -> Select the desired optical link.

## PLL Lock Check

- Check the status light on the digitizer to ensure it is on.
- Verify the correct PLL file is installed:
  - For configuration with v1782 as master and v1730 as slave: Set the PLL frequency range from 50.0 to 62.5.
  - For configuration with v1782 as master and v1782 as slave: Set the PLL frequency range to 50.0.

## BGO Setup

### Cable Check

- Verify the cabling in the DAQ: Ensure that the LaBr detectors in the DAQ correspond to the correct BGO shield.

### Logical BGO CFD Signal Connection

- Connect the logical BGO CFD signal and perform the following steps:
  - Check the voltage level on the scope to ensure it is 1V positive.
  - Plug the logical BGO CFD signal into the NIM-to-TTL converter (black box). Put the scope in 2-channel mode and check, if the BGO and corresponding LaBr signals are within a 1  $\mu$ s range. Adjust the delay screw of the NUM-to-TTL converter, that both signals are as close as possible. first the LaBr and usually some 100 ns later the BGO signal.
  - Connect the TTL outputs from the NIM-to-TTL converter to the TTL-to-LVDS converter (red NIM box with wide band cable output).
  - Note: The BGO vetos from the LVDS converter occupy two DAQ channels each. For example, the veto from LVDS channel 0 is for DAQ channels 0 and 1, LVDS ch. 1 is for DAQ channels 2 and 3, LVDS ch. 2 is for DAQ ch. 4 and 5, and so on.
  - Plug the blue wide band cable from the LVDS converter into the LVDS input of the v1730 module used for the LaBr detectors with BGO shields.

## Configuration Files

- Locate the FreeWritesFiles on the acquisition server (e.g., on darkwing they are in the home directory of the user experiment under FreeWritesFiles/v1730/LVDSvetosFT.txt).
- In these files, you can set the shaped trigger window register ( $x1n70$ , where  $n$  corresponds to a DAQ channel).
- The delay range value is given in hexadecimal values in multiples of 8ns, corresponding to the clock reference speed of 62.5MHz.
- A recommended delay value is 400ns for the trigger window, but the value has to be adjusted to the delay between the LaBr signal and the BGO signal from Sec. 7.3.





# List of Figures

1	The principles of the fast-timing methods. The dashed blue distribution represents the PRF and $C_P$ is the centroid position of the PRF. The shifted distribution is obtained when the lifetime of the state under investigation is in the range of the resolution of the PRF. The lifetime $\tau$ is found in the delayed shift of the centroid of the time-difference distribution $C_D$ . The exponential slope is obtained when the lifetime is greater than the resolution of the PRF. The straight line fit to the exponential part of the slope to extract the lifetime is shown in red. The right half of the figure shows the simple centroid shift approach of the fast-timing analysis. The right and pale left part together illustrate the centroid difference method. The doubled time walk is the prompt response difference, also known as PRD. . . . .	5
2	The schematic drawing depicts the differences between a digital and an analogue fast-timing setup using two $\text{LaBr}_3(\text{Ce})$ detectors. The components that are exclusively utilized in an analogue setup are illustrated in a grey shade . . . . .	7
3	Total conversion coefficients in dependency of $E_\gamma$ , multipolarity of transition with $\sigma L = \text{E1-5}$ and $Z = 20, 50, 90$ . The lowest line of each color belong to the E1 transitions and the others increase up to E5 transition. The plot looks similar for magnetic multipoles. The lines are meant to guide the eyes. Data is taken from Ref. [31]. . . . .	14
4	Electron trajectories with different entrance angles. Figure taken from Ref. [30]. .	15
5	Conversion electron spectrum of $^{180}\text{W}$ as measured with the Orange spectrometer of the IKP. Conversion electron peaks of low yrast transitions and the $\delta$ -electron background are indicated. . . . .	16
6	Schematic representation of the current Orange setup of the IKP. Thin solid lines represent digital input/output streams, dashed lines represent analogue data streams.	17
7	On top: Front panel of the 19" rack enclosure. Middle: Back panel of the 19" rack enclosure. Bottom: Internal structure and connections of the 19" rack enclosure. .	18
8	a) $\gamma$ -ray spectrum between E0 transition $0_2^+ \rightarrow 0^+1$ and coincident $\gamma$ -rays. No background subtraction was applied. The transitions in coincidence with the conversion electron decay are indicated. b) Level scheme corresponding to the coincidence spectrum. The widths of the arrows indicate the relative ratio between the transitions. c) Scintillator spectrum of the electron counter in coincidence with $\gamma$ -ray spectrum in (a) at an Orange current of 563 A. d) Time-difference distribution between conversion electrons of the E0 transition $0_2^+ \rightarrow 0_1^+$ with 743.8 keV. The lifetime amounts to $\tau = 31.4(7)$ ns. e) Conversion electron spectrum obtained from a scan of the current range 110 A to 600 A. Note the logarithmic scaling of the y-axis in the low-energy range. The $\delta$ -electron background shows a perfect exponential decay. . . . .	20

9	a) The Casten triangle with indicated $U(5)$ , $SU(3)$ and $O(6)$ symmetries and critical point symmetries $X(5)$ and $E(5)$ [1]. b) Level spacing, $R_{4/2}$ and $B_{4/2}$ signatures of each symmetry. . . . .	24
10	Proposed water cooling system for the Bruker power supply. . . . .	72
11	Left: CAD drawing of the proposed source frame for the calibration source of the Orange spectrometer. Right: Schematic drawing of the new, proposed (top) and the old, ill-suited (bottom) source frame. . . . .	73
12	Left: Side view of the new honeycomb shaped detector mount frame, taken over by the Cologne Plunger setup. Right: Schematic top view of the Orange spectrometer in combination with the new detector mount frame. . . . .	74
13	Fast-timing test stand for four LaBr detectors and a source socket. . . . .	75
14	Schematic drawing of the generation of synthetic data (a), the training process of the timestamp determining neural network with synthetic data with well-defined timestamp (b) and the application of the well-trained neural network to real data (c). . . . .	76
15	The main window of the software <b>NewOrange</b> during the operation of a conversion electron scan. The single control elements are labeled. The status LEDs indicate the states of the different sub-processes like temperature monitoring, cup current monitoring or scintillator count rate. . . . .	83
16	The monitoring window for the current applied to the Orange spectrometer. Here, the Orange spectrometer is running in a scan mode: the current successively rises. . . . .	84
17	The monitoring window for the temperatures of the coils in overview mode. . . . .	85
18	The monitoring window for the temperatures of the single coils in detailed mode. The x-axis represents the sensor number. . . . .	85
19	The monitoring window for the cup current. . . . .	86
20	Input file <code>peak.lst</code> and output of the <code>calB_rho.py</code> script. . . . .	87
21	Usage and output of <code>I_element.pl</code> and <code>E_element.pl</code> . . . . .	88
22	The connection between the individual scintillator spectra of each current step from the scan, the conversion electron spectra generated by <code>create_ospec.py</code> and the heatmap generated by <code>heatmap.py</code> . In the heatmap, the colored integration limits correspond to the conversion electron spectra on the right. The colors of the scintillator spectra (bottom) correspond to the marked areas in the heatmap. . . . .	90

# List of publications

## Publications in refereed journals

- [1] A. Esmaylzadeh, V. Karayonchev, K. Nomura, J. Jolie, M. Beckers, A. Blazhev, A. Dewald, C. Fransen, R.-B. Gerst, G. Häfner, A. Harter, L. Knafla, M. Ley, L. M. Robledo, R. Rodríguez-Guzmán and M. Rudigier.  
**Lifetime measurements to investigate  $\gamma$  softness and shape coexistence in  $^{102}\text{Mo}$ .**  
*Phys. Rev. C* 104 (2021), 064314.
- [2] A. Harter, L. Knafla, G. Frießner, G. Häfner, J. Jolie, A. Blazhev, A. Dewald, F. Dunkel, A. Esmaylzadeh, C. Fransen, V. Karayonchev, K. Lawless, M. Ley, J.-M. Régis and K. O. Zell.  
**Lifetime measurements in the tungsten isotopes  $^{176,178,180}\text{W}$ .**  
*Phys. Rev. C* 106 (2022), 024326.
- [3] A. Esmaylzadeh, A. Blazhev, K. Nomura, J. Jolie, M. Beckers, C. Fransen, R.-B. Gerst, A. Harter, V. Karayonchev, L. Knafla, M. Ley and F. von Spee.  
**Investigation of  $\gamma$  softness: Lifetime measurements in  $^{104,106}\text{Ru}$ .**  
*Phys. Rev. C* 106 (2022), 064323.
- [4] L. Knafla, A. Esmaylzadeh, A. Harter, J. Jolie, U. Köster, M. Ley, C. Michelagnoli and J.-M. Régis.  
**Development of a new  $\gamma$ - $\gamma$  angular correlation analysis method using a symmetric ring of clover detectors.**  
*Nuclear Instruments and Methods in Physics Research Section A: Accelerators, Spectrometers, Detectors and Associated Equipment* 1042 (2022), 167463.
- [5] L. Knafla, A. Harter, M. Ley, A. Esmaylzadeh, J.-M. Régis, D. Bittner, A. Blazhev, F. von Spee and J. Jolie.  
**Improving fast-timing time-walk calibration standards: Lifetime measurement of the  $2_1^+$  state in  $^{152}\text{Gd}$ .**  
*Nuclear Instruments and Methods in Physics Research Section A: Accelerators, Spectrometers, Detectors and Associated Equipment* 1052 (2023), 168279.
- [6] A. Harter, M. Weinert, L. Knafla, J.-M. Régis, A. Esmaylzadeh, M. Ley and J. Jolie.  
**Systematic investigation of time walk and time resolution characteristics of CAEN digitizers V1730 and V1751 for application to fast-timing lifetime measurement.**  
*Nuclear Instruments and Methods in Physics Research Section A: Accelerators, Spectrometers, Detectors and Associated Equipment* 1053 (2023), 168356.



# Acknowledgements – *Danksagungen*

An dieser Stelle möchte ich gerne allen danken, die mich über die Jahre der Promotion begleitet und unterstützt haben. Mein besonderer Dank gilt:

- Prof. Dr. Jan Jolie für die Möglichkeit, meine persönlichen Interessen in dieser Arbeit verwirklichen zu können und mich auf die technischen Entwicklungen ebenso wie die damit gemessene Physik konzentrieren zu können. Ganz besonders auch für jede Unterstützung, die mir durch ihn zuteil wurde, das Projekt Doktorarbeit neben Familie umsetzen zu können, was keinesfall selbstverständlich ist. Nicht zu vergessen seine Wertschätzung und Förderung meiner Arbeit als Systemadministrator des IKP gegenüber.
- Prof. Dr. Peter Reiter für seine Zeit und Bereitschaft, als Zweitgutachter meine Arbeit zu prüfen. Ebenfalls auch dafür, dass er meine Arbeit als Systemadministrator immer sehr geschätzt und unterstützt hat.
- Prof. Dr. Andreas Schadschneider für seine Bereitschaft und Zeit den Vorsitz der Prüfungskommission zu führen.
- Dr. Christoph Fransen, dafür dass er immer für mich ansprechbar war, wenn es technische oder organisatorische Schwierigkeiten zu lösen gab. Sei es im Bezug auf den Beschleuniger, die Umsetzung und die Einrichtung von Experimenten. Aber auch für viele nützliche Gespräche im Bezug auf die physikalische Deutung oder Darstellung von Messergebnissen und noch vieles, vieles mehr! Danke für Deine Geduld!
- Dr. Stefan Heinze, der ebenfalls immer ansprechbar für mich war, wenn es um organisatorische und praktische Schwierigkeiten meiner Promotionszeit ging und mir mit seiner persönlichen Erfahrung (insbesondere als ehemaliger Sysop) vielfach weitergeholfen hat.
- Dr. Jean-Marc Régis für seine Expertise in der Fast-Timing-Methode und seine Hilfe bei Analyse und Weiterentwicklung der Methode. Ebenfalls für seine Expertise im Umgang mit dem Orange-Spektrometer, die er in großen Teilen an mich weitergeben hat.
- Nima Saed-Samii, der mir mit viel Geduld die Kunst des C++-Programmierens vermittelt hat und mir viel Hilfe zur Selbsthilfe auf diesem Gebiet geleistet hat.
- Dr. Claus Müller-Gattermann für seine Hilfe bei verschiedenen Experimenten, nützliche Diskussionen über die verschiedensten Themen von Umsetzung von fixen Ideen über Planung von Experimenten bishin zu vielen hilfreichen Tipps für Analysen und Ideen für Weiterentwicklungen.
- Meinen Kollegen im Sysop-Team, ganz besonders Martin Müller, für viele gemeinsame Arbeitsstunden, seine Zuverlässigkeit und seinen Mut, die Hauptverantwortung für das System des Institutes zu übernehmen.

- Dem Operateursteam unter Leitung von Frank Bielau, dass zuverlässig die benötigten Strahle zur gewünschten Zeit bereitgestellt hat, die zur Durchführung der Experimente für diese Arbeit von Nöten waren. Besonders auch Sebastian Brünsing, der oft mit viel Arbeitsaufwand besondere technische Anforderungen gelöst und bereitgestellt hat und der sich auch nicht zu schade war mittlere Katastrophen zu beseitigen. Viktor Rehl und Otto Rudolph, die immer sorgfältige Arbeit geleistet haben, besonders wenn es um die Orange-Experimente ging. Aber auch für viele unterhaltsame und interessante Gespräche in Spätschichten.
- Hr. Stefan Thiel, dem Chef der Feinmechanikwerkstatt, der immer bereit war für die Umsetzung von großen und kleinen Projekten.
- Allen Mitgliedern der Elektronikwerkstatt, die mich bei der Umsetzung meiner Projekte immer unterstützt haben.
- Allen Schichtleitern während meiner Experimente und allen Mitgliedern des IKP Köln für eine angenehme Arbeitsatmosphäre.
- Lukas Knafla, Arwin Esmaylzadeh, Michael Weinert, Mario Ley und Franziskus v. Spee für die vielen guten und intensiven Gespräche im Bezug auf Kernphysik, Fast-Timing, Datenaufnahme, Orange und vieles mehr und für die Geduld beim Korrekturlesen meiner Arbeiten. Danke auch, dass ihr mich immer wieder ermutigt habt!
- Allen meinen Freunden, besonders Moritz Will, Stefan Müller, Lukas Gawlik, Reinhild Bues und Lukas Golla, die mich immer wieder motiviert und durchgängig an mich geglaubt haben.
- Das Wichtigste zuletzt: meiner Frau Ursula, die mich durchgängig unterstützt und gestärkt hat, auch wenn es manchmal sehr schwierig war, durchzuhalten. Danke, dass Du immer für mich da warst! Meinen Kindern Charlotte, Jakob und Ida-Marie, die immer mitgefiebert haben und alle Höhen und Tiefen mitgetragen haben!

# Contribution to publications essential for this thesis

## Publication I:

### Lifetime measurements in the tungsten isotopes $^{176,178,180}\text{W}$

- A. Harter, A. Esmaylzadeh, L. Knafla, F. Dunkel, V. Karayonchev and J.-M. Régis commissioned the setup at the Orange spectrometer
- A. Harter, A. Esmaylzadeh, L. Knafla, M. Ley and V. Karayonchev commissioned the setup at the HORUS spectrometer
- A. Harter, L. Knafla, A. Esmaylzadeh, V. Karayonchev, M. Ley, F. Dunkel and J.-M. Régis planned and carried out the Orange experiments
- A. Harter, A. Esmaylzadeh, L. Knafla, M. Ley and V. Karayonchev planned and carried out the HORUS experiment
- A. Harter performed the data analysis of the Orange and the HORUS experiments
- A. Harter and J. Jolie performed the interacting boson model calculation
- A. Harter wrote the paper

## Publication II:

### Systematic investigation of time walk and time resolution characteristics of CAEN digitizers V1730 and V1751 for application to fast-timing lifetime

- A. Harter commissioned the fast-timing source test stand
- A. Harter and M. Weinert commissioned the new data acquisition for fast-timing
- A. Harter planned and carried out the experiments
- A. Harter performed the data analysis of the experiments
- A. Harter wrote the paper

## Publication III:

### Lifetime measurements in low yrast states and spectroscopic peculiarities in $^{182}\text{Os}$

- A. Harter, A. Esmaylzadeh, L. Knafla, V. Karayonchev, M. Ley and C. Fransen commissioned the Horus setup
- A. Harter, J. Jolie, A. Esmaylzadeh, L. Knafla, M. Ley and V. Karayonchev planned and carried out the experiment
- A. Harter performed the data analysis of the experiment
- A. Harter and J. Jolie classified and discussed the results
- A. Harter wrote the paper





# Curriculum vitae

## Persönliche Daten

Name: Nikolaus Andreas Harter  
Anschrift: Arnoldstr. 6a, 53225 Bonn  
Geburtsdatum: 17. Februar 1990  
Geburtsort: Bergisch Gladbach  
Nationalität: deutsch  
Familienstand: verheiratet, drei Kinder

## Hochschulstudium und Promotion

2018-2023 Promotion an der Universität zu Köln  
im Fach Experimentalphysik  
2010-2018 Studium Lehramt Mathematik und Physik an der Universität  
zu Köln  
(1. Staatsexamen)

## Arbeitsverhältnisse

seit 2019 Wissenschaftlicher Mitarbeiter am Institut für Kernphysik  
der Universität zu Köln  
2018-2019 Wissenschaftliche Hilfskraft am Institut für Kernphysik  
der Universität zu Köln  
2016-2018 Studentische Hilfskraft am Institut für Kernphysik  
der Universität zu Köln

## Schulbildung

1999-2009 Dietrich-Bonhoeffer-Gymnasium, Bergisch Gladbach  
1996-1999 Katholische Grundschule Hand, Bergisch Gladbach



# Erklärung zur Dissertation

Hiermit versichere ich an Eides statt, dass ich die vorliegende Dissertation selbstständig und ohne die Benutzung anderer als der angegebenen Hilfsmittel und Literatur angefertigt habe. Alle Stellen, die wörtlich oder sinngemäß aus veröffentlichten und nicht veröffentlichten Werken dem Wortlaut oder dem Sinn nach entnommen wurden, sind als solche kenntlich gemacht. Ich versichere an Eides statt, dass diese Dissertation noch keiner anderen Fakultät oder Universität zur Prüfung vorgelegen hat; dass sie - abgesehen von unten angegebenen Teilpublikationen und eingebundenen Artikeln und Manuskripten - noch nicht veröffentlicht worden ist sowie, dass ich eine Veröffentlichung der Dissertation vor Abschluss der Promotion nicht ohne Genehmigung des Promotionsausschusses vornehmen werde. Die Bestimmungen dieser Ordnung sind mir bekannt. Darüber hinaus erkläre ich hiermit, dass ich die Ordnung zur Sicherung guter wissenschaftlicher Praxis und zum Umgang mit wissenschaftlichem Fehlverhalten der Universität zu Köln gelesen und sie bei der Durchführung der Dissertation zugrundeliegenden Arbeiten und der schriftlich verfassten Dissertation beachtet habe und verpflichte mich hiermit, die dort genannten Vorgaben bei allen wissenschaftlichen Tätigkeiten zu beachten und umzusetzen. Ich versichere, dass die eingereichte elektronische Fassung der eingereichten Druckfassung vollständig entspricht.

## Teilpublikationen

- A. Harter *et al.* "Lifetime measurements in the tungsten isotopes  $^{176,178,180}\text{W}$ ".  
*Phys. Rev. C* 106, 024326 (2022)
- A. Harter *et al.* "Systematic investigation of time walk and time resolution characteristics of CAEN digitizers V1730 and V1751 for application to fast-timing lifetime measurement".  
*NIM A* 1035, 168356 (2023)
- A. Harter *et al.* "Lifetime measurements in low yrast states and spectroscopic peculiarities in  $^{182}\text{Os}$ ".  
*Phys. Rev. C* 108, 024305 (2023)

Köln, den 16. Juni 2023



(Nikolaus Andreas Harter)

Die Dissertation beinhaltet die Gewinnung und Analyse von Primärdaten. Diese Daten sind auf den Servern des Instituts für Kernphysik gesichert und zugänglich.